2015

Rational design of TiO2 architectures as photoanodes for efficient dye-sensitized solar cells

Jianjian Lin
University of Wollongong, jl824@uowmail.edu.au

UNIVERSITY OF WOLLONGONG

Rational Design of TiO_2 Architectures as Photoanodes for Efficient Dye-sensitized Solar Cells

This thesis is presented as part of the requirement for the

Award of the Degree of

Doctor of Philosophy

of the

University of Wollongong

By

Jianjian Lin

Institute for Superconducting and Electronic Materials

March 2015

ABSTRACT

Solar energy is the largest source of carbon-free energy that can be converted into heat and electricity. Since the early 1990s, dye-sensitized solar cells (DSCs) have received a great deal of attention as a promising alternative photovoltaic technology on account of their projected low costs and reduced energy input in manufacture. Considerable efforts have been made to improve the energy conversion efficiency, by developing or modifying DSC components, such as sensitizers, photoanodes, electrolytes, and counter electrodes. However, a number of challenging issues remain, such as new optimised structures are required as DSCs evolve. The aims of this thesis are to design, develop and investigate new semiconductor TiO_2 architectures for use as photoanodes in different types of DSC (such as flexible DSCs, cobalt-based DSCs, rutile TiO_2-based DSCs) applications.

Among the novel materials developed as part of this thesis, a new type of highly connected hierarchical textured TiO_2 spheres (HCHT) was rationally designed for DSCs. An overall energy conversion efficiency of up to 9.0 % can be achieved by using these HCHT as the photoelectrode with N719 dye, a considerable improvement over state-of-the-art commercial available TiO_2 particles (Dyesol TiO_2 paste) (8.2 %) under the same conditions.

A new photoanode architecture for cold isostatic pressing (CIP), with a new mesoporous hierarchical anatase TiO_2 (MHAT) architecture deposited onto P25, was rationally designed for efficient charge transport and better light management in flexible dye-sensitized solar cells, with a 5.6 % conversion efficiency realized.

Mesoporous anatase single crystals (MASCs) with special polyhedral pores (~ 7 nm) is employed to construct MK-2–sensitized solar cells using a cobalt redox shuttle,

with a maximum efficiency of 8.7 % achieved, which is significantly higher than for analogous devices based on commercial Dyesol TiO_2 (6.3 %).

A DSC combining a well-defined 3D hierarchical rutile TiO_2 architecture (HRT) is reported in conjunction with a high-extinction-coefficient metal-free organic sensitizer (D149), achieving a conversion efficiency of 5.5 %, which is superior to ones employing P25 (4.5 %), comparable to state-of-the-art commercial transparent titania anatase paste (5.8 %). Further to this, an overall conversion efficiency 8.6 % was achieved when HRT was used as the light scattering layer, a considerable improvement over the commercial transparent/reflector titania anatase paste (7.6 %), a significantly smaller gap in performance than has been seen previously. In addition, two dyes, N719 and D149, were used as sensitizers of the modified HRT-based DSCs, with maximum η of 5.6 % and 5.8 % achieved, respectively.

ACKNOWLEDGEMENTS

The thesis was carried out and completed in the Institute for Superconducting and Electronic Materials (ISEM) and Intelligent Polymer Research Institute (IPRI) at the University of Wollongong (UOW, Australia), the University of Queensland (UQ, Australia), Monash University (Australia), and Sungkyunkwan University (SKKU, South Korea).

Firstly I would like to give my deepest thanks to my supervisor Prof. Shi Xue Dou, who provided me with this great opportunity to work in ISEM. I am deeply grateful to my supervisors Prof. Jung Ho Kim (ISEM) and Dr. Andrew Nattestad (IPRI). Both of them not only gave me valuable guidance and excellent supervision during my study, but they are also good friends in my life. I feel very lucky to have been supervised by them.

I would like to thanks Prof. Lianzhou Wang of UQ, Prof. Yi-Bing Cheng of Monash University, Prof. Sang-Woo Kim of SKKU, Prof. Yusuke Yamauchi of the National Institute for Materials Science (NIMS, Japan) and their group members for their strong support and great help during my visits to their laboratories.

I would like to thanks Prof. Yoon-Uk Heo (Pohang University of Science and Technology, South Korea) very much for his professional TEM support for my work.

Many thanks to my group members Dr. Ziqi Sun, Dr. Jae-Geun Kim, Dr. Fargol Hasani Bijarbooneh, Dr. Victor Magras, and Mr. Yuhai Dou for their great help and useful discussions.

Many thanks to my colleges Dr. Hua Yu (UQ), Dr. Yang Bai (UQ), Dr. Attila Janos Mozer (IPRI), Mr. Long Zhao (IPRI), Dr. Yong Peng (Monash Uni.), Mr. Alexander R. Pascoe (Monash Uni.), Dr. Fuzhi Huang (Monash Uni.), Mr. Wanchul Seung (SKKU) for their great help on my work.

I also would like to thanks my good friends Dr. Yun Zhang (ISEM), and Dr. Jonathan Read (UQ) for their love to me.

Finally but not the least, I would like to thanks my parents, sisters, and brothers very much for their strong support and love to me.

Table of Contents

LIST OF SELECTED PUBLICATIONS DURING PHD

1. **J. Lin**, L. Zhao, Y.-U. Heo, L. Wang, F. H. Bijarbooneh, A. J. Mozer, A. Nattestad, Y. Yamauchi, S. X. Dou, and J. H. Kim, *"Mesoporous Anatase Single Crystals for Efficient Cobalt$^{(2+/3+)}$-based Dye-sensitized Solar Cells" Nano Energy*, 2015, **11**, 567. **(IF: 10.325)**

2. **J. Lin**, Y.-U. Heo, A. Nattestad, Z. Sun, L. Wang, J. H. Kim, and S. X. Dou, *"3D Hierarchical Rutile TiO_2 and Metal-free Organic Sensitizer Producing Dye-sensitized Solar Cells 8.6 % Conversion Efficiency" Sci. Rep.,* 2014, **4**, 5769. **(Nature Publishing Group, IF: 5.578)**

3. **J. Lin**, Y. Peng, A. R. Pascoe, F. Huang, Y.-B. Cheng, Y.-U. Heo, A. Nattestad, W. Seung, S. K. Kim, H. J. Yoon, S.-W. Kim, Y. Yamauchi, S. X. Dou, and J. H. Kim, *"A Bi-layer TiO_2 Photoanode for Highly Durable, Flexible Dye-sensitized Solar Cells" J. Mater. Chem. A*, 2015, **3**, 4679. **(IF: 7.443)**

4. **J. Lin**, A. Nattestad, H. Yu, Y. Bai, L. Wang, S. X. Dou and J. H. Kim, *"Highly Connected Hierarchical Textured TiO_2 Spheres as Photoanodes for Dye-sensitized Solar Cells" J. Mater. Chem. A*, 2014, **2**, 8902. **(IF: 7.443)**

5. **J. Lin**, Y.-U. Heo, A. Nattestad, S. X. Dou and J. H. Kim, *"N719- and D149-sensitized 3D Hierarchical Rutile TiO_2 Solar Cells - A Comparative Study" Phys. Chem. Chem. Phys.*, 2015, **17**, 7208. **(IF: 4.493)**

6. **J. Lin**, Y.-U. Heo, A. Nattestad, Y. Yamauchi, S. X. Dou and J. H. Kim, *"Mesoporous Hierarchical Anatase for Dye-sensitized Solar Cells Achieving Over 10 % Conversion Efficiency" Electrochim. Acta*, 2015, **153**, 393. **(IF: 4.504)**

7. R. R. Salunkhe, **J. Lin**, V. Malgras, S. X. Dou, J. H. Kim, and Y. Yamauchi, *"Large-Scale Synthesis of Coaxial Carbon Nanotube/Ni(OH)$_2$ Composites for Asymmetric Supercapacitor Application" Nano Energy*, 2015, **11**, 211. **(IF: 10.325)**

8. Y. Chen, **J. Lin**, L. Zhang, M. Wu, H. Chen, L. Zhang, J. H. Kim, L. Wang, and J. Shi, *"Controlled Synthesis of Single-Crystalline Mesoporous TiO_2 Nanoparticles for High-Performance Stimuli-Responsive Drug Delivery" Adv. Funct. Mater.* (under review, **IF: 10.4**)

9. M. Pramanik, V. Malgras, **J. Lin,** J. H. Kim and Y. Yamauchi, *"Shape-Controlled Synthesis of Mesoporous Iron Phosphate with Crystalized Frameworks" Chem. Comm*.2015 (Accepted, **IF: 6.834**)

10. M. Pramanik, V. Malgras, **J. Lin,** J. H. Kim and Y. Yamauchi, *"Electrochemical Property of Mesoporous Crystalline Iron Phosphonate Anode in Li-ion Rechargeable Battery" J. Nanosci. Nanotech*. (Accepted, **IF: 2.4**)

11. W. Seung, M. K. Gupta, K. Y. Lee, K.-S. Shin, J.-H. Lee, T. Y. Kim, S. Kim, **J. Lin**, J. H. Kim, S.-W. Kim, *"Nanopatterned Textile Based Wearable Triboelectric Nanogenerator" ASC Nano,* 2015, **9**, 3501. **(IF: 12.881)**

LIST OF FIGURES

(*J-V*) curves of solar cells with well-defined spheres (DSC-1), deformed spheres (DSC-2), and commercial nanoparticles (DSC-3).

Figure 2.8 SEM and TEM images of hierarchical anatase TiO_2 microsphere (HTS) via acid thermal reaction before (a) and after (b–d) calcination. Electron transport time as a function of incident light intensity (e) and lifetime as a function of open-circuit voltage (f) for DSCs based on Film I (P25), II (P25 + HTS), and III (HTS).

Figure 2.9 (a) Appearance of the TiO_2 electrodes before and after processed by CIP. (b) Variation of the transmittance of the TiO_2 films on ITO-PEN substrates processed at different CIP pressures. All the films had the same thickness (12 mm) before CIP compression.

Figure 2.10 (a) Top view and (b) cross-sectional SEM image of a TiO_2 : PS = 20:1 photoanode. (c) *I-V* curves of devices made from 4 mm films of D18NR-T and PS-assisted pastes with ACN-Co(bpy) and MPN-Co(dtb) electrolytes at 0.1 and 1 sun.

Figure 2.11 (a-c) Morphology of rutile TiO_2 nanowire arrays on FTO-coated glass substrate. Comparison of (d) electron diffusion coefficients as a function of the photoelectron density (*n*) and (e) the photoelectron density as a function of the voltage for rutile nanowire- and nanoparticle-based DSCs with a laser illumination at 680 nm. (f) Comparison of recombination lifetimes for rutile nanowire- and nanoparticle-based DSCs as a function of the photoelectron density with laser illumination at 680 nm. (g) *J-V* characteristics of DSCs based on a 4.5 mm long nanowire array and a nanoparticle film under simulated AM 1.5 light (*J* = photocurrent density).

Figure 2.12 Field emission SEM (FESEM) images of oriented rutile TiO_2 nanorod film grown on FTO substrate in 30 mL deionized water, 30 mL hydrochloric acid, and 1 mL titanium butoxide at 150 °C for 20 h. (a) Top view, (b) cross-sectional view, (c) tilted cross-sectional view, (d) HRTEM image of the single TiO_2 nanorod shown in

the inset, (e) Photocurrent-photovoltage characteristics of DSCs assembled from 4 μm thick rutile TiO_2 nanorod films (1) without and (2) with $TiCl_4$ treatment.

Figure 2.13 (a, b) TEM images of TiO_2-Nanobranch synthesized by a seeding method. (c) HRTEM image of the TiO_2-Nanobranch. The inset is the fast Fourier transform (FFT) pattern. (d) Schematic illustration of the formation of the rutile TiO_2-Nanobranch. (e) *J-V* curves measured using TiO_2-Nanobranch and TiO_2-Nanowire as photoelectrodes.

Figure 2.14 (a-e) Morphology of the bilayer TiO2 nanostructures synthesized from a solution with a composition of TTIP (aq) : EG = 1:1 and (f) the corresponding SAED pattern of (e), (g) *J–V* curves of the DSCs with different photoanodes.

Figure 3.1 Physical characterization of the calcined HCHT: (a) low magnification SEM image; (b) particle size distribution; (c) SEM image of an individual sphere; (d) bright-field TEM image visualizing the nanosheet building blocks, with inset: selected area electron diffraction (SAED) pattern of the whole sphere in (d); (e) TEM image of two typical interconnected spheres; (f) enlarged TEM image revealing details of the interconnection of nanosheets; (g) HRTEM image showing the fringe spacing of anatase TiO_2 nanocrystals; and (h) XRD pattern of the calcined HCHT, indicating TiO_2 crystals with the tetragonal anatase phase (JCPDS No. 21-1272, a = 3.785 Å, b = 3.785 Å, c = 9.514 Å) after the calcination treatment, without any impurity phase.

Figure 3.2 (a) Low magnification SEM image of the calcined HCHT, (b) higher magnification image of the nanosheet building blocks, (c) low magnification TEM image of the urchin-like spheres, (d) enlarged TEM image of the nanosheet building blocks; (e) Raman spectrum of the calcined HCHT clearly identifies the anatase phase from the characteristic Raman modes at 142.1 cm^{-1} (E_g), 194.5 cm^{-1} (E_g), 396.1 cm^{-1}

(B_{1g}), 515.8 cm^{-1} (A_{1g}), and 638.4 cm^{-1} (E_g), which can be assigned to the Raman active modes ($A_{1g}+B_{1g}+3E_g$) of anatase.

Figure 3.3 Schematic diagram of the formation process of HCHT.

Figure 3.4 TEM images, with the insets showing higher magnification, of as-prepared precipitates obtained after different reaction times (a) 1 h, (b) 5 h, (c) 12 h, via hydrothermal reaction of a solution containing 0.5 mL TB and 30 mL HAc at 150 ^oC.

Figure 3.5 XRD patterns of as-prepared precipitates obtained after different reaction times via hydrothermal reaction of a solution containing 0.5 mL TB and 30 mL HAc at 150 ^oC, as well as a sample obtained after 12 h of reaction and 3 h of calcination at 500 ^oC.

Figure 3.6 (a) FTIR spectra of HAc, TB, and the precipitates obtained after different reaction times via a hydrothermal reaction of a solution containing 0.5 mL TB and 30 mL HAc at 150 ^oC; (b) magnification of (a) in the range of 1000-2000 cm^{-1}.

Figure 3.7 Thermogravimetric analysis and differential scanning calorimetry curves of the dried precipitate prepared via hydrothermal reaction of a solution containing 0.5 mL TB and 30 mL HAc at 150 ^oC for 12 h.

Figure 3.8 (a) N_2 adsorption-desorption isotherms of the HCHT (red closed triangles), the Dyesol-transparent layer (Dyesol-T, 18NR-T, black closed circles) and the Dyesol-scattering layer (Dyesol-S, WER2-O, blue closed circles); and (b) corresponding pore size distributions calculated by the BJH method from the adsorption branch. Before BET measurements, all the particles were dried and then calcined at 500 ºC for 3 h.

Figure 3.9 *J-V* characteristics of Dyesol- and HCHT-based DSCs. Illumination intensity of 100 mW cm^{-2} with AM 1.5 and active area of 0.16 cm^2 were applied. Inset is a SEM cross-sectional image of the nanosheet-based highly connected hierarchical

the pore size distribution calculated from the adsorption branch of a nitrogen isotherm by the Barrett-Joyner-Halenda (BJH) method.

Figure 4.3 a) XRD pattern of the MHAT, indicating that the spheres are anatase TiO_2 phase (JCPDS No. 21-1272, a = 3.785 Å, b = 3.785 Å, c = 9.514 Å); b) Raman spectrum of the MHAT, confirming the anatase phase from the characteristic Raman modes at 142.1 cm^{-1} (E_g), 194.5 cm^{-1} (E_g), 396.1 cm^{-1} (B_{1g}), 515.8 cm^{-1} (A_{1g}), and 638.4 cm^{-1} (E_g), which can be assigned to the Raman active modes ($A_{1g}+B_{1g}+3E_g$) of anatase.

Figure 4.4 a) Schematic illustration of P25 and MHAT photoanode structures for flexible DSCs on ITO|PEN substrate; b) relationship between the pressure applied during a cold isostatic pressing (CIP) and the photovoltaic parameters: short-circuit photocurrent density (J_{sc}), open-circuit photovoltage (V_{oc}), fill factor (FF), and total power conversion efficiency (η); c) diffuse reflectance spectra of TiO_2 films before and after CIP: P25 (left) and MHAT (right), with corresponding digital photograph of P25 (12 μm) and MHAT (12 μm) films before and after CIP as insets.

Figure 4.5 Normalized PCE of P25- and MHAT-based flexible DSCs as a function of bending cycles, with radius of 50 mm.

Figure 4.6 a) Schematic illustration of P25/MHAT (6 μm + 6 μm) photoanode structure for flexible DSCs on ITO|PEN substrate; cross-sectional BF-STEM images of P25/MHAT (6 μm + 6 μm) photoanode structure: b) shows the interface between the P25 and the ITO|PEN substrate, c) shows the interface between the P25 and the MHAT, with the highlighted part showing the MHAT nanoribbon units penetrating into the P25 nanoparticle layer.

Figure 4.7 Low magnification FE-SEM images of different TiO_2 films on ITO|PEN substrates: P25 film a) before and b) after CIP; MHAT film c) before and d) after CIP; P25/MHAT film (e) before and (f) after CIP.

Figure 4.8 FE-SEM images of different TiO_2 films on ITO/PEN substrate: P25 film (a) before and (b) after CIP; MHAT film (c) before and (d) after CIP; P25/MHAT film (e) before and (f) after CIP.

Figure 4.9 a) *J-V* characteristics of DSCs; b) IPCE curves of DSCs based on flexible ITO|PEN substrates covered with layers of P25 (~ 12 μm), MHAT (~ 12 μm), and a MHAT film layer over a P25 under-layer [P25/MHAT (6 μm + 6 μm)].

Figure 4.10 *J-V* characteristics of P25-, MHAT-, P25/MHAT-based flexible DSCs under dark current.

Figure 4.11 Diffuse reflectance spectra of P25, P25/MHAT and MHAT (a) before and (b) after CIP.

Figure 4.12 Scheme of light scattering in P25, MHAT, and P25/MHAT films.

Figure 4.13 a) Electron lifetime (τ_n), b) electron diffusion coefficient ($D_{n,\,EIS}$), and c) electron diffusion length (L_n) as measured through impedance spectroscopy; d) electron diffusion coefficient ($D_{n,\,IMPS}$) measured though intensity modulated photocurrent spectroscopy (IMPS).

Figure 4.14 (a) Nyquist plots, with the inset showing the equivalent circuit, and (b) Bode phase plots of flexible DSCs based on P25, MHAT, and P25/MHAT.

Figure 4.15 a) Comparison of photovoltaic properties of normalized J_{sc}, normalized V_{oc}, normalized *FF* and normalized η of P25-, MHAT-, and P25/MHAT-based flexible DSCs as a function of bending cycles, with radius of 400 mm. Bending of photoanode was performed before constructing the DSCs. Cell performances were normalized compared with the cell without bending. b) Normalized PCE of

P25/MHAT-based flexible DSCs measured after bending the ITO|PEN substrate (100 cycles) within a specified radius of 400 mm to 30 mm. The insets show the digital photographs bent according to 400 mm, 100 mm, and 50 mm bending radii, respectively. c) Normalized PCE of P25/MHAT-based flexible DSCs as a function of bending radii of 400 mm, 100 mm, and 50 mm. The insets show the digital photographs bent by a bending machine during the test. The error bar represents the standard deviation from four devices.

Figure 4.16 Illustration of bending machine.

Figure 4.17 Normalized PCE of P25-, MHAT-, and P25/MHAT-based flexible DSCs as a function of bending cycles, with radius of 50 mm.

Figure 5.1 a) Low magnification FE-SEM image and b) ADF-STEM image, with inset: ED pattern, of as-prepared precipitate. c) Broad survey FE-SEM image of MASCs obtained after calcination at 500 ˚C for 3 h of the precipitate in a). d) FE-SEM image highlighting one single MASC. e) HAADF-STEM image of MASC, revealing homogeneous pores within a single crystal, with inset: ED pattern. f) HRTEM image of single MASC, with inset: scheme of polyhedral pore.

Figure 5.2 Physical characterization of MASCs: a) dynamic light scattering (DLS), showing particle size distribution; b) N_2 adsorption-desorption isotherms of MASCs; c) pore size distribution calculated by the Barrett-Joyner-Halenda (BJH) method from the adsorption branch of b); d) XRD pattern; e) Raman spectrum; and f) HR-TEM image, showing the fringe spacing of MASCs.

Figure 5.3 ADF-STEM images of one single MASC and its FFT pattern: a) a MASC particle, b) magnified image, c) high resolution image of a faceted pore, and d) FFT pattern of c).

Figure 5.4 High resolution image of a MASC facet, with inset FFT pattern.

Figure 5.13 a) IPCE curves of Dyesol (~ 4 µm)-, MASC (~ 4 µm)-, and Dyesol (~ 2 µm) + Reflector (~ 2 µm)-based DSCs; b) diffuse reflectance spectra of Dyesol (~ 4 µm), MASC (~ 4 µm), and Dyesol (~ 2 µm) + Reflector (~ 2 µm) films.

Figure 5.14 Electron lifetime versus a) short circuit current density (J_{sc}) and b) electron density (ED); c) diffusion coefficient versus J_{sc}; and d) open circuit voltage (V_{oc}) versus ED for the devices fabricated with MK-2 dye containing Dyesol or MASCs (two devices for each dye).

ED = ED (bulk)/ porosity.

Figure 5.15 Diffusion coefficient versus short circuit current density (J_{sc}) of the devices fabricated with MK-2 dye using MASCs, with both front side illumination (FSI) and back side illumination (BSI). (a and b indicate two different devices.)

Figure 6.1 XRD patterns of the as-prepared 3D hierarchical rutile TiO_2 architectures (HRT) [denoted as from HRT-1 to HRT-8] from a reaction solution containing 0.5 mL aqueous tetrabutyl titanate (TT) solution with 25 mL X M HCl (X = 1-8).

Figure 6.2 A typical Raman spectrum collected from the as-prepared HRT-1 with nanorod constituent units.

Figure 6.3 FESEM images of the as-prepared 3D hierarchical rutile TiO_2 architectures (HRT) [denoted as HRT-1 (a), HRT-2 (b), HRT-3 (c), HRT-4 (d), HRT-5 (e), HRT-6 (f), HRT-7 (g), HRT-8 (h)], synthesized from a reaction solution containing 0.5 mL aqueous tetrabutyl titanate (TT) solution with 25 mL X M hydrochloric acid (HCl) (X = 1-8).

Figure 6.4 (a) Low magnification SEM image of the as-prepared HRT-1 synthesized from a reaction solution containing 0.5 mL aqueous TT solution with 1M HCl; (b) a cross-sectional view, showing the core.

Figure 6.5 (a, c, e, g, i, k, m, o) High-magnification SEM images of HRT-1 to HRT-8, respectively; (b, d, f, h, j) TEM images of individual nanorods; (l, n, p) TEM images of nanorod bundles. The insets of (b, d, f, h, j, l, n, p) are the corresponding FFTs (b, d, f, h, j) and electron diffraction patterns (l, n, p).

Figure 6.6 Ledgewise growth of rutile nanorod (HRT-1). (a) Macro growth direction of a rutile nanorode; preferential growth to [001] direction, (b) Thickening of a nanorode by ledgewise growth of $(1\bar{1}0)$ surface, (c) atomic structure of a rutile nanorod.

Figure 6.7 (a) Schematic description of growth morphology of a rutile nanorod, (b) Enlarged image of stepped surface of Figure 6(a).

Figure 6.8 N_2 adsorption/desorption isotherms of the as-prepared HRT-1, HRT-2, HRT-3, and HRT-4, synthesized from a reaction solution containing 0.5 mL aqueous TT solution with 25 mL 1 M-4 M HCl concentrations.

Figure 6.9 Optical absorption of dye desorbed from P25, HRT-1 and Dyesol-T films by dissolving sensitized samples into 0.4 M NaOH in methanol solution.

Figure 6.10 (a) N_2 adsorption-desorption isotherms of P25 (black closed circles), HRT-1 (red closed triangles) and Dyesol-T (blue closed stars); and (b) corresponding pore size distributions calculated by the BJH method from the adsorption branch.

Figure 6.11 (a) *J-V* characteristics of P25-, HRT-1- and Dyesol-T-based DSCs. Cells were illuminated at an intensity of 100 mW cm^{-2} with a spectrum approximately AM 1.5 G and an active area of 0.16 cm^2; inset: incident photon to current conversion efficiency (IPCE) curves of P25-, HRT-1- and Dyesol-T-based DSCs. (b) diffuse reflectance spectra of P25, HRT-1 and Dyesol-T films.

HRTA film thickness: (a) open-circuit voltage, V_{oc}, (b) short circuit photocurrent density, J_{sc}, (c) fill factor, *FF*, and (d) solar-to-electric energy conversion efficiency, η.

Figure 7.4 (a) *I-V* curves, (b) IPCE spectra of champion DSCs with N719-based (black solid dots) and D149-based (red open dots) sensitizers (light intensity: 100mA cm^{-2}, AM 1.5).

Figure 7.5 (a) Nyquist plots, inset: the equivalent circuit, (b) Bode phase plots of DSCs with N719-based (black solid dots) and D149-based (red open dots) sensitizers at V_{oc} under 1 sun illumination.

LIST OF TABLES

LIST OF ABBREVIATION

Abbreviation	Name
DSCs	dye-sensitized solar cells
0D	zero dimensional
1D	one dimensional
3D	three dimensional
FTO	fluorine-doped tin oxide
TCO	transparent conducting oxide
I^-/I_3^-	iodide/triiodide
HOMO	the highest occupied molecular orbital
LUMO	the lowest unoccupied molecular orbital
η	solar-to-electric conversion efficiency
J_{sc}	the short-circuit photocurrent density
V_{oc}	the open-circuit photovoltage
FF	the fill factor
P_{in}	the incident light intensity
AM	air mass
I-V	photocurrent-photovoltage
IPCE	incident photon to current conversion efficiency
EIS	electrochemical impedance spectroscopy

I_{sc}	the short circuit current density
R_s	the series resistance
CPE	constant phase element
P_{max}	the maximum power
E_g	band gap
L_n	the electron diffusion length
D_n	the electron diffusion coefficient
τ_n	the electron lifetime
τ_r	the recombination times
TEM	transmission electron microscopy
HRTEM	high resolution transmission electron microscopy
BF-STEM	bright-field scanning transmission electron microscopy
ADF-STEM	the annular dark-field scanning transmission electron microscopy
HAADF-STEM	the high-angle annular dark-field scanning transmission electron microscope
FESEM	Field emission scanning electron microscope
SAED	the selected area electron diffraction

UV-Vis	Ultraviolet-visible
XRD	X-ray diffraction
FTIR	Fourier transform infrared spectroscopy
TGA	thermogravimetric analysis
BET	Brunauer-Emmett-Teller
BJH	Barrett-Joyner-Halenda
V_p	the specific cumulative pore volume
ρ	the density
R	roughness factor
P	the porosity
PEN	polyethylene naphthalate
PET	polyethylene terephthalate
CIP	Cold isostatic pressing
IMPS	Intensity modulated photocurrent spectroscopy
HCHT	highly connected hierarchical textured TiO_2 spheres
MHAT	Mesoporous Hierarchical Anatase TiO_2
MASCs	Mesoporous Anatase Single Crystals
HRT	3D Hierarchical Rutile TiO_2 Architectures

1 INTRODUCTION

It is energy that makes the world sustainably working. The humankind consumes energy ~ 4.7×10^{20} J and the energy consumption will continuously grow year by year in the future. The increasing global demand for energy in the world is expected to represent twice the current usage by 2050. However, the earth's resources are very limited; it is humanity's duty to find out a way for the development the sustainable society and economics. Photovoltaics (PV) solar cells are one type of renewable sources; The PV market has been growing exponentially, and will grow by 25-30 % as expected in the following decades. As one of the most feasible renewable energy sources, dye-sensitized solar cells (DSCs) have attracted great research and industry attention since 1990s, on account of the features as listed below: 1) in contrast to the conventional photovoltaic cells, DSCs have relatively high efficiency under the standard conditions; 2) lower dependence on the temperature, irradiation, and the angle of incident light; 3) easy fabrication; 4) environmentally-friendly; 5) flexible and lightweight; 6) rational design, such as multiple colour choices and transparency. [1]

Typically, a DSC is composed of four parts: a working electrode [typically a dye-sensitized nanocrystalline titanium dioxide (TiO_2) film], the dye, an electrolyte [most often containing iodide (I^-)/tri-iodide (I_3^-) redox couple], and a counter electrode [typically platinum (Pt)]. [2]

In this thesis, different TiO_2 architectures were designed and fabricated for high efficiency DSCs, with emphasis on the materials design and synthesis, as well as novel designs for different types of DSCs, such as flexible DSCs, cobalt-based DSCs, and rutile TiO_2-based DSCs. The microstructures and electrochemical properties of

the synthesized TiO_2 architectures were examined through experimental and theoretical analysis.

An overview of the thesis in each chapter:

Chapter 2 is a review of the DSCs and is a comprehensive background of DSCs, including the working principle of the DSCs; key parameters and characterizations for the performance of a DSC; photoanode materials in DSCs; development of TiO_2 morphologies for high efficient DSCs; and optimization of TiO_2 photoanode for flexible/cobalt-based/rutile TiO_2-based DSCs.

Chapter 3 presents a new type of highly connected hierarchical textured TiO_2 spheres as the photoanode. An overall energy conversion efficiency of up to 9.0 % can be achieved by using these spheres, beneficial to enhanced dye loading and efficient light scattering, as well as the efficient electron transfer pathways because of the interpenetrating individual sheets of the spheres.

Chapter 4 introduces a new type of photoanode, where microstructured TiO_2 sea urchin-like assemblies, composed of high aspect-ratio nanoribbons were deposited onto a nanoparticle layer (P25), with 5.8 % conversion efficiency realized; this morphology and assembly is beneficial due to its enhanced dye loading as well as enhanced light scattering. Importantly, we also show the benefits of a bi-layer structure where the nanoribbons penetrate into the nanoparticle layer (P25) after CIP, resulting in improved adhesion between the TiO_2 anode film and the P25 under layer on the indium tin oxide-coated polyethylene naphthalate (ITO|PEN) substrate, leading to improved mechanical stability and durability, efficient electron transfer pathways.

Chapter 5 presents mesoporous anatase single crystals (MASCs) with unique polyhedral pores for cobalt-based DSCs, with a maximum efficiency of 8.7 % achieved. The enhanced performance for devices containing MASCs is attributable to

the good electronic connectivity throughout the single crystal structure, as well as high surface area without compromising the large crystal size, which affords a high light harvesting efficiency (LHE).

Chapter 6 presents a DSC combining a 3D hierarchical rutile TiO_2 architecture (HRT) in conjunction with a high-extinction-coefficient metal-free organic sensitizer (D149), achieving a conversion efficiency of 5.5 %. Further to this, an overall conversion efficiency of 8.6 % was achieved when HRT was used as the light scattering layer, a considerable improvement over the commercial transparent/reflector titania anatase paste (7.6 %).

Chapter 7 compares two commercially available dyes (a ruthenium complex, N719 and a metal-free organic indoline D149) used as sensitizers, with maximum solar-to-electric conversion efficiency (η) of 5.6 % and 5.8 % achieved, respectively. The higher η of D149-sensitized DSC is ascribed to its higher molar extinction co-efficient. Hence, metal-free organic D149 sensitizer can be considered as a better candidate for low-cost rutile-based DSC application.

Chapter 8 summarizes the conclusions of the thesis.

2 LITERATURE REVIEW

As one of the key elements of DSCs, TiO_2 plays significant roles, such as facilitating high dye loading (by way of a high and accessible surface area), facilitating efficient electron injection (by way of conduction band edge potential), and electron transportation and collection, and hence, significantly influences the photocurrent, photovoltage and final power conversion efficiency. Previous research has shown that the efficiency of DSCs is greatly influenced by the composition, crystal phase and crystallinity, specific surface area, porosity, and most importantly, morphology of TiO_2. Therefore, tremendous efforts have been recently devoted to designing the structure and morphology of TiO_2, including zero-dimensional (0D) nanoparticles, one-dimensional (1D) structures, two-dimensional (2D) structures and three-dimensional (3D) hierarchical architectures. For example, it has been shown that because the units of 1D nanostructures are single crystals, ordered arrays of 1D TiO_2 nanostructures (such as TiO_2 nanotubes, nanowires, nanorods, nanofibers, *etc.*) have higher charge collection efficiencies, higher electron lifetimes and lower recombination rates, and thus, higher short-circuit current densities than those based on TiO_2 nanoparticles. [3-9] In addition, spherical anatase TiO_2 beads have shown great DSC performance because of the increased dye loading (due to the higher surface area) and efficient light-scattering ability (due to different particle sizes), as well as the efficient electron transport and diffusion (due to the well interconnected network among the nanoparticles in the anatase beads). [10-12] As the packing materials for selective phosphopeptide enrichment and chromatographic separation, micron-scale anatase or rutile TiO_2 spheres with variable pore sizes have shown good performance in DSCs application. [13-15]

2.1 Working Principle of Dye-sensitized Solar Cells (DSCs)

Since the pioneer working in 1991, the configurations and componentry of a DSC have been further modified and developed. [16] The operation of a DSC is based on the concepts of nanotechnology and molecular engineering. The typical DSC configuration is fabricated by sandwiching a dye-anchored mesoporous metal oxide (most often TiO_2), between two conducting glass or plastic substrates in the presence of a redox electrolyte. At the heart of the device is the mesoporous oxide layer composed of a network of TiO_2 nanoparticles, known as the photoelectrode, that have been sintered together to establish electronically conductive pathways. Typically, the film thickness is ~ 10 μm, the nanoparticle size in the range of 10-30 nm in diameter, and the porosity is 50-60 %.

Figure 2.1 is a schematic illustration of the working principle of a DSC, with the Eqs. (1) to (6) listed, showing the photocurrent generation processes. [17] Under illumination, the dye molecules are excited from the ground state to their excited state [Eq. (1)], whereupon an electron from this excited state molecule can be injected into the conduction band of TiO_2 [Eq. (2)]; the electron then travels to the counter electrode through the external circuit, while at the same time, leaving the dye molecule in an oxidized state. The dye molecules recover to their ground state by accepting electrons from the electrolyte [mainly an organic solvent which contains the iodide/triiodide (I^-/I_3^-) redox couple [Eq. (3)] or an organic hole conductor which penetrates into the mesoporous film]. The oxidated state of I_3^- is further restored by accepting the electrons that are transferred from the counter electrode (typically a Pt counter electrode) [Eq. (4)]. In the whole process, the electrons migrate through the outside load and one closed circuit is completed by converting the sun light into the electricity without any net chemical transformation. Apart from the processes shown

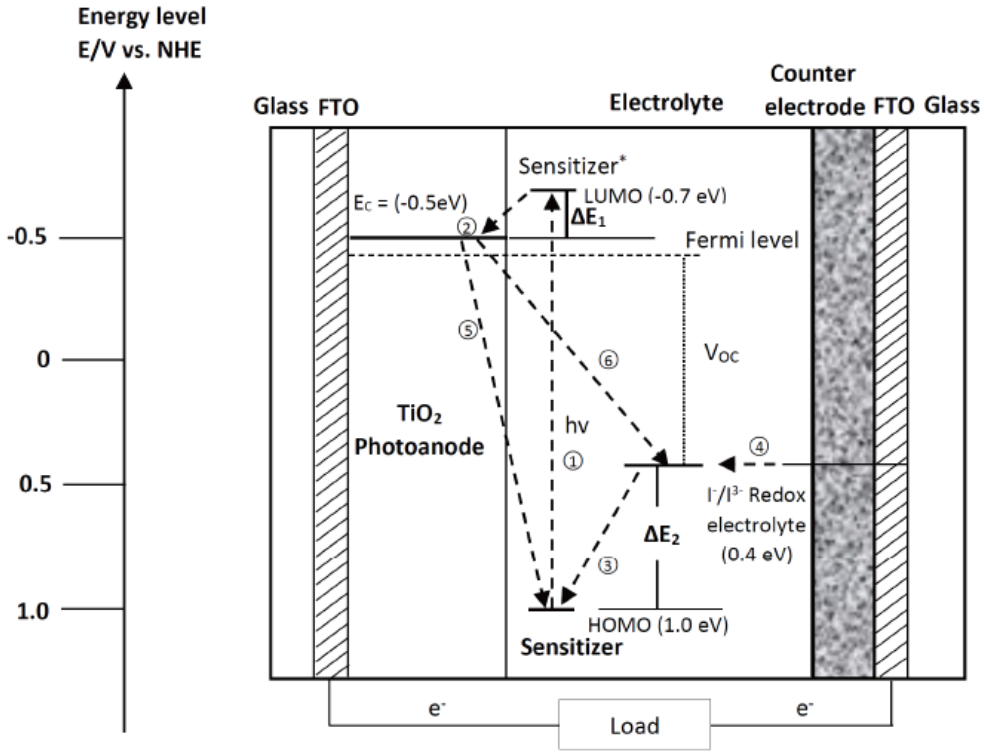

Figure 2.1 A schematic illustration of the working principle of a DSC from Hara *et al*. [17]

in the Eqs. (1) - (4) relating to the electron transfer processes, there are also some undesired reactions that occur as listed in Eqs. (5) and (6). By recombining with the oxidized dye molecules [Eq. (5)] or the acceptors of the electrolyte [Eq. (6)], the electrons which are injected into the conduction band of TiO_2 can also be exhausted. Therefore, to obtain a stable photocurrent, the reactions of Eqs. (2) and (3) should be kinetically more favourable than the side reactions of Eqs. (5) and (6). In principle, when the electrons are transferred to the redox couple (I_3^-), it can occur either at the interface between TiO_2 and I^-/I_3^-, or in the areas of the photoanode connection which are exposed to I^-/I_3^-. For example, a dense TiO_2 blocking layer can be used to suppress the second route, with spray pyrolysis used to deposit the oxide on the anode.

$$S + h\nu \rightarrow S^* \qquad (1)$$

$$S^{*} \rightarrow S^{+} + e_{cb-}(TiO_2) \quad (2)$$

$$2S^{+} + 3I^{-} \rightarrow 2S + I_3^{-} \quad (3)$$

$$I_3^{-} + 2e_{cb} \rightarrow 3I^{-} \quad (4)$$

$$S^{+}(TiO_2) + e^{-}(TiO_2) \rightarrow S(TiO_2) \quad (5)$$

$$I_3^{-} + 2e^{-}(TiO_2) \rightarrow 3I^{-} \quad (6)$$

2.2 Key Parameters and Characterizations of the Performance of a DSCs

The efficiency of a DSC is defined by the following equation:

$$\eta = P_{out}/P_{in} = J_{max} V_{max} / P_{in} \quad (7)$$

$$FF = J_{max} V_{max} / V_{oc} J_{sc} \quad (8)$$

Where η is the quantum efficiency, J_{sc} is the short-circuit photocurrent density, V_{oc} is the open-circuit photovoltage, *FF* is the fill factor, and P_{in} is the incident light intensity on the device, 100 mW cm^{-2} under one sun or air mass (AM) 1.5. The *FF* is a value between 0 and 1, which is defined as the ratio of the maximum power (P_{max}) of the solar cell to the V_{oc} and the short circuit current density (J_{sc}). The P_{max} is obtained as the product of the photocurrent and the photovoltage at the voltage where the power output of the cell is maximal.

From this Equation, it can be seen that higher $J_{sc,}$ $V_{oc,}$ and *FF* are the key parameters for increased η. Therefore, the way to increase the η is to increase the $J_{sc,}$ $V_{oc,}$ and/or the *FF*.

Usually, the performance of a DSC is judged by its overall solar-to-electric conversion efficiency, cost, and stability. To determine the efficiency, the current as a function of bias and potential are the two main required measurements, which are measured through an external variable resistance and at a particular intensity of the incident light.

Three of the most utilised techniques which are used for DSC characterizations: photocurrent-voltage (*I-V*) measurements, incident photon to current conversion efficiency (IPCE), and electrochemical impedance spectroscopy (EIS). [19]

2.2.1 *I-V*

I-V: Photoelectric current (*I-V*) measurements are used to calculate the electric output of DSCs. The η is measured under the standard conditions: usually the measurement is carried out under room temperature (~ 25 ^{o}C) and the intensity of incident light should be 1000 W/m^2, under AM 1.5.

The J_{sc} is the photocurrent (I_{sc}) per active area (A) when the potential that applied on the DSC device is zero, defined as I_{sc}/A. Under one sun conditions, the J_{sc} is determined by the amount of dye molecules that are anchored onto the surface of the metal oxide, the light harvesting efficiency of those dyes, the injection efficiency and the charge collection efficiency.

The V_{oc} corresponds to the energy difference between the quasi Fermi level of TiO_2 photoelectrode and the potential of the electrolyte. This implies that for the same photoelectrode-electrolyte system, the V_{oc} should be a constant. It was found, however, that except for the sensitizer and the adsorption mode, the recombination rate also effects the V_{oc}. The adsorption geometry of the sensitizer can substantially decrease conduction band energy of TiO_2, and hence, the V_{oc} is reduced. [1]

The value of *FF* indicates the quality of a DSC device. *FF* reflects the losses of electrical (Ohmic) and electrochemical (overvoltage) that occur when a DSC is in operation. The *FF* can be defined as the decrease of the photocurrent when the photovoltage increases. Usually the *FF* is calculated by the squareness in the *I-V* curve. There are many reasons for the poor *FF*, including the charge recombination,

electron back transfer within the DSC device, as well as the magnitude of the series resistances. [1] [20]

2.2.2 *IPCE*

IPCE: The IPCE is an acronym for the incident photon to current conversion efficiency. It is defined, under the short circuit conditions at the fixed wavelength, as the ratio of the electron numbers that flow through the outside circuit to the incident photons. It also equals to the produced photocurrent density divided by the photons in the outside circuit when the monochromatic illuminates on the DSC device.

$$IPCE\ (\lambda) = \frac{n\ electron\ (\lambda)}{n\ photons\ (\lambda)} = \frac{1\ (\lambda)hc}{P_{in}\ (\lambda)e\lambda} = \frac{J_{sc}}{\exp(\lambda)} = 1240\frac{J_{sc}\ (\lambda)\ [A\ cm^{-2}]}{(\lambda)[nm]\ P_{in}\ (\lambda)\ [Wcm^{-2}]} \quad (9)$$

Where I (λ) is the photocurrent, P_{in} (λ) is the input power, λ is the irradiation wavelength, and e is the elementary charge. It is obvious to see that the more incident photons converted into mobile electrons, the high DSC performance will be obtained.

2.2.3 *EIS*

EIS: Electrochemical impedance spectroscopy (EIS) is used to investigate electronic and ionic charge transport processes in the DSCs. The impedance spectrum combined with the electrical equivalent model on top is shown in Figure 2.2. A DSC system is combined with resistors and capacitors. In the electrical equivalent model, the r_{ct} refers to the charge-transfer resistance between electrons in mesoporous metal oxide (typically TiO_2) film and ions of the electrolyte during the process of charge recombination; C_m refers to the chemical capacitance in mesoporous metal oxide (typically TiO_2) film; r_t refers to electron transport resistance of the mesoporous metal oxide (typically TiO_2) film; Z_d is Warburg element which shows the ion Nernst diffusion of the electrolyte; C_{Pt} and R_{Pt} refer to double-layer capacitance at Pt

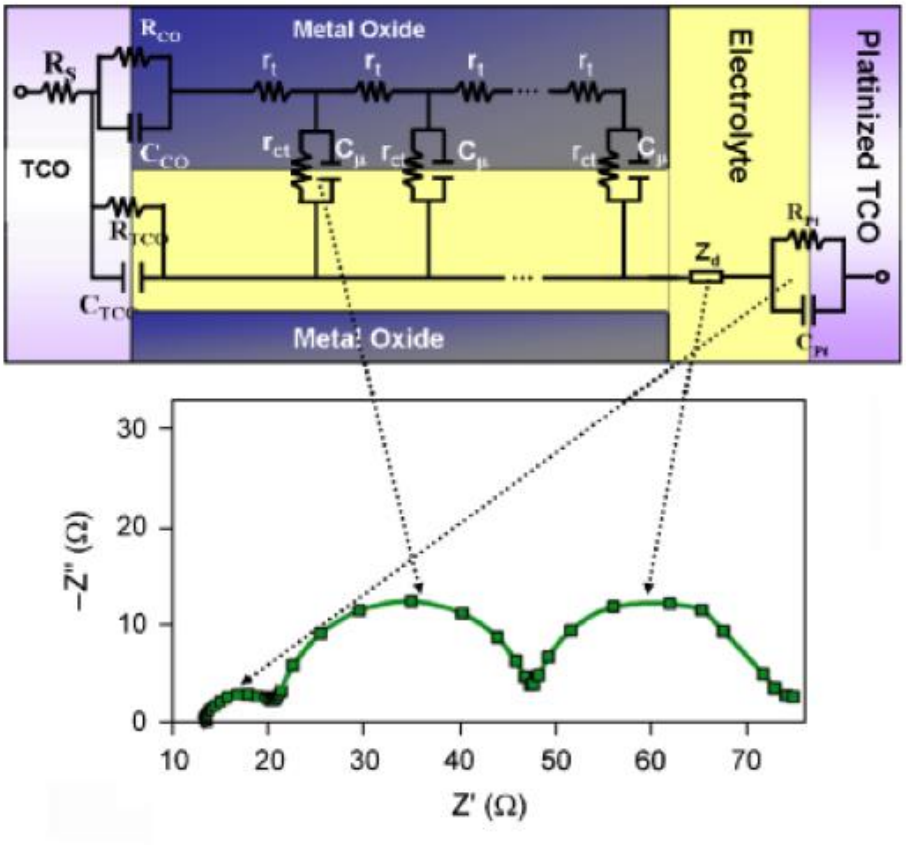

Figure 2.2 The impedance spectrum of DSCs, combined with the electrical equivalent model on top. [19]

electrode and charge-transfer resistance, respectively; R_s refer to the series resistance. [19]

2.3 Photoanode Materials in DSCs

In principle, to obtain higher solar-to-electric conversion efficiency in a DSC, a photoanode material should meet the following requirements: 1) the surface area should be high enough to efficiently absorb the dye; 2) the porosity should be high enough for efficient electrolyte diffusion and effective mass transportation; 3) particle size should be large enough for efficient light scattering; 4) grain boundaries should be minimized for faster electron transportation.

2.3.1 Comparison of DSC Performances with Different Photoanode Materials

Because of their good electronic properties and good stability, metal oxide semiconductors with wide band gaps (E_g > 3 eV), such as TiO_2, ZnO, SnO_2, and Nb_2O_5 are well known as photoanode materials, with DSC efficiencies summarized in Table 2.1. It can be seen that the TiO_2 nanoparticle-based DSC shows the highest recorded efficiency (12.3 %), compared to the other metal oxide materials. In addition, TiO_2 has been reported as a low cost, non-toxic, widely available, biocompatible material.

As a promising photoanode for DSCs, ZnO (with a similar conduction band edge potential as TiO_2) was reported to have higher carrier mobility than its TiO_2 counterpart. ZnO is unstable in acid, however, and the dye aggregates easily, leading to a deterioration of ZnO-based DSC performance. Furthermore, $SrTiO_3$, WO_3, and Zn_2SnO_4 *etc* semiconductors are also used for DSC electrodes.

Table 2.1 Comparison of photoanode materials applied in DSCs.

Photoanode material	Band gap (eV)	η (%)	Reference
TiO_2	3.2	12.3	[21]
ZnO	3.3	5.6	[22]
Nb_2O_5	3.49	5.00	[23]
Zn_2SnO_4	3.7	3.70	[24]
$SrTiO_3$	3.2	1.80	[25]
WO_3	2.6-3.0	0.75	[26]
SnO_2	3.6	0.30	[27]

2.4 Development of TiO_2 Morphologies in High Efficient DSCs

2.4.1 Zero-dimensional (0D) TiO_2 Nanoparticles

Zero-dimensional (0D) TiO_2 nanoparticles (such as uniform particle arrays, core-shell quantum dots *etc.*) have been synthesized through a variety of physical or chemical procedures, with wide applications in various energy systems, such as solar cells, lasers, single electron transistors, *etc.* It is well known that an impressive breakthrough in DSCs was made by Grätzel *et al.* in 1991, where semiconductor films consisting of nanometer-sized TiO_2 particles were sensitized with a trimeric ruthenium complex, with overall conversion efficiencies of 7.1-7.9 % obtained (as shown in Figure 2.3). [16] One of the key reasons for the high efficiency is that the photoelectrode films were made of crystalline nanosized particles that have an extremely high surface area for dye adsorption.

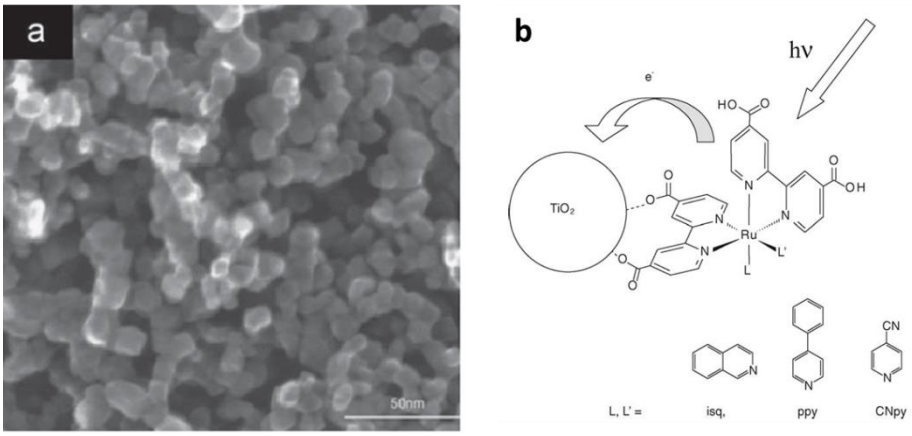

Figure 2.3 Dye-sensitized DSCs made of 0D nanoparticles: (a) Scanning electron microscope (SEM) film of 0D TiO_2 nanoparticles image, and (b) a dye molecule adsorbed on TiO_2. [16, 28]

2.4.2 One-dimensional (1D) TiO_2 Nanostructures

Nanoparticles are well-known and are widely used to make porous photoelectrode films in DSC applications. The films made from nanoparticles are not ideal, however, because of the slower electron transportation caused by the many interfaces. The electron diffusion length can be calculated by the following equation using the electron diffusion coefficient, as:

$$L_n = \sqrt{D_n \tau_n} \qquad (10)$$

where L_n represents electron diffusion length, D_n refers to electron diffusion coefficient, and τ_n shows electron lifetime.

The typical L_n for nanoparticle-based films is ~ 10-14 μm; for 1D nanostructures, however, is larger due to the direct pathways for electron transportation.

2.4.2.1 TiO_2 Nanowires

TiO_2 nanowires are one of the most important 1D nanostructures and have attracted broad interest for DSC application. [5-7] It has been reported that TiO_2 nanowire arrays on FTO glass substrates can be synthesized by a hydrothermal growth method. [29] HCl solution was mixed with the precursor solution (containing titanium tetrachloride and/or tetrabutyl titanate). Rutile TiO_2 based nanowires (35-90 nm in width, ~ 4 μm in length) were formed after heat treatment at 180-220 ^oC for ~ 24 h in an oven (Figure 2.4). Under one sun conditions, the TiO_2 nanowires-based DSC revealed an overall solar-to-electric conversion efficiency of 5 % because of faster electron transportation. [5, 30]

Electrospinning is another reported facile method to producing TiO_2 nanowires directly on FTO substrate. The precursor solution typically includes titanium alkoxide, acetic acid, ethanol, and polyvinylpyrrolidone (PVP) for the electrospinning

procedure. Anatase TiO_2 nanowires are finally obtained after sintering at 500 ^oC. An overall efficiency of ~ 5.8 % was obtained when the TiO_2 nanowires were used as the photoelectrode with a film thickness of ~ 20 μm. [31, 32]

In addition, TiO_2 nanowire-based solar cell performance was compared with that of nanoparticles. It is interesting to find that the efficiency for the TiO_2 nanowire-based DSC (at a film thickness of 2-3 μm) is much higher than for that with the nanoparticle film (5 μm thick), which is good evidence to show that charge transport is faster in the 1D nanostructures. [33]

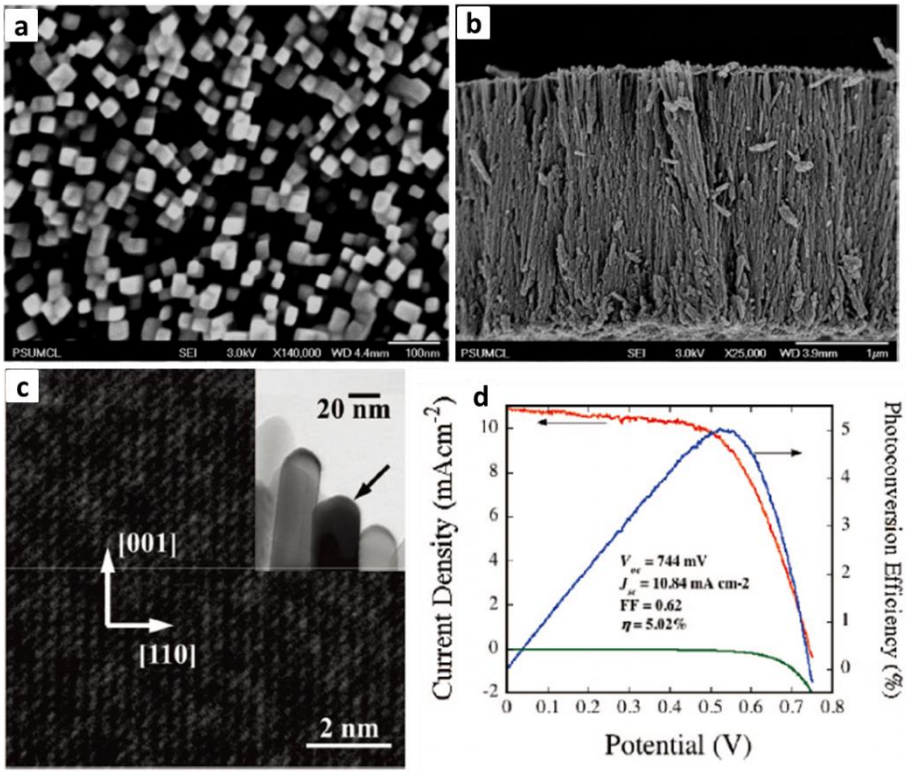

Figure 2.4 DSCs with 1D TiO_2 nanowire arrays on FTO glass substrates: (a) top view field emission SEM (FESEM) image, (b) cross-sectional FESEM image, (c) transmission electron microscope (TEM) image illustrating the [001] orientation of TiO_2 nanowires, (d) photocurrent density (red), dark current density (green), and power density (blue) of 2.0 μm long TiO_2 nanowire-array-based dye sensitized solar cells under AM 1.5 illumination (100 mW/cm^2). [29]

2.4.2.2 TiO_2 Nanotubes

Nanotubes with hollow structure usually have larger surface area than that of nanowires or nanorods, so they are a very attractive 1D nanostructure in DSC applications. [3, 4]

Anodization has been widely reported as a method for the synthesis of TiO_2 nanotubes. [34, 35] In this process, under constant potential conditions, titanium foil is simply oxidized at the anode in a fluoride-based solution. TiO_2 nanotubes with different lengths (ranging from tens of micrometers to millimeters) and different wall thicknesses (in the range of 20-30 nm) were finally formed on the titanium foil

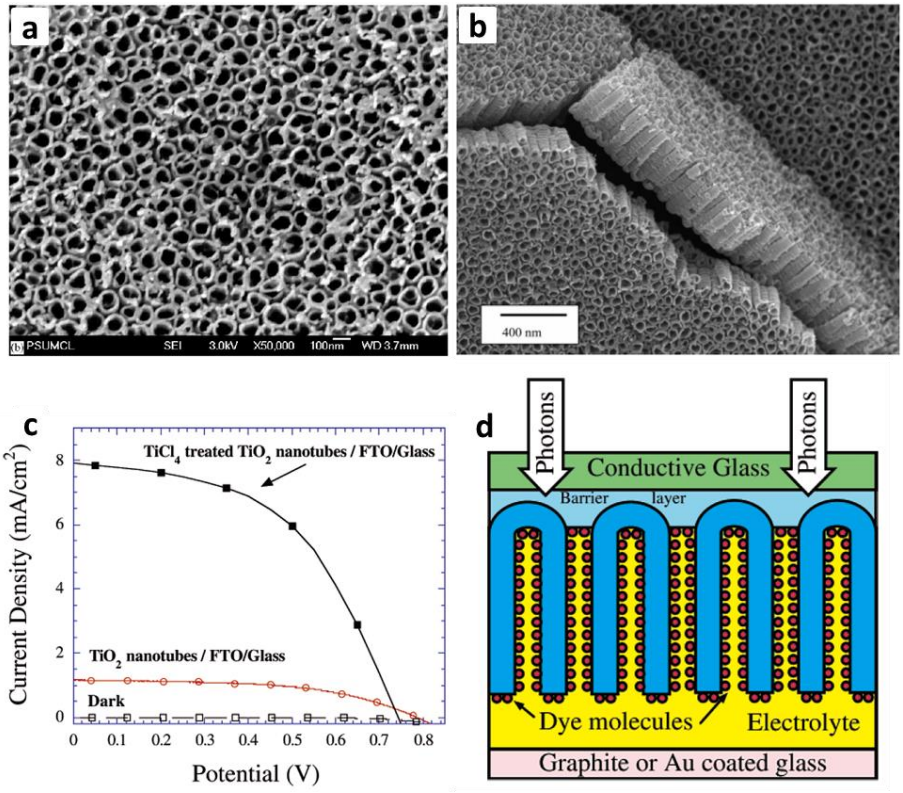

Figure 2.5 DSCs with TiO_2 nanotubes prepared by an anodization method as the photoanode: (a, b) SEM images of the TiO_2 nanotube array, (c) Photocurrent-photovoltage characteristics of a transparent nanotube-array DSC under 100 % AM-1.5 illumination, (d) growth mechanism of the nanotubes and formation of a barrier layer under the nanotube film. [4]

(Figure 2.5), with the morphology determined by the composition of the electrolyte, the growth time, and the applied bias. It is worth noting that 450 ^{o}C calcination in air is necessary for anatase TiO_2 transformation from the amorphous state. [4]

2.4.3 Two-dimensional (2D) TiO_2 Nanostructures

2D TiO_2 nanostructures, such as nanosheets, have also shown great potential for application in DSCs. [36-38] For example, using $Ti(OC_4H_9)_4$ as precursor and HF as a morphology controlling agent, anatase TiO_2 nanosheets (denoted as TiO_2-NSs) with exposed {001} facets were successfully fabricated via a simple one-pot hydrothermal method. [36] From the FESEM image of the synthesized TiO_2-NSs (Figure 2.6), it can be clearly observed that the large scale nanosheets are 70-80 nm in length, and ~ 8 nm in thickness. The high resolution TEM (HRTEM) clearly shows the lattice spacing of ~ 0.235 nm, which corresponds well to the (001) plane of anatase TiO_2. The calculated percentage of exposed {001} facet for TiO_2-NSs is about 75 %.

Compared with commercial P25 (η = 3.64 %) and TiO_2 nanoparticles (TiO_2-NPs) (4.24 %), the synthesized TiO_2-NSs showed the best efficiency (4.56 %). The reasons for the enhanced solar cell performance of TiO_2-NSs-based DSCs are summarized as follows: (1) TiO_2-NSs have higher porosity/pore volume than P25 and TiO_2-NPs, which is beneficial to electrolyte transport and diffusion; (2) TiO_2-NSs have more exposed {001} facets, which are proved to be more reactive than the (101) surface, demonstrating that the surface of TiO_2-NSs can facilitate higher dye loading; [39, 40] (3) TiO_2-NSs have good crystallization and fewer defects, which reduces the electron-hole recombination; (4) TiO_2-NSs have enhanced light scattering capability, extending the distance of light in the photoelectrode film, and hence the dye molecules can absorb more photons. This study also demonstrates that the efficiency

of DSCs can be further improved by using anatase TiO_2 nanosheets with exposed {001} facets due to their high activity.

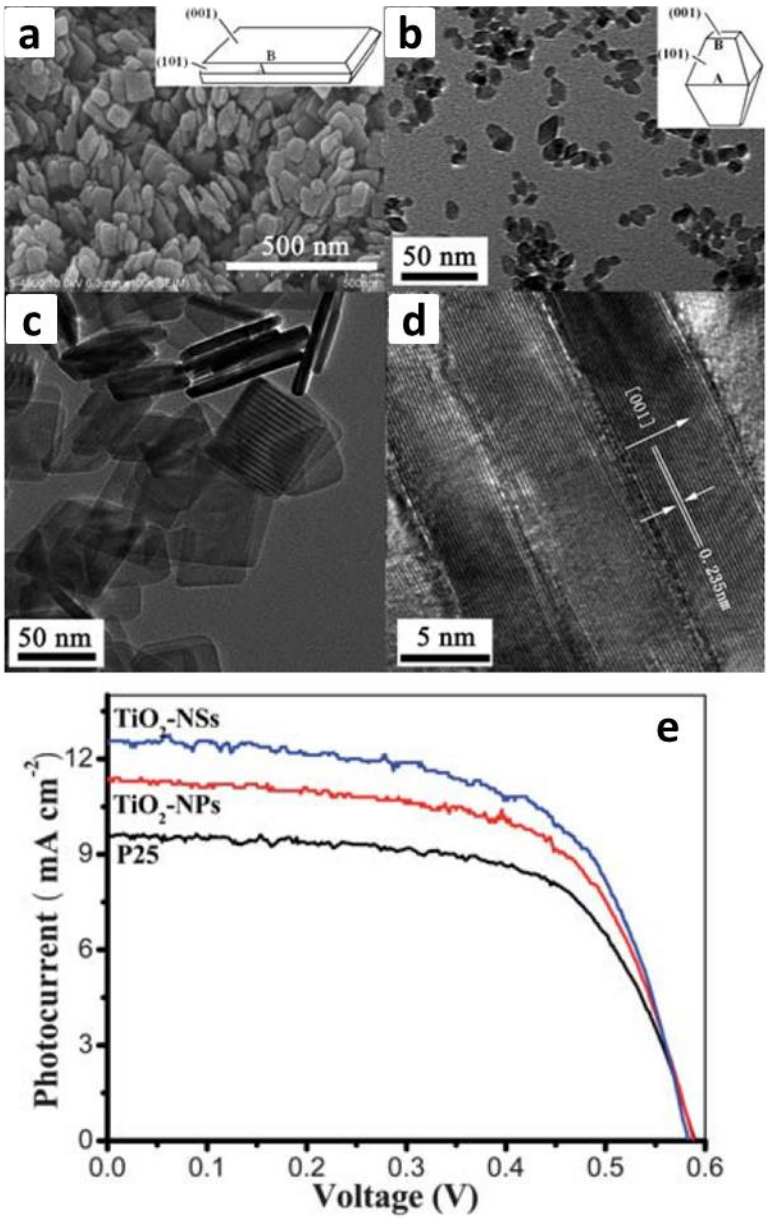

Figure 2.6 (a) SEM, (b) and (c) TEM, and (d) HRTEM images of anatase TiO_2 nanosheets (TiO_2-NSs), (e) Comparison of the *I-V* characteristics of DSCs made from TiO_2-NSs, TiO_2 nanoparticles (TiO_2-NPs), and P25 films calcined at 450 °C.

2.4.4 Three-dimensional (3D) TiO_2 Nanostructures

2.4.4.1 TiO_2 Aggregates

TiO_2 aggregates have been well developed for the application of DSCs. [41, 42] A two-step process for synthesizing TiO_2 spheres was reported by Y. J. Kim *et al.* [42] For the first step, a controlled hydrolysis process was used to fabricate the TiO_2 aggregates, and then the aggregates were treated under hydrothermal conditions; the second step converts the spheres to a highly nanoporous crystallized structure, with the particles ~ 250 nm in diameter. [Figure 2.7 (b, c)] The spheres are composed of ~ 12 nm nanocrystallites. These synthesized TiO_2 aggregates show a high surface area of ~ 117.9 m^2/g, 1.7 times higher than that of nanoparticles. When these aggregates were employed to fabricate DSCs, a high efficiency of 10.5 % was obtained. Because of the 150-300 nm pores in the 250 nm spheres, TiO_2 aggregates are able to provide a ‘‘highway’’ for efficient electrolyte diffusion. [Figure 2.7(a)]

In this film, two types of pores were finally generated: the large pores (55 nm) that are formed by the interstitial voids among the spheres and the tiny internal pores (9.1 nm) that are formed inside the TiO_2 aggregates. Both of these types of pores can shorten the diffusion paths of ions and further facilitate efficient diffusion of the electrolyte. For the commercial TiO_2 nanoparticles, the diffusion constant of I_3^- is 4.1×10^{-6} cm^2 s^{-1}, however, it increases to 4.9×10^{-6} cm^2 s^{-1} for the TiO_2 aggregate-based DSC.

Therefore, compared with the nanoparticle-based film, this hierarchical spherical nanostructure-based DSC (with multiscale porous structure) obtained a higher overall conversion efficiency (8.44 %). This unique porous structure is quite beneficial for efficient electrolyte diffusion, especially for particular types of electrolytes such as solid state electrolytes, gel electrolytes, and ionic liquid electrolytes.

Apart from the widely used hydrothermal method, multi-scale pores can also be prepared by other methods, such as self-assembly techniques, template methods, and electrohydrodynamic (EHD) methods. [43-47] For example, by using a facile EHD approach, a photoanode film that made of TiO_2 spheres with inside channels of micro-/nano-porous hierarchically branched structures can be obtained. [47] An overall conversion efficiency of 7.1 % was obtained; the hierarchical porous structure in the films is beneficial for efficient light harvesting and efficient electrolyte diffusion. Sub-micrometer-sized TiO_2 spheres with inside hierarchical pores could be synthesized by a grafting polymerization process and subsequently, a sol-gel procedure. [46]

By a dual template method, for example, using mesoscale colloidal particles and holographic patterns as the templates, respectively, a TiO_2 photoelectrode with mesoporous and macroporous structures was successfully prepared. The two types of spheres showed good solar cell performance when they were used as photoanode materials for application in DSCs. [44]

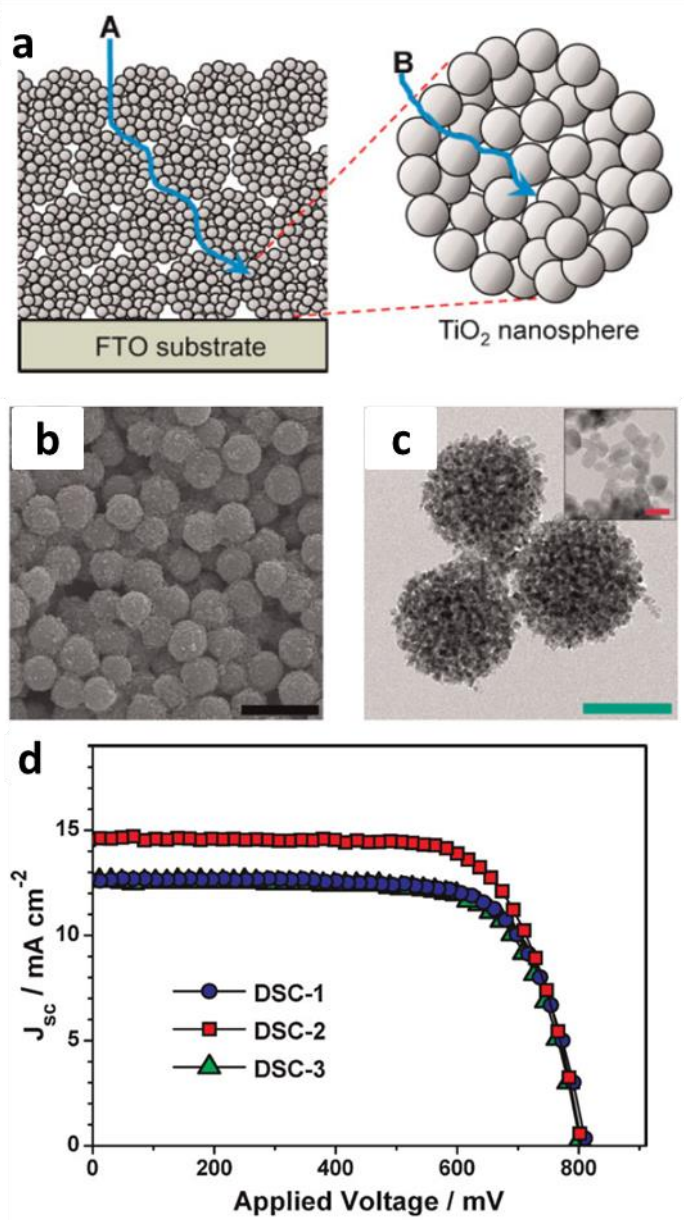

Figure 2.7 (a) Schematic illustration of the electrolyte diffusion through the external (A) and internal (B) pores in the nanoporous TiO_2 sphere film; (b) SEM and (c) TEM images of TiO_2 spheres, scale bar: 200 nm (inset: 20 nm); (d) current density-voltage (*J*-*V*) curves of solar cells with well-defined spheres (DSC-1), deformed spheres (DSC-2), and commercial nanoparticles (DSC-3). [42]

2.4.4.2 Hierarchical Quasi-1D Micro-/Nano-architectures

The assembly of 1D nanoscale primary particles as building blocks may provide enhanced electron transport for better performance. In addition, higher light scattering efficiency could be obtained when the 1D nanostructures are used as the photoanode rather than nanoparticles. The hierarchical structures, including quasi-1D spherical micro-/nano-architectures assembled from the 1D building units can be formed by growing 1D building units on the surface of 1D architectures.

D. B. Kuang's group reported one new type of photoanode, composed of anatase hierarchical TiO_2 microspheres (HTS), which consist of nanorods and nanoparticles. [48] This architecture works as a tri-functional photoelectrode in DSC application, achieving high conversion efficiency, with longer electron lifetime and faster electron transport. By using acetic acid and titanium n-butoxide as the precursor, the HTS were synthesized via a simple acid hydrothermal method. Figure 2.8 (a) shows the HTS, which are composed of nanoribbons with a diameter of ~ 2.1 mm after the acid hydrothermal process. After a subsequent calcination at 500 °C, the Ti-complex intermediates were converted to the HTS assembled from nanorods and nanoparticles.

A total efficiency of 10.34 % was obtained for the HTS-based DSC, much higher than that with the commercial P25 nanoparticles (8.1 %), [Figure 2.8(e)], and this DSC has the following advantages: the higher surface area, with the HTS able to adsorb dye at 149.85 nmol cm^{-2}, which is much greater than for P25 (121.14 nmol cm^{-2}); enhanced light scattering due to the micrometer-sized spheres; and slower recombination and more efficient electron transfer pathways [as shown in Figure 2.8(f, g)] because of the quasi-1D building blocks of the HTS architecture.

The above results demonstrate that the hierarchical quasi-1D TiO_2 micro-/nano-architecture has good potential as an efficient photoanode material for application in DSCs, which may overcome many disadvantages, such as the weak light scattering ability of nanoparticles, as well as the low surface area of 1D nanostructures.

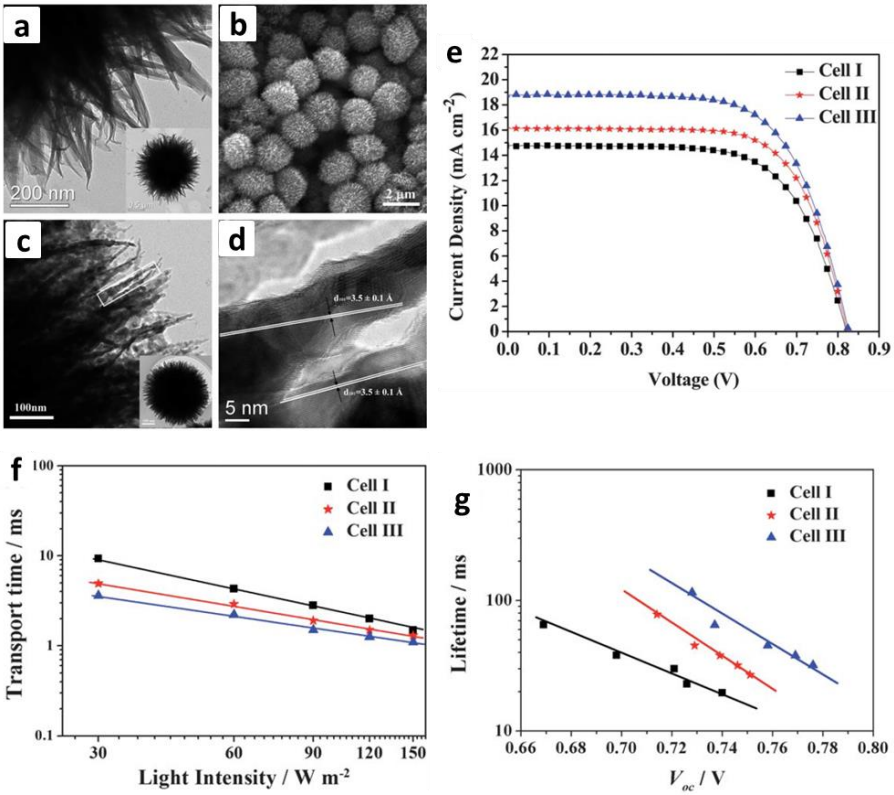

Figure 2.8 SEM and TEM images of hierarchical anatase TiO_2 microspheres (HTS) synthesized via acid thermal reaction before (a) and after (b–d) calcination. *J-V* curves (e), electron transport time as a function of incident light intensity (f) and lifetime as a function of open-circuit voltage (g) for DSCs based on Films I (P25), II (P25 + HTS), and III (HTS). [48]

2.4.5 Photoanode Architecture in DSCs

2.4.5.1 Nanocomposites

Compared to nanoparticle (NP)-based DSCs, 1D TiO_2 nanostructure-based DSCs exhibit lower conversion efficiency because of their lower surface area and hence dye loading. To improve the surface area and dye adsorption, nanoparticles are mixed with 1D materials, which is an effective method to achieve higher efficiencies as shown in Table 2.2. In addition, to further enhance the efficiency of charge collection, TiO_2 materials are often mixed with highly electronically conductive materials, including graphene, carbon nanotubes, *etc*. Table 2.2 shows the efficiency of TiO_2 composites with various materials in DSCs.

It can be seen from Table 2.2 that, the mixture of 1D nanostructured materials and nanoparticles has a higher efficiency than that of pure nanoparticles. The 0.025 wt% multi-walled carbon nanotube (MWCNT)/TiO_2 NP) nanocomposite exhibits the best efficiency, with 10.29 % achieved, due to the high electronic conductivity and large electron-storage capacity of CNTs. [53]

Table 2.2 Solar-to-electric conversion efficiency (η) of TiO_2 nanocomposites with different materials in DSCs. [49]

Nanomaterial/Nanoparticle (NP)	η (%)	Reference
TiO_2 Nanotube/2% NP	8.43/5.01	[50]
TiO_2 Nanorod/NP	7.12/5.82	[51]
TiO_2 Nanowire/NP	3.8/2.45	[52]
0.025wt% MWCNT/TiO_2 NP	10.29/6.31	[53]
1wt% graphene/TiO_2 NP	6.86/5.98	[54]

In addition, incorporating graphene into the 1D TiO_2 nanostructure not only enhances the electron transport, but also reduces charge recombination.

2.4.5.2 Light Scattering Layer

A bi-layer structure with 1D material on top of a TiO_2 nanoparticle underlayer has been proven to be an effective approach to improve light scattering ability, and hence enhance dye loading and final conversion efficiency. Table 2.3 lists the bi-layer structures of DSCs and gives a comparison of efficiencies, with nanoparticles as the underlayer.

It can be seen from Table 2.3 that by using the hollow spherical TiO_2 as the light scattering layer, an efficiency of 9.43 % (highest among all the other tested structures) was obtained, which is due to contributions from the higher J_{sc}, the efficient dye adsorption, and the effective light scattering. [55]

Table 2.3 Solar-to-electric conversion efficiency (η) of bi-layer structured DSCs with a scattering layer. [49]

Light scattering layer (LSL, top layer)	Underlayer TiO_2 Nanoparticle (TiO_2-NP)	η (%) with LSL (without LSL)	Reference
Hollow spherical TiO_2	TiO_2-NP	9.43 (7.79)	[55]
400-nm sized TiO_2	TiO_2-NP	8.96 (7.79)	[55]
TiO_2 beads	TiO_2-NP	8.84 (7.38)	[11]

2.4.6 Optimization of TiO_2 Photoanode for Flexible DSCs

Flexible polymer-based DSCs [usually ITO-polyethylene naphthalate (PEN) and ITO-polyethylene terephthalate (PET)] have gained a great deal of interest among the researchers because of their amenability to large-scale roll-to-roll manufacturing processes, low temperature, light weight, flexibility [so that they are easily incorporated into other objects (such as laptops, mobile phones, or even clothing)], and low production costs.

As the upper working temperature for most polymer substrates is ~ 150 °C, it remains a great challenge to deposit the TiO_2 film on these substrates. Organic binders that are usually used in the fabrication of FTO-based DSCs are removed by a 400 °C sintering process. For the low temperature solar cells, there are following challenges: (1) binders are excluded from the paste, and thus, as the TiO_2 films dry, more cracking occurs and subsequently the electrical resistivity will increase; (2) the adhesion between the TiO_2 film and the polymer substrate, and the electrical contact between the particles are very poor; and (3) the stability of the flexible devices is very poor because of the penetration of oxygen and moisture. [56-58] Therefore, there are a number of synthetic techniques that have been well developed for fabricating flexible photoanodes on plastic substrates, as shown in Table 2.4.

The earliest approach to prepare a low temperature paste was based on hydrothermal synthesis. [73, 77, 78] TiO_2 crystals were mixed with $TiOSO_4$ or $TiCl_4$, and then, after an autoclaving reaction, one layer of deposited paste was transformed from the Ti-monomers. [77] The TiO_2 paste made the adhesion between the substrate and the TiO_2 particles very firm. With this method, a low efficiency of 2.5 % on ITO-PET was achieved. [73]

Table 2.4 Various synthetic techniques for preparing flexible photoanodes on ITO-PEN substrates. [59, 60]

Paste	Pre-treatment	Deposition method	Post-treatment	η (%)	Reference
TiO_2,water	UV-O_3	Doctor blading	Mechanical pressing	8.1	[61]
TiO_2 beads, ethanol	$TiCl_4$ treatment	Doctor blading	CIP compression	7.5	[62]
P25, ethanol	none	Doctor blading	CIP compression	6.3	[63]
P25, ethanol	none	Electrophoretic deposition	Compression	6.2	[64]
P25, ethanol	none	Doctor blading /Screen printing	Heating 110-125°C	5.8	[65]
P25, ethanol	Acid, base treatment	Doctor blading	none	5	[66]
P25, ethanol, water	none	Doctor blading	none	4.9	[67]
P25, ethanol	Ball milling	Doctor blading	none	4.2	[68]
TiO_2 (F-5, G-2 from Showa Denko)	none	Electrophoretic deposition	UV Treatment	4.1	[69]
TiO_2 (F-5, G-2), titanium tert-butyl alcohol and acetonitrile (95:5) mixture	none	Electrophoretic deposition	CVD/UV Treatment	3.8	[70]
P25, water, nitric acid, Triton, ethanol, methanol	none	Spray deposition or pulsed laser	UV Treatment	3.3	[71]
TiO_2 100nm and 12 nm particles, P25, butanol	none	Doctor blading	Chemical sintering	3.1	[72]
P25, [Ti(IV)-tetraisopropoxide]	none	hydrothermal	Autoclaving 100 °C	2.5	[73]
P25, 20 wt% ethanol	none	Doctor blading	Mechanical pressing	2.3	[74]
TiO_2 (TAYCA Corp., TKS-201)	hydrothermal	Doctor blading	Microwave heating	2.2	[75]
P25, ethanol, Hydroxybenzoic acid	Pre-sintering	Spray-dried	none	2.1	[76]

Chemical vapour deposition (CVD) has also been used to make TiO_2 paste. [70, 73] Microwave or ultraviolet (UV)-treatments were especially selected to promote crystalinity and the necking between TiO_2 particles. A higher efficiency of 3.8 % was obtained compared to the product of the hydrothermal method. [70]

One method, called "lift off", was introduced by Dürr *et al.*, in which one substrate was first used to prepare one layer of TiO_2 paste, which was then transferred to another plastic substrate. This approach combines a high-temperature sintering process with the compression method for the first time, which can be used in a roll-to-roll process. An overall efficiency of 5.8 % was finally obtained by using this method.

This binder-free paste was coated on ITO-PEN substrate, with 5.8 % achieved. [65] The agent *t*-butanol was the key to reducing the surface tension when making the paste. This is an ideal method for high volume production with fewer steps in the procedure and hence, lower production costs.

One of the most widely used methods to make TiO_2 paste on plastic substrate is mechanical compression. [61, 74, 79] The Arakawa's group has so far reported the highest efficiency of 8.1 %, based on polymer substrate DSCs. [61] They reported that in order to enhance the connection between particles and the adhesion between film and substrate, the dried doctor bladed film was subjected to an external compressive pressure, with the maximum pressure up to 100 MPa. If the TiO_2 film is large, however, it is still great challenge to obtain a highly homogeneous film with a thickness of ~ 10 μm after such uniaxial pressure.

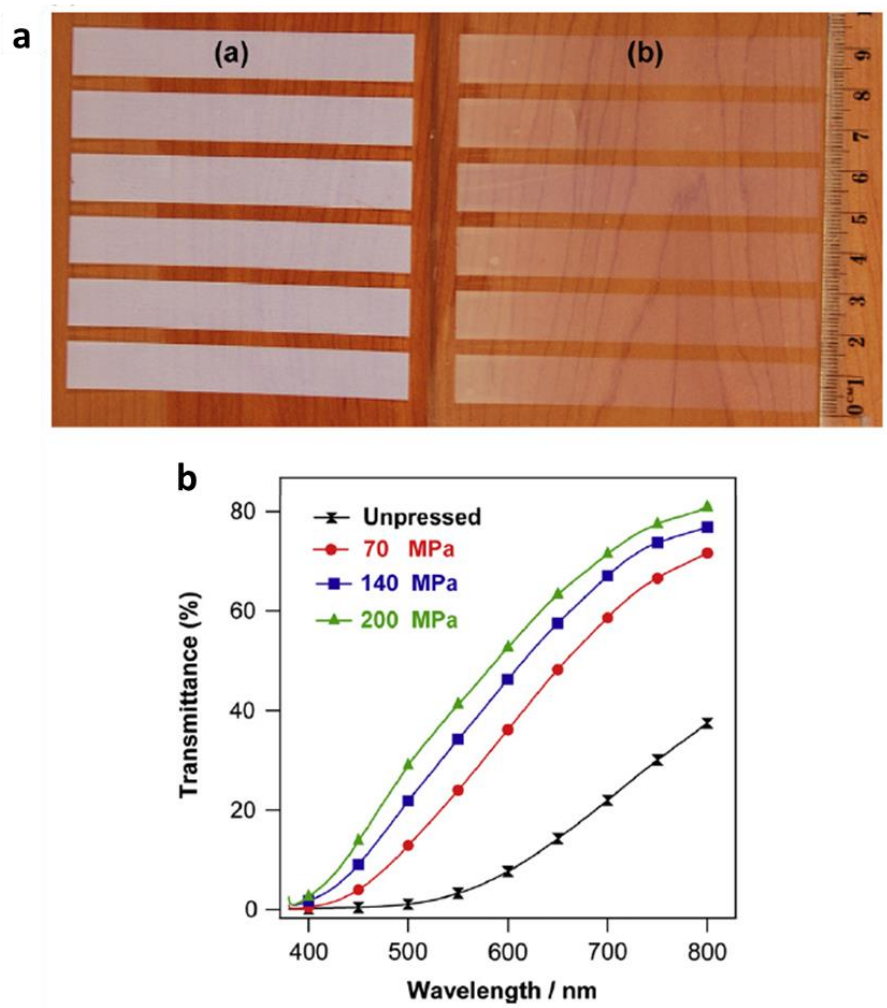

Figure 2.9 (a) Appearance of the TiO_2 electrodes before and after processing by CIP. (b) Variation of the transmittance of the TiO_2 films on ITO-PEN substrates processed at different CIP pressures. All the films had the same thickness (12 mm) before CIP compression. [63]

To solve this problem, Cheng's group introduced a cold isostatic pressing (CIP) method to make TiO_2 films on plastic substrates for the first time. [63] CIP is widely used in the ceramic and powder metallurgy industries and is used for pressing powders into different shapes. During the CIP process, pressure is applied through a liquid medium in all directions, regardless of the material's size and the shape of the component, or in this case, the TiO_2 film. It can be seen in Figure 2.9 that the pressed

TiO_2 films after CIP became more transparent, and light transmittance increased with increasing pressure, which means that the uniformity of the film was improved, and the thickness of the film was reduced after CIP. Conversion efficiencies of 6.3 % and 7.4 % were obtained after the CIP process under 100 and 15 mW cm^{-2}, respectively, which are much higher than the values prior to the CIP.

2.4.7 Optimization of TiO_2 Photoanode for Cobalt-based DSCs

Iodide/triiodide (I^-/I_3^-)-based electrolytes have been the most extensively studied in DSCs. Nevertheless, there are many disadvantages for this redox couple, which limit the efficiency. For example, I_3^- can only absorb light in the blue region, which limits the J_{sc}. [80] Most importantly, I^-/I_3^- is very corrosive to the interconnects, such as Ag or Cu. Instead of I^-/I_3^-, many alternatives have gained considerable interest, such as the organic redox shuttle, ferrocene, or cobalt complexes, which have obtained a higher V_{oc} than iodide/triiodide (I^-/I_3^-)-based electrolytes and are not as corrosive. [81-89] Among the alternatives, cobalt complexes have gained a great deal of interest and being used in record setting DSC papers (12.3 and subsequently 13 %) due to their low absorption throughout the visible spectrum, easily tunable redox potentials, and being less corrosive toward Ag. Previous reports have shown that the recombination rate of electrons is very fast from the conduction band of TiO_2 to the Co^{3+} species, and the mass transport in the electrolyte in the mesoporous TiO_2 photoanode poses great challenges. [90-92] It remains a great challenge, however, to optimize the TiO_2 photoanode in cobalt-based DSCs to achieve higher conversion efficiencies.

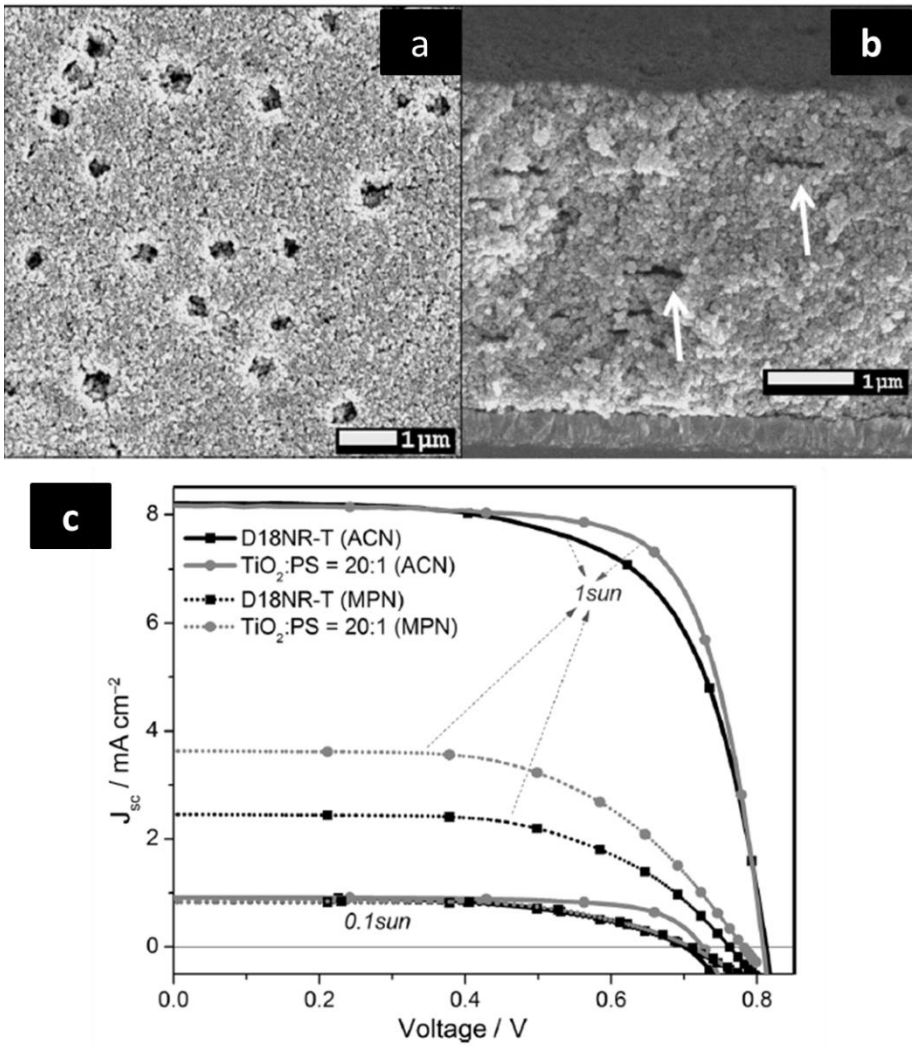

Figure 2.10 (a) Top view and (b) cross-sectional SEM images of a TiO_2 : PS = 20:1 photoanode. (c) *I-V* curves of devices made from 4 mm films of D18NR-T and PS-assisted pastes with ACN-Co(bpy) and MPN-Co(dtb) electrolytes at 0.1 and 1 sun. [95]

One of the most effective methods to retard the recombination between the electrons from the conduction band of TiO_2 and the Co^{3+} electrolyte is to incorporate a blocking layer on the TiO_2 surface. [93, 94]

Cobalt complexes have great bulk, so in mesoporous TiO_2 based DSCs, the pores should be sufficiently large to solve the mass transportation problem. In Figure 2.10, a

unique morphology of TiO_2 with macroporous-mesoporous structure [polystyrene spheres (PS) were mixed with TiO_2 paste, TiO_2 : PS = 20:1 weight ratio] was introduced to allow efficient cobalt electrolyte diffusion. Figure 2.10(c) shows the *I-V* curves of four devices with the same thickness (~ 4 μm) with cobalt electrolyte. At one sun illumination, the photoanode with PS-assisted paste shows the highest photocurrent due to improved diffusion and slower recombination. [93] In addition, Yella *et al.* have also tried to avoid mass transport by controlling the pore size of TiO_2 (ranging from 23 nm to 32 nm) and reducing the TiO_2 film thickness. [85]

2.4.8 Optimization of TiO_2 Photoanode for Rutile TiO_2-based DSCs

Based on most synthetic techniques, 1D nanostructure-based DSCs have been limited to polycrystalline TiO_2 nanowires/nanotubes or single crystal ZnO nanowires/nanorods. [4, 94-97] ZnO-based DSCs, however, showed poorer performance than TiO_2, mainly because ZnO is unstable in dye solution. [94] In addition, single crystal nanowires or nanorods could increase the electron transport rate due to their direct electrical pathways, and hence, may improve the DSC performance. [96] Therefore, the synthesis of 1D TiO_2 nanostructures on FTO for use in DSC application is a good direction.

2.4.8.1 Vertically Aligned Single-Crystal Rutile TiO_2 Nanowires on FTO

1D single-crystal rutile TiO_2 arrays of uniform and well-separated nanowires (Figure 2.11) were successfully synthesized on FTO substrate via a ketone-HCl solvothermal process. [97] The TiO_2 nanowires began to grow in the first 15 min, and then after 2 h, nanowires of 10 μm in length could be obtained. For the first time, the electron transport differences between 1D TiO_2 nanostructures and nanoparticle-based DSCs were compared.

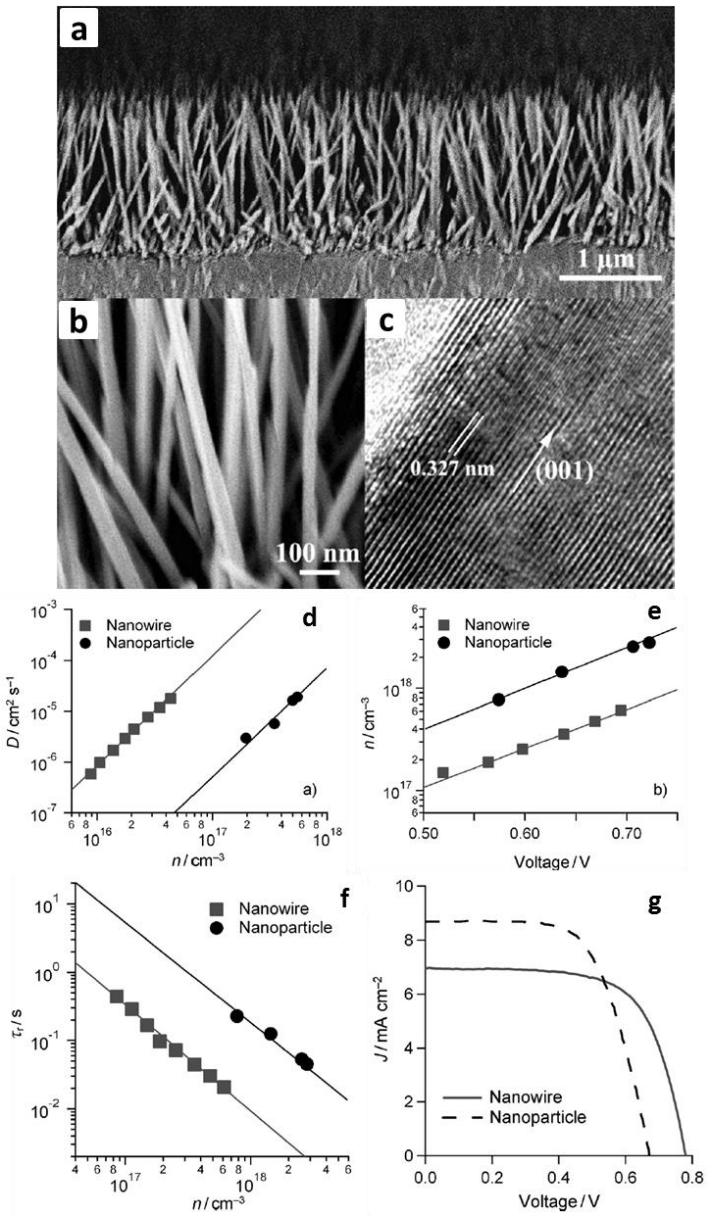

Figure 2.11 (a-c) Morphology of rutile TiO_2 nanowire arrays on FTO-coated glass substrate. Comparison of (d) the electron diffusion coefficient as a function of the photoelectron density (*n*) and (e) the photoelectron density as a function of the voltage for rutile nanowire- and nanoparticle-based DSCs with laser illumination at 680 nm. (f) Comparison of recombination lifetimes for rutile nanowire- and nanoparticle-based DSCs as a function of the photoelectron density with laser illumination at 680 nm. (g) *J*-*V* characteristics of DSCs based on a 4.5 mm long nanowire array and a nanoparticle film under simulated AM 1.5 light (*J* = photocurrent density). [99]

In the authors' report, they concluded that the rutile-based 1D nanostructures had significantly improved electronic transport properties when used in DSCs. The vertical rutile nanowire-based DSCs showed dramatically increased electron diffusion coefficient (*D*) (over 200 times higher than that of the rutile TiO_2 nanoparticle-based DSCs), and increased electron transport and much shorter recombination times (τ_r) (for example, in rutile nanowire-based DSCs the lifetime is one order of magnitude shorter than rutile TiO_2 nanoparticle-based DSCs). In addition, it was found that the nanowire-based DSCs had much lower density of sub-bandgap defect sites than the nanoparticles.

2.4.8.2 Vertically Aligned Single-Crystal Rutile TiO_2 Nanorods on FTO

Because of TiO_2 properties such as crystal structure and symmetry, it is very difficult to synthesize oriented anisotropic single-crystal TiO_2 on a transparent conducting substrate (FTO), although this is a prerequisite for solar cell applications. A few methods that synthesized oriented single-crystalline TiO_2 nanowires/nanorods have been reported. [5-8] B. Liu *et al*. reported for the first time the synthesis of oriented rutile TiO_2 nanorods with single-crystal nature on FTO substrate via a facile, simple hydrothermal method. [8] By using titanium butoxide and hydrochloric acid as the precursor solutions, uniform TiO_2 nanorods were grown on the surface of the FTO substrate, as shown in Figure 2.12. By controlling the growth parameters, such as growth temperature, reaction time, the precursor concentrations, additives, and acidity, different kinds of TiO_2 nanorods with various lengths and densities were successfully prepared. This report showed that one of the key parameters for growing rutile TiO_2 nanorods on FTO is the small lattice mismatch between rutile TiO_2 and the FTO substrate. After treatment by $TiCl_4$, a conversion efficiency of 3 % was obtained by using the synthesized TiO_2 nanorod film with a thickness of ~ 4 μm as the

photoanode, which is higher than the conversion efficiency without the $TiCl_4$ treatment.

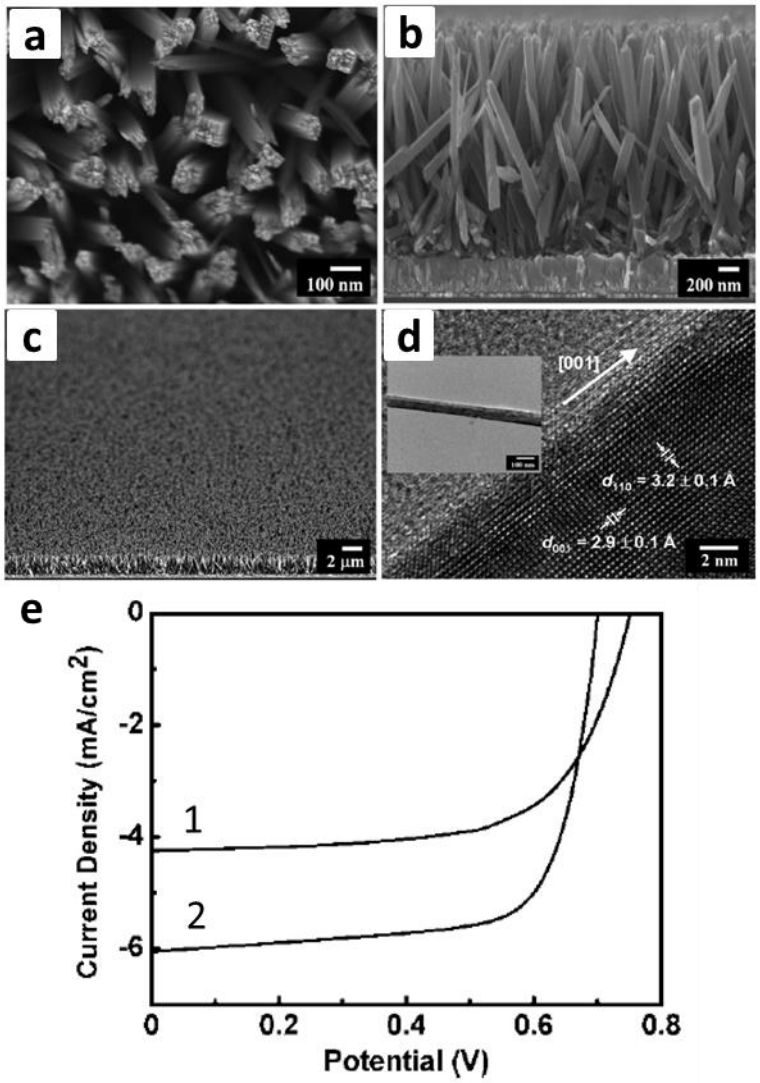

Figure 2.12 Field emission SEM (FESEM) images of oriented rutile TiO_2 nanorod film grown on FTO substrate in 30 mL deionized water, 30 mL hydrochloric acid, and 1 mL titanium butoxide at 150 °C for 20 h. (a) Top view, (b) cross-sectional view, (c) tilted cross-sectional view, (d) HRTEM image of the single TiO_2 nanorod shown in the inset, (e) Photocurrent-photovoltage characteristics of DSCs assembled from 4 μm thick rutile TiO_2 nanorod films (1) without and (2) with $TiCl_4$ treatment. [8]

2.4.8.3 Rutile TiO_2 Branched Nanostructured Photoanode

Even though 1D nanostructures show good properties in the DSC performance, such as rapid electron collection and charge transport, they usually suffer from low specific surface area, and hence, lower efficiency. In addition, 1D nanostructures tend to lie in the film plane, which is not good for electron extraction.

Branched nanostructures have been reported by many groups *via* different approaches, such as the wet chemical process, the vapour-liquid-solid (VLS) growth method, and the hydrothermal method. [100-102] For example, the Park's group synthesized one type of rutile TiO_2 branched nanostructure composed of nanowires, as shown in Figure 2.13. [103] Using TiO_2 nanowires as seeds, TiO_2 branched nanoparticles were synthesized. In this work, they reported that the TiO_2 architectures are derived from nanowire to nanobranch during the seeding process. By further characterizations with HRTEM, XRD, *etc.*, they confirmed that the rutile TiO_2 branched nanostructure is three-dimensional and grows from the rutile TiO_2 nanowire backbone. Compared to the nanowire-based DSCs, the new type of TiO_2 branched nanostructure-based DSCs show improved photocurrent density (from 6.25 to 12.18 mA cm^{-2}) and conversion efficiency (from 2.6 to 4.3 %) because of the higher specific surface area, increased roughness factor, and enhanced charge harvesting efficiency.

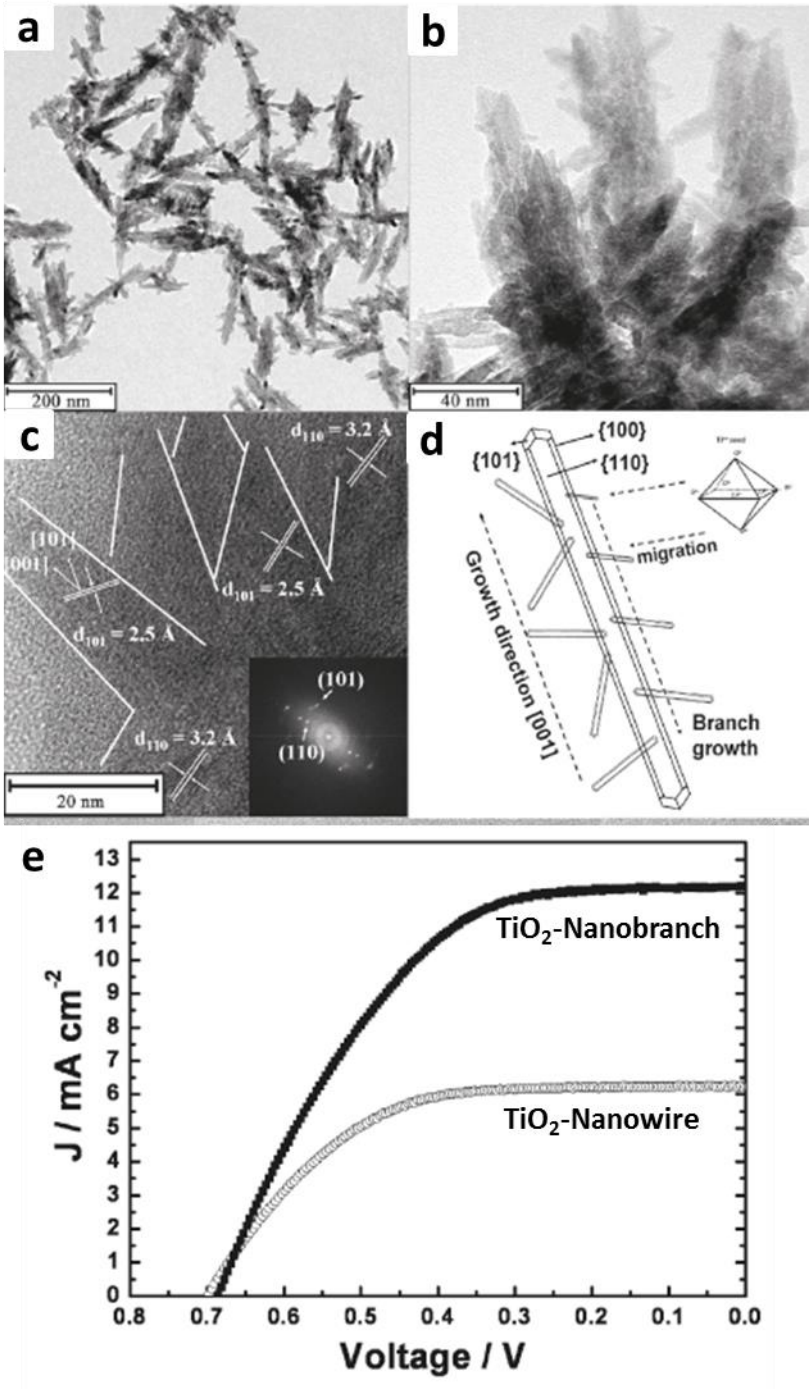

Figure 2.13 (a, b) TEM images of TiO_2-Nanobranch synthesized by a seeding method. (c) HRTEM image of the TiO_2-Nanobranch. The inset is the fast Fourier transform (FFT) pattern. (d) Schematic illustration of the formation of the rutile TiO_2-Nanobranch. (e) *J-V* curves measured using TiO_2-Nanobranch and TiO_2-Nanowire as photoelectrodes. [103]

2.4.8.4 1D-3D Nanostructured TiO_2 Bilayer Photoanode

Usually, there are two ways to increase solar energy harvesting efficiency, enhancing light scattering and changing the electron diffusion length. [104-106] Large-sized nanostructures, usually ~ 400-800 nm, are used to enhance the solar cell light scattering; 1D nanostructures are employed to enhance the electron diffusion length. [107, 108] J. H. Kim's group reported one new type of bilayer TiO_2 photoanode which is composed of a 1D-3D architecture via a one-step synthesis, as shown in Figure 2.14. [109] In this work, titanium tetraisopropoxide (TTIP), ethylene glycol (EG), and cetyltrimethylammonium bromide (CTAB) were used for the precursor solution. During the hydrothermal process, oriented 1D TiO_2 nanowire arrays were first grown on top of a FTO surface, and then again on top of these arrays, the 3D TiO_2 dendritic nanostructures were formed. In addition, by adjusting the ratio of EG to TTIP (aq), the morphology and the size of the 1D arrays at the bottom and the 3D dendritic nanostructures on the top can be controlled. The synthesized bilayer photoanode provided a conversion efficiency of 7.2 % after treatment by $TiCl_4$, much higher than that of commercial P25 nanoparticles (4.7 %), due to the higher surface area, enhanced light scattering ability, and fast electron transport.

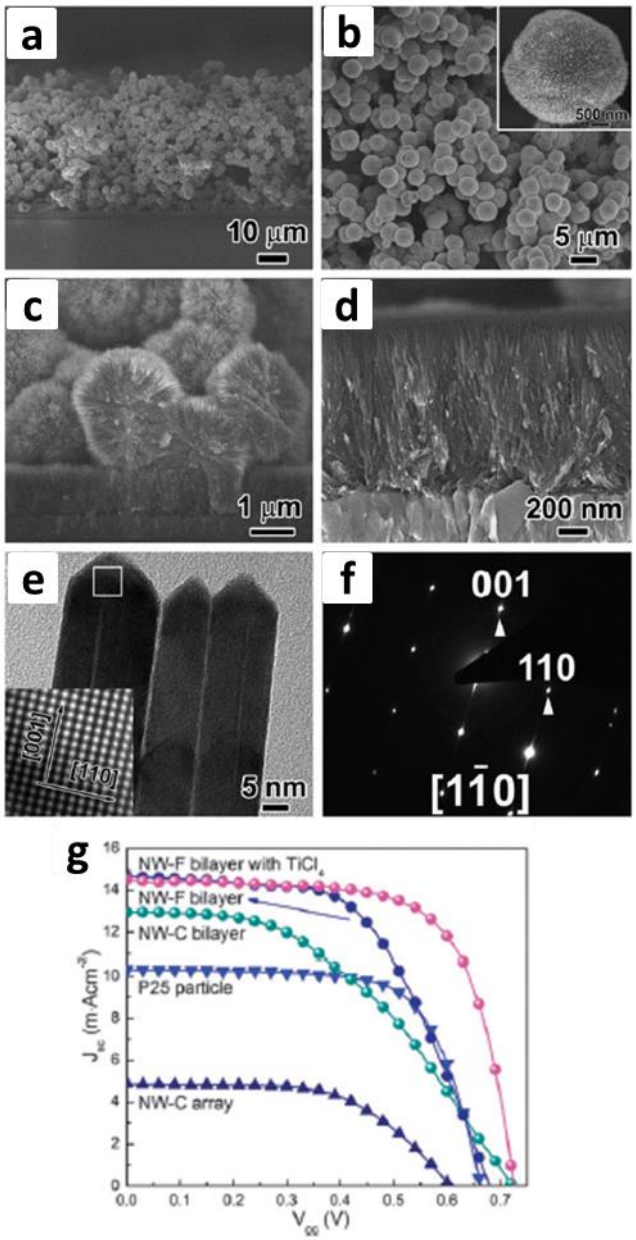

Figure 2.14 (a-e) Morphology of the bilayer TiO2 nanostructures synthesized from a solution with a composition of TTIP (aq) : EG = 1:1 and (f) the corresponding SAED pattern of (e), (g) *J*–*V* curves of the DSCs with different photoanodes. [109]

2.5 Aims and Contributions of the Thesis

This aim of this research thesis was to synthesize and investigate novel TiO_2 architectures for highly efficient DSCs, including flexible DSCs, cobalt electrolyte-based DSCs, and rutile TiO_2-based DSCs. Despite the tremendous worldwide research efforts devoted to design the structure and the morphology of TiO_2, vast improvements can be made in order to help optimise the efficiency of DSCs. The contributions of this thesis toward that end are listed in the following Chapters.

In Chapter 3, a photoanode material with a new type of architecture which has high specific surface area, enhanced light scattering capability and efficient electron transfer pathways for high performance of DSCs was designed and synthesized, with 9.0 % conversion efficiency realized.

In Chapter 4, a bi-layer photoanode for cold isostatic pressing (CIP) was designed, with a 5.6 % conversion efficiency realized on flexible substrate.

In Chapter 5, one new type of photoanode material composed of mesoporous anatase single crystals with special polyhedral pores was designed for $Co^{(2+/3+)}$-based DSCs, with conversion efficiencies up to an impressive 8.7 % achieved.

In Chapter 6, 3D hierarchical rutile TiO_2 architecture was combined with metal-free organic sensitizer (D149) for rutile TiO_2-based DSCs, with 8.6 % conversion efficiency achieved. And Chapter 7 compared two dyes (N719 and D149) used as sensitizers for the rutile TiO_2-based DSCs for the first time.

2.6 References

1. A. Hagfeldt, G. Boschloo, L. Sun, L. Kloo, and H. Pettersson, *Chem. Rev.*, 2010, **110**, 6595-6663.

2. M. Grätzel, *J. Photochem. Photobiol. C*, 2003, **4**, 145-153.

3. K. Zhu, N. R. Neale, A. Miedaner, and A. J. Frank, *Nano Lett.*, 2007, **7**, 69-74.

4. G. K. Mor, K. Shankar, M. Paulose, O. K. Varghese, and C. A. Grimes, *Nano Lett.*, 2006, **6**, 215-218.

5. M. Law, L. E. Greene, J. C. Johnson, R. Saykally, and P. Yang, *Nature Mater.*, 2005, **4**, 455-459.

6. J.-Y. Liao, B.-X. Lei, H.-Y. Chen, D.-B Kuang, and C.-Y. Su, *Energy Environ. Sci.*, 2012, **5**, 5750-5757.

7. M. Adachi, Y. Murata, J. Takao, J. Jiu, M. Sakamoto, and F. Wang, *J. Am. Chem. Soc.*, 2004, **126**, 14943-14949.

8. B. Liu, and E. S. Aydil, *J. Am. Chem. Soc.*, 2009, **131**, 3985-3990.

9. F. H. Bijarbooneh, Y. Zhao, Z. Sun, Y.-U. Heo, V. Margras, J. H. Kim, S. X. Dou, *APL Mat.*, 2013, **1**, 1-7.

10. D. H. Chen, F. Z. Huang, Y.-B. Cheng, and R. A. Caruso, *Adv. Mater.*, 2009, **21**, 2206-2210.

11. F. Z. Huang, D. H. Chen, X. L. Zhang, R. A. Caruso, and Y.-B. Cheng, *Adv. Funct. Mater.*, 2010, **20**, 1301-1305.

12. D. H. Chen, L. Cao, F. Z. Huang, P. Imperia, Y.-B. Cheng, and R. A. Caruso , *J. Am. Chem. Soc.*, 2010, **132**, 4438-4444.

13. J. Nawrocki, C. Dunlap, A. McCormick, and P. W. Carr, *J. Chromatogr. A*, 2004, **1028**, 1-30.

14. T. E. Thingholm, T. J. D. Jorgensen, O. N. Jensen, and M. R. Larsen, *Nat. Protoc.,* 2006, **1**, 1929-1935.

15. Z. D. Lu, M. M. Ye, N. Li, W. W. Zhong, and Y. D. Yin, *Angew. Chem. Int. Ed.*, 2010, **49**, 1862-1866.

16. B. O'Regan, and M. Grätzel, *Nature*, 1991, **353**, 737-740.

17. K. Hara, and K. Arakawa, *Handbook of Photovoltaic Science and Engineering*, England: John Wiley & Sons Ltd, 2003.

18. B. Grob, and M.E. Schultz, *Basic Electronics*, Gregg Division, 1977.

19. R. Jose, V. Thavasi, and S. Ramakrishna, *J. Am. Ceram. Soc.*, 2009, **92**, 289-301.

20. A. Jena, S. P. Mohanty, P. Kumar, J. Naduvath, V. Gondane, P. Lekha, J. Das, H. K. Narula, S. Mallick, and P. Bhargave, *T. Indian Ceram. Soc.*, 2012, **71**, 1-16.

21. A. Yella, H. W. Lee, H. N. Tsao, C. Yi, A. K. Chandiran, M. K. Nazeeruddin, E. W. G. Diau, C. Y. Yeh, S. M. Zakeeruddin, and M. Grätzel, *Science*, 2011, **334**, 629-634.

22. H. Minoura, and T. Yoshida, *Electrochemistry*, Tokyo, 2008, **76**, 109.

23. P. Guo, and M.A. Aegerter, *Thin Solid Films*, 1999, **351**, 290-294.

24. B. Tan, E. Toman, Y. Li, and Y. Wu, *J. Am. Chem. Soc.*, 2007, **129**, 4162-4163.

25. S. Burnside, J.-E. Moser, K. Brooks, M. Grätzel, and D. Cahen, *J. Phys. Chem. B*, 1999, **103**, 9328-9332.

26. H. Zheng, Y. Tachibana, and K. Kalantar-Zadeh, *Langmuir*, 2010, **26**, 19148-19152.

27. N. Nang Dinh, M.C. Bernard, A. Hugot-Le Goff, T. Stergiopoulos, and P. Falaras, *C. R. Chim.*, 2006, **9**, 676-683.

28. A. Polo, M. Itokazu, and N. Murakami Iha, Coord. *Chem. Rev.*, 2004, **248**, 1343-1361.

29. X. J. Feng, K. Shankar, O. K. Varghese, M. Paulose, T. J. Latempa, and C. A. Grimes, *Nano Lett.*, 2008, **8**, 3781-3786.

30. J. J. Qiu, X. M. Li, F. W. Zhuge, X. Y. Gan, X. D. Gao, W. Z. He, S. J. Park, H. K. Kim, and Y. H. Hwang, *Nanotechnology*, 2010, **21**, 195602.

31. H. Kokubo, B. Ding, T. Naka, H. Tsuchihira, and S. Shiratori, *Nanotechnology*, 2007, **18**, 165604.

32. K. Fujihara, A. Kumar, R. Jose, S. Ramakrishna, and S. Uchida, *Nanotechnology*, 2007, **18**, 365709.

33. N. G. Park, J. van de Lagemaat, and A. J. Frank, *J. Phys. Chem. B*, 2000, **104**, 8989-8994.

34. A. Ghicov and P. Schmuki, *Chem. Commun.*, 2009, **455**, 2791-2808.

35. G. K. Mor, O. K. Varghese, M. Paulose, K. Shankar, and C. A. Grimes, *Sol. Energy Mater. Sol. Cells*, 2006, **90**, 2011-2075.

36. J. Yu, J. Fan, and K. Lv, *Nanoscale*, 2010, **2**, 2144-2149.

37. N. Yang, J. Zhai, D. Wang, Y. Chen, and L. Jiang, *ACS Nano*, 2010, **4**, 887-894.

38. Z. Zheng, B. Huang, X. Qin, X. Zhang, Y. Dai, M. Jiang, P. Wang, and M.-H. Whangbo, *Chem.–Eur. J.*, 2009, **15**, 12576-12579.

39. H. G. Yang, C. H. Sun, S. Z. Qiao, J. Zou, G. Liu, S. C. Smith, H. M. Cheng and G. Q. Lu, *Nature*, 2008, **453**, 638-641.

40. Q. J. Xiang, K. L. Lv and J. G. Yu, *Appl. Catal. B*, 2010, **96**, 557-564.

41. H. J. Koo, Y. J. Kim, Y. H. Lee, W. I. Lee, K. Kim, and N. G. Park, *Adv. Mater.*, 2008, **20**, 195-199.

42. Y. J. Kim, M. H. Lee, H. J. Kim, G. Lim, Y. S. Choi, N. G. Park, K. Kim, W. I. Lee, *Adv. Mater.*, 2009, **21**, 3668-3673.

43. S. Ahmed, A. Du Pasquier, D. P. Birnie, and T. Asefa, *ACS Appl. Mater. Interfaces*, 2011, **3**, 3002-3010.

44. C.-Y. Cho and J. H. Moon, *Adv. Mater.*, 2011, **23**, 2971-2975.

45. J. T. Park, J. H. Koh, J. A. Seo, and J. H. Kim, *J. Mater. Chem.*, 2011, **21**, 17872-17880.

46. J. T. Park, D. K. Roh, R. Patel, E. Kim, D. Y. Ryu, and J. H. Kim, *J. Mater. Chem.*, 2010, **20**, 8521-8530.

47. J. Zhai, Y. Zhao, X. L. Sheng, L. Jiang, C. H. Yang, Z. W. Sun, Y. F. Li, and D. B. Zhu, *ChemPhysChem*, 2007, **8**, 856-861.

48. J.-Y. Liao, B.-X. Lei, D.-B. Kuang, and C. Y. Su, *Energy Environ. Sci.*, 2011, **4**, 4079-4085.

49. S. C. T. Lau, J. Dayou, C. S. Sipaut, and R. F. Mansa, *Int. J. Renew. Energy Res.*, 2014, **4**, 665-674.

50. S. Ngamsinlapasathian, S. Sakulkhaemaruethai, S. Pavasupree, A. Kitiyanan, T. Sreethawong, Y. Suzuki, and S. Yoshikawa, *J. Photoch. Photobio. A*, 2004, **164**, 145-151.

51. S. Pavasupree, S. Ngamsinlapasathian, M. Nakajima, Y. Suzuki, and S. Yoshikawa, *J. Photoch. Photobio. A*, 2006, **184**, 163-169.

52. P. Sun, X. Zhang, C. Wang, Y. Wei, L. Wang, and Y. Liu, *J. Mater. Chem. A*, 2013, **1**, 3309-3314.

53. T. Sawatsuk, A. Chindaduang, C. Sae-kung, S. Pratontep, and G. Tumcharern, *Diam. Relat. Mater.*, 2009, **18**, 524-527.

54. T.-H. Tsai, S.-C. Chiou, and S.-M. Chen, *Int. J. Electrochem. Sci.*, 2011, **6**,

3333-3343.

55. H. J. Koo, Y. J. Kim, Y. H. Lee, W. I. Lee, K. Kim, and N. G. Park, *Adv. Mater.*, 2008, **20**, 195-199.

56. W. Wang, Q. Zhao, H. Li, H. Wu, D. Zou, and D. Yu, *Adv. Funct. Mater.*, 2012, **22**, 2775-2782.

57. T. Chen, L. Qiu, Z. Cai, F. Gong, Z. Yang, Z. Wang, and H. Peng, *Nano Lett.* 2012, **12**, 2568-2572.

58. Y. Peng, J. Zhong, K. Wang, B. Xue, and Y.-B. Cheng, *Nano Energy* 2013, **2**, 235-240.

59. H. C. Weerasinghe, F. Huang, and Y.-B. Cheng, *Nano Energy*, 2013, **2**, 174-189.

60. G. Hashmi, K. Miettunen, T. Peltola, J. Halme, I. Asghar, K. Aitola, M. Toivola, and P. Lund, *Renew. Sust. Energy Rev.*, 2011, **15**, 3717-3732.

61. T. Yamaguchi, N. Tobe, D. Matsumoto, T. Nagai, and H. Arakawa, *Sol. Energy Mater. Sol. Cells*, 2010, **94**, 812-816.

62. F. Huang, D. Chen, Q. Li, R.A. Caruso, and Y.-B. Cheng, *Appl. Phys. Lett.*, 2012, **100**, 123102-123104.

63. H. C. Weerasinghe, P. M. Sirimanne, G. P. Simon, and Y.-B. Cheng, *Prog. Photovolt: Res. Appl.*, 2012, **20**, 321-332.

64. L. Grinis, S. Kotlyar, S. Ruhle, J. Grinblat, and A. Zaban, *Adv. Funct. Mater.*, 2010, **20**, 282-288.

65. T. Miyasaka, M. Ikegami, and Y. Kijitori, *J. Electrochem. Soc.*, 2007, **154**, 455-461.

66. H. C. Weerasinghe, P. M. Sirimanne, G. V. Franks, G. P. Simon, and Y.-B. Cheng, *J. Photoch. Photobio. A*, 2010, **213**, 30-36.

67. H. C. Weerasinghe, G. V. Franks, J. D. Plessis, G. P. Simon, and Y.-B. Cheng, *J. Mater. Chem.*, 2010, **20**, 9954-9961.

68. H. C. Weerasinghe, P. M. Sirimanne, G. P. Simon, and Y.-B. Cheng, *J. Photoch. Photobio. A*, 2009, **206**, 64-70.

69. T. Miyasaka and Y. Kijitori, *J. Electrochem. Soc.*, 2004, **151**, 1767-1773.

70. T. N. Murakami, Y. Kijitori, N. Kawashima, and T. Miyasaka, *Chem. Lett.*, 2003, **32**, 1076-1077.

71. H. Pan, S. H. Ko, N. Misra, and C. P. Grigoropoulos, *Appl. Phys. Lett.*, 2009, **94**, 071117/1-3.

72. X. Li, H. Lin, J.B. Li, N. Wang, C. F. Lin, and L. Z. Zhang, *J. Photoch. Photobio. A*, 2008, **195**, 247-253.

73. D. Zhang, T. Yoshida, K. Furuta, and H. Minoura, *J. Photoch. Photobio. A*, 2004, **164**, 159-166.

74. H. Lindstrom, A. Holmberg, E. Magnusson, L. Malmqvist, and A. Hagfeldt, *J. Photoch. Photobio. A*, 2001, **145**, 107-112.

75. S. Uchida, M. Timiha, H. Takizawa, and M. Kawaraya, *J. Photoch. Photobio. A*, 2004, **164**, 93-96.

76. S. I. Cha, B. K. Koo, K. H. Hwang, S. H. Seo, and D. Y. Lee, *J. Mater. Chem.*, 2011, **21**, 6300-6304.

77. D. Zhang, T. Yoshida, and H. Minoura, *Chem. Lett.*, 2002, **9**, 874-875.

78. D. Zhang, T. Yoshida, and H. Minoura, *Adv. Mater.*, 2003, **15**, 814-817.

79. H. Santa-Nokki, J. Kallioinen, T. Kololuoma, V. Tuboltsev, and J. Korppi-Tommola, *J. Photoch. Photobio. A*, 2006, **182**, 187-191.

80. J.-H. Yum, E. Baranoff, F. Kessler, T. Moehl, S. Ahmad, T. Bessho, A. Marchioro, E. Ghadiri, J.-E. Moser, C. Yi, M. K. Nazeeruddin, and M. Grätzel,

Nat. Commun., 2012, **3**, 631.

81. H. Tian, Z. Yu, A. Hagfeldt, L. Kloo, and L. Sun, *J. Am. Chem. Soc.*, 2011, **133**, 9413-9422.

82. M. Wang, N. Chamberland, L. Breau, J.-E. Moser, R. Humphry-Baker, B. Marsan, S. M. Zakeeruddin, and M. Grätzel, *Nat. Chem.*, 2010, **2**, 385-389.

83. T. Daeneke, T.-H. Kwon, A. B. Holmes, N. W. Duffy, U. Bach, and L. Spiccia, *Nat. Chem.*, 2011, **3**, 213-217.

84. S. M. Feldt, E. A. Gibson, E. Gabrielsson, L. Sun, G. Boschloo, and A. Hagfeldt, *J. Am. Chem. Soc.*, 2010, **132**, 16714-16724.

85. A. Yella, H.-W. Lee, H. N. Tsao, C. Yi, A. K. Chandiran, M. K. Nazeeruddin, E. W.-G. Diau, C.-Y. Yeh, S. M. Zakeeruddin, and M. Grätzel, *Science*, 2011, **334**, 629-634.

86. H. Nusbaumer, J.-E. Moser, S. M. Zakeeruddin, M. K. Nazeeruddin, and M. Grätzel, *J. Phys. Chem. B*, 2001, **105**, 10461-10464.

87. S. Ahmad, E. Dell'Orto, J.-H. Yum, F. Kessler, M. K. Nazeeruddin, and M. Grätzel, *Chem. Commun.*, 2012, **48**, 9714-9716.

88. L. E. Polander, A. Yella, B. F. Curchod, N. Ashari Astani, J. Teuscher, R. Scopelliti, P. Gao, S. Mathew, J. E. Moser, and I. Tavernelli, *Angew. Chem., Int. Ed.*, 2013, **52**, 8731-8735.

89. S. Mathew, A. Yella, P. Gao, R. Humphry-Baker, B. F. Curchod, N. Ashari-Astani, I. Tavernelli, U. Rothlisberger, M. K. Nazeeruddin, and M. Grätzel, *Nat. Chem.*, 2014, **6**, 242-247.

90. A. Hagfeldt, G. Boschloo, L. Sun, L. Kloo, and H. Pettersson, *Chem. Rev.*, 2010, **110**, 6595-6663.

91. S. M. Feldt, E. A. Gibson, E. Gabrielsson, L. Sun, G. Boschloo, and A.

Hagfeldt, *J. Am. Chem. Soc.*, 2010, **132**, 16714-16724.

92. B. M. Klahr and T. W. Hamann, *J. Phys. Chem. C*, 2009, **113**, 14040-14045.

93. T. T. T. Pham, T. M. Koh, K. Nonomura, Y. M. Lam, N. Mathews, and S. Mhaisalkar, *ChemPhysChem*, 2014, **15**, 1216-1221.

94. E. Enache-Pommer, J. E. Boercker, and E. S. Aydil, *Appl. Phys. Lett.*, 2007, **91**, 123116-123118.

95. J. B. Baxter and E. S. Aydil, *Appl. Phys. Lett.*, 2005, **86**, 053114.

96. M. Law, L. E. Greene, A. Radenovic, T. Kuykendall, J. Liphardt, and P. D. Yang, *J. Phys. Chem. B*, 2006, **110**, 22652-22663.

97. J. B. Baxter, A. M. Walker, K. van Ommering, and E. S. Aydil, *Nanotechnology*, 2006, **17**, 304-312.

98. S. H. Kang, S.-H. Choi, M.-S. Kang, J.-Y. Kim, H.-S. Kim, T. Hyeon, and Y.-E. Sung, *Adv. Mater.*, 2008, **20**, 54-58.

99. X. Feng, K. Zhu, A. J. Frank, C. A. Grimes, and T. E. Mallouk, *Angew. Chem. Int. Ed.*, 2012, **51**, 2727-2730.

100. A. Dong, R. Tang, and W. E. Buhro, *J. Am. Chem. Soc.*, 2007, **129**, 12254-12262.

101. Y. Jung, D.-K. Ko, and R. Agarwal, *Nano Lett.*, 2007, **7**, 264-268.

102. B. Sun, E. Marx, and N. C. Greenham, *Nano Lett.*, 2003, **3**, 961-963.

103. J.-K. Oh, J.-K. Lee, H.-S. Kim, S.-B. Han, and K.-W. Park, *Chem. Mater.*, 2010, **22**, 1114-1118.

104. O. K. Varghese, M. Paulose, and C. A. Grimes, *Nat. Nanotechnol.*, 2009, **4**, 592-597.

105. J. Boucle, S. Chyla, M. Shaffer, J. Durrant, D. Bradley, and J. Nelson, *Adv. Funct. Mater.*, 2008, **18**, 622-633.

106. J. R. Jennings, A. Ghicov, L. M. Peter, P. Schmuki, and A. B. Walker, *J. Am. Chem. Soc.*, 2008, **130**, 13364-13372.

107. S. Ito, S. M. Zakeeruddin, R. Humphty-Baker, P. Liska, and R. Charvet, *Adv. Mater.*, 2006, **18**, 1202-1205.

108. W. Shao, F. Gu, L. Gai, and C. Li, *Chem. Commun.*, 2011, **47**, 5046-5048.

109. Z. Sun, J. H. Kim, Y. Zhao, D. Attard, and S. X. Dou, *Chem. Commun.*, 2013, **49**, 966-968.

3 HIGHLY CONNECTED HIERARCHICAL TEXTURED TIO_2 SPHERES AS PHOTOANODES FOR DYE-SENSITIZED SOLAR CELLS

The aim of this chapter is to design a photoanode material with a new architecture which has high specific surface area, enhanced light scattering capability and efficient electron transfer pathways for high performance of DSCs.

In general, to obtain higher solar-to-electric conversion efficiency in DSC, a photoanode material should meet the following requirements: 1) the surface area should be high enough to efficiently absorb the dye solution; 2) the porosity should be high enough for efficient electrolyte diffusion and effective mass transportation; 3) particle size should be big enough for efficient light scattering; 4) grain boundaries should be minimized for faster electron transportation. However, the requirements cannot be meet in one system.

In this chapter, a new type of microstructured TiO_2 sea urchin-like assembly, composed of high aspect-ratio nanosheets was presented. It is also demonstrated the applicability of these structures as photoanodes in dye-sensitized solar cells, with 9.0 % conversion efficiency realized, a considerable improvement over commercial Dyesol paste (8.2 %) under the same conditions. We reveal that this new TiO_2 nanostructure is beneficial to enhanced dye loading and efficient light scattering. In particular, the interpenetrating individual sheets of the spheres result in more intimate interparticle connections and provide efficient electron transfer pathways.

This chapter has been published in *J. Mater. Chem. A*, 2014, **2**, 8902.

3.1 Introduction

Dye-sensitized electrochemical photovoltaic cell technology has been recognized as a viable option for power generation. [1] Dye-sensitized Solar Cells (DSCs) have attracted much attention over the past two decades on account of features such as shorter energy pay-back time, lower dependence on the angle of incidence of light, insensitivity to temperature changes, easy fabrication on rigid and flexible substrates, and relatively high energy conversion efficiency. [2-8] One of the core components in the DSC system is usually a wide-band-gap titanium oxide (TiO_2) thin film that serves as a support for the dye molecules and as an electron-transporting medium. Typically, in the photoanode, an insufficient electron diffusion coefficient in electrodes composed of nanometer-sized TiO_2 particles is believed to limit the power conversion efficiency. This is because electron collection is determined by trapping/detrapping events at the sites of the electron traps (defects, surface states, grain boundaries, self-trapping, etc.). [9] With this as the motivation, there is an overwhelming desire among researchers to design and synthesize materials that simultaneously have large surface areas (to absorb more dye molecules), efficient light scattering capability, and faster electron transport. In addition, the pores formed in the TiO_2 layer must be sufficiently large in size, with good connectivity for efficient diffusion of electrolyte components. [10] One solution to this requirement is to use one-dimensional (1D) nanostructures, which can provide direct channels for the rapid collection of the photogenerated electrons, reduce charge recombination, and simultaneously enhance the electrolyte diffusion. [11-15] The typical low surface area of the 1D nanostructures, however, leads to reduced dye loading, and hence reduced light harvesting, resulting in lower photocurrents.

Alternatively, bi-layer structured nanoparticle films have been designed, to confine the incident light within the photoanode. [16-21] Such a configuration, however, increases the thickness of the photoanode film, so that photogenerated electrons at the light scattering layer have to be transported a longer distance within the photoelectrode film to reach the current collector electrode and therefore suffer from a high rate of recombination. Many groups have also tried to combine nanometer-sized particles with micrometer-sized particles to make full use of the combined size advantages. [22-24] Most of these structures, however, were obtained on the basis of separate TiO_2 materials with different morphologies, which unavoidably bring in tedious fabrication procedures. [25]

In this work, we introduce a novel material structure for use in DSC photoanodes, which consists of hierarchical assemblies of polycrystalline anatase TiO_2 nanosheets that appear to resemble sea urchins. These spheres have a bimodal distribution of sizes, leading to both effective dye adsorption and effective light-scattering behaviour, as well as enhanced electronic interconnectivity within the photoanode. An overall energy conversion efficiency of up to 9.0 % can be achieved by using these highly connected hierarchical textured TiO_2 spheres (HCHT) as the photoelectrode with N719 dye.

3.2 Experimental

3.2.1 Synthesis of Highly Connected Hierarchical Textured TiO_2 Spheres (HCHT)

Acetic acid (HAc, ACS reagent, ≥ 99.7 %) and titanium butoxide (TB, Ti $(OCH_2CH_2CH_2CH_3)_4$, 97 %, analytical reagent) were purchased from Sigma-Aldrich, and used without further purification. The fabrication of HCHT from a TB-HAc solution was simply obtained by a hydrothermal approach. In detail, 0.5 mL of TB was added into 30 mL of HAc solution under magnetic stirring and kept for 1 h at room temperature, before being transferred to a Teflon-lined stainless steel pressure vessel (45 mL capacity, Parr Instrument Company) and heated in oven to 150 ^oC for 12 h (heating ramp rate of 1 $^oC\ min^{-1}$). After the autoclave cooled down to room temperature, the product was collected by centrifugation, washed with distilled water and ethanol several times, dried at 90 ^oC overnight, and calcined at 500 ^oC for 3 h to remove the residual organics.

3.2.2 Preparation of TiO_2 Photoanodes

To prepare the DSC working electrodes, fluorine doped tin oxide (FTO) glass as current collector (2.3 mm thickness, 8 Ω/sq, Hartford Glass) was first cleaned with soapy water for 20 min and rinsed with distilled water, then soaked in acetone and then ethanol in an ultrasonic bath for 30 min. Firstly, the blocking layer solution was created by diluting titanium diisopropoxide bis(acetylacetonate), 75 % in isopropanol (Aldrich, 32525-2), in absolute ethanol in the volume ratio of 1:9. After drying in nitrogen, the blocking layer was deposited on the clean FTO glass by spray pyrolysis. Then, a layer of TiO_2 paste was cast onto the FTO glass plates by the doctor-blade method. The paste fabrication process is as follows: briefly, TiO_2 powders (1.0 g) were ground in a mixture of ethanol (20 mL), distilled water (0.833 mL), acetic acid

(0.167 mL), terpineol (4 g), and ethyl cellulose (0.5 g) to form a slurry, and then the slurry was sonicated for 1 h in an ultrasonic bath and stirred for 1 h. A viscous white TiO_2 paste was finally obtained after an evaporation process. After a heating process (at 150 ^oC for 10 min, at 325 ^oC for 5 min, at 375 ^oC for 5 min, at 450 ^oC for 30 min, and then at 500 ^oC for 15 min) to remove organic substances, the TiO_2 films were soaked in 0.02 M aqueous titanium tetrachloride solution ($TiCl_4$) at 70 ^oC for 30 min. As a final step, the films were washed with water, and then ethanol, dried, and sintered again (500 ^oC for 30 min). Before the TiO_2 paste was cast onto the FTO glass, a single blocking layer [with the solution created by diluting titanium diisopropoxide bis (acetylacetonate), 75 % in isopropanol (Aldrich, 32525-2), in absolute ethanol with volume ratio 1:9] was deposited on FTO glass by the pyrolysis method.

3.2.3 Fabrication of DSCs

The resultant TiO_2 films were immersed in a 0.5 mM N719 (Solaronix) dye solution in a 1:1 (v/v) mixture of acetonitrile (HPLC, Lab-scan) and *tert*-butanol (LR, Ajax Chemicals) for about 24 h once the temperature had decreased to approximately 110 ^oC. After dyeing, the samples were taken out of the dye bath, washed with acetonitrile, and dried. The Pt counter electrode was produced using a pre-drilled piece of 2.3 mm FTO glass, coated with one drop of 10 mM platinic acid solution (H_2PtCl_6) and heated to 400 ^oC for 20 min. The working electrode and Pt counter electrode were assembled into a sandwich type cell and sealed with a spacer of 25 μm Surlyn (Solaronix). An I^-/I_3^- organic solvent based electrolyte solution [85:15 vol % of acetonitrile/valeronitrile, 0.03 M iodine (I_2), 0.5 M 4 tertbutylpyridine (4-tBP), 0.6 M 1-butyl-3- methylimidazolium iodide (BMII), and 0.1 M guanidinium thiocyanate

(GuSCN)] was introduced via vacuum back-filling. The hole was sealed using another piece of aluminium-backed Surlyn.

3.2.4 Characterizations

The crystalline structure of the samples was characterized by using a Bruker Advance X-Ray Diffractometer (40 kV, 30 mA) with Cu Kα (λ = 0.15406 nm) radiation at a scan rate of 1° /min from 20º to 80º (2θ). The morphology of the samples was examined by scanning electron microscopy (SEM, JEOL 7001) and transmission electron microscopy (TEM, JEM-2100F). Brunauer–Emmett–Teller (BET) surface areas (S_{BET}) were determined by using a nitrogen adsorption apparatus (Tristar 3030, Micromeritics Instrument Corporation). All samples were degassed at 150 °C overnight before measurement. Dye desorption was performed by dipping the sensitized sample into 0.1 M NaOH in ethanol-water (1:1) solution. The effective dye loading was determined from the absorption value for each NaOH/dye solution according to Beer's law. The light absorption and scattering properties of the samples were investigated by ultraviolet (UV)-visible light absorption/diffuse reflectance spectrometry (Shimadzu UV-3600). Thermogravimetric (TG) and differential thermal analysis (DTA) were carried out on a Mettler Toledo GC200 instrument from 25 to 600 °C with a heating rate of 3 °C min^{-1}. Film thickness was measured with a Veeco Dektak 150 Surface Profiler. Photocurrent density – voltage (*J*–*V*) curves were measured using a Keithley 2400 sourcemeter, a simulated 100 mW cm^{-2} air mass (AM) 1.5 light source (Oriel), and customized LabView software. The device area was masked with a metallic mask slightly larger than the active area. The intensity was adjusted to give 100 mW cm^{-2} on a calibrated Si photodiode (PECCELL) equipped with a cut-off filter giving a spectral response similar to N719. Incident photon-to-current quantum conversion efficiency (IPCE) was measured using a 300

W Xe lamp, a monocromator with sorting filters focused on a spot with additional optics. The short circuit current response of the devices was recorded in 5 nm steps using a Keithley 2400 SMU. The measured currents were referenced to a calibrated Si photodiode (PECCELL).

3.3 Results and Discussion

HCHT were synthesized by hydrothermal treatment of a solution of titanium butoxide (TB) and acetic acid (HAc), which was followed subsequently by calcination at 500 ˚C. Figure 3.1(a, c) shows scanning electron microscope (SEM) images of the final product. The thin two-dimensional (2D) nanosheets can be seen to be the primary building units of these larger structures, with an average thickness of approximately 10 nm. These can be more clearly distinguished in Figure 3.1(d) and Figure 3.2(c), where they are assembled into hierarchical spheres. Interestingly, the size distribution in Figure 3.1(b) reveals a bimodal distribution centered at ~ 0.4 and 2.0 μm. Kuang's group could obtain different morphologies and sizes by adjusting hydrothermal conditions, such as precursor concentrations or reaction temperature. [26, 27] The microstructure of the hierarchical spheres was directly observed by transmission electron microscopy (TEM). In the higher resolution images in Figure 3.1(e, f), it can be seen that the nanosheets are perpendicular to the sphere surface and are interlocked with the nanosheets of neighbouring spheres. The small features, created by these sheets, also allow for high dye loading, a feature typically counterposed to effective light scattering. The high resolution TEM (HRTEM) image [Figure 3.1(g)] confirms that the calcined hierarchical TiO_2 spheres are composed of crystalline TiO_2 nanocrystals with a fringe spacing of approximately 3.5 Å, corresponding to the (101) plane of anatase phase. The related selected area electron diffraction (SAED) pattern in Figure 3.1(d) also confirms the polycrystalline nature of the hierarchical spheres, with the three most distinct concentric diffraction rings, moving outward from the centre, assigned to the (101), (103), and (200) planes of anatase TiO_2, respectively.

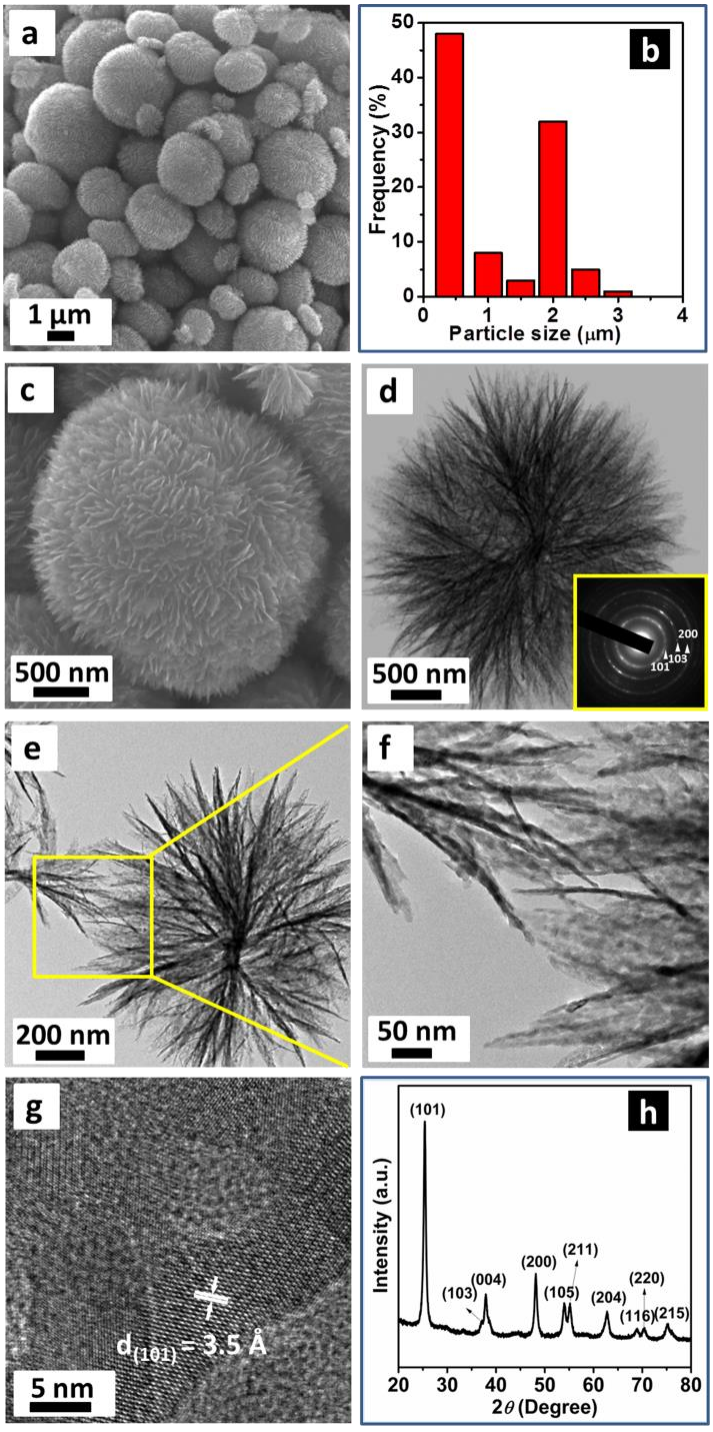

Figure 3.1 Physical characterization of the calcined HCHT: (a) low magnification SEM image; (b) particle size distribution, based on 600 particles from Figure 3.2(a) using Image J software; (c) SEM image of an individual sphere; (d) bright-field TEM image visualizing the nanosheet building blocks, with inset: selected area electron diffraction (SAED) pattern of the whole sphere in (d); (e) TEM image of two typical interconnected spheres; (f) enlarged TEM image revealing details of the interconnection of nanosheets; (g) HRTEM image showing the fringe spacing of anatase TiO_2 nanocrystals; and (h) XRD pattern of the calcined HCHT, indicating TiO_2 crystals with the tetragonal anatase phase (JCPDS No. 21-1272, a = 3.785 Å, b = 3.785 Å, c = 9.514 Å) after the calcination treatment, without any impurity phase.

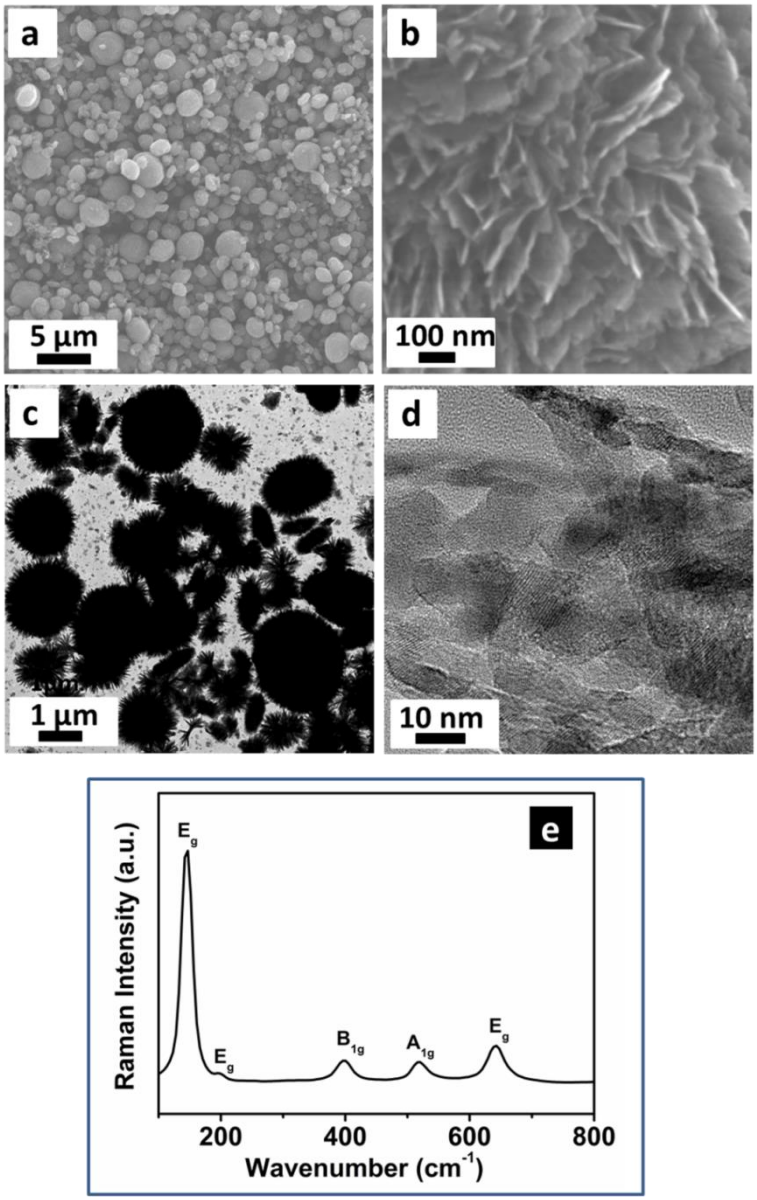

Figure 3.2 (a) Low magnification SEM image of the calcined HCHT, (b) higher magnification image of the nanosheet building blocks, (c) low magnification TEM image of the urchin-like spheres, (d) enlarged TEM image of the nanosheet building blocks; (e) Raman spectrum of the calcined HCHT clearly identifies the anatase phase from the characteristic Raman modes at 142.1 cm^{-1} (E_g), 194.5 cm^{-1} (E_g), 396.1 cm^{-1} (B_{1g}), 515.8 cm^{-1} (A_{1g}), and 638.4 cm^{-1} (E_g), which can be assigned to the Raman active modes ($A_{1g}+B_{1g}+3E_g$) of anatase.

In addition, the successful preparation of anatase is further demonstrated by the X-ray diffraction (XRD) pattern [Figure 3.1(h)] and the Raman spectrum [Figure 3.2(e)].The formation mechanism of such a nanosheet-based hierarchical structure can be understood by examining precipitates extracted at different stages of the reaction, as shown in Figure 3.3.

Based on TEM (Figure 3.4), XRD (Figure 3.5), and Fourier transform infrared spectroscopy (FTIR) characterizations (Figure 3.6), it can be determined that HAc does not fully react with TB during a short reaction time such as 1 h, and the sample features agglomerated nanocrystals [Figure 3.4(a)]. The presence of the asymmetric and symmetric stretching vibrations of the carboxylic groups centered at 1566, 1452, and 1421 cm^{-1} [Figure 3.6(b)] reveals the coordination of HAc to the titanium centres, [28, 29] indicating the formation of a titanium-containing intermediate (Figure 3.7). With an extended reaction time (5 h), the Ti-complex intermediates

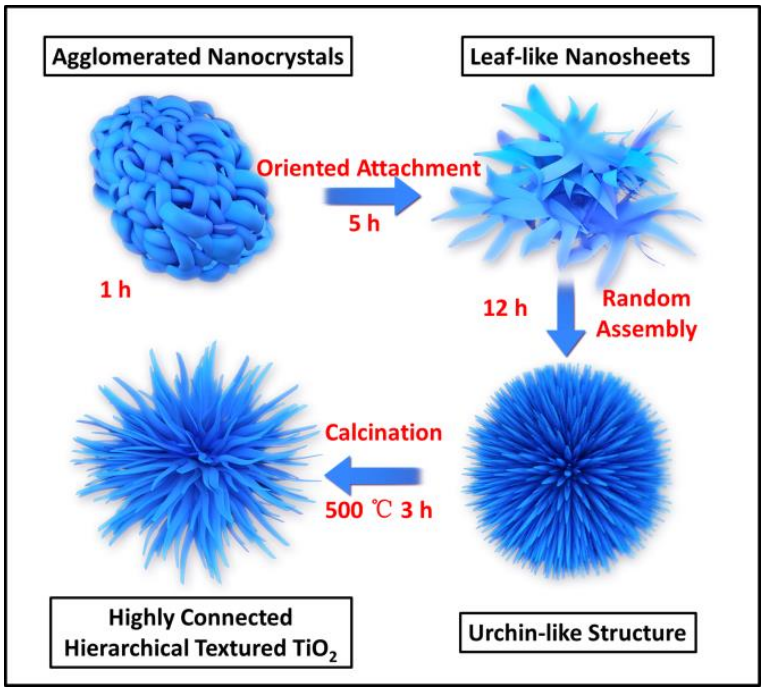

Figure 3.3 Schematic diagram of the formation process of HCHT.

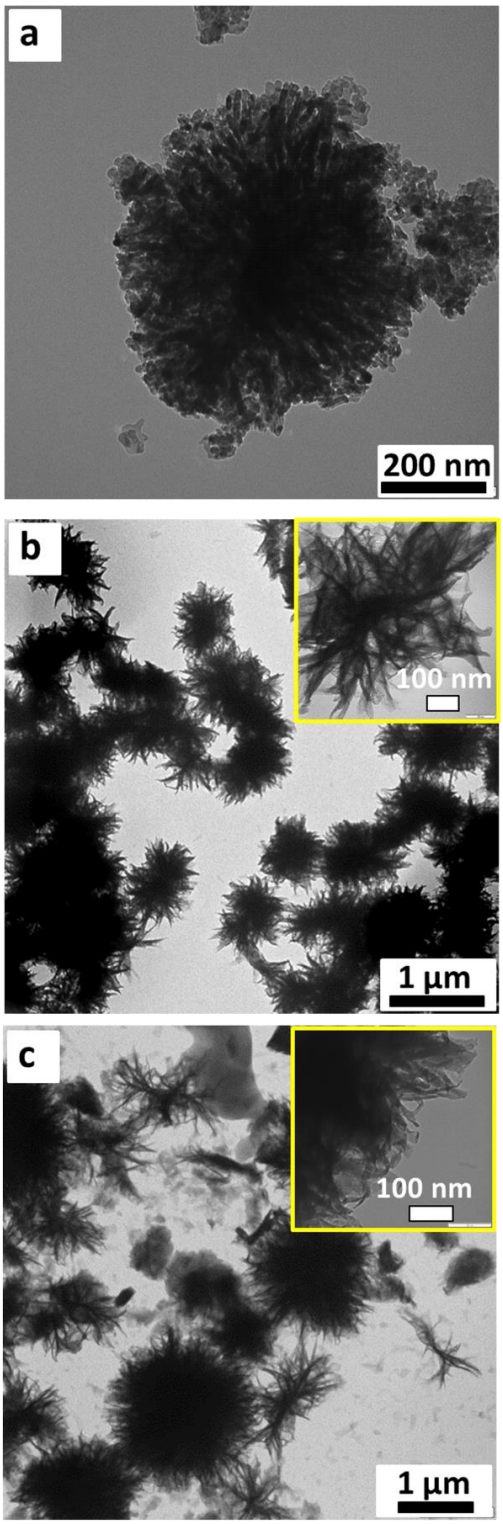

Figure 3.4 TEM images, with the insets showing higher magnification, of as-prepared precipitates obtained after different reaction times (a) 1 h, (b) 5 h, (c) 12 h, via hydrothermal reaction of a solution containing 0.5 mL TB and 30 mL HAc at 150 ^{o}C.

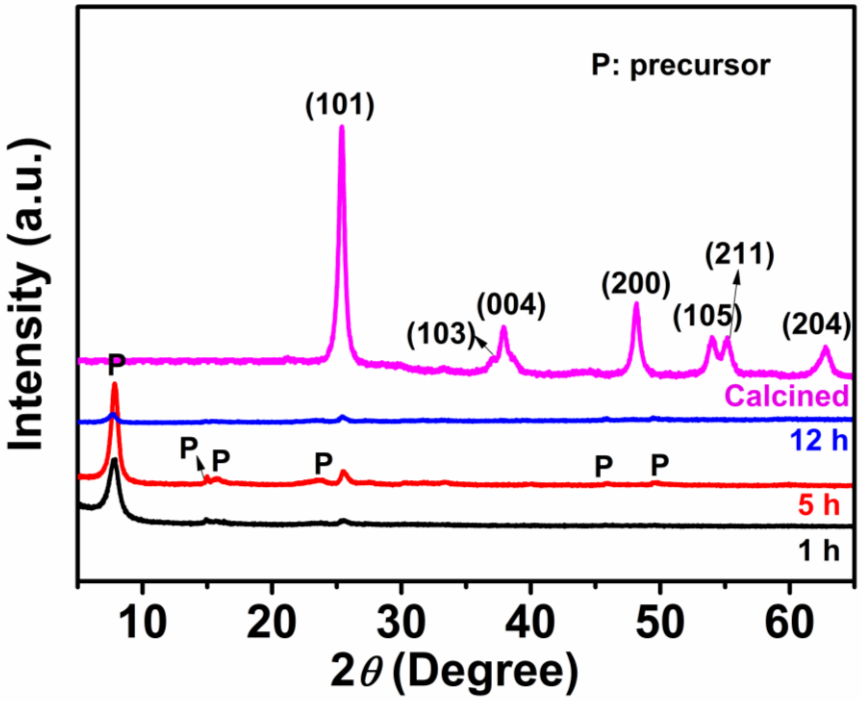

Figure 3.5 XRD patterns of as-prepared precipitates obtained after different reaction times via hydrothermal reaction of a solution containing 0.5 mL TB and 30 mL HAc at 150 ^{o}C, as well as a sample obtained after 12 h of reaction and 3 h of calcination at 500 ^{o}C.

assembled to form leaf- like nanosheets through an oriented attachment process, to bear some resemblance to the HCHT particles [Figure 3.4(b)].

This was, however, only seen to be fully complete after 12 h, with urchin-like structures appearing [Figure 3.4(c)]. It should be noted that XRD of these structures (Figure 3.5) reveals that this material still has low crystallinity. Calcination is required to obtain the highly crystalline material, from the decomposition of the as-prepared Ti-complex intermediate spheres to TiO_2.

The formation of the leaf-like nanosheets is concluded to occur via the following mechanism of acidolysis of TB, catalyzed by HAc through the formation of a Ti-acetate complex. Evidence of this TB-HAc complex is seen with FTIR

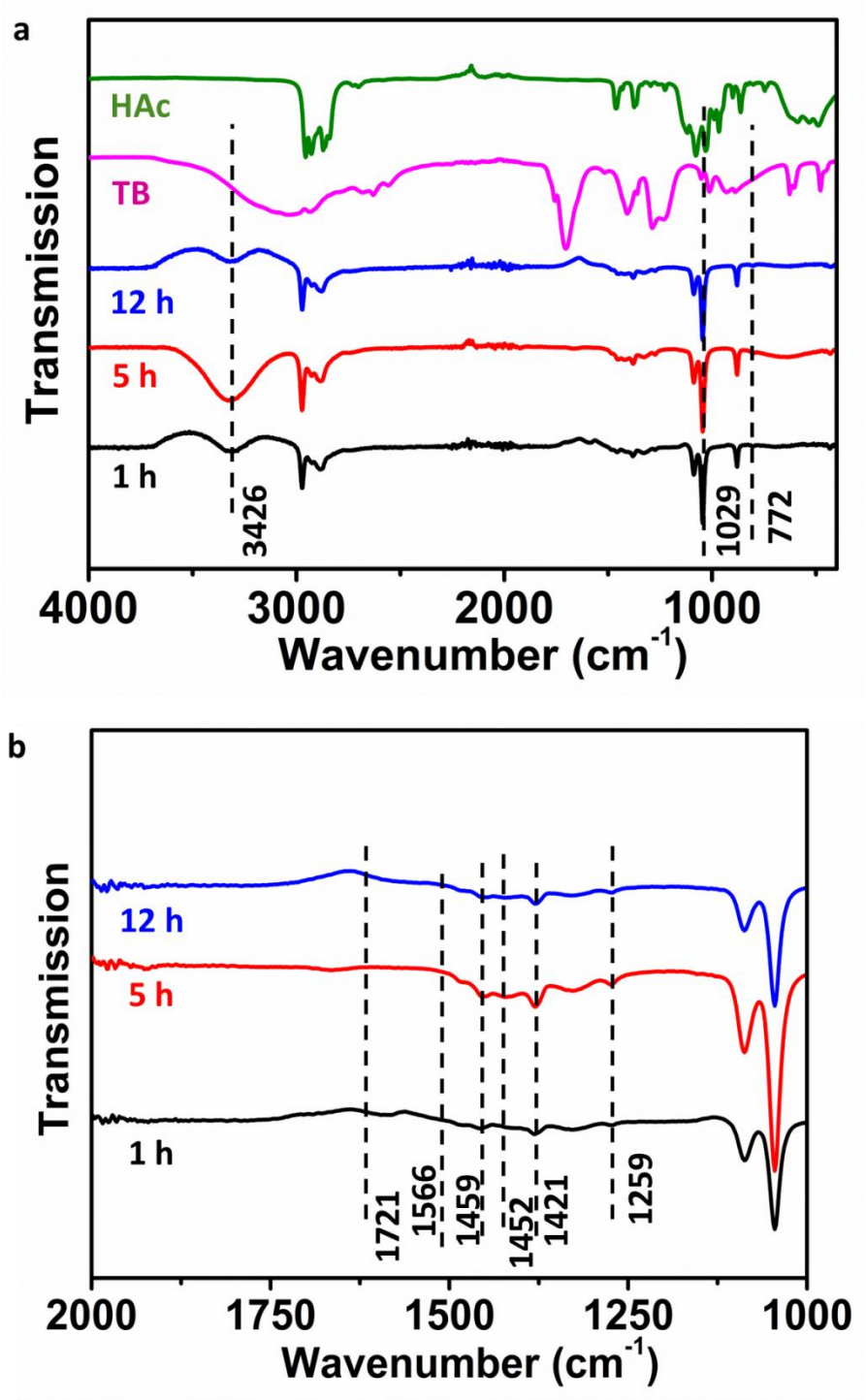

Figure 3.6 (a) FTIR spectra of HAc, TB, and the precipitates obtained after different reaction times via a hydrothermal reaction of a solution containing 0.5 mL TB and 30 mL HAc at 150 ^{o}C; (b) magnification of (a) in the range of 1000-2000 cm^{-1}.

[Figure 3.6(a, b)], [30] with a weak band at 1721 cm^{-1} corresponding to the stretching vibration of the C=O group of HAc.

In comparison with pure TB and HAc, new bands are observed at 3426, 1566, 1452, 1421, and 1259 cm^{-1}. It is well known that acetate ligands are produced by the reaction of TB with HAc and have several modes of coordination, including monodentate and bidentate (chelating and bridging). [31-33] The alcohol nC_4H_9OH is also generated as a by-product in the formation process of these acetate ligands. The peak at 3426 cm^{-1}, (observed for all intermediates), should be assigned to the stretching vibration of the hydroxyl groups on nC_4H_9OH. [34] Moreover, the separation ($\Delta\nu$ = 140 cm^{-1}) between 1566 and 1426 cm^{-1} suggests that some acetate groups act as bridging ligands between two titanium atoms. [31-33]

The presence of the 1721 cm^{-1} (C=O) band can be attributed to the contribution of monodentate-coordinated acetates, while the weak absorption indicates the small amount of such monodentate-coordinated acetates, so that, it can be concluded that most of the Ti-acetate complexes are bidentate-coordinated acetates.

Through the acidolysis process, the nascent TiO_2 nanocrystals are surrounded by numerous bidentate-coordinated acetates. Given the direction of the π-π interactions, amorphous leaf-like nanosheets are constructed by the oriented aggregation of these TiO_2 nanocrystals. [30]

In addition, thermogravimetric analysis (TGA) of the as-prepared precipitates, measured under flowing air (Figure 3.7), indicated that a considerable amount of nC_4H_9OH (~ 29 wt%) was trapped inside the Ti-complex intermediate spheres, and the complete decomposition of the organics occurred at approximately 400 ºC. [31]

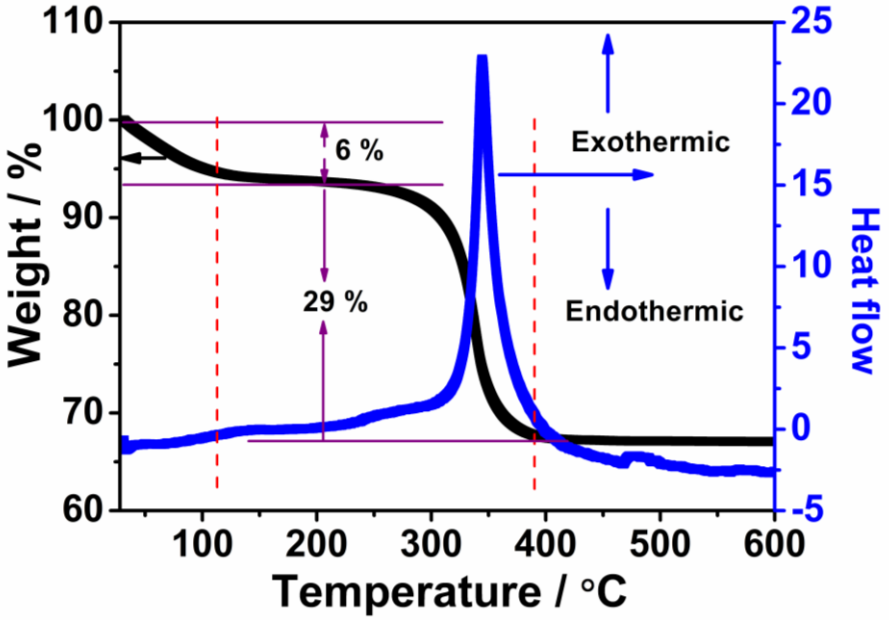

Figure 3.7 Thermogravimetric analysis and differential scanning calorimetry curves of the dried precipitate prepared via hydrothermal reaction of a solution containing 0.5 mL TB and 30 mL HAc at 150 °C for 12 h.

Above 400 ºC, the weight of the sample remains almost constant. The sharp peak in the differential scanning calorimetry (Figure 3.7) curve, starting at approximate 350 ºC, corresponds to the crystallization of the amorphous residue into anatase. Finally, calcination at 500 ºC for 3 h resulted in the formation of pure HCHT, as shown in Figure 3.1.

Nitrogen adsorption-desorption measurements were performed to obtain the Brunauer-Emmett-Teller (BET) specific surface area, porosity, and pore size distribution for the state of the art commercial TiO_2 screen printing pastes [18NR-T Transparent Titania Paste"(hereafter, Dyesol-T) and WER2-O Reflector Titania Paste (hereafter, Dyesol-S), obtained from Dyesol (Australia)], and HCHT materials. As observed in Figure 3.8(a), the isotherm of the HCHT appears to be a Type IV curve with an H3 hysteresis, which is usually ascribed to slit-like mesopores formed by sheet-like particles. [35]

The two hysteresis loops in the isotherm suggest that hierarchical nanoporous structures exist within the matrix, which can be directly verified by the pore size distribution plot in Figure 3.8(b) [determined by Barrett-Joyner-Halenda (BJH) analysis]. The pore size distribution of the HCHT ranges between 2 and 100 nm, with a bimodal pore size distribution centered at 2.5 nm and 10 nm (as might be expected given the hierarchical structure). Interestingly, the mean average pore diameter is 17.6 nm due to large mesopores with diameters of more than 10 nm, accounting for the majority of the slit-like mesopores, which result from the gaps between the randomly assembled nanosheets and can be seen clearly in Figure 3.2(b). [36] In addition, the voids formed by aggregated spheres may also contribute to the large pores [Figure

Table 3.1 Specific surface area, porosity, and roughness factor of Dyesol and HCHT materials.

Samples	Specific surface area ($m^2\ g^{-1}$)	Porosity[a)] (%)	Roughness factor[b)] (μm^{-1})
Dyesol-S	10	9.82	35.2
Dyesol-T	74	64.2	103.3
HCHT	103	66.9	133.0

[a)] The porosities (P) of Dyesol-S, Dyesol-T and HCHT were calculated according to: $P=V_p/(\rho^{-1} + V_p)$, where V_p is the specific cumulative pore volume ($cm^3\ g^{-1}$) and ρ^{-1} is the inverse of the density of anatase TiO_2 (ρ^{-1} = 0.257 $cm^3\ g^{-1}$). [38]

[b)]An estimation of the roughness factor (R) per unit film thickness of the films is obtained by $R = \rho(1-P)S$, where ρ is the density (g cm^{-3}) of anatase TiO_2, P is the porosity (%) of the film, and S is the specific surface area($m^2\ g^{-1}$). [39]

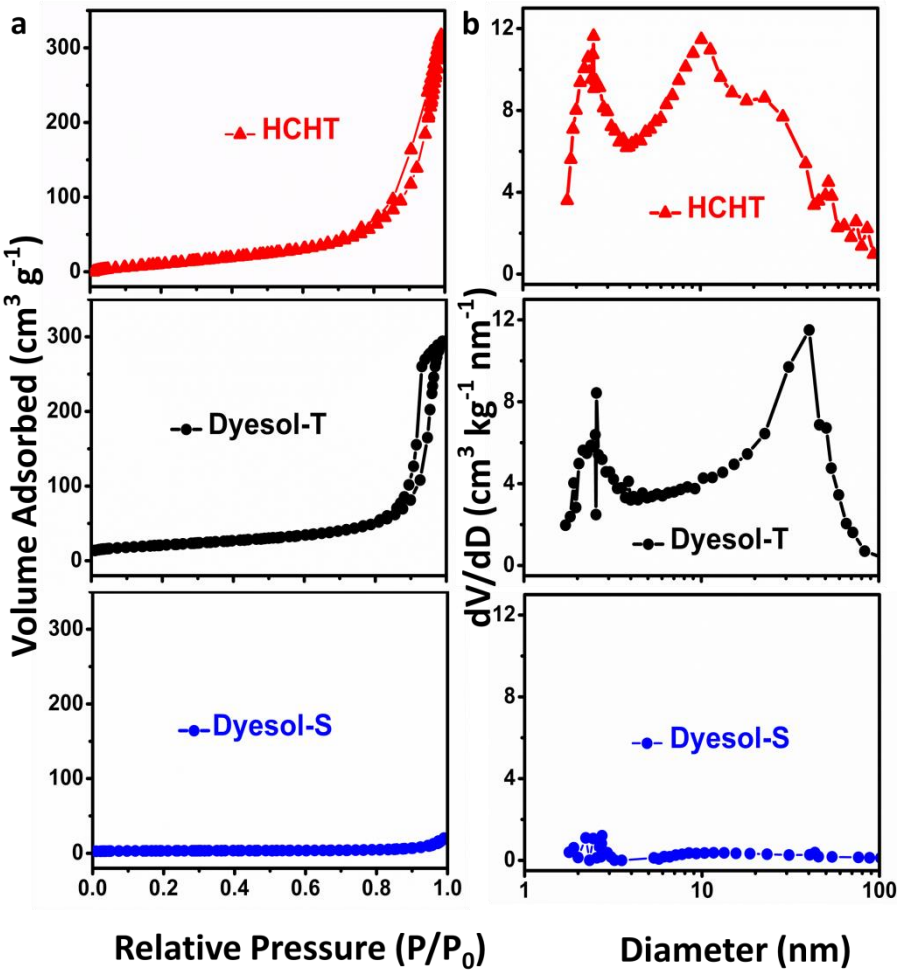

Figure 3.8 (a) N_2 adsorption-desorption isotherms of the HCHT (red closed triangles), the Dyesol-transparent layer (Dyesol-T, 18NR-T, black closed circles) and the Dyesol-scattering layer (Dyesol-S, WER2-O, blue closed circles); and (b) corresponding pore size distributions calculated by the BJH method from the adsorption branch. Before BET measurements, all the particles were dried and then calcined at 500 ºC for 3 h.

3.1(a)]. [37] It is well known that for good performance the pores formed in the TiO_2 layer must be sufficiently large in size with excellent mutual connectivity for the efficient diffusion of electrolyte; [10]

As such, larger pores (between spheres) in HCHT can serve as “highways” for efficient electrolyte diffusion. The data on the BET specific surface areas, porosities, and roughness factors for the Dyesol-S, Dyesol-T, and HCHT are summarized in Table 3.1. The data show that the HCHT film has a larger surface area and higher porosity than the Dyesol film, indicating that HCHT have higher dye adsorption capability. The approximately 1.3 times higher roughness factor in the HCHT film leads to an increase in the light harvesting efficiency due to the larger amount of dye adsorption, which will be further discussed below.

The HCHT were applied in photoanodes of DSCs. The thickness of the film derived from the spheres was around 15 μm. The morphology of the spherical TiO_2 structures is clearly seen in the film prepared from HCHT [shown in the inset of Figure 3.9 and Figure 3.10(a)]. For comparison, a Dyesol-based film with a double layer [12 μm transparent layer (Dyesol-T) + 4 μm scattering layer (Dyesol-S)] was prepared under analogous conditions (refer to Experimental section).

Figure 3.9 shows the current density-voltage (*J*-*V*) characteristics of the Dyesol-based and HCHT-based DSCs. As listed in Table 3.2, the Dyesol-based DSCs showed an open-circuit photovoltage (V_{oc}) of 0.805 V, a short-circuit photocurrent density (J_{sc}) of 14.3 mA cm^{-2}, and an energy conversion efficiency (η) of 8.2 %, while the HCHT-based DSCs showed a V_{oc} of 0.850 V, a J_{sc} of 17.1 mA cm^{-2}, and an η of 9.0 % under one sun conditions, resulting in a 19.6 % and 6 % increase in J_{sc} and V_{oc}, respectively.

The remarkable increase in J_{sc} is probably attributable to the larger surface area due to the hierarchical and mesoporous morphology of the HCHT photoanode, allowing it to take up more dye molecules (5.9×10^{-7} mol cm^{-2}), in tandem with light scattering (discussed in more detail below).

Table 3.2 Photovoltaic parameters of cells based on Dyesol and HCHT photoanodes measured under air mass (AM) 1.5 global (1.5G) one sun illumination (100 mW cm^{-2}). J_{sc}: short-circuit photocurrent density; V_{oc}: open-circuit photovoltage; *FF*: fill factor; η: total power conversion efficiency. The active areas were ~ 0.16 cm^2 for all of the cells (with the mask area 0.25 cm^2), and the data presented are average values obtained after testing four cells.

Samples	J_{sc} (mA cm^{-2})	V_{oc} (V)	*FF* (%)	η (%)	Amount of dye[a] (10^{-7} mol cm^{-2})	Film thickness[b] (μm)
Dyesol	14.3 ± 0.2	0.805 ± 0.01	71.0 ± 2	8.2 ± 0.2	3.7	16 ± 0.3
HCHT	17.1 ± 0.5	0.850 ± 0.02	62.0 ± 2	9.0 ± 0.2	5.9	15 ± 0.5

[a] The dyed electrodes were soaked in a 0.1 M alkaline solution in ethanol and water to desorb the dye from the electrodes. The amount of desorbed dye was quantified by measuring its optical absorption spectrum.

[b] Measurement of film thickness was carried out on a surface profile system (Veeco Dektak 150).

To quantify the dye loading, N719 stained films were exposed to a 0.1 M NaOH solution and the amount of desorbed dye molecules was examined by ultraviolet-visible (UV-Vis) spectroscopy [shown in Figure 3.10(b)]. The absorption spectrum of the desorbed dye represents the amount of dye adsorbed at the photoanode. The two spectra show two peaks at 378 nm and 512 nm which are blue-shifted from the original N719 dye absorption peaks, as typically occurs in alkaline solutions. [40]

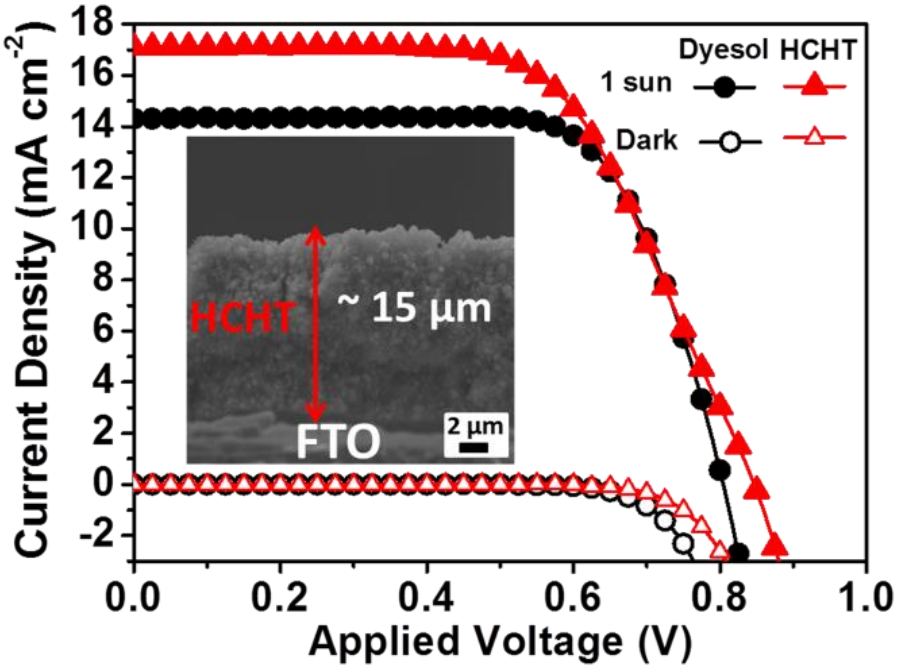

Figure 3.9 *J-V* characteristics of Dyesol- and HCHT-based DSCs. Illumination intensity of 100 mW cm^{-2} with AM 1.5 and active area of 0.16 cm^2 were applied. Inset is a SEM cross-sectional image of the nanosheet-based highly connected hierarchical anatase TiO_2 sphere film on the fluorine-doped tin oxide (FTO) layer, with the film applied by the doctor blade method.

In general, as the amount of dye adsorption increases, more light can be harvested, so that there is a larger photocurrent density. [41] The amount of adsorbed dye for the HCHT photoanode (5.9×10^{-7} mol cm^{-2}) is significantly higher than for the Dyesol photoanode (3.7×10^{-7} mol cm^{-2}), which may contribute to the remarkably improved J_{sc} for the HCHT-based DSCs.

Even if the dark current cannot be directly related to the back electron transfer process, since the electrolyte concentration in the films and the potential distribution across the nanoporous electrode in dark current are different from those under illumination, it has been considered as a qualitative technique to describe the extent of the back electron transfer. [42] Furthermore, dark *J-V* curves show the dark current

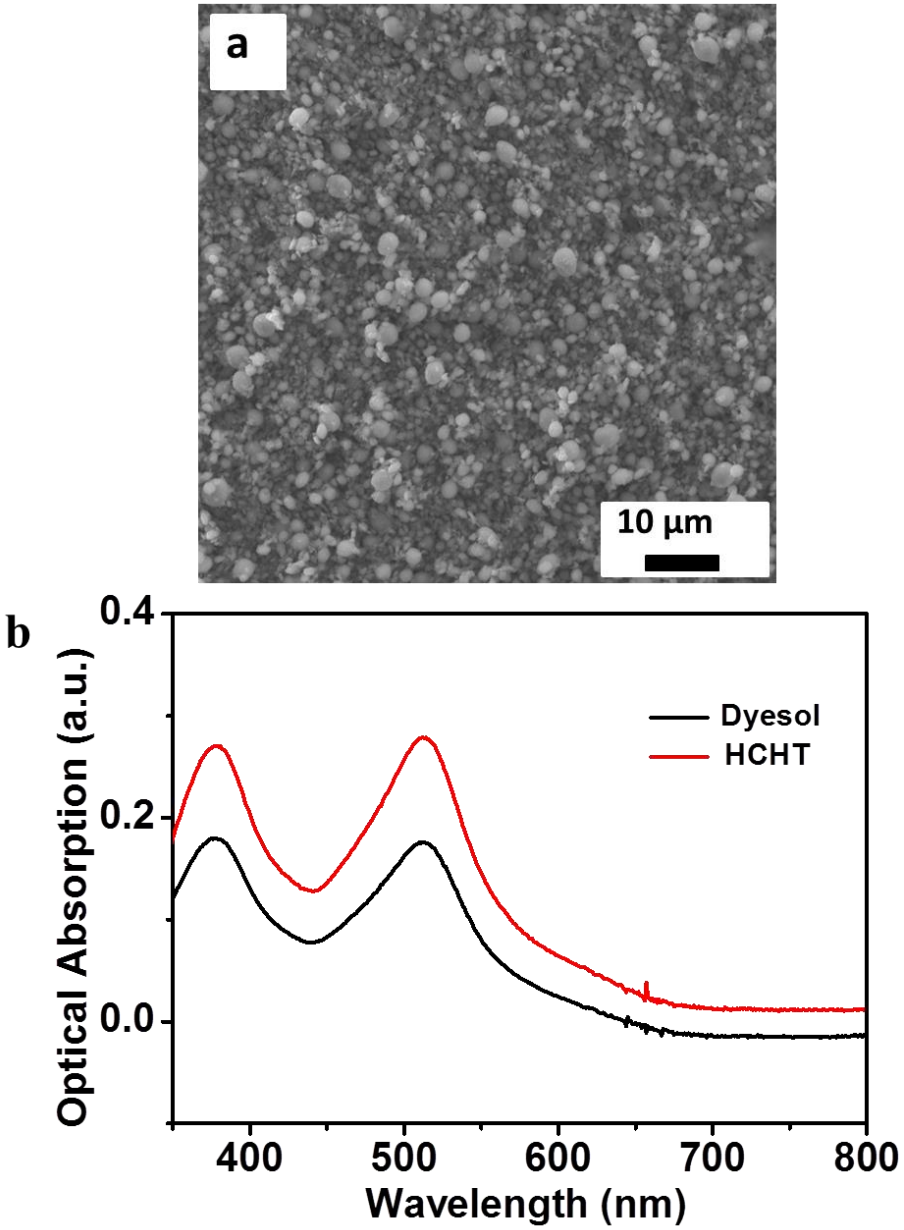

Figure 3.10 (a) Top-view SEM image of HCHT film on FTO glass. (b) Optical absorption of dye desorbed from the Dyesol and HCHT films by dissolving it in 0.1 M NaOH.

onset of the HCHT-based DSC has shifted to a higher potential, and a smaller dark current is produced at the same potential above 0.7 V. These observations indicate a lower recombination rate between transferred electrons and I_3^- ions for the HCHT.

To investigate the scattering efficiency of the Dyesol and HCHT films, the reflectivity of each film was studied. Figure 3.11(b) shows the diffuse reflectance spectra of the Dyesol film and the HCHT film. Both films show highly diffuse reflection capability across most of the visible spectrum. Diffuse reflectivity is observed to be lower for the Dyesol film for wavelengths from 600 nm to 800 nm, which is actually the region in which diffuse reflectivity is most critical, as the extinction co-efficient of the dye (N719) is comparatively low. The HCHT film scattered this light more effectively, which gave it a higher probability of being absorbed. Films produced from the HCHT show superior diffuse reflection capabilities for longer wavelengths (600–800 nm) due to the larger particle size, which is comparable to the wavelength of the incident light in question.

Figure 3.11(a) displays the wavelength distribution of the incident monochromatic photon to current conversion efficiency (IPCE) for both the Dyesol and the HCHT films. The IPCE is determined by the light absorption efficiency of the dye, the quantum yield of electron injection, and the efficiency with which electrons are collected at the conducting glass substrate, which is strongly affected by the morphology and surface area of the photoelectrode. Both films result in reasonably broad IPCE response, with the HCHT film giving a higher response across the whole spectrum. Closer analysis (Figure 3.12) reveals the enhancement in IPCE to be most marked at $\lambda > 650$ nm. In the short-wavelength spectral region (400-450 nm), the IPCE of the Dyesol film is about 8 % lower than that of the HCHT film. In this spectral region, iodide species (I_3^-) in the electrolyte absorb strongly, in conjunction with the lower dye loading absorbed, attenuating the amount of light reaching the sensitizing dye and thus limiting the photocurrent. At the maximum value of the IPCE

spectra at 535 nm, the IPCE of the HCHT film is approximately 6 % higher than that of the Dyesol film.

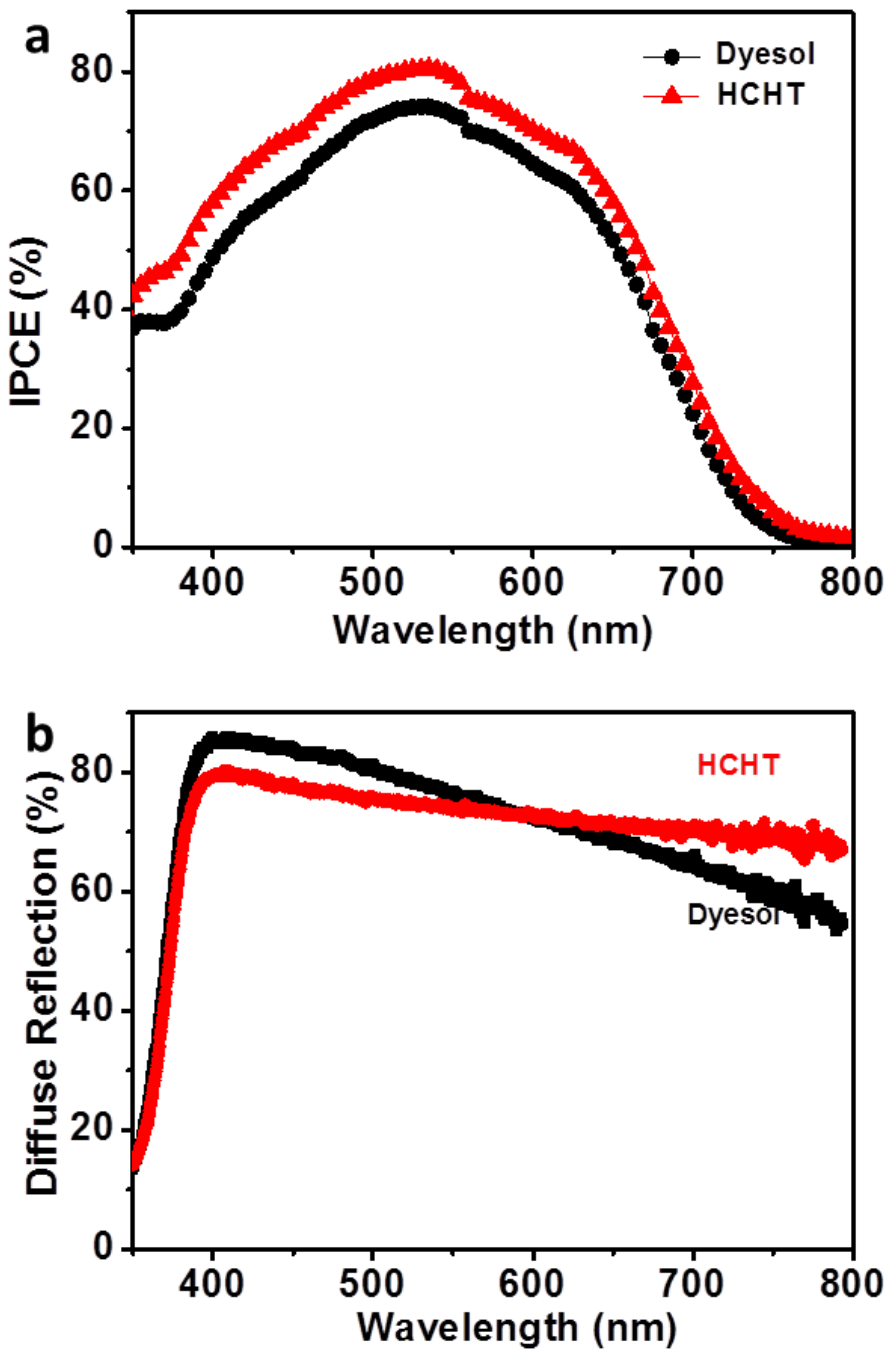

Figure 3.11 (a) Incident photon to current conversion efficiency (IPCE) curves of Dyesol-based (12 µm transparent layer + 4 µm scattering layer film) and HCHT-based (15 µm film) DSCs. (b) diffuse reflectance spectra of the Dyesol and HCHT films.

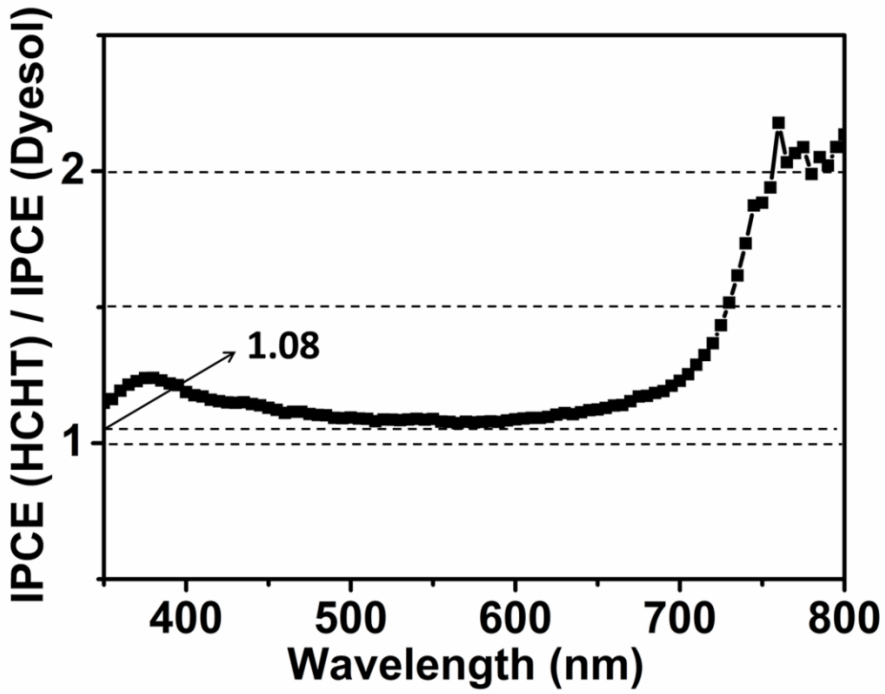

Figure 3.12 Ratio of IPCE value of HCHT to that of Dyesol, depending on the wavelength of the incident light.

In order to study the interfacial reactions of photoexcited electrons and better understand the kinetics of electrochemical and photoelectrochemical processes occurring in DSC operations, electrochemical impedance spectroscopy (EIS) was performed. [43-46] Figure 3.13(a) presents the Nyquist plots of the impedance spectra obtained under one sun illumination for DSCs assembled with the Dyesol and HCHT films under V_{oc}. The equivalent circuit is shown as the inset and the fitting data are given in Figure 3.14 and Table 3.1.

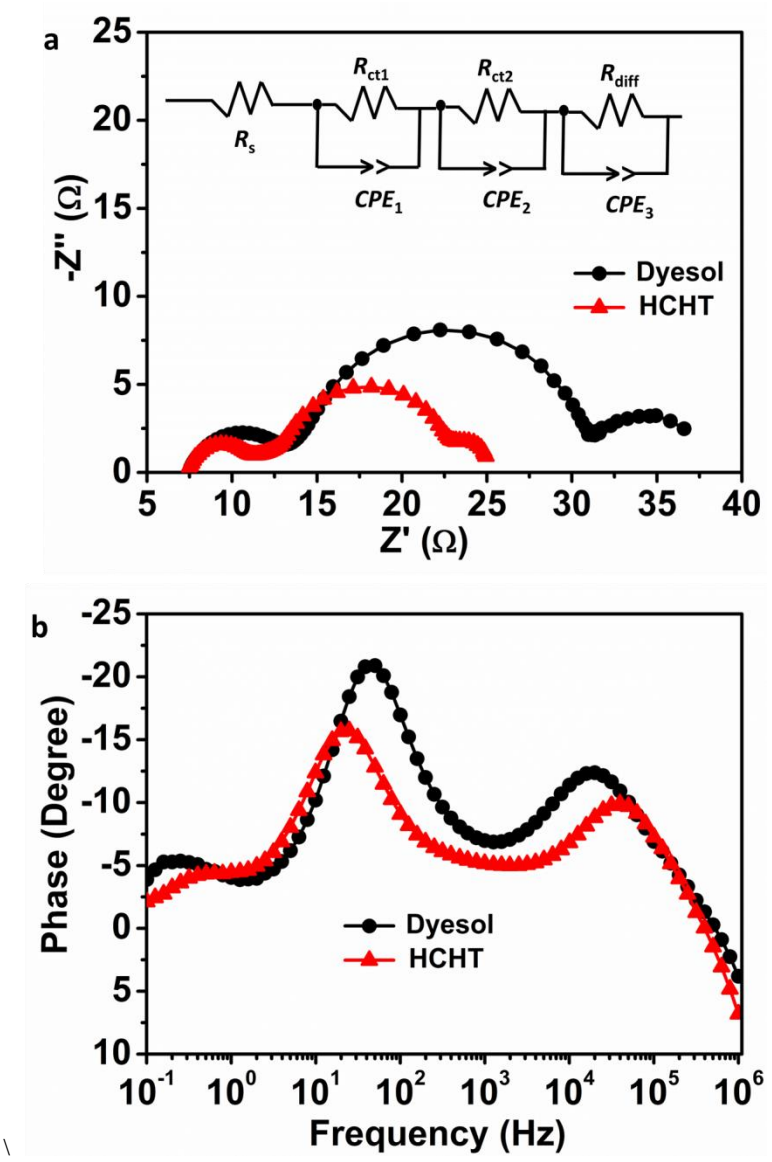

Figure 3.13 Impedance spectra of DSCs containing Dyesol and HCHT photoanodes measured at V_{oc} under illumination of 100 mW cm^{-2}: (a) Nyquist plots, with the inset showing the equivalent circuit, and (b) Bode phase plots.

In general, three semicircles extending from the total series resistance (R_s) can be recognized and fitted according to an equivalent circuit model, where the finite diffusion element is also represented by the shunt resistance and low frequency constant phase element (CPE). The semicircle in the high frequency region represents the impedance corresponding to charge transfer at the counter electrode (R_{ct1}), while those at intermediate frequency and low-frequency give information on the impedance

at the TiO_2/electrolyte interface (R_{ct2}), related to the charge transport/recombination, and the finite diffusion of the electrolyte (R_{diff}), respectively. [44, 46-48]

According to the approach of Adachi *et al.*, [49] several parameters related to the properties of electron transport in the semiconductor can be deduced from the Nyquist plot. In particular, the charge transfer (recombination) resistance (R_{ct2}) related to electron-hole recombination can be determined from the central arc diameter. In our case, it was found that the recombination resistance at the TiO_2/dye/electrolyte interface (R_{ct2}) for HCHT was smaller than for the devices made using the commercial paste, which indicates that electrons are easier to move at the HCHT surface and contribute to the charge transport at the photoanode. The Bode phase plots shown in Figure 3.13(b) likewise support the differences in the electron lifetime for the TiO_2 films derived from Dyesol and HCHT. Three main frequency peaks are observed. These peaks correspond to the charge transfer processes at different interfaces within the DSCs. Interestingly, the maximum frequency in the intermediate frequency regime, which is related to electron transfer in the HCHT-based film, is lower than that for the Dyesol-based film. According to the EIS model developed by Kern *et al.*, [50] the electron lifetime (τ_{eff}) of injected electrons in a TiO_2 film can be calculated from the low frequency results as:

$$\tau_{eff} = \frac{1}{2\pi f_{max}} \qquad (1)$$

where the characteristic f_{max} is the maximum frequency in the mid-frequency peak.

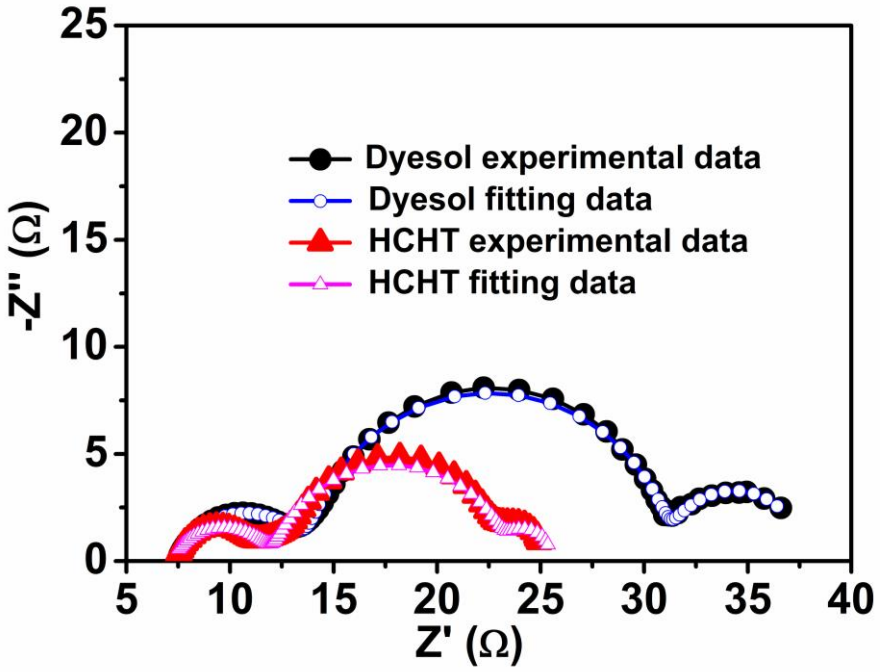

Figure 3.14 Impedance spectra of DSCs containing Dyesol and IHTT photoanodes measured at V_{oc} under illumination at 100 mW cm^{-2}: Nyquist plots, with the experimental data and the fitting data.

The middle-frequency peak of the Dyesol particle containing DSC is at a higher frequency (50.22 Hz) compared to the HCHT-based DSC (24.93 Hz), indicating a longer lifetime (6.4 ms) for the HCHT (3.2 ms for the Dyesol). Longer electron lifetimes are observed for HCHT-sensitized solar cells, indicating more effective suppression of the back-reaction of the injected electrons with the I_3^- ions in the electrolyte.

To summarize, based on the above characterizations, HCHT particles have several functions particularly well suited for application in DSCs. This is shown in Figure 3.15. The sheet-like building blocks result in a high active surface area, which, in turn, allows for improved dye loading. Concurrently the spheres formed by these sheets are effective light-scattering centres across a broad range of incident

wavelengths. Because of the bimodal pore size distributions, the large external pores can serve as “highways” for efficient electrolyte diffusion. Finally, the overlapping and interconnected 2D nansheets provide improved conduction pathways for electron transfer.

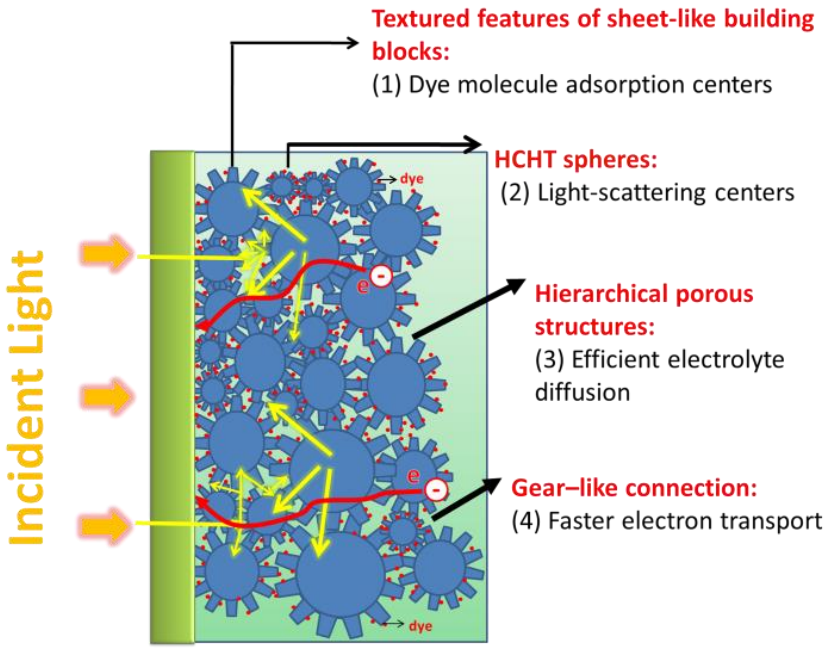

Figure 3.15 Schematic illustration of photoanode structure with four functions.

3.4 Conclusions

A new type of highly connected hierarchical textured TiO_2 spheres (HCHT) was successfully synthesized by a facile hydrothermal process. This new architecture demonstrates a method to overcome the seemingly contradictory requirements of a semiconductor scaffold for DSC application. The HCHT with well-defined mesopores simultaneously possess high specific surface area, a pronounced light-scattering effect (especially for $\lambda > 600$ nm), and fast electron transport. The DSCs made from HCHT

exhibit higher energy conversion efficiency of 9.0 %, compared to 8.2 % for the commercial Dyesol TiO_2 double layer photoanode.

3.5 References

1. M. Grätzel, *Nature*, 2001, **414**, 338-344.
2. B. Oregan and M. Grätzel, *Nature*, 1991, **353**, 737-740.
3. Z. B. Yang, T. Chen, R. X. He, G. Z. Guan, H. P. Li, L. B. Qiu and H. S. Peng, *Adv. Mater.*, 2011, **23**, 5436-5439.
4. A. Yella, H. W. Lee, H. N. Tsao, C. Y. Yi, A. K. Chandiran, M. K. Nazeeruddin, E. W. G. Diau, C. Y. Yeh, S. M. Zakeeruddin and M. Grätzel, *Science*, 2011, **334**, 629-634.
5. T. Chen, L. B. Qiu, H. G. Kia, Z. B. Yang, and H. S. Peng, *Adv.Mater.*, 2012, **24**, 4623-4628.
6. H. S. Kim, C. R. Lee, J. H. Im, K. B. Lee, T. Moehl, A. Marchioro, S. J. Moon, R. Humphry-Baker, J. H. Yum, J. E. Moser, M. Grätzel and N. G. Park, *Sci. Rep.*, 2012, **2**. 591.
7. J. Burschka, N. Pellet, S. J. Moon, R. Humphry-Baker, P. Gao, M. K. Nazeeruddin and M. Grätzel, *Nature*, 2013, **499**, 316-319.
8. S. W. Pan, Z. B. Yang, H. P. Li, L. B. Qiu, H. Sun and H. S. Peng, *J. Am. Chem. Soc.*,2013, **135**, 10622-10625.
9. Y. C. Park, Y. J. Chang, B. G. Kum, E. H. Kong, J. Y. Son, Y. S. Kwon, T. Park and H. M. Jang, *J. Mater. Chem.*, 2011, **21**, 9582-9586.
10. Y. J. Kim, M. H. Lee, H. J. Kim, G. Lim, Y. S. Choi, N.-G. Park, K. Kim and W. I. Lee, *Adv. Mater.*, 2009, **21**, 3668-3673.
11. K. Zhu, N. R. Neale, A. Miedaner and A. J. Frank, *Nano Lett.*, 2007, **7**, 69-74.

12. G. K. Mor, K. Shankar, M. Paulose, O. K. Varghese and C. A. Grimes, *Nano Lett.*, 2006, **6**, 215-218.

13. C. Y. Lin, Y. H. Lai, H. W. Chen, J. G. Chen, C. W. Kung, R. Vittal and K. C. Ho, *Energy Environ. Sci.*, 2011, **4**, 3448-3455.

14. Y. L. Wang, M. Guo, M. Zhang and X. D. Wang, *CrystEngComm*, 2010, **12**, 4024-4027.

15. M. Law, L. E. Greene, J. C. Johnson, R. Saykally and P. Yang, *Nat. Mater.*, 2005, **4**, 455-459.

16. S. Ito, T. N. Murakami, P. Comte, P. Liska, C. Grätzel, M. K. Nazeeruddin and M. Grätzel, *Thin Solid Films*, 2008, **516**, 4613-4619.

17. X. H. Miao, K. Pan, Y. P. Liao, W. Zhou, Q. J. Pan, G. H. Tian and G. F. Wang, *J. Mater. Chem. A*, 2013, **1**, 9853-9861.

18. X. H. Sun, Y. M. Liu, Q. D. Tai, B. L. Chen, T. Peng, N. Huang, S. Xu, T. Y. Peng and X. Z. Zhao, *J. Phys. Chem. C*, 2012, **116**, 11859-11866.

19. Z. P. Zhang, S. Ito, B. O'Regan, D. B. Kuang, S. M. Zakeeruddin, P. Liska, R. Charvet, P. Comte, M. K. Nazeeruddin, P. Pechy, R. Humphry-Baker, T. Koyanagi, T. Mizuno and M. Grätzel, *Z. Phys. Chemie-Int. J. Res. Phys. Chem. Chem. Phys.*, 2007, **221**, 319-327.

20. L. Zhao, J. Li, Y. Shi, S. M. Wang, J. H. Hu, B. H. Dong, H. B. Lu and P. Wang, *J. Alloy. Compd.*, 2013, **575**, 168-173.

21. X. Wu, G. Q. Lu and L. Z. Wang, *Energy Environ. Sci.*, 2011, **4**, 3565-3572.

22. Z. S. Wang, H. Kawauchi, T. Kashima and H. Arakawa, *Coord. Chem. Rev.*, 2004, **248**, 1381-1389.

23. C. J. Barbe, F. Arendse, P. Comte, M. Jirousek, F. Lenzmann, V. Shklover and M. Grätzel, *J. Am. Ceram. Soc.*, 1997, **80**, 3157-3171.

24. L. Yang, Y. Lin, J. G. Jia, X. R. Xiao, X. P. Li and X. W. Zhou, *J. Power Sources*, 2008, **182**, 370-376.

25. V. Suryanarayanan, K. M. Lee, J. G. Chen and K. C. Ho, *J. Electroanal. Chem.*, 2009, **633**, 146-152.

26. Y. Liao, B. X. Lei, D. B. Kuang and C. Y. Su, *Energy Environ. Sci.*, 2011, **4**, 4079-4085.

27. J. Y. Liao, J. W. He, H. Y. Xu, D. B. Kuang and C. Y. Su, *J. Mater. Chem.*, 2012, **22**, 7910-7918.

28. Z. H. Zhang, X. H. Zhong, S. H. Liu, D. F. Li and M. Y. Han, *Angew. Chem., Int. Ed.*, 2005, **44**, 3466-3470.

29. D. Jiang, Y. Xu, B. Hou, D. Wu and Y. H. Sun, *Eur. J. Inorg. Chem.*, 2008, **8**, 1236-1240.

30. L. Li and C.-y. Liu, *CrystEngComm*, 2010, **12**, 2073-2078.

31. S. Doeuff, M. Henry, C. Sanchez and J. Livage, *J. Non-Cryst. Solids.*, 1987, **89**, 206-216.

32. J. C. S. Wu, I. H. Teseng and W. C. Chang, *J. Nanopart. Res.*, 2001, **3**, 113-118.

33. Z. Zhang, X. Zhong, S. Liu, D. Li and M. Han, *Angew. Chem., Int. Ed.*, 2005, **44**, 3466-3470.

34. U. Hwang, H. Park and K. Koo, *Ind. Eng. Chem. Res.*, 2004, **43**, 728-734.

35. M. Kruk and M. Jaroniec, *Chem. Mat.*, 2001, **13**, 3169-3183.

36. W. Yang, J. Li, Y. Wang, F. Zhu, W. Shi, F. Wan and D. Xu, *Chem. Commun.*, 2011, **47**, 1809-1811.

37. J. Jiang, F. Gu, W. Shao and C. Z. Li, *Ind. Eng. Chem. Res.*, 2012, **51**, 2838-2845.

38. J. van de Lagemaat, K. D. Benkstein and A. J. Frank, *J. Phys. Chem. B*, 2001, **105**, 12433-12436.

39. K. D. Benkstein, N. Kopidakis, J. van de Lagemaat, A. J. Frank, *J. Phys. Chem. B*, 2003, **107**, 7759-7767.

40. E. Palomares, R. Vilar and J. R. Durrant, *Chem. Commun.*, 2004, **10**, 362-363.

41. G. Schlichthorl, S. Y. Huang, J. Sprague and A. J. Frank, *J. Phys. Chem. B*, 1997, **101**, 8141-8155.

42. S. Ito, P. Liska, P. Comte, R. L. Charvet, P. Pechy, U. Bach, L. Schmidt-Mende, S. M. Zakeeruddin, A. Kay, M. K. Nazeeruddin and M. Grätzel, *Chem. Commun.*, 2005, **34**, 4351-4353.

43. Q. Wang, J. E. Moser and M. Gratzel, *J. Phys. Chem. B*, 2005, **109**, 1 4945-14953.

44. C. Longo, A. Nogueira, M.-A. De Paoli and H. Cachet, *J. Phys. Chem. B*, 2002, **106**, 5925-5930.

45. Q. Wang, S. Ito and M. Grätzel, *J. Phys. Chem. B*, 2006, **110**, 25210-25221.

46. T. Hoshikawa, M. Yamada, R. Kikuchi and K. Eguchi, *J. Electrochem. Soc.*, 2005, **152**, E68-E73.

47. Y. Yoshida, S. Tokashiki, K. Kubota, R. Shiratuchi, Y. Yamaguchi, M. Kono and S. Hayase, *Sol. Energy Mater. Sol. Cells*, 2008, **92**, 646-650.

48. L. Han, N. Koide, Y. Chiba and T. Mitate, *Appl. Phys. Lett.*, 2004, **84**, 2433-2435.

49. M. Adachi, M. Sakamoto, J. Jiu, Y. Ogata and S. Isoda, *J. Phys. Chem. B*, 2006, **110**, 13872-13880.

50. R. Kern, R. Sastrawan, J. Ferber, R. Stangl, and J. Luther, *Electrochim.Acta*, 2002, **47**, 4213-4242.

4 A BI-LAYER TiO_2 PHOTOANODE FOR HIGHLY DURABLE, FLEXIBLE DYE-SENSITIZED SOLAR CELLS

In this chapter, a new type of photoanode was rationally designed for flexible DSCs.

Low-temperature processing of DSCs is crucial to enable their commercialization with low-cost plastic substrates. Much of the previous work in this area has focused on mechanical compression of premade particles on plastic substrates; however, many reported that this technique did not yield sufficient interconnections for high charge carrier transport. Cold isostatic pressing (CIP) was first reported as a means to prepare TiO_2 films on flexible substrates by Cheng *et al.*, however, CIP has, to date, been limited with regards to the choice of particles that can be used.

In this chapter, bi-layer photoanodes that incorporate microstructured TiO_2 sea-urchin-like assemblies, composed of high-aspect-ratio single crystalline nanoribbons, i.e., two-dimensional subunits, which were deposited onto a nanoparticle layer (commercial P25) was presented, with a 5.6 % conversion efficiency realized. It was demonstrated that this hierarchical TiO_2 nanostructure is beneficial due to its enhanced dye loading as well as enhanced light scattering. Importantly, it also revealed the benefits of a bi-layer structure where the nanoribbons penetrate into the nanoparticle layer (P25) after CIP, resulting in improved adhesion between the TiO_2 anode film and the P25 under layer on the indium tin oxide-coated polyethylene naphthalate (ITO|PEN) substrate, leading to improved mechanical stability and durability, efficient electron transfer pathways, and ultimately, higher solar-to-electric conversion efficiencies.

This chapter has been published in *J. Mater. Chem. A*, 2015, **3**, 4679.

4.1 Introduction

The tailoring of nanomaterials is paving the way toward meeting some of society's major challenges, particularly in the domain of photoelectrochemistry, with the development of water photocatalysis and dye-sensitized solar cells (DSCs), which are based on mesostructured metal oxide semiconductor and have gained attention due to their low environmental impact, their projected low capital cost (hence short energy pay-back time), and low sensitivity to temperature changes or solar incident angle, along with the fact that they can be produced in a flexible form. [1-6] The prototypical DSC is a sandwich composed of a titanium dioxide (TiO_2) photoanode, sensitized with a monolayer of organometallic dye molecules, and a platinum-coated counter electrode, with a redox electrolyte in between. High-surface-area, porous, and electronically well connected TiO_2 films serve both as a means of transport for photogenerated free charges to the external electrical contact and as a host for sensitizer molecules.

In reports of high conversion efficiency (η) DSCs, TiO_2 is generally synthesized by a hydrothermal route or sol-gel method, and made into a paste with polymeric binders, which are either screen-printed or doctor-bladed onto the conducting glass (fluorine-doped tin oxide, FTO). [7-9] This is followed by a high temperature sintering process (typically ~ 500 °C). The high temperature step is carried out to (1) remove the binders, (2) ensure better electronic connections, and (3) improve mechanical contact between particles.

Transport of injected electrons through the oxide network to the back contact is understood to occur by trap-limited diffusion, with trapping and detrapping occurring both within particles and at grain boundaries. Recombination of carriers with the

oxidized species in the electrolyte at the interface can compete with this slow electron transport process, especially if the interparticle connections are weak. The limitations imposed on the electron transport by the mesoporous structure hinders progress in achieving higher η.

Flexible DSCs with plastic substrates have attracted much attention for a number of reasons including: (1) greater amenability to the large-scale roll-to-roll process than their glass-based counterparts; (2) being light weight; (3) able to be integrated into other objects (e.g. clothing). [10-17] Fabrication of flexible devices on plastic substrates, however, necessitates low-temperature processing. Previously, low-temperature DSCs have been made by mechanically compressing the TiO_2 particles; by spraying coating binder-free colloidal TiO_2 on the conducting substrate; or by cold isostatic pressing (CIP). [18-23] One of the key objectives with these processing methods is the creation of electronic contact between particles to ensure better charge carrier transport. After deposition, the interfaces between particles typically have poor electrical connectivity, to the detriment of electron transport through the nanoparticle film. Thus, many prior approaches to low-temperature DSC photoanode preparation have resulted in low η due to the poor particle interconnections. Early studies that focused on mechanical compression of premade particles on plastic or glass substrates did not yield sufficient interconnections for good charge carrier transport.

CIP is a powder compaction technology, which is used in materials processing engineering. [24] In this process, the equal pressure is applied in all directions, resulting in better uniformity and high compaction, regardless of the electrode shape. This method was first applied as a means to prepare TiO_2 films on flexible substrates by Cheng *et al.* in 2012, however, CIP has, to date, been limited with regards to the choice of particles. [23] Either small particles (e.g., P25, 20-30 nm) or mesoporous

beads (< 1 μm) comprised of ~ 10 nm features have been used. [22, 23, 25, 26] CIP has faced problems when processing larger particles, such as microspheres, which may be desirable due to their light-scattering capabilities. [9] As such, the optimization of the photoanode structure for flexible DSCs when using CIP has remained a challenge.

In this work, we demonstrate a bi-layer photoanode architecture, with good light scattering properties and improved electronic interconnections, for efficient charge percolation. Microstructured TiO_2 sea-urchin-like spherical assemblies, composed of high-aspect-ratio single-crystal nanoribbons (MHAT) were deposited onto a layer of nanoparticles (commercially available P25). Using this bi-layer electrode (sensitized by N719 dye and using I_3^-/I^- electrolyte), a 5.6 % conversion efficiency was obtained. This is a considerable improvement compared to P25 (4.3 %) by itself or the single spheres (5.1 %). These differences are attributed in part to enhanced dye loading and efficient light management in the hierarchical architecture. In addition, the interpenetration of the nanoribbons into the P25 under layer results in more intimate interparticle connections after a CIP step, which provides enhanced adhesion between the film and the indium-tin-oxide-coated polyethylene naphthalate (ITO|PEN) substrate, enhanced mechanical stability and durability, and efficient electron transfer pathways.

4.2 Experimental

4.2.1 Synthesis of Mesoporous Hierarchical Anatase TiO_2 (MHAT)

Acetic acid (AA, ACS reagent, ≥ 99.7 %, Sigma-Aldrich) and titanium butoxide (TB, Ti $(OCH_2CH_2CH_2CH_3)_4$, 97 %, analytical reagent, Sigma-Aldrich) were used without further purification. MHAT was prepared via a very simple acid thermal process. [9] Briefly, 1.0 mL TB, was added at room temperature to 30 mL AA solution under stirring (with stirring maintained for 24 h). This solution was then transferred to a Teflon lined reactor (Parr Instrument Company, 45 mL) and heated to 150 °C for 12 h. Afterwards, the sample was cooled before being centrifuged and sequentially washed with distilled water and ethanol (3 cycles). Following this, the samples were dried at 90 °C overnight and calcined at 500 °C for 3 h.

4.2.2 Materials Characterizations

XRD was employed to examine the crystal structures of the resultant products using an X-ray diffractometer (Bruker Advance, 40 kV, 30 mA) (Cu Kα, λ = 0.15406 nm) from 20º to 80º (2θ) (1 º/min), while the morphology was examined by FE-SEM (Megallan 200) and TEM (JEM-2100F). The surface area and porosity were examined using Brunauner-Emmett-Teller (BET) analysis of nitrogen adsorption-desorption data collected on a Tristar 3030 system (Micrometrics Instrument Corporation), after degassing overnight at 150 °C.

4.2.3 Film Fabrication and Characterizations

Titania suspensions of ~ 25 wt % were prepared by dispersing 3 g TiO_2 powders [P25 (Degussa, Hanau, Germany) and MHAT, respectively] in 99.7 % ethanol followed by ball milling. [27] Briefly, P25 (or MHAT) powders were mixed with

ethanol to make a slurry with a TiO_2 content of about 30 wt% in an agate balling milling jar, with different size of agate balls. The mixture was then milled at 250 rmp speed for 2 h. Then TiO_2 films with different thicknesses were coated by the doctor-blade technique on the ITO|PEN substrates, purchased from Peccell Technologies (Kanagawa, Japan) and allowed to dry in air. These TiO_2-coated electrodes were then transferred to a polyethylene envelope (thickness ~ 80 μm) and sealed under a vacuum of 10^{-1} Torr. Vacuum-sealed electrodes were then pressed at room temperature using a cold isostatic pressing (CIP) instrument (ABB Autoclave Systems, Columbus, OH, USA) at different pressures varying between 50 and 200 MPa. [28] The surface morphology of films was examined by FE-SEM (Megallan 200) under ambient conditions.

4.2.4 Fabrication of DSCs

The resultant TiO_2 films were immersed in a 0.3 mM N719 (Solaronix, *cis*-bis(isothiocyanato)bis(2,2′-bipyridyl-4,4′-dicarboxylate) ruthenium(II) bis-tetra-*n*-butylammonium) dye solution in a 1:1 (v/v) mixture of acetonitrile (HPLC, Lab-scan) and *tert*-butanol (LR, Ajax Chemicals) for about 24 h. After dyeing, the samples were taken out of the dye bath, washed with acetonitrile, and dried under N_2 flow, then sandwiched with a Pt-sputtered ITO|PEN counter electrode. After that, cells were sealed together at 110 °C by using a 25 μm Surlyn (Dupont) spacer. An I^-/I_3^- organic solvent-based electrolyte solution [85:15 vol % acetonitrile/valeronitrile, 0.03 M iodine (I_2), 0.5 M 4 tertbutylpyridine (4-tBP), 0.6 M 1-butyl-3-methylimidazolium iodide (BMII), and 0.1 M guanidinium thiocyanate (GuSCN)] was introduced via vacuum back-filling. The electrolyte filling holes were blocked with an UV curable silicone glue (3M).

4.2.5 Solar Cell Characterizations

Dye desorption experiments were performed by washing the photoanodes in 0.1 M NaOH solution (1:1 vol ratio water : ethanol). Absorption/diffuse reflectance spectrometry of ultraviolet (UV)-visible light was used for investigating the light absorption and scattering properties (Shimadzu UV-3600). A Veeco Dektak 150 Surface Profiler was used for the film thickness measurements. *J-V* curves of the DSCs were obtained by using a Keithley 2400 Source Meter under illumination of simulated sunlight (100 mW cm^{-2}) provided by an Oriel solar simulator with an air mass (AM) 1.5 filter. Black metal with a circular aperture (4.5 mm in diameter) was put on top of the device during mm photovoltaic testing. IPCE spectra were recorded on a Keithley 2400 Source Meter under the irradiation of a 300 W xenon lamp with an Oriel Cornerstone™ 260 1/4 m monochromator. Electrochemical impedance spectroscopy (EIS) was performed using a 10 mV applied perturbation in the 100 mHz to 500 kHz frequency range at open-circuit under illumination. The impedance spectra were fitted using a transmission line equivalent circuit model, as reported in previous studies. [29, 30] Intensity modulated photocurrent spectroscopy (IMPS) was performed using a < 5% perturbation of the steady state illumination. EIS and IMPS data were analyzed using Zview equivalent circuit modeling software (Scribner).

4.3 Results and Discussion

MHAT particles, obtained by a facile hydrothermal process are shown in Figure 4.1(a) [low magnification bright-field transmission electron microscope (TEM) image] and Figure 4.2(a) [scanning electron microscope (SEM) image].

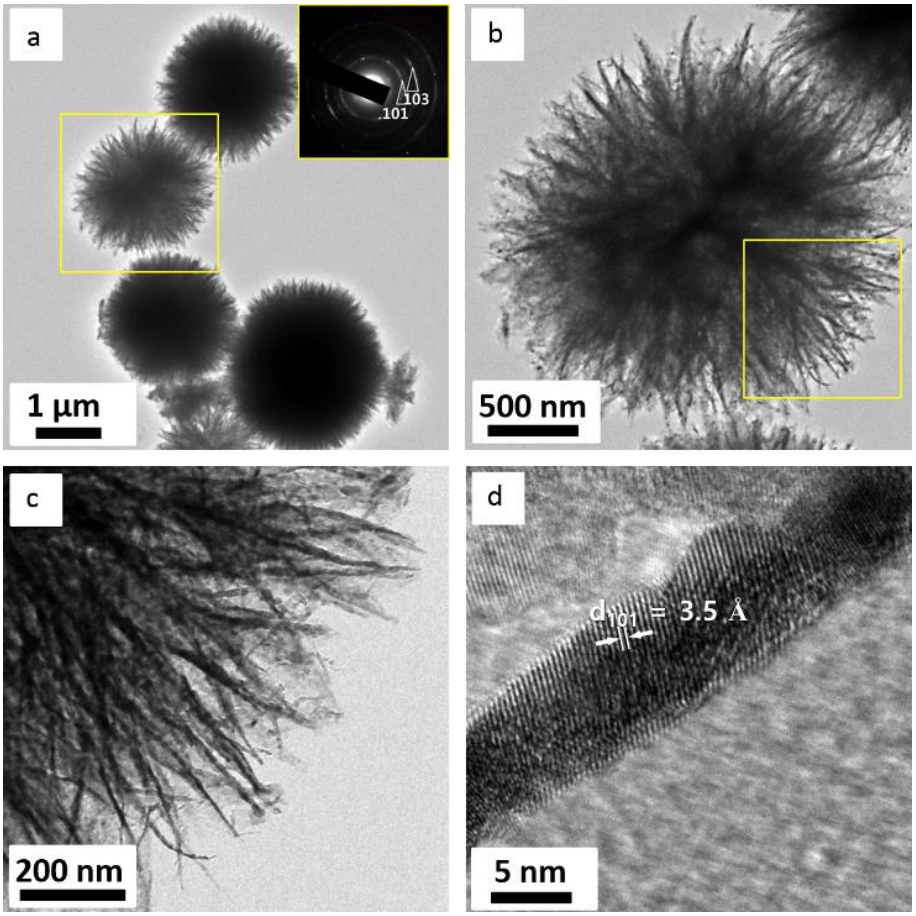

Figure 4.1 Characterization of mesoporous hierarchical anatase TiO_2 (MHAT): a) low magnification bright-field TEM image, with the inset showing the corresponding SAED pattern; b) TEM image of a selected sphere; c) enlarged TEM image of the marked area in (b), revealing the nanoribbon building units; d) HRTEM image of one single nanoribbon showing the fringe spacing of anatase TiO_2.

As compared to our previous reports of similar particles, from which this method was adapted, the concentration of titanium butoxide was increased [from 2 vol% to 4 vol%, (25 mL total)] as well as the stirring time (from 1 h to 24 h). [9] As a result more uniform particle sizing was achieved. Additionally the spheres here are comprised of ribbons rather than open sheets. These can be observed in the TEM images of Figure 4.1(b) and (c). The specific surface area (115 m^2 g^{-1}) [Figure 4.2(b)] is higher than for either reported highly connected hierarchical textured TiO_2 spheres (103 m^2 g^{-1}) or P25 (42 m^2 g^{-1}). [9, 31]

In addition, MHAT would be expected to show a higher dye-loading capacity, because of its significantly higher porosity (65.6 %) and higher roughness factor (156 μm^{-1}), compared to those of P25 (corresponding values of 34.9 % and 118 μm^{-1}, respectively).

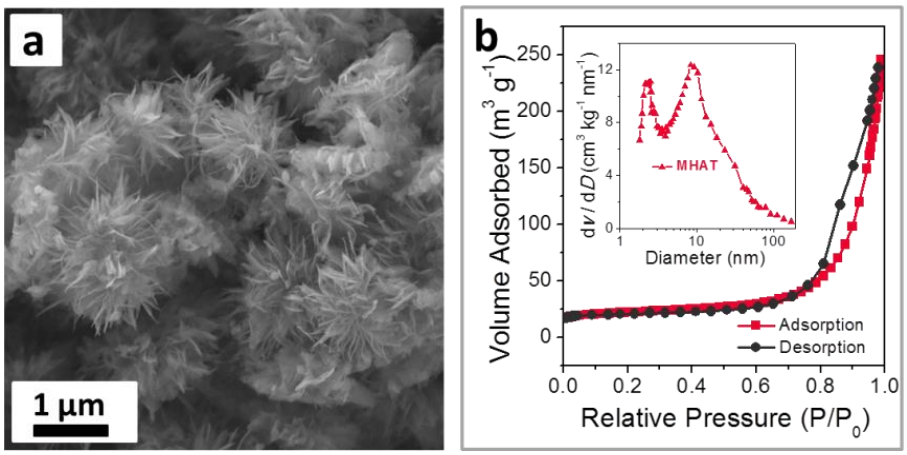

Figure 4.2 (a) Low magnification FE-SEM image of mesoporous hierarchical anatase TiO_2 (MHAT); (b) N_2 adsorption-desorption isotherm, with the inset image showing the pore size distribution calculated from the adsorption branch of a nitrogen isotherm by the Barrett-Joyner-Halenda (BJH) method.

The high resolution TEM (HRTEM) image in Figure 4.1(d) further confirms that the MHAT is composed of single crystalline nanoribbons, with a fringe spacing of 3.5 Å, which corresponds to the (101) plane of anatase TiO_2. The selected area electron diffraction (SAED) rings [inset of Figure 4.1(a)] show that the TiO_2 spheres are anatase crystals, consistent with the X-ray diffraction (XRD) data [Figure 4.3(a)] and the Raman spectrum [Figure 4.3(b)].

P25 and MHAT films [schematically shown in Figure 4.4(a)] with different thicknesses (6 µm and 12 µm, after CIP) were dyed with N719 and employed as electrodes in unsealed DSC devices, utilizing a I_3^-/I^- based electrolyte, with a Pt sputter-coated ITO|PEN counter electrode.

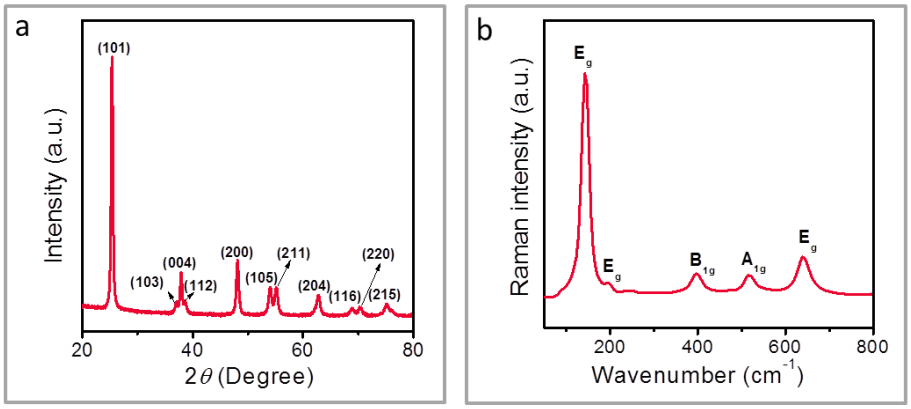

Figure 4.3 a) XRD pattern of the MHAT, indicating that the spheres are anatase TiO_2 phase (JCPDS No. 21-1272, *a* = 3.785 Å, *b* = 3.785 Å, *c* = 9.514 Å); b) Raman spectrum of the MHAT, confirming the anatase phase from the characteristic Raman modes at 142.1 cm^{-1} (E_g), 194.5 cm^{-1} (E_g), 396.1 cm^{-1} (B_{1g}), 515.8 cm^{-1} (A_{1g}), and 638.4 cm^{-1} (E_g), which can be assigned to the Raman active modes ($A_{1g}+B_{1g}+3E_g$) of anatase.

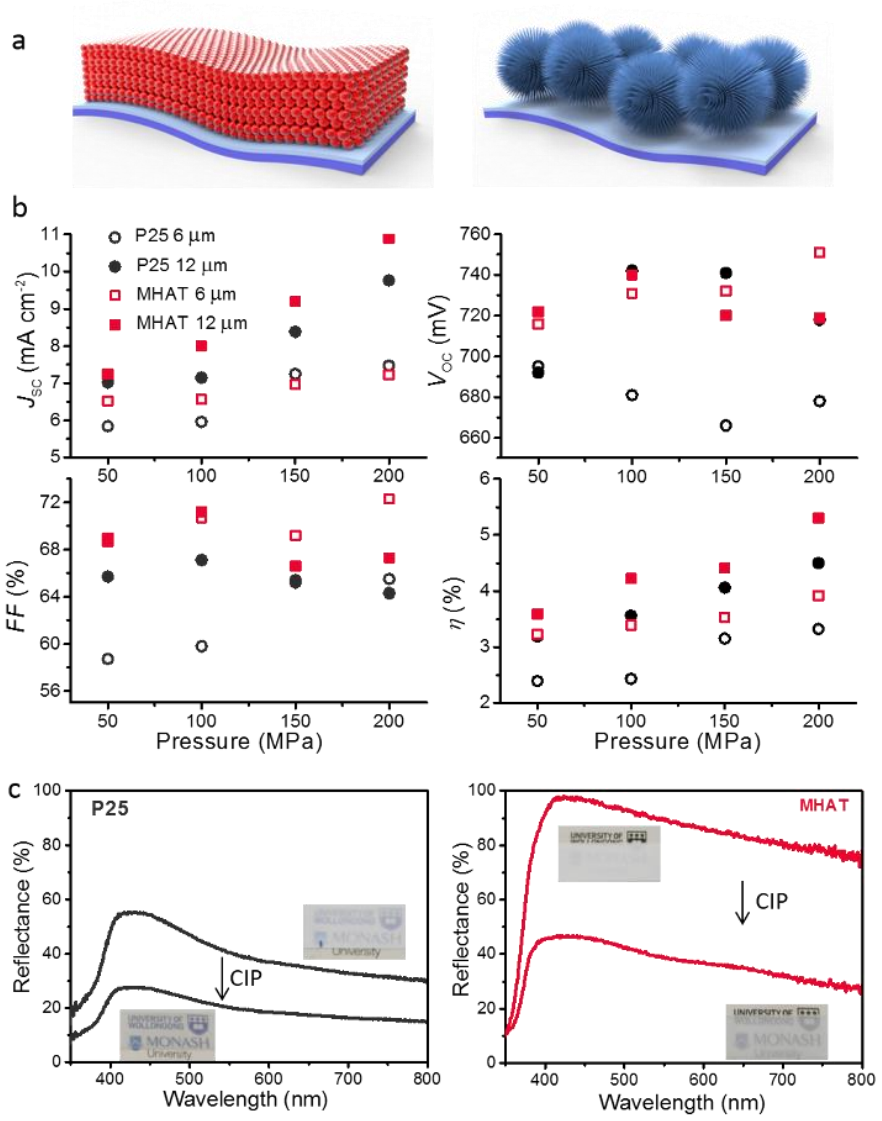

Figure 4.4 a) Schematic illustration of P25 and MHAT photoanode structures for flexible DSCs on ITO|PEN substrate; b) relationship between the pressure applied during a cold isostatic pressing (CIP) and the photovoltaic parameters: short-circuit photocurrent density (J_{sc}), open-circuit photovoltage (V_{oc}), fill factor (*FF*), and total power conversion efficiency (η); c) diffuse reflectance spectra of TiO_2 films before and after CIP: P25 (left) and MHAT (right), with corresponding digital photograph of P25 (12 µm) and MHAT (12 µm) films before and after CIP as insets.

Table 4.1 Photovoltaic characteristics of the DSCs made from P25 and MHAT films with different thicknesses pressed under different applied pressure.

Samples	Pressure (MPa)	Thickness (μm)	J_{sc} (mA cm^{-2})	V_{oc} (mV)	*FF* (%)	η (%)
P25	50	6	5.84	695	58.7	2.39
P25	100	6	5.96	681	59.8	2.43
P25	150	6	7.25	666	65.2	3.15
P25	200	6	7.47	678	65.5	3.32
P25	50	12	7.02	692	65.7	3.19
P25	100	12	7.15	742	67.1	3.56
P25	150	12	8.38	741	65.4	4.06
P25	200	12	9.76	718	64.3	4.50
MHAT	50	6	6.52	716	69.0	3.22
MHAT	100	6	6.56	731	70.7	3.39
MHAT	150	6	6.97	732	69.2	3.53
MHAT	200	6	7.23	751	72.3	3.92
MHAT	50	12	7.24	722	68.7	3.59
MHAT	100	12	8.00	740	71.2	4.22
MHAT	150	12	9.20	720	66.6	4.41
MHAT	200	12	10.90	719	67.3	5.30

Figure 4.4(b) and Table 4.1 report the photovoltaic characteristics of the unsealed DSCs mentioned above (with *J-V* measurements completed directly after assembly). In all cases, the efficiency increased with thickness and applied pressure, predominantly as a result of an increase in the short-circuit photocurrent density (J_{sc}). For 6 µm films, the open-circuit photovoltage (V_{oc}) and fill factor (*FF*) of the MHAT-based DSCs were higher than those of the P25-based DSCs. With the highest compression force, the MHAT film (12 µm thick) showed an overall conversion efficiency of 5.1 %, an 18.0 % improvement compared to the corresponding film employing P25 (4.50 %).

Good adhesion between the TiO_2 nano-particles in the porous film, and the film with the conducting substrate is essential for achieving desirable levels of electrical conductivity and thus high efficiency of the DSC. The connection between the MHAT and the ITO|PEN substrate, however, was poor, as the large spheres have limited contact with the substrate even after the CIP, further confirmed by mechanical bendability properties test (Figure 4.5). Films were bent at radius of 50 mm by a

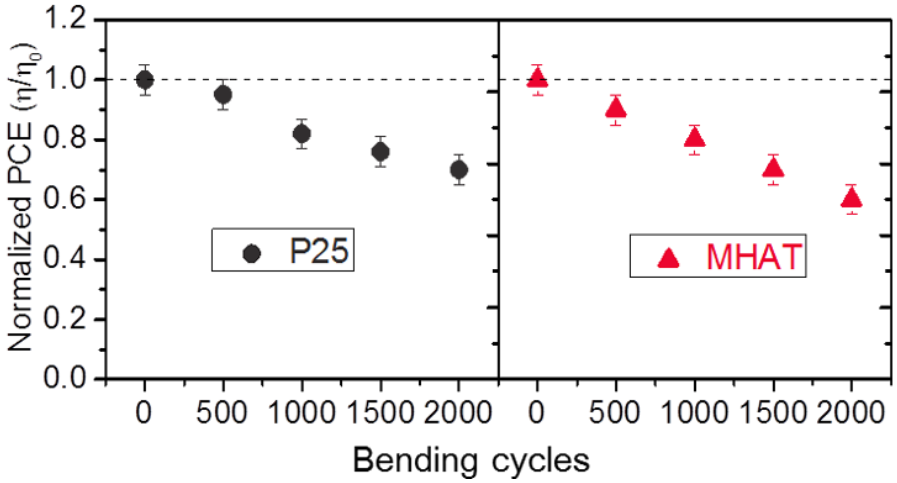

Figure 4.5 Normalized PCE of P25- and MHAT-based flexible DSCs as a function of bending cycles, with radius of 50 mm.

bending machine (further discussed in details below). From Figure 4.5 we can see that, the efficiency of MHAT-based devices decreased to 60 % after 2000 cycles compared with 70 % for P25-based devices, demonstrating the poor connection between MHAT and the ITO|PEN substrate.

To solve this problem, the MHAT material was deposited on top of a layer of P25 particles [schematically shown in Figure 4.6(a) and in the bright-field scanning transmission electron microscope (BF-STEM) images in Figure 4.6(b, c)]. During the CIP process, the two-dimensional (2D) nanoribbon building blocks of the MHAT

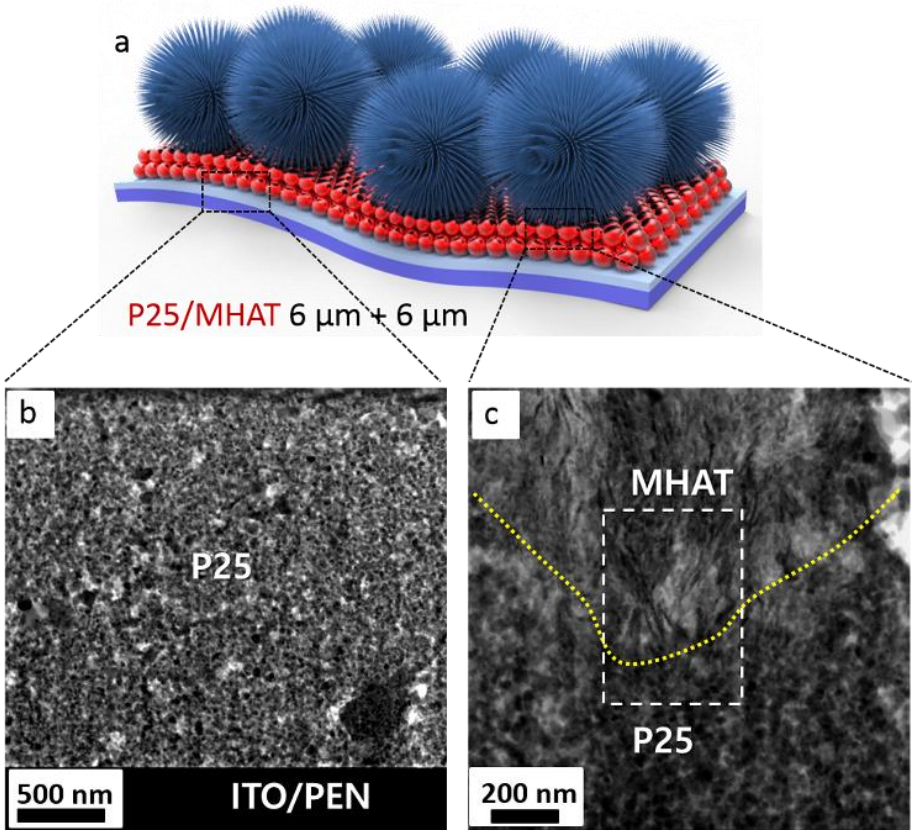

Figure 4.6 a) Schematic illustration of P25/MHAT (6 µm + 6 µm) photoanode structure for flexible DSCs on ITO|PEN substrate; cross-sectional BF-STEM images of P25/MHAT (6 µm + 6 µm) photoanode structure: b) shows the interface between the P25 and the ITO|PEN substrate, c) shows the interface between the P25 and the MHAT, with the highlighted part showing the MHAT nanoribbon units penetrating into the P25 nanoparticle layer.

penetrate into the P25 particle layer, improving adhesion between them [Figure 4.6(c)]. P25 is then able to form a good contact with the ITO|PEN substrate [Figure 4.6(b)]. It is well known that device performance is critically dependent on good contact between the mesoporous TiO_2 particles, as well as good adhesion between the TiO_2 particles and the substrate (ITO|PEN). In addition, as shown in the HRTEM image [Figure 4.1(d)], the individual nanoribbons are single-crystal in nature, which is beneficial for faster electron transportation.

Figure 4.7 (FE-SEM images) illustrates the surface morphology of TiO_2 films before and after pressing at 200 MPa. Uncompressed P25 film displays noticeable cracking [Figure 4.7(a) and Figure 4.8(a)]. These microcracks are formed due to shrinkage during the air-drying process in the absence of binders in the TiO_2 slurry. In addition, the films are easily scatched away from the substrate compared to the films post CIP, suggesting that the poor connection between the particles and the substrate leads to the lower J_{sc} of non-pressed P25 films. In contrast, the films post CIP had a uniform, mesoporous, and crack-free structure [Figure 4.7(b), Figure 4.8(b)].

In the MHAT and P25/MHAT films prior to CIP, the MHAT spheres are packed inefficiently with limited contact between adjacent spheres [Figure 4.7(c, e)]. Post application of CIP, up to 200 MPa, the MHAT spheres are much more densly packed, and it is evident that this increased packing efficiency results in greater connections between the spheres [Figure 4.7(d, f) and Figure 4.8]. It is worth noting here that the MHAT spheres were not crushed by the pressing. Initially there was concern that the particles may be destroyed during CIP and that this was responsible for decreased light scattering, however, images in both Figure 4.6(c) and Figure 4.7(d, f) reveal that the spheres remain intact.

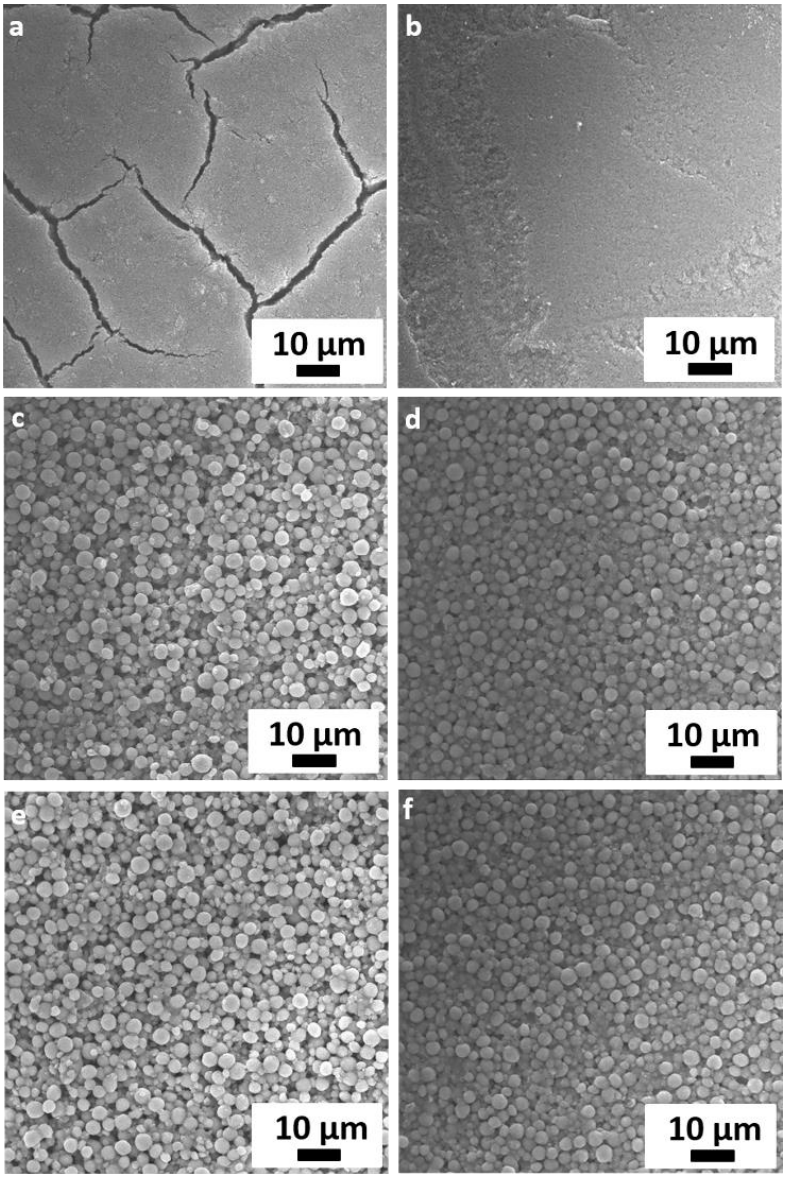

Figure 4.7 Low magnification FE-SEM images of different TiO_2 films on ITO|PEN substrates: P25 film a) before and b) after CIP; MHAT film c) before and d) after CIP; P25/MHAT film (e) before and (f) after CIP.

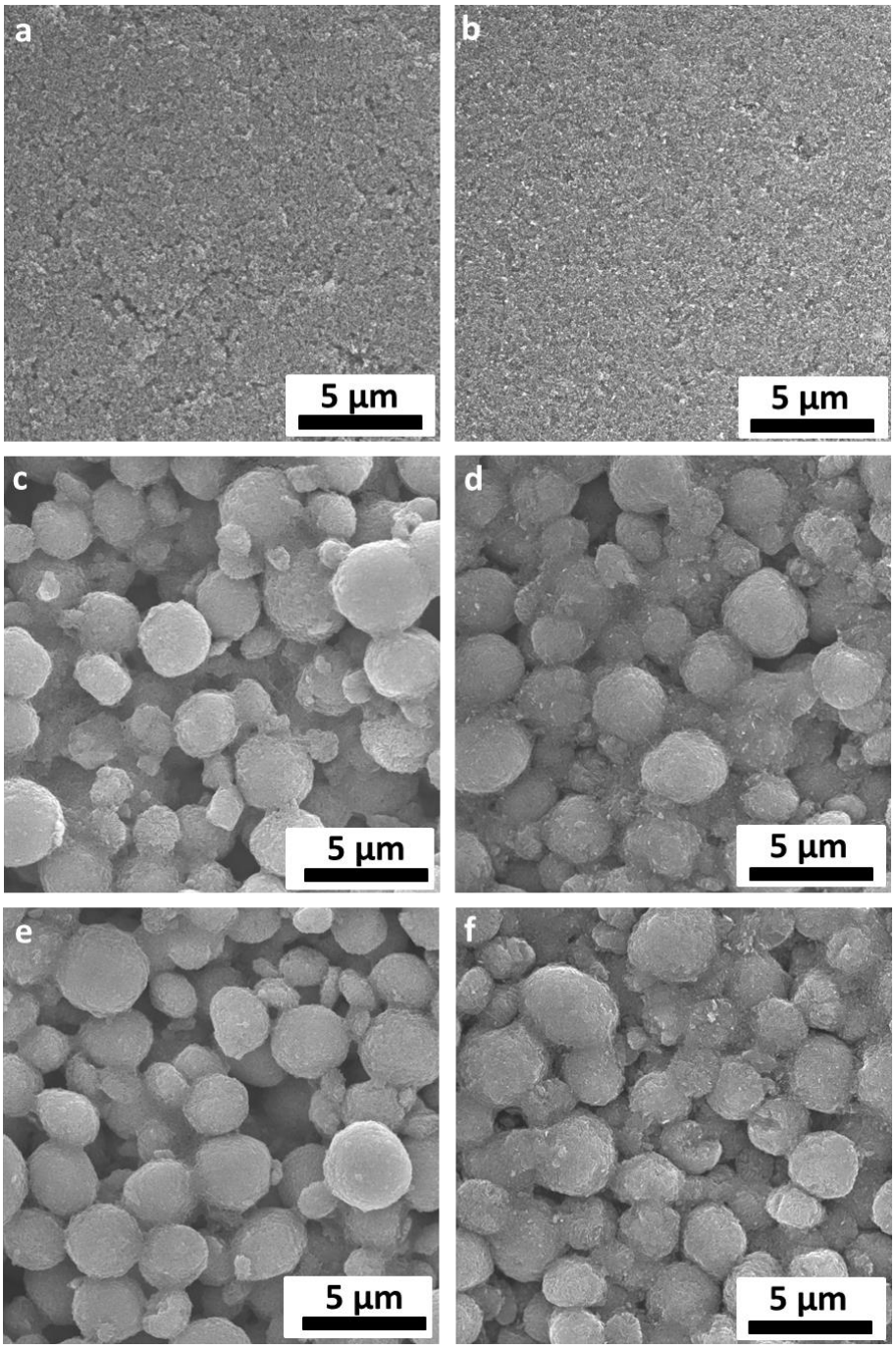

Figure 4.8 FE-SEM images of different TiO_2 films on ITO/PEN substrate: P25 film (a) before and (b) after CIP; MHAT film (c) before and (d) after CIP; P25/MHAT film (e) before and (f) after CIP.

Upon increasing the applied pressure, the connections between the particles are strengthened. [17] Unfortunately, higher pressures could not be applied due to limitations of the equipment. At 200 MPa, the diffuse reflectance spectra of the pressed MHAT films also showed a significant decrease in reflectivity compared to the films before CIP [Figure 4.4(c)]. The diffuse reflection capability of the pressed MHAT film, however, remains much higher than that of the pressed P25 film from 350 to 800 nm.

Table 4.2 Photovoltaic parameters of DSCs on flexible ITO/PEN substrates based on P25, MHAT and a MHAT film layer over a P25 under layer (P25/MHAT), which were measured under air mass (AM) 1.5 global (1.5G) one sun illumination (100 mW cm^{-2}). J_{sc}: short-circuit photocurrent density; V_{oc}: open-circuit photovoltage; *FF*: fill factor; η: total power conversion efficiency. The active areas were ~ 0.16 cm^2 for all of the cells (with the mask area 0.16 cm^2), and the data presented are the average value obtained after testing four cells and finding the standard deviation thereof.

Sample	J_{sc} [mA cm^{-2}]	V_{oc} [mV]	*FF* [%]	η [%]	Thickness[a)] [μm]	Amount of dye[b)] [10^{-7} mol cm^{-2}]
P25	9.4 ± 0.3	721 ± 5	64 ± 2	4.3 ± 0.2	12 ± 2	0.8
MHAT	10.9 ± 0.3	725 ± 5	64 ± 2	5.1 ± 0.2	12 ± 2	1.2
P25/ MHAT	11.7 ± 0.3	733 ± 5	65 ± 2	5.6 ± 0.2	12 ± 2	1.7

[a)] Measurement of film thickness was carried out on a surface profile system (Veeco Dektak 150).

[b)] 0.1 M NaOH solution in mixed ethanol and water (1:1) solvent was used as the desorbent. The amount of desorbed dye was quantified by measuring its optical absorption spectrum against known concentrations.

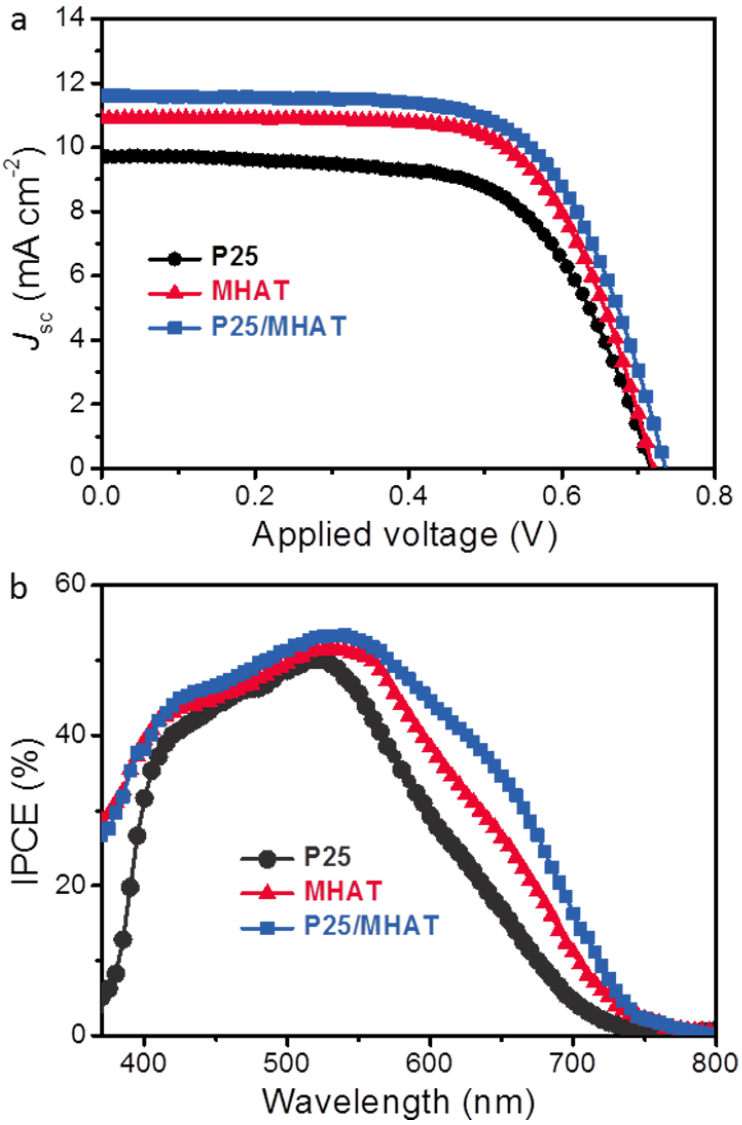

Figure 4.9 a) *J-V* characteristics of DSCs; b) IPCE curves of DSCs based on flexible ITO|PEN substrates covered with layers of P25 (~ 12 µm), MHAT (~ 12 µm), and a MHAT film layer over a P25 under-layer [P25/MHAT (6 µm + 6 µm)].

The photocurrent density-voltage (*J-V*) characteristic curves of P25-, MHAT- and P25/MHAT-based sealed DSCs (each with a porous TiO_2 layer ~ 12 µm in optimized thickness), are shown in Figure 4.9(a) (with key properties summarized in Table 4.2).

Table 4.3 Photovoltaic parameters of DSCs on flexible ITO/PEN substrates based on a MHAT film layer over a P25 under layer (P25/MHAT) before CIP and after CIP (200 MPa), which were measured under air mass (AM) 1.5 global (1.5G) one sun illumination (100 mW cm^{-2}). J_{sc}: short-circuit photocurrent density; V_{oc}: open-circuit photovoltage; *FF*: fill factor; η: total power conversion efficiency. The active areas were ~ 0.16 cm^2 for all of the cells (with the mask area 0.16 cm^2), and the data presented are the average value obtained after testing four cells and finding the standard deviation thereof.

Sample	J_{sc} [mA cm^{-2}]	V_{oc} [mV]	*FF* [%]	η [%]	Thickness[a)] [μm]
P25/MHAT before CIP	8.6 ± 0.3	727 ± 5	64 ± 2	4.0 ± 0.2	12 ± 2
P25/MHAT after CIP	11.7 ± 0.3	733 ± 5	65 ± 2	5.6 ± 0.2	12 ± 2

[a)] Measurement of film thickness was carried out on a surface profile system (Veeco Dektak 150).

The P25/MHAT-based DSCs showed an average V_{oc} of 0.733 V, J_{sc} of 11.7 mA cm^{-2}, *FF* of 65.1 %, and an overall energy conversion efficiency (η) of 5.6 % under one sun conditions, much higher than the ones before CIP (4.0 %, summarized in Table 4.3). However, by further increasing the thickness to ~ 16 μm (12 μm P25 + 4

Table 4.4 Photovoltaic parameters of DSCs on flexible ITO/PEN substrates based on a MHAT film layer over a P25 under layer [P25/MHAT ~ 16 μm (12μm P25+ 4μm MHAT)], which were measured under air mass (AM) 1.5 global (1.5G) one sun illumination (100 mW cm^{-2}). J_{sc}: short-circuit photocurrent density; V_{oc}: open-circuit photovoltage; *FF*: fill factor; η: total power conversion efficiency. The active areas were ~ 0.16 cm^2 for all of the cells (with the mask area 0.16 cm^2), and the data presented are the average value obtained after testing four cells and finding the standard deviation thereof.

Sample	J_{sc} [mA cm^{-2}]	V_{oc} [mV]	*FF* [%]	η [%]	Thickness[a)] [μm]
P25/MHAT	11.2 ± 0.3	728 ± 5	64 ± 2	5.2 ± 0.2	16 ± 2

[a)] Measurement of film thickness was carried out on a surface profile system (Veeco Dektak 150).

μm MHAT), the η was lower, with efficiency ~ 5.2 % obtained. (summarized in Table 4.4).

Compared to P25, the higher J_{sc} for MHAT-based devices can be mainly attributed to the higher specific surface area, leading to higher dye adsorption (1.2×10^{-7} mol cm^{-2}, compared with 0.8×10^{-7} mol cm^{-2} for P25 and 1.7×10^{-7} mol cm^{-2} for P25/MHAT), based on the measured specific surface area, and porosity, as well as the light scattering properties of the MHAT films.

More importantly, as observed in Figure 4.6(c), by depositing the MHAT onto a thin P25 layer, the MHAT nanoribbons are able to penetrate into the P25 layer,

producing more intimate interparticle connections post CIP, and thus forming better contact with the ITO|PEN substrate.

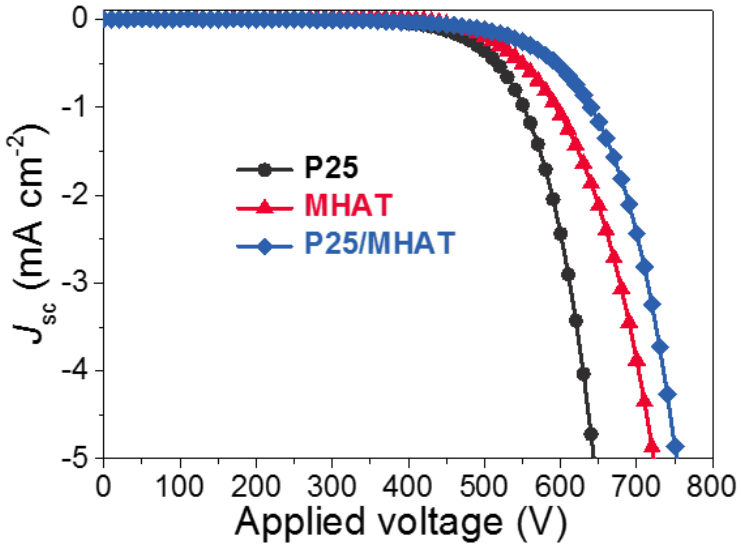

Figure 4.10 *J-V* characteristics of P25-, MHAT-, P25/MHAT-based flexible DSCs under dark current.

In addition, this enhances mechanical stability and provides efficient pathways for electron transfer. Dark current can be used to describe the extent of the back electron transfer. From Figure 4.10, it can be seen that the dark current onset of the P25/MHAT-based DSC shifted to a higher potential, indicating a lower recombination rate between transferred electrons and I_3^- ions for P25/MHAT.

The incident photon to current conversion efficiency (IPCE) spectra of the devices fabricated using the three materials are shown in Figure 4.9(b). IPCE spectra of all the cells with N719 dye exhibited a maximum value at approximately 535 nm, where one would expect, given the dye absorbance. At this wavelength, there is minimal difference between the three films; however, in the red part of the spectrum

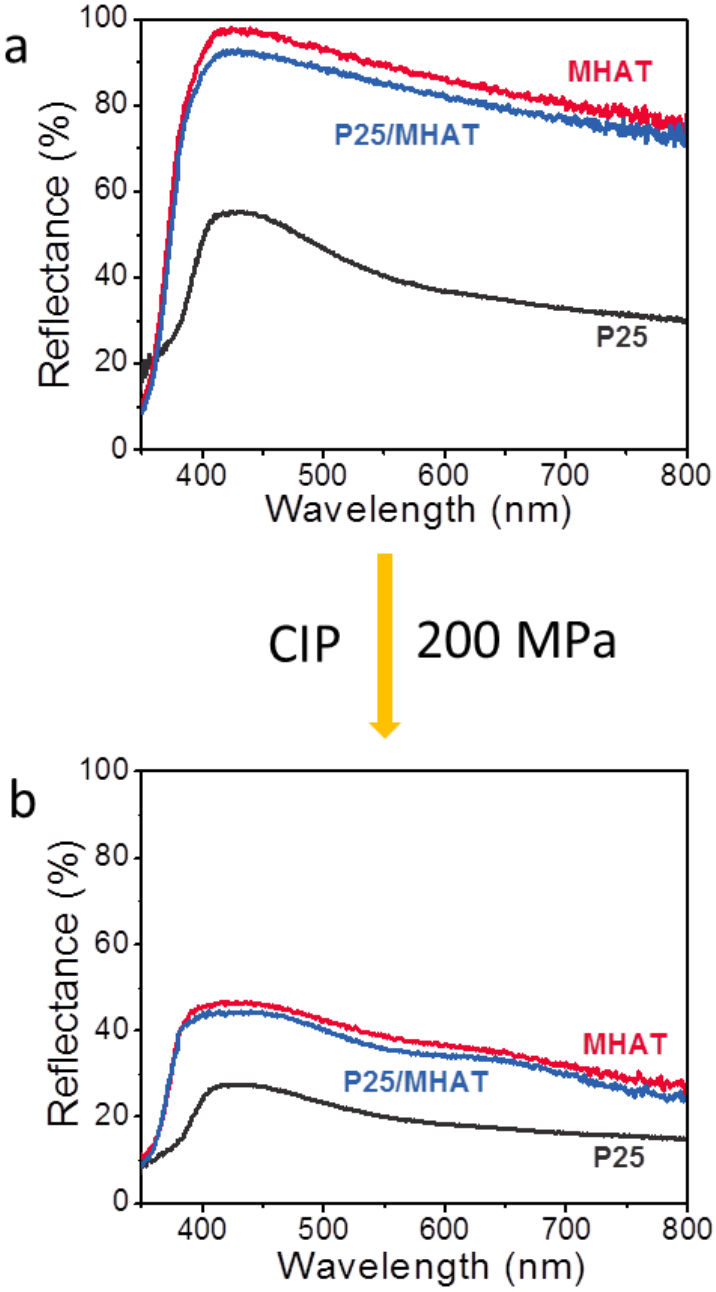

Figure 4.11 Diffuse reflectance spectra of P25, P25/MHAT and MHAT (a) before and (b) after CIP.

there is substantial variation (especially in the 600-750 nm regions, where the extinction coefficient of N719 is comparatively low).

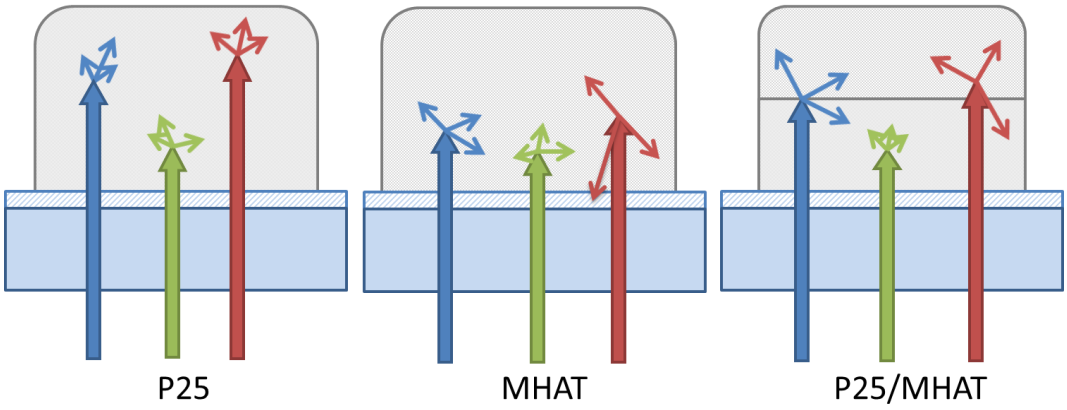

Figure 4.12 Scheme of light scattering in P25, MHAT, and P25/MHAT films.

The MHAT and P25/MHAT films scattered this light more effectively than P25, giving this red light a higher probability of being absorbed. Compared to MHAT-based DSCs, P25/MHAT-based DSCs displayed a significantly higher IPCE response from 600-750 nm. In the ultraviolet-visible (UV-Vis) spectrum (Figure 4.11), light reflectance of the P25/MHAT film is slightly lower than that of MHAT at the same thickness. When there is a bi-layer, there is very little scattering throughout the P25, light transmitted through this layer, however, can be reflected or scattered, giving it more chance of being absorbed. Only a small amount of light will be reflected back out the front face as it will have to have made at least two passes through the P25 layer. In the case of single MHAT spheres (large particles), there is more probability that light will be reflected out of the device (through the front face) (with scheme shown in Figure 4.12). The result is consistent with the IPCE curves in Figure 4.9(b).

Figure 4.13 displays (a) the electron lifetime (τ_n), (b) electron diffusion coefficient ($D_{n,\ EIS}$), and (c) electron diffusion length (L_n) as measured through electrochemical impedance spectroscopy (EIS), all as functions of V_{oc}, which was controlled by adjusting the illumination intensity. [32-34] The data presented in Figure 4.13(d) describes the electron diffusion coefficients ($D_{n,\ IMPS}$) measured by

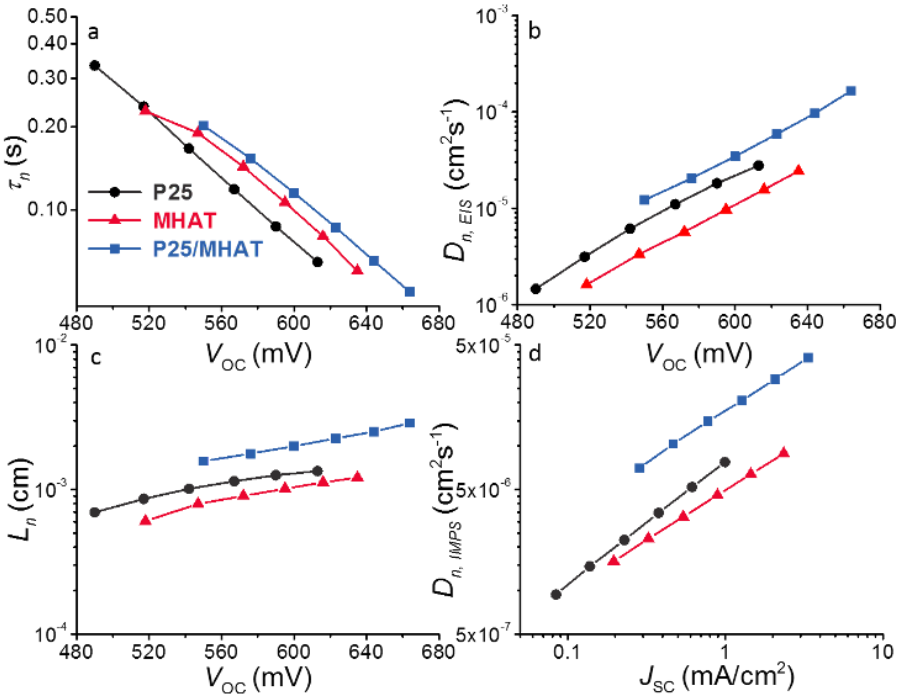

Figure 4.13 a) Electron lifetime (τ_n), b) electron diffusion coefficient ($D_{n,\ EIS}$), and c) electron diffusion length (L_n) as measured through impedance spectroscopy; d) electron diffusion coefficient ($D_{n,\ IMPS}$) measured though intensity modulated photocurrent spectroscopy (IMPS).

intensity modulated photocurrent spectroscopy (IMPS). Figure 4.13(a) shows longer lifetimes for the two cells using the MHAT TiO_2 material, which suggests electron recombination may be slower between the MHAT TiO_2 architecture with the adjacent electrolyte species, consistent with the results studied by EIS (Figure 4.14). Figure 4.13(b) illustrates the faster charge diffusion rates achieved in a P25 film when compared to the MHAT film. This trend is equally reflected by the IMPS data in Figure 4.13(d). This result appears counterintuitive, given that the 2D nanoribbon unit of the MHAT should lend itself towards faster charge transfer rates than the TiO_2 nanoparticle assembly.

The slower diffusion rates observed in the MHAT film, however, are expected not due to transport limitations within the 2D nanoribbons, but rather the poor electrical contact between the tips of the ribbons and the underlying substrate. When a P25 film is deposited beneath the MHAT TiO_2 network, this poor contact resistance at the tip of the ribbons is overcome, and significantly faster diffusion rates in the bi-layer film were observed, when compared to a uniform P25 film. The P25 underlayer allows the ribbons to anchor themselves to the substrate and increases the relative contact area from which electrons may be extracted. The faster diffusion rates shown in the bi-layer film indicate that transport rates within the ribbons themselves may be faster than in a conventional P25 nanoparticle film because of their single-crystal nature [Figure 4.1(d)].

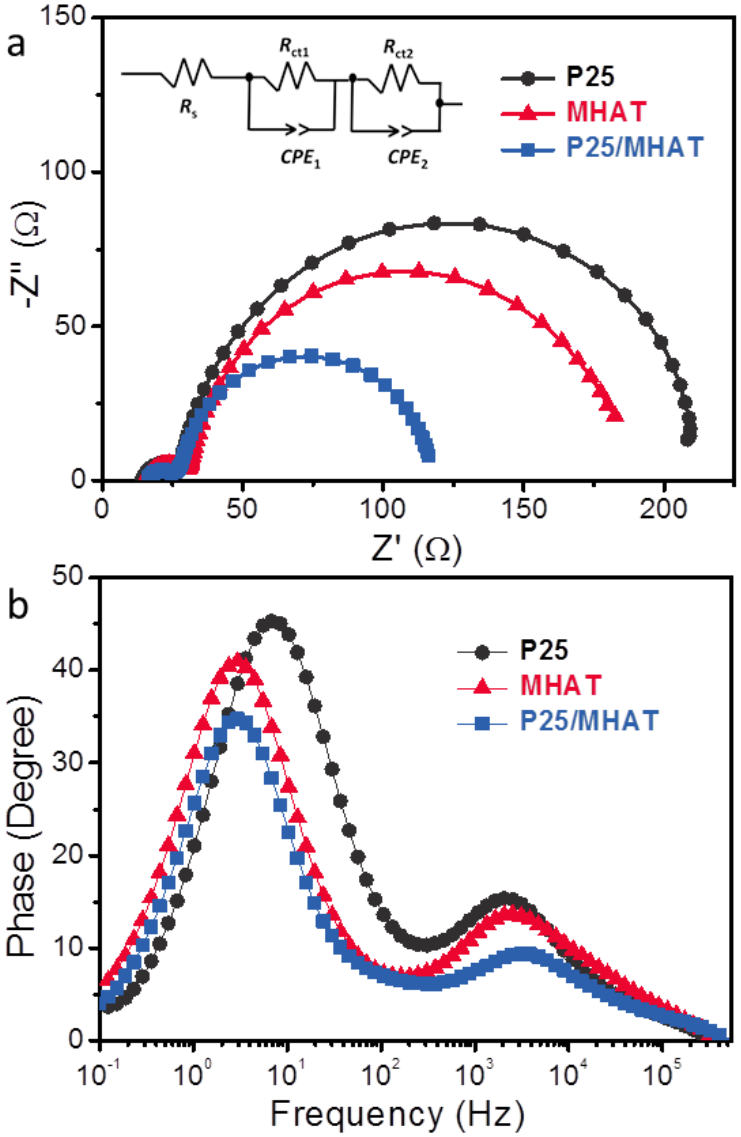

Figure 4.14 (a) Nyquist plots, with the inset showing the equivalent circuit, and (b) Bode phase plots of flexible DSCs based on P25, MHAT, and P25/MHAT.

Figure 4.13(c) reveals the electron diffusion lengths in the three films, measured through impedance spectroscopy. The electron diffusion lengths for all the films show a weak dependence on the illumination intensity, as predicted by the quasi-static approximation and as noted in previous work. [35, 36] This plot shows the longer electron diffusion lengths presented by the bi-layer P25 and MHAT film compared to the other two films. The slower recombination kinetics of the MHAT particles and the faster charge transport rates that they offer when coupled with the underlayer, ensure

the longer diffusion lengths of the bi-layer system. This result, in combination with the increased IPCE response of the bi-layer film shown in Figure 4.9(b), accounts for the improved efficiencies reported for the P25 and MHAT double layered architecture.

To investigate the mechanical durability of the flexible DSCs, a bending test was performed taking into account of the bending cycles and radii. In Figure 4.15(a), films were bent over with radius of ~ 400 mm by a bending machine before constructing cells (with experimental procedure shown in Figure 4.16). No distinct decrease of the key performance indicators was observed compared to unbent films. For P25-, MHAT-, and P25/MHAT-based flexible DSCs, J_{sc}, V_{oc}, and *FF* remained identical throughout the test, which led the η constant as a function of the number of bending cycles, even after 2000 cycles of bending, demonstrating highly durability of flexible DSCs. The η of bi-layer P25/MHAT-based flexible DSC was measured after film being bent repeatedly (100 cycles) with different radii of curvature. The PCE exhibited no significant decrease in efficiency even with 50 mm of bending radius, retaining 99 % of the original PCE value [Figure 4.15(b)].

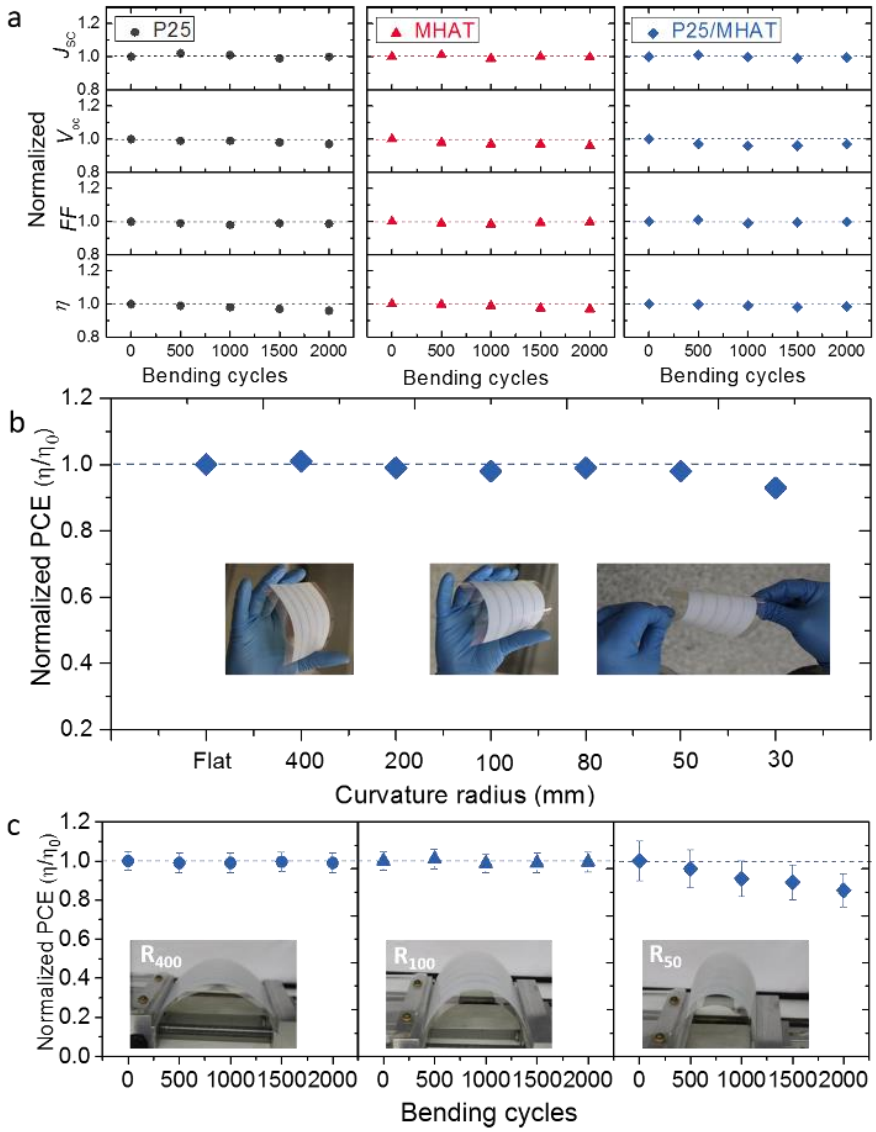

Figure 4.15 a) Comparison of photovoltaic properties of normalized J_{sc}, normalized V_{oc}, normalized *FF* and normalized η of P25-, MHAT-, and P25/MHAT-based flexible DSCs as a function of bending cycles, with radius of 400 mm. Bending of photoanode was performed before constructing the DSCs. Cell performances were normalized compared with the cell without bending. b) Normalized PCE of P25/MHAT-based flexible DSCs measured after bending the ITO|PEN substrate (100 cycles) within a specified radius of 400 mm to 30 mm. The insets show the digital photographs bent according to 400 mm, 100 mm, and 50 mm bending radii, respectively. c) Normalized PCE of P25/MHAT-based flexible DSCs as a function of bending radii of 400 mm, 100 mm, and 50 mm. The insets show the digital photographs bent by a bending machine during the test. The error bar represents the standard deviation from four devices.

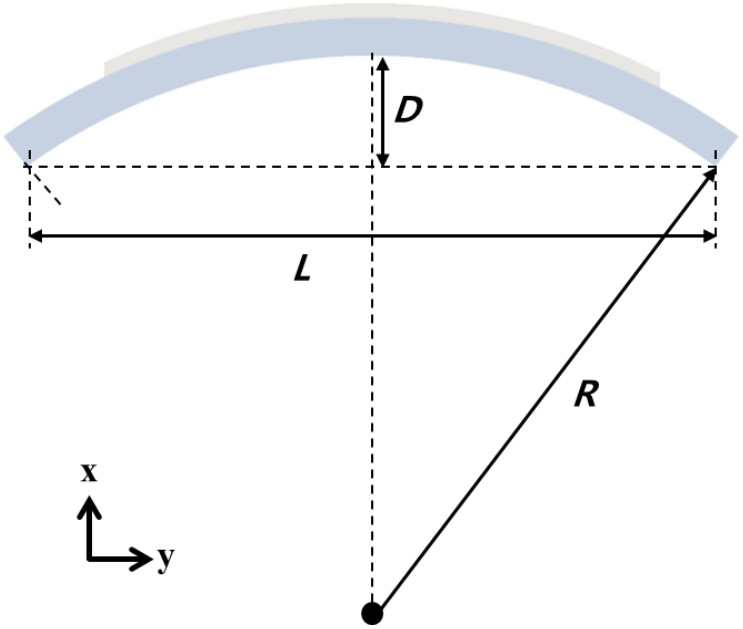

Figure 4.16 Illustration of bending machine, R can be calculated by the following equation:

$$R = \frac{L^2 + 4D^2}{8D}$$

Where L and D can be measured by ruler during test.

The effects of mechanical bending on device performance were further evaluated during 2000 consecutive bending cycles at three different values of radii of curvature, *i.e.*, at 400 mm, 100 mm, and 50 mm, respectively (R_{400}, R_{100}, and R_{50}). The bi-layer P25/MHAT-based flexible DSCs revealed fairly promising mechanical bending stability. No significant reduction on PCE was observed when the device was bent with R_{400} or R_{100}, even after up to 2000 bending cycles. For the case of R_{50}, however, 90 % of initial PCE was retained after 1000 cycles, and further decreased to approximately 80 % after 2000 cycles (compared with 70 % and 60 % for P25-, and MHAT-based devices after 2000 cycles, with results shown in Figure 4.17). The above results demonstrated that the rational designed bi-layer P25/MHAT-based

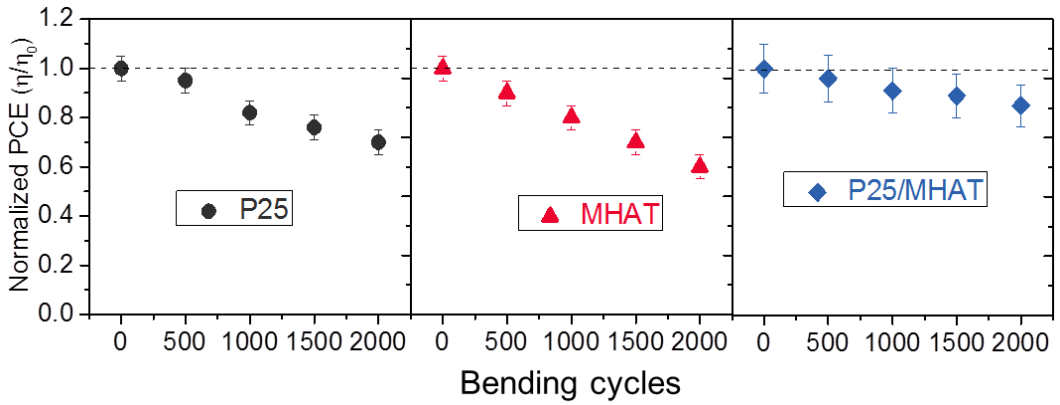

Figure 4.17 Normalized PCE of P25-, MHAT-, and P25/MHAT-based flexible DSCs as a function of bending cycles, with radius of 50 mm.

flexible devices possess high bending durability. As a result, the cell performance will degrade due to the limitation flexibility of ITO|PEN substrate, under an acute bending radius (< 50 mm).

4.4 Conclusions

In summary, a new photoanode architecture for cold isostatic pressing (CIP), with microstructured TiO_2 sea-urchin-like assemblies, composed of high aspect-ratio single-crystal nanoribbons deposited onto P25, was rationally designed for efficient charge transport and better light management in flexible dye-sensitized solar cells. We demonstrate that this TiO_2 nanostructure is beneficial due to enhanced dye loading as well as light scattering. We find that the interpenetration of the nanoribbons into the P25 under layer coated on the ITO|PEN film via CIP results in more intimate interparticle connections between the TiO_2 photo electrode and the ITO|PEN substrate, and enhanced mechanical stability and durability, while providing efficient electron transfer pathways. A 5.6 % solar-to-electric conversion efficiency was realized.

Even though the efficiency of the device is lower than the previous report, [23] this work, however, addresses a major technical problem that experienced by researchers trying to enhance the adhesion between the TiO_2 film and the ITO|PEN substrate.

4.5 References

1. B. Oregan, and M. Grätzel, *Nature*, 1991, **353**, 737-740.

2. A. Hagfeldt, G. Boschloo, L. Sun, L. Kloo, and H. Pettersson, *Chem. Rev.*, 2010, **110**, 6595-6663.

3. D. Chen, and R. A. Caruso, *Adv. Funct. Mater.*, 2013, **23**, 1356-1374.

4. S. K. Balasingam, M. G. Kang, and Y. Jun, *Chem. Commun.*, 2013, **49**, 11457-11475.

5. F. Huang, D. Chen, X. L. Zhang, R. A. Caruso, and Y.-B. Cheng, *Adv. Funct. Mater.*, 2010, **20**, 1301-1305.

6. S. Huang, Z. Yang, L. Zhang, R. He, T. Chen, Z. Cai, Y. Luo, H. Lin, H. Cao, X. Zhu, and H. Sheng, *J. Mater. Chem.*, 2012, **22**, 16833-16838.

7. Y. J. Kim, M. H. Lee, H. J. Kim, G. Lim, Y. S. Choi, N.-G. Park, K. Kim, and W. I. Lee, *Adv. Mater.*, 2009, **21**, 3668-3673.

8. S. Ito, P. Chen, P. Comte, M. K. Nazeeruddin, P. Liska, P. Pechy, and M. Grätzel, *Prog. Photovolt: Res. Appl.*, 2007, **15**, 603-612.

9. J. Lin, A. Nattestad, H. Yu, Y. Bai, L. Wang, S. X. Dou, and J. H. Kim, *J. Mater. Chem. A*, 2014, **2**, 8902-8909.

10. J.-Y. Liao, B.-X. Lei, H.-Y. Chen, D.-B. Kuang, and C.-Y. Su, *Energy Environ. Sci.*, 2012, **5**, 5750-5757.

11. Y. Peng, J. Zhong, K. Wang, B. Xue, and Y.-B. Cheng, *Nano Energy*, 2013, **2**, 235-240.

12. M. G. Kang, N.-G. Park, K. S. Ryu, S. H. Chang, and K.-J. Kim, *Sol. Energy Mater. Sol. Cells*, 2006, **90**, 574-581.

13. W. Wang, Q. Zhao, H. Li, H. Wu, D. Zou, and D. Yu, *Adv. Funct. Mater.*, 2012, **22**, 2775-2782.

14. T. Chen, L. Qiu, Z. Cai, F. Gong, Z. Yang, Z. Wang, and H. Peng, *Nano Lett.*, 2012, **12**, 2568-2572.

15. W. Guo, C. Xu, X. Wang, S. Wang, C. Pan, C. Lin, and Z. L. Wang, *J. Am. Chem. Soc.*, 2012, **134**, 4437-4441.

16. H. Dai, Y. Zhou, L. Chen, B. Guo, A. Li, J. Liu, T. Yu, and Z. Zou, *Nanoscale*, 2013, **5**, 5102-5108.

17. F. Huang, D. Chen, Y. Chen, R. A. Caruso, and Y.-B. Cheng, *J. Mater. Chem. C*, 2014, **2**, 1284-1289.

18. S. Senthilarasu, T. A. N. Peiris, J. García-Canadas, and K. G. U. Wijayantha, *J. Phys. Chem. C*, 2012, **116**, 19053-19061.

19. G. Boscholl, H. Lindstrom, E. Magnusson, A. Holmberg, and A. Hagfeldt, *J. Photochem. Photobiol. A*, 2002, **148**, 11-15.

20. T. Yamaguchi, N. Tobe, D. Matsumoto, and H. Arakawa, *Chem. Commun.*, 2007, **45**, 4767-4769.

21. S. Uchida, M. Tomiha, H. Takizawa and M. Kawaraya, *J. Photochem. Photobiol., A*, 2004, **164**, 93-96.

22. H. C. Weerasinghe, F. Huang, and Y.-B. Cheng, *Nano Energy*, 2013, **2**, 174-189.

23. H. C. Weerasinghe, P. M. Sirimanne, G. P. Simon, and Y.-B. Cheng, *Prog. Photovolt: Res. Appl.*, 2012, **20**, 321-332.

24. R. M. Govindarajan, and N. Aravas, *Int. J. Mech. Sci.*, 1994, **36**, 343-357.

25. F. Huang, D. Chen, L. Cao, R. A. Caruso, and Y.-B. Cheng, *Energy Environ. Sci.* 2011, **4**, 2803-2806.

26. H. C. Weerasinghe, P. M. Sirimanne, G. V. Franks, G. P. Simon, and Y.-B. Cheng, *J. Photochem. Photobiol. A*, 2010, **213**, 30-36.

27. H. C. Weerasinghe, P. M. Sirimanne, G. P. Simon, and Y.-B. Cheng, *J. Photochem. Photobiol., A* 2009, **206**, 64-71.

28. Y. Peng, J. Z. Liu, K. Wang, and Y.-B. Cheng, *Int. J. Photoenergy*, 2011, **2011**, 10352.

29. Q. Wang, J. E. Moser, and M. Grätzel, *J. Phys. Chem. B*, 2005, **109**, 14945-14953.

30. J. Bisquert, *J. Phys. Chem. B*, 2002, **106**, 325-333.

31. J. Lin, Y.-U. Heo, A. Nattestad, Z. Sun, L. Wang, J. H. Kim, and S. X. Dou, *Sci. Rep.*, 2014, **4**, 5769.

32. M. Bailes, P. J. Cameron, K. Lobato, and L. M. Peter, *J. Phys. Chem. B*, 2005, **109**, 15429-15435.

33. A. C. Fisher, L. M. Peter, E. A. Ponomarev, A. B. Walker, and K. G. U. Wijayantha, *J. Phys. Chem. B*, 2000,**104**, 949-958.

34. L. Peter, *Electrochem. Commun.*, 1999, **1**, 576-580.

35. J. Bisquert, and V. S. Vikhrenko, *J. Phys. Chem. B*, 2004, **108**, 2313-2322.

36. A. R. Pascoe, D. Chen, F. Huang, N. W. Duffy, R. A. Caruso, and Y.-B. Cheng, *J. Phys. Chem. C*, 2014, **118**, 16635-16642.

5 MESOPOROUS ANATASE SINGLE CRYSTALS FOR EFFICIENT $CO^{(2+/3+)}$-BASED DYE-SENSITIZED SOLAR CELLS

This chapter presented one new type of photoanode material which is composed of mesoporous anatase single crystals (MASCs) with special polyhedral pores (~ 7 nm) for $Co^{(2+/3+)}$-based DSCs.

Until recently, most reports of DSCs employed the triiodide/iodide redox couple (I_3^-/I^-). This introduces technical problems with regards to scaling up and module design due to its corrosive and volatile nature. In addition, polyiodides absorb through the visible spectrum, to the detriment of the sensitizer (parasitic light harvesting). Cobalt complexes are of particular interest due to their low absorption throughout the visible spectrum, easily tunable redox potentials, and lack of corrosivity towards metals typically used as interconnects in modules. In spite of record DSC device efficiency values being achieved with a $Co^{(2+/3+)}$ redox electrolyte, recombination of electrons from TiO_2 with the oxidized Co^{3+} species and mass transport in the electrolyte due to low diffusion coefficients continue to pose challenges.

In this chapter, the preparation of MASCs by a facile one-step hydrothermal route, without additives or templates, is reported for the first time. The resultant material comprises ellipsoidal mesoporous particles with long range crystallinity. Films composed of these particles were sensitised with an organic dye, MK-2, and employed as a photoanode in DSCs with a cobalt redox shuttle. These devices displayed photon-to-electron conversion efficiencies up to an impressive 8.7 % under air mass (AM) 1.5 irradiation, significantly higher than for analogous devices based on commercial Dyesol TiO_2 (6.3 %). The enhanced performance for devices containing MASCs is mainly attributable to the good electronic connectivity throughout the single crystal structure, resulting in faster electron transportation in the

TiO_2, and thus a higher fill factor (*FF*). The well-defined mesoporous structure allows fast diffusion of electrolyte components, as well as leading to high surface area without compromising the large crystal size, which affords a high light harvesting efficiency (LHE). Additionally, the crystals are large enough that the material effectively scatters incident light, further increasing the LHE.

This chapter has been published in *Nano Energy*, 2015, **11**, 557.

5.1 Introduction

Since the early 1990s, dye-sensitized solar cells (DSCs) have received a great deal of attention as a promising alternative photovoltaic technology on account of their projected low costs and reduced energy input in manufacture. [1-11] Until recently, most reports of DSCs employed the triiodide/iodide redox couple (I_3^-/I^-). This introduces technical problems with regards to scaling up and module design due to its corrosive and volatile nature. [12] In addition, polyiodides absorb through the visible spectrum, to the detriment of the sensitizer (parasitic light harvesting). Lately a number of promising alternatives to I_3^-/I^- have been reported, among them, polysulfide, organometallic compounds (including $Fe^{(2+/3+)}$, $Ni^{(2+/3+)}$, $Co^{(2+/3+)}$), and organic radical based couples [such as 2,2,6,6-Tetramethylpiperidine 1-oxyl (TEMPO)].

Cobalt complexes are of particular interest due to their low absorption throughout the visible spectrum, easily tunable redox potentials, and lack of corrosivity towards metals typically used as interconnects in modules. In spite of record DSC device efficiency values being achieved with a $Co^{(2+/3+)}$ redox electrolyte, recombination of electrons from TiO_2 with the oxidized Co^{3+} species and mass transport in the electrolyte due to low diffusion coefficients continue to pose challenges. [13-15] In order to overcome these problems, attention has been given to the modification of the cobalt complex ligands and/or the use of high extinction organic dyes, thereby decreasing the total surface area available for recombination. [16-19] In addition to this, Kim *et al.* reported that by controlling film porosity and pore size it is possible to significantly improve its mass transport properties, thereby improving device performance. [20]

Mesoporous metal-oxide semiconductors have previously been demonstrated as promising candidates for photoanodes in DSCs. Mesoporous architecure with high surface area can simultaneously provide faster electron transfer paths, enhancement of dye loading, and fast diffusion of electrolyte components. Titanium dioxide (TiO_2) is the most widely used metal oxide for DSC photoanodes for several reasons, including its low cost, non-toxicity, and high energy conversion efficiency. Previously, mesoporous TiO_2 was synthesized by using either soft templates (such as block copolymers, or ionic or nonionic surfactants) or hard templates (mesoporous silica or carbon). [25-28] Both these approaches require template removal, making them somewhat cumbersome. In almost all cases, the resultant frameworks are poorly crystallized or even amorphous, which limits their practical usage. Fully crystallized frameworks are important with regards to electron diffusion rates (competing with recombination rates). Mesoporous TiO_2 materials made of preformed nanocrystals with high surface area have been developed recently, but possible carrier trapping or recombination at grain boundaries may significantly decrease the device performance. [29-31] Fabrication of mesoporous single crystalline TiO_2 via a rapid, reproducible, and simple method has remained an important challenge.

Herein, the preparation of mesoporous anatase single crystals (MASCs) by a facile one-step hydrothermal route, without additives or templates, is reported for the first time. The resultant material comprises ellipsoidal mesoporous particles with long range crystallinity. Films composed of these particles were sensitised with an organic dye, MK-2, and employed as a photoanode in DSCs with a cobalt redox shuttle. These devices displayed photon-to-electron conversion efficiencies up to an impressive 8.7 % under air mass (AM) 1.5 irradiation, significantly higher than for analogous devices based on commercial Dyesol TiO_2 (6.3 %). The enhanced performance for devices

containing MASCs is mainly attributable to the good electronic connectivity throughout the single crystal structure, resulting in faster electron transportation in the TiO_2, and thus a higher fill factor (*FF*). The well-defined mesoporous structure allows fast diffusion of electrolyte components, as well as leading to high surface area without compromising the large crystal size, which affords a high light harvesting efficiency (LHE). Additionally, the crystals are large enough that the material effectively scatters incident light, further increasing the LHE.

5.2 Experimental

5.2.1 Synthesis of Mesoporous Anatase Single Crystals (MASCs)

Titanium butoxide (TB, Ti $(OCH_2CH_2CH_2CH_3)_4$, 97 %, analytical reagent, Sigma-Aldrich) and acetic acid (AA, ACS reagent, ≥ 99.7 %, Sigma-Aldrich) were used without further purification. MASCs were prepared in a hydrothermal reaction using 1.0 mL of TB, added at room temperature to 25 mL of AA solution whilst under stirring. This was then transferred to a Teflon lined reactor (Parr Instrument Company, 45 mL) and heated to 150 °C for a certain time. Afterwards the sample was cooled before being centrifuged and washed with distilled water and ethanol sequentially (3 cycles). Following this the samples were dried at 90 °C overnight and calcined at 500 °C for 3 h.

5.2.2 Preparation of Photoanodes

Photoanodes were prepared in a manner similar to reported previously. [32] Briefly, F: SnO_2 glass was cleaned using first soapy water, then acetone and finally ethanol before being dried. A dense TiO_2 layer was applied using spray pyrolysis of a Titanium (IV) diisoproxide-*bis*-acetylacetonate (75 wt % in isopropanol, Aldrich) solution (dilution 1:9 in ethanol) at 450 °C. A screen printing paste of the MHAT was prepared using 1.0 g TiO_2, ground in ethanol and water. To this was added 0.167 mL AA, 4 g terpineol and 0.5 g ethyl cellulose (in the form of a 10 wt % solution in ethanol). Water and ethanol were then removed using rotary evaporation and the resulting paste printed using a semiautomatic screen printer and custom patterned 43T screen to create 4 mm × 4 mm electrodes. These were dried at 125 °C before subsequent layers deposited in order to realise thicker electrodes. After all printing steps were complete the electrodes were subjected to an extended sintering process (10 min at 150 °C, 5 min at 325 °C, 5 min at 375 °C, 30 min at 450 °C then 15 min at

500 °C). Finally a post-treatment was completed by soaking electrodes in a 20 mM aqueous solution of $TiCl_4$ (Sigma) for 30 min at 70 °C and then resintering (500 °C, 30 min).

5.2.3 Device Assembly

After cooling to ≤ 110 °C, the photoanodes, described above, were immersed in a 0.2 mM solution of MK-2 organic dye in acetonitrile : toluene (1:1 by volume) for 6 h. After this time photoanodes are removed from the dye bath and washed in clean acetonitrile before being dried. Counter electrodes were prepared by drilling a hole in another piece of F: SnO_2 glass, to be used as a filling port for introduction of the electrolyte solution. These are then cleaned as per the photoanode, before having a drop of 10 mM H_2PtCl_6 solution (in ethanol) applied and smeared. After heating to 400 °C for 20 min the electrodes are cooled before being sandwiched together with the photoande, using a 25 µm Surlyn (Solaronix) spacer. These are affixed together through the application of heat (~ 120 °C). The electrolyte solution [0.22 M $Co(bpy)_3(NTf)_2$, (bpy = 2,2′-bipyridine, NTf = {(trifluoromethyl)sulfonyl}amide), 0.033 M $Co(bpy)_3(NTf)_3$, 0.2 M $LiClO_4$, 0.2 M 4-tertbutylpyridine (4-tBP)] was introduced by a vacuum back-filling technique and the filling port closed with a piece of Surlyn laminated to aluminium foil. It should be noted here that for the champion device, two or three electrolyte injections were necessary, in case of degradation.

5.2.4 Characterizations

XRD was employed to examine the crystal structures of the resultant products using an X-ray diffractometer (Bruker Advance, 40 kV, 30 mA) (Cu Kα, λ = 0.15406 nm) from 5º to 80º (2θ) (1 º/min), while the morphology was examined by FE-SEM (Megallan 200) and TEM (JEM-2100F). The surface area and porosity were examined

using Brunauner-Emmet-Teller (BET) analysis of nitrogen adsorption-desorption data collected on a Tristar 3030 system (Micrometrics Instrument Corporation), after degassing overnight at 150 °C. Dye desorption experiments were performed by washing of photoanodes in 0.1 M NaOH solution (1:1 vol ratio toluene:ethanol). Ultraviolet (UV)-visible light absorption/diffuse reflectance spectrometry (Shimadzu UV-3600) was used to investigate the light absorption and scattering properties. Thermogravimetric (TG) and differential thermal analysis (DTA) measurements were recorded on a Mettler Toledo GC200 instrument from 25 to 700 °C (3 °C min^{-1}). Veeco Dektak 150 Surface Profiler was used for measuing film thickness. Absorption/diffuse reflectance spectrometry of ultraviolet(UV)-visible light was used for investigating the light absorption and scattering properties (Shimadzu UV-3600). A Veeco Dektak 150 Surface Profiler was used for the film thickness measurements. A Keithley 2400 sourcemeter was used for photocurrent density - voltage (*J*-*V*) curve measurements, under air mass (AM) 1.5 global (1.5G) one sun illumination (100 mW cm^{-2}). A 300 W Xe lamp was used for IPCE measurements. A Keithley 2400 SMU was used for recording the short circuit current response of the devices (5 nm steps).

Stepped light-induced measurements of photocurrent and photovoltage (SLIM-PCV) were used to measure electron lifetime and electron diffusion coefficient. These measurements were carried out after a five hours cure for the devices to ensure stability. A 635 nm diode laser was employed; by varying the laser intensity, J_{sc} or V_{oc} decays were obtained. A fast multimeter (ADCMT 7461A) was employed to accumulate the current or voltage signals. For electron lifetime measurements, the device was controlled in the open circuit condition; the laser intensity was turned down to give a less than 1 mV photovoltage change. For electron diffusion coefficient measurements, the short circuit condition was applied; the laser intensity was reduced

to obtain less than 10 % photocurrent change. Electron density in TiO_2 films was determined by a charge extraction method. The laser intensity was switched off completely, while the device was simultaneously switched from open circuit to short circuit.

5.3 Results and Discussion

5.3.1 Synthesis and Characterization of Mesoporous Anatase Single Crystals (MASCs)

MASCs were prepared by the hydrothermal treatment of a solution of titanium butoxide (TB) in acetic acid (AA) and subsequent calcination. Figure 5.1(a) shows a low magnification field emission scanning electron microscope (FE-SEM) image of the as-prepared precipitate, obtained after hydrothermal reaction at 150 ˚C for 12 h, demonstrating the large-scale formation of nanoscale, ellipsoidal-shaped particles. The annular dark-field scanning transmission electron microscope (ADF-STEM) image in Figure 5.1(b) highlights a single particle, revealing that the particle surface is relatively rough but without pores. The electron diffraction (ED) pattern in Figure 5.1(b), along with the X-ray diffraction (XRD) data [Figure 5.2(d)], confirms the formation of anatase TiO_2 crystals. MASCs were obtained after the as-prepared precipitate was calcined at 500 ˚C for 3 h.

Figure 5.1(c) shows a low-magnification FE-SEM image of MASCs, displaying good uniformity of the ellipsoidal nanoparticles, which are 190 nm long on average, with 100 nm diameter, consistent with the dynamic light scattering (DLS) measurements [Figure 5.2(a)]. Higher magnification FE-SEM [Figure 5.1(d)] reveals that the particle surface has a rough texture in addition to the above-mentioned pores. The dimensions of these pores were more closely examined by high-angle annular dark-field scanning transmission electron microscope (HAADF-STEM) [Figure 5.1(e)] and ADF-STEM [Figure 5.3(a)] images of a single TiO_2 particle with pore structure, where the regions of low contrast indicate that a large number of pores (or interstitial regions) are present in the particle.

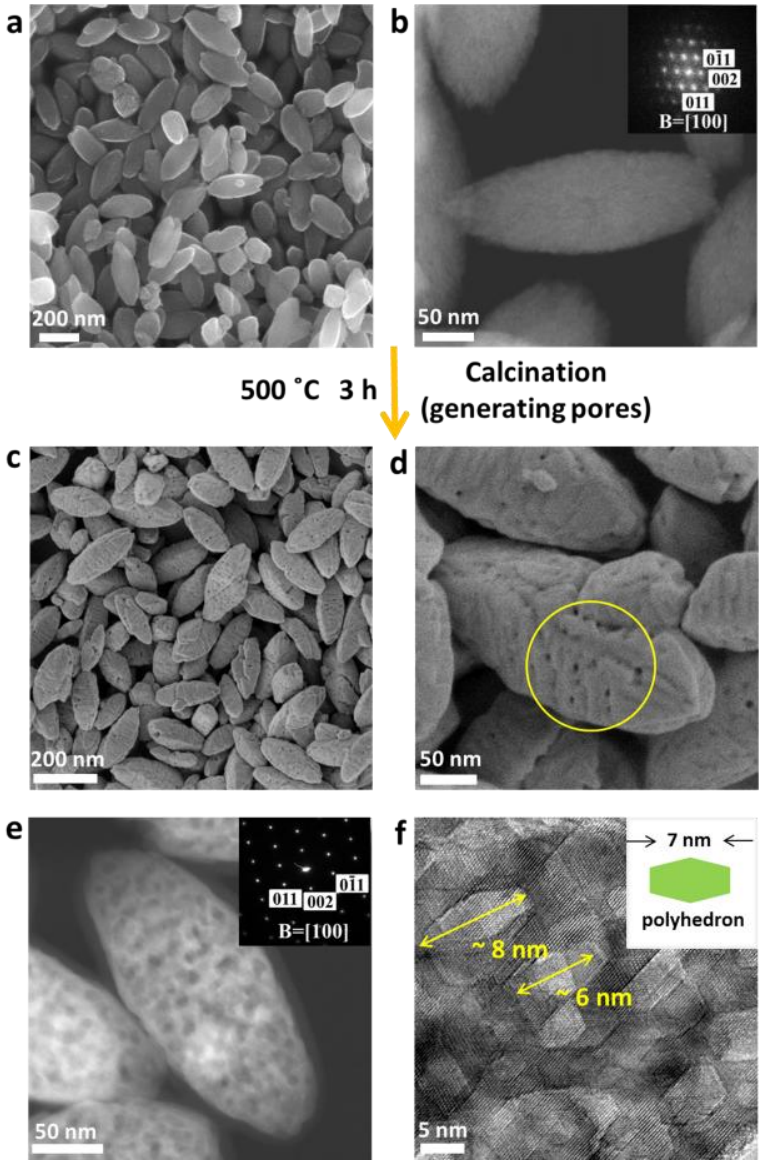

Figure 5.1 a) Low magnification FE-SEM image and b) ADF-STEM image, with inset: ED pattern, of as-prepared precipitate. c) Broad survey FE-SEM image of MASCs obtained after calcination at 500 ˚C for 3 h of the precipitate in a). d) FE-SEM image highlighting one single MASC. e) HAADF-STEM image of MASC, revealing homogeneous pores within a single crystal, with inset: ED pattern. f) HRTEM image of single MASC, with inset: scheme of polyhedral pore.

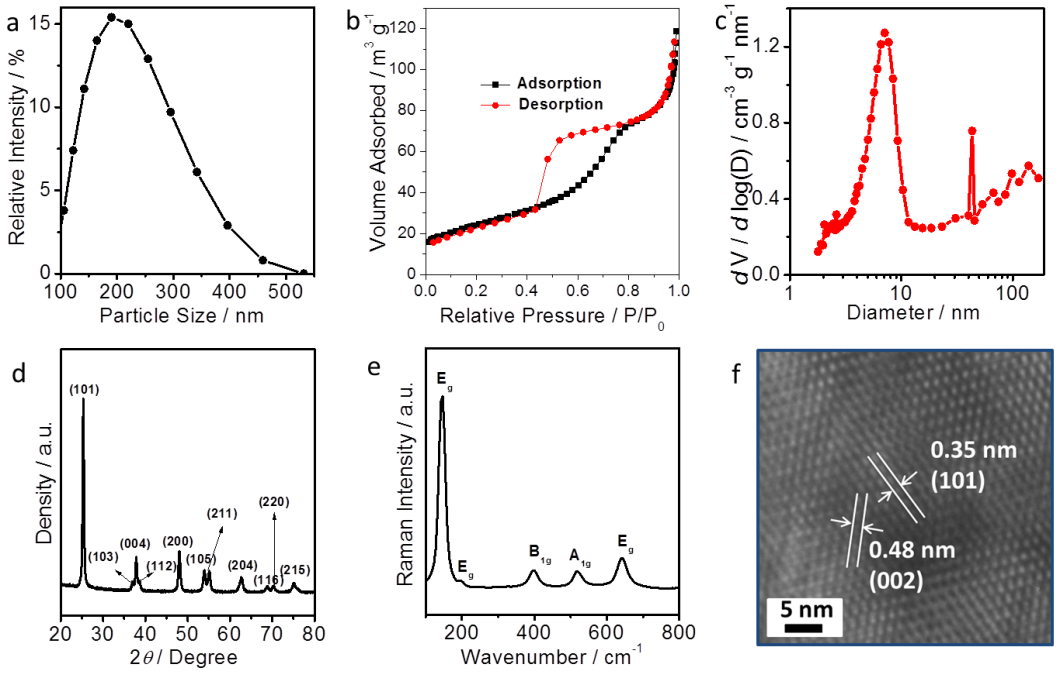

Figure 5.2 Physical characterization of MASCs: a) dynamic light scattering (DLS), showing particle size distribution; b) N_2 adsorption-desorption isotherms of MASCs; c) pore size distribution calculated by the Barrett-Joyner-Halenda (BJH) method from the adsorption branch of b); d) XRD pattern; e) Raman spectrum; and f) HR-TEM image, showing the fringe spacing of MASCs.

The morphology of the pores in Figure 5.3(a) is not clear due to overlapping of adjacent pores in the depth direction. To avoid confusion, a thin edge of the particle was selected for the observation. Figure 5.3(b) shows the morphology of one single pore, with diameter ~ 7 nm, corresponding well to Figure 5.1(f) [high resolution (HRTEM) image, with inset showing scheme of polyhedral pore] and the nitrogen (N_2) adsorption/desorption data [Figure 5.2(b)], which shows the IV isotherm that is typical of a mesoporous material, and the particle size distribution [Figure 5.2(c)].

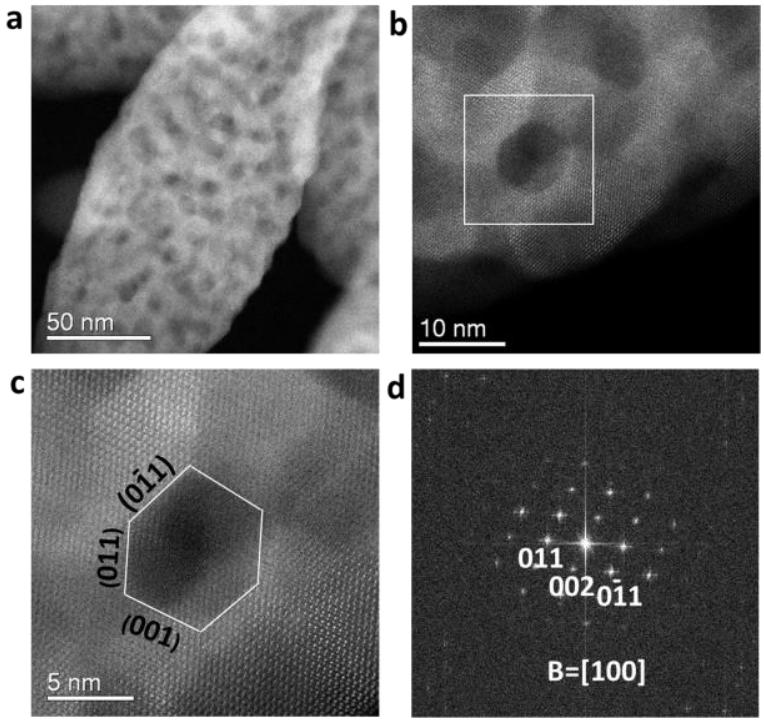

Figure 5.3 ADF-STEM images of one single MASC and its FFT pattern: a) a MASC particle, b) magified image, c) high resolution image of a faceted pore, and d) FFT pattern of c).

The Brunauer-Emmett-Teller (BET) surface area and the pore volume were determined to be 50.1 m^2 g^{-1} and 0.35 cm^3 g^{-1}, respectively. Such mesoporous structure can provide facile channels for the efficient diffusion of electrolyte. It is interesting to see that the single pore in Figure 5.3(c) has a faceted shape. The faceted pore surfaces were identified as (001), (011), and $(0\bar{1}1)$ planes by comparative analysis of the high resolution image [Figure 5.3(c)] and its fast Fourier transform (FFT) pattern [Figure 5.3(d)]. To the best of our knowledge, this is the first report on pore facets. In the case of the MASCs obtained in this study, the surface energies of low-index facets are in the order of (110) (1.09 J m^{-2}) > (001) (0.90 J m^{-2}) > (010) (0.53 J m^{-2}) > (101) (0.44 J m^{-2}). It is well known that the (001) facet of anatase with

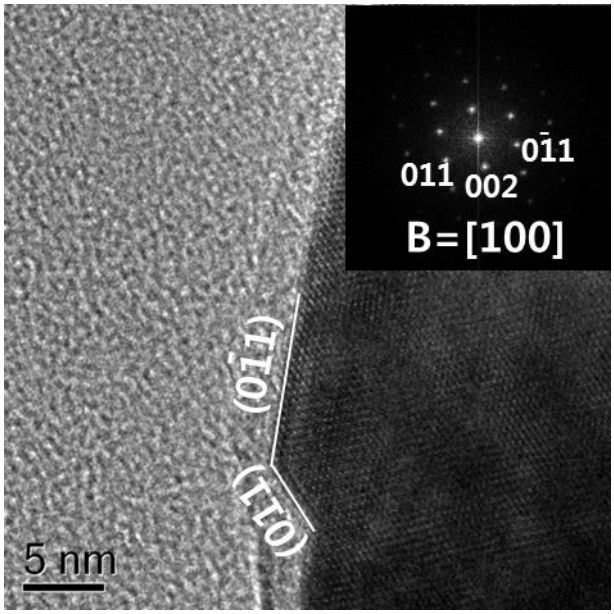

Figure 5.4 High resolution image of a MASC facet, with inset FFT pattern.

tetragonal structure is equivalent to (101). Thus to minimize surface energy, the facets of pores are composed of $(0\bar{1}1)$, (011) and (001). More interestingly, ellipsoidal-shaped MASCs also have (011) facets, the same as the pores (Figure 5.4).

The ED pattern [inset of Figure 5.1(e)] exhibits diffraction spots corresponding to the [100] zone axis of the anatase phase, confirming a single crystalline nature. Interestingly, each spot is very intense one without extended arcs, indicating the absence of any crystal defect or distortion. It has been generally known that mesoporous TiO_2 materials made of performed nanocrystals (i.e., mesocrystals) have some crystal defects or distortions. [29-31] In contrast, as clearly seen in Figure 5.3(c) and Figure 5.1(f), the lattice fringes are coherently extended in the same direction over the whole of the particles. Our results indicate the formation of perfect single crystals with mesoporous architectures.

The phase purity and crystal structure of the MASCs were also examined by XRD [Figure 5.2(d)], Raman spectroscopy [Figure 5.2(e)], and HRTEM [Figure

5.2(f)]. All these confirm that the materials are well-crystallized anatase phase (JCPDS No. 21-1272). This represents the first example of porous nanocrystalline anatase fabricated without any surfactant or template.

5.3.2 Growth Mechanism of MASCs

In order to investigate the formation mechanism of these MASCs, particularly in light of the fact that no surfactant was used, their production was interrupted at various stages of the hydrothermal process and the resultant products examined. These materials were characterized by TEM [Figure 5.5(a-d), Figure 5.6(a-d)], Fourier transform infrared (FTIR) spectroscopy [Figure 5.5(e)], XRD [Figure 5.6(e)], and Raman spectroscopy [Figure 5.6(f)].

Disordered and winding chain bundles about 0.5-1 μm in diameter were the exclusive product after the first hour of the reaction [Figure 5.5(a), Figure 5.6(a)]. Interestingly, when the reaction was allowed to proceed to 3 h, a number of ellipsoidal aggregates were formed [Figure 5.5(b), Figure 5.6(b)]. They look identical to the particles observed after the full run [Figure 5.1(a-b)], although they only account for a small percentage of the overall material. These are expected to be created through the rotation and twisting of the chain bundles (shown schematically in Figure 5.7). As the reaction time increased to 5 h, more of these ellipsoidal particles appeared, in addition to some residual chain bundles [Figure 5.5(c), Figure 5.6(c)]. When the reaction time was prolonged to 12 h, the TEM images [Figure 5.5(d), Figure 5.6(d)] suggest that all the chain bundles had been converted to ellipsoidal particles, with lengths of 190 nm and diameters of 100 nm.

TEM images of the products from the interrupted reactions suggest that the actual transition from the bundles to the ellipsoidal particles takes place rapidly.

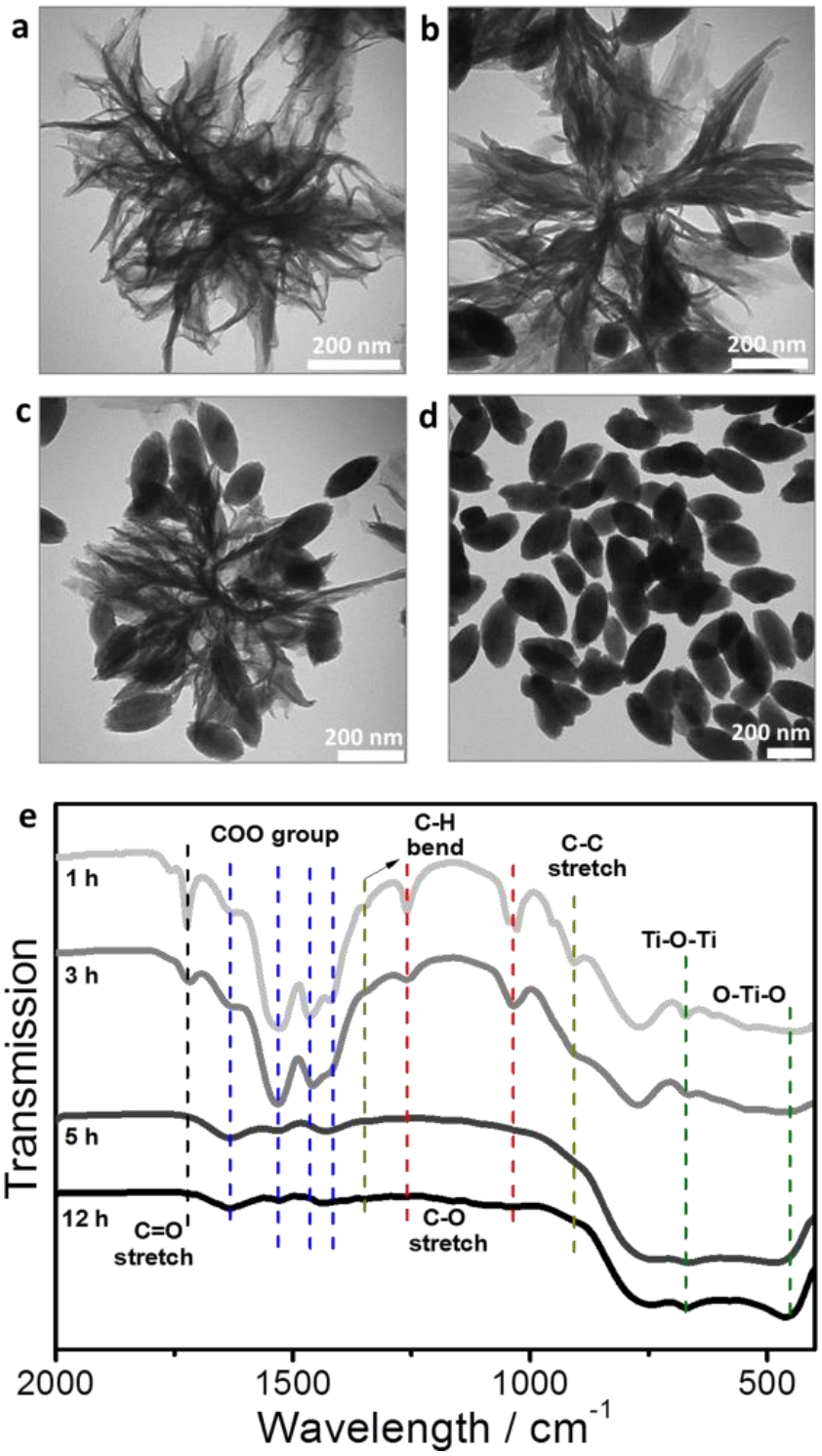

Figure 5.5 TEM images of as-prepared precipitates obtained via hydrothermal reaction of a solution containing 1.0 mL TB and 25 mL AA at 150 ˚C after a) 1 h, b) 3 h, c) 5 h and d) 12 h. e) FTIR spectra of as-prepared precipitates obtained after different reaction times.

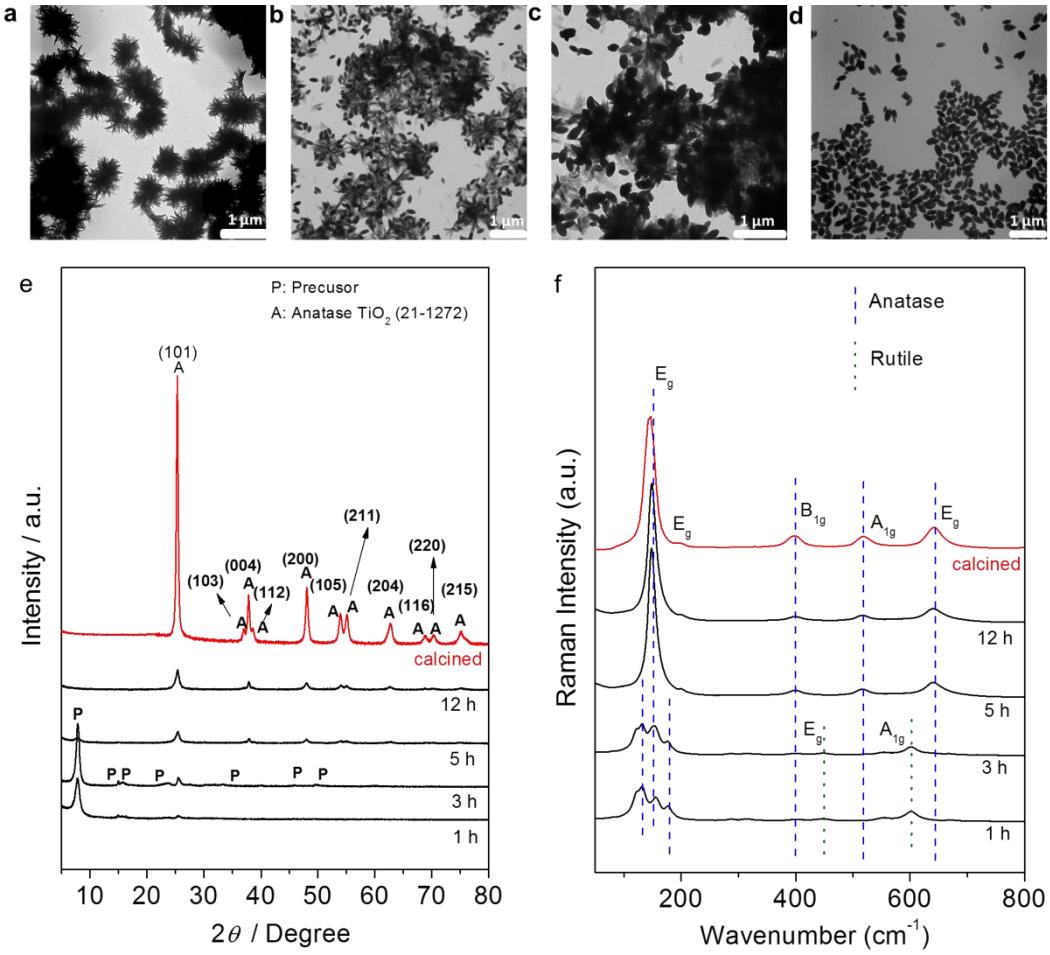

Figure 5.6 Low magnification TEM images of as-prepared precipitates obtained after different reaction times: a) 1 h, b) 3 h, c) 5 h, d) 12 h; e) XRD patterns of as-prepared precipitates obtained after different reaction times and of calcined MASCs; f) Raman spectra of as-prepared precipitates obtained after different reaction times and of calcined MASCs.

In order to understand the preceding steps that lead to this transformation, FTIR was employed [Figure 5.5(e)], and it shows that esterification of the organic acid with alcohol (released as TB dissociates) in the system appears to control the porosity of the chain aggregates through the partitioning of space.

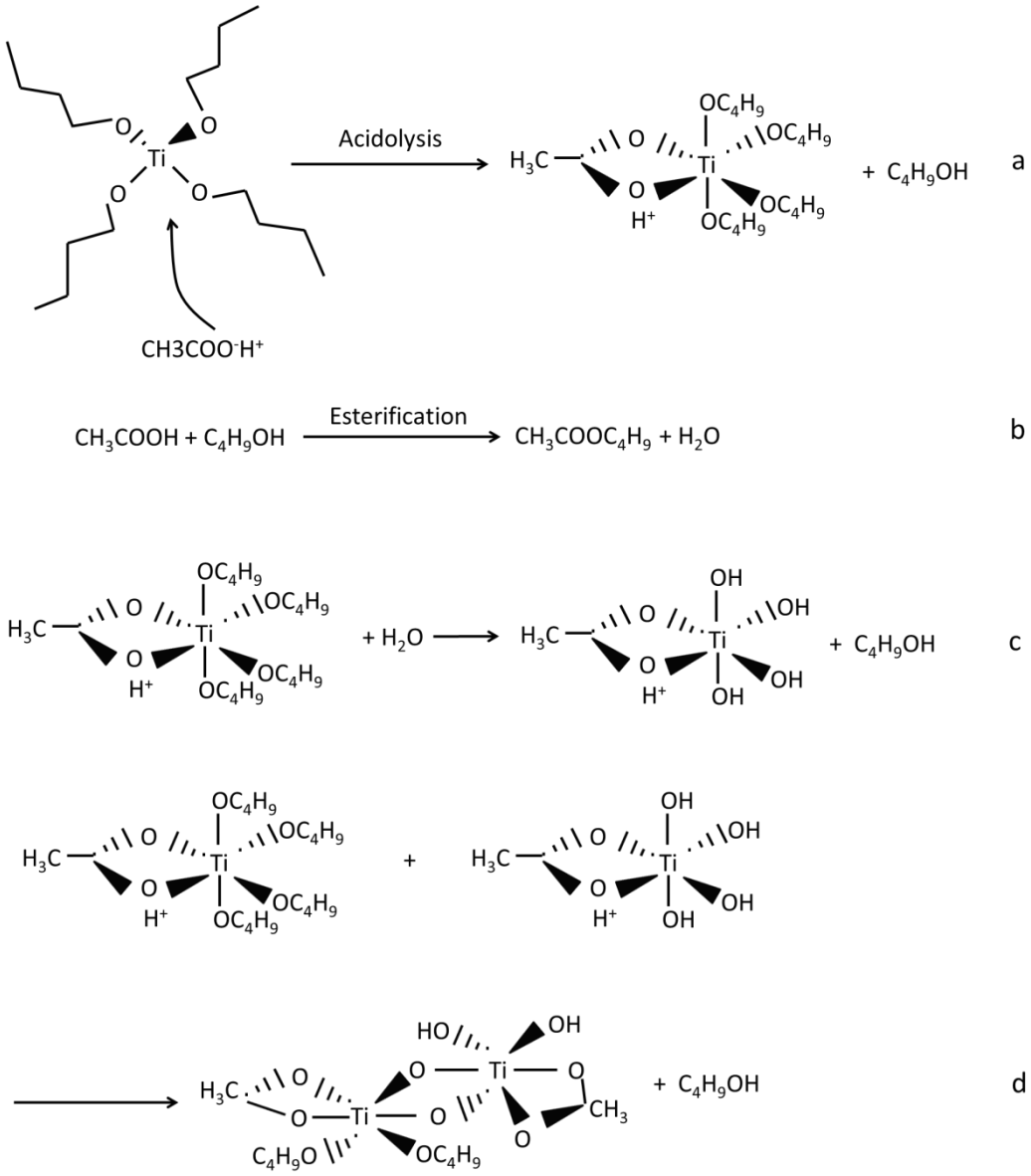

Figure 5.7 Formation mechanism of MASCs.

In the initial stages of the reaction (< 3 h), through the acidolysis process [Figure 5.7(a)], nascent TiO_2 bundles are surrounded by hydrophobic acetate groups. The surfaces of these chains selectively bond with esters in the system [Figure 5.7(b)]. From Figure 5.5(e), the most important features here are the strong sharp bands at 1721 cm^{-1}, corresponding to a stretching vibration of the C=O group of benzoate ester [33]. The doublets at 1632 cm^{-1} and 1529 cm^{-1}, and at 1460 cm^{-1} and 1419 cm^{-1} are

assigned respectively to the asymmetric and symmetric stretching vibrations of the COO groups, coordinated to Ti atoms, through the formation of bi-dentate complexes via an organic-ligand interaction, which can be assigned to the titanium-containing precursor, as indicated by the XRD patterns [Figure 5.6(e)]. [34]

The bands at 1258 cm^{-1} and 1024 cm^{-1} correspond to the stretching vibration modes of the C-O bond. The C-O stretching in TB appears at 1034 cm^{-1}. The position of the band ascribed to C-O stretching is shifted to a lower wavenumber, i. e. from 1034 to 1024 cm^{-1}, with respect to the precursor, showing a weakening of the C-O bond due to its chelation with TiO_6 octaedra. [35]

With the full 12 h reaction time [Figure 5.7(c-d)], in addition to COO groups, broad absorption bands centered at 662 and 458 cm^{-1} are observed, which can be assigned to the Ti-O-Ti and O-Ti-O networks of anatase TiO_2. The XRD pattern [Figure 5.6(e)] exhibits only the diffraction peaks of anatase crystals, and all the Raman [Figure 5.6(f)] peaks can be assigned to the E_g, E_g, B_{1g}, A_{1g}, and E_g modes of the anatase phase of TiO_2, respectively. It is proposed that in addition to the interaction of the Ti source and the solvent, the by-products of the initial reaction between tBuOH and AA play a significant role in controlling the morphology and porous structure of the TiO_2 products. This is further confirmed by the thermogravimetric analysis (TGA) and differential scanning calorimetry curves (Figure 5.8).

The TGA curve of the sample collected after 12 h reaction time, measured under flowing air, indicates that a considerable amount of butyl acetate (~ 32 wt %) was entrapped inside the pores and/or adsorbed on the surface. [34, 36] The complete decomposition of the organics was not realized until T ~ 450 ºC. The sharp peak in the

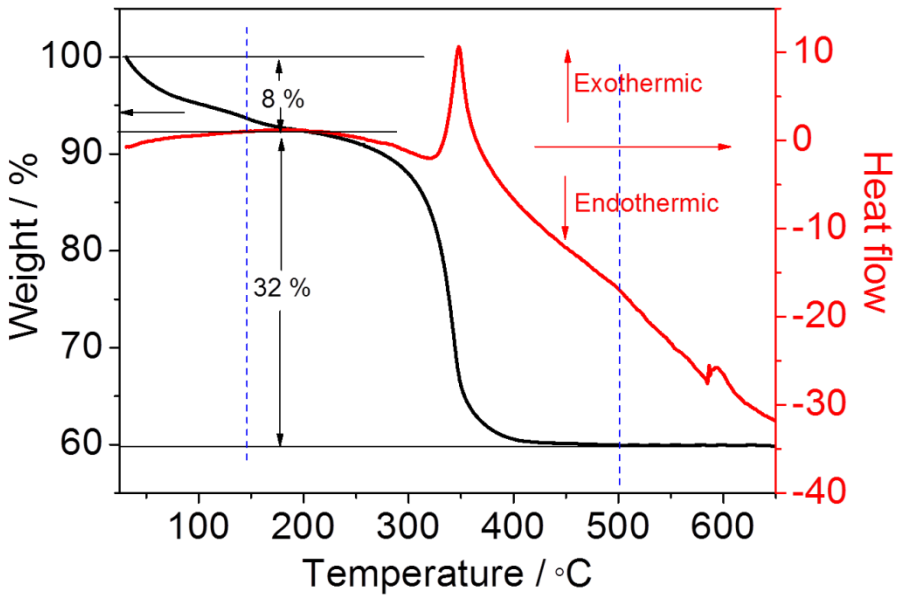

Figure 5.8 Thermogravimetric analysis and differential scanning calorimetry curves of the dried precipitate prepared via hydrothermal reaction of a solution containing 1.0 mL TB and 25 mL AA at 150 ˚C for 12 h.

differential scanning calorimetry curve, centered at 350 ºC, corresponds to the crystallization of the amorphous residue into crystalline anatase TiO_2.

The proposed formation process of the MASCs is as follows. Initially, chain bundles are formed through the acidolysis of TB catalysed by AA, under the direction of π-π interactions. These nascent nanochains, surrounded by hydrophobic groups, are drawn together through interactions mediated by esters and assembled into regular repeating structures. Finally, calcination at 500 ºC for 3 h results in the formation of MASCs, as shown in Figure 1(c-f). Based on these observations it can be postulated that the esters act as a de facto template during the formation of MASCs.

5.3.3 Electrochemical Properties of MASCs

Here, the MASCs were deposited on F: SnO_2 glass (with the SEM cross-sectional image shown in Figure 5.9) and used to fabricate DSCs (sensitized with an

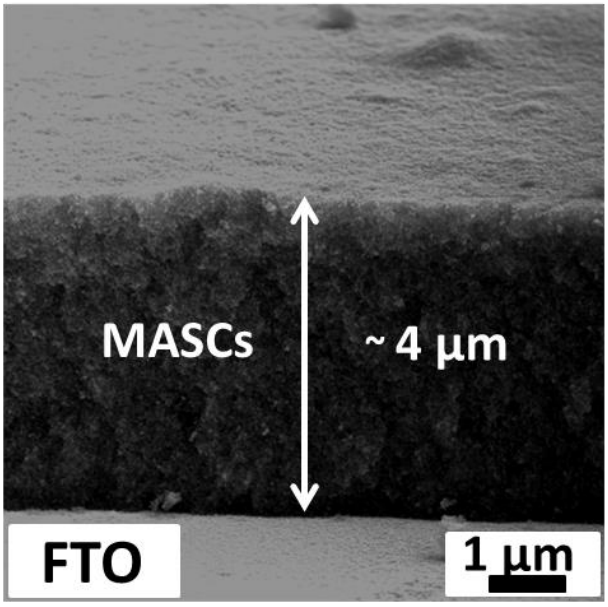

Figure 5.9 SEM cross-sectional image of the mesoporous anatase single crystals (MASCs) film on the fluorine-doped tin oxide (FTO).

.

organic dye, MK-2, and employing a $Co^{(2+/3+)}$ redox mediator). Analogous devices were created using commercial TiO_2 paste [18NR-T, denoted as Dyesol, obtained from Dyesol (Australia)] and their performances were compared at the same 4.0 ± 0.2 µm thickness where the performance of the Dyesol paste was the highest.

Table 5.1 summarizes the photovoltaic characteristics of these devices under 100 mW cm^{-2} simulated AM 1.5 illumination. A DSC employing MASCs gave a photocurrent density (J_{sc}) of 14.5 mA cm^{-2} and an open-circuit potential (V_{oc}) of 855 mV, yielding an average power conversion efficiency (η) of 8.3 %, while a DSC made using Dyesol paste displayed around 6.3 % conversion efficiency [Figure 5.10(a)].

The main difference between MASC-based and Dyesol-based DSCs is the higher fill factor (*FF*, 67.0 % compared to 54.0 %). The champion device among the MASC DSCs could reach 8.7 % conversion efficiency, and the photovoltaic data are presented in Figure 5.11.

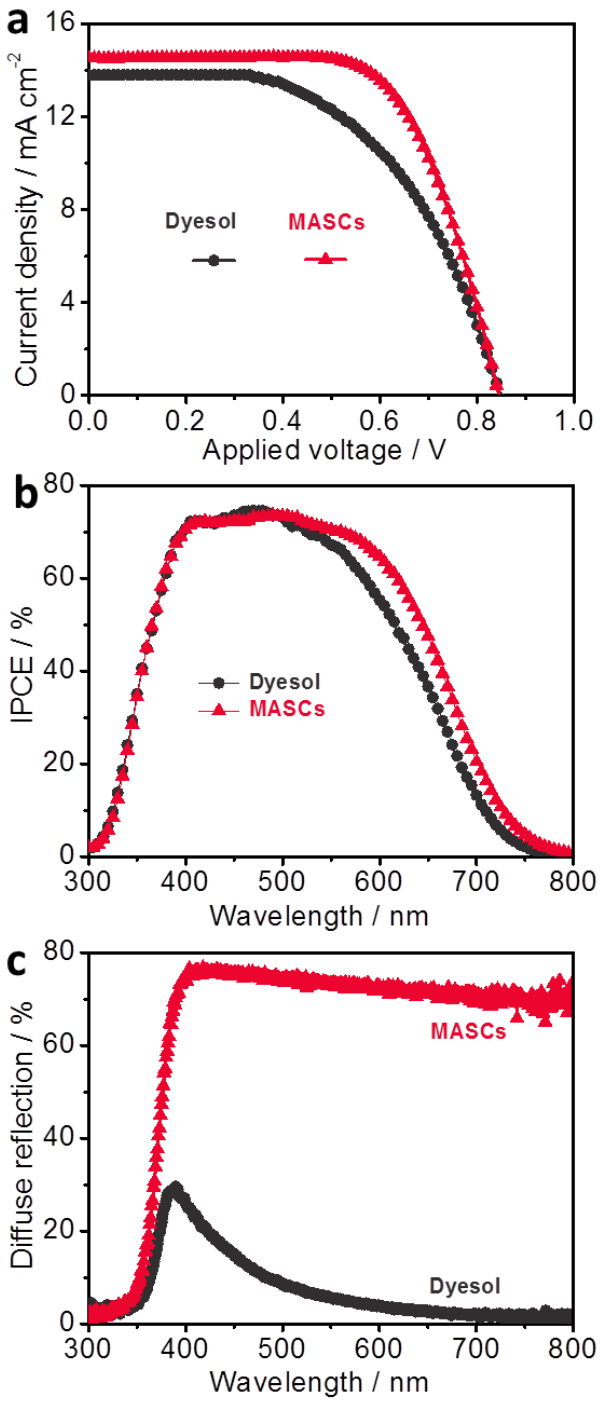

Figure 5.10 a) *J-V* characteristics of Dyesol- and MASC-based DSCs (4.0 ± 0.2 µm thick TiO_2 films, sensitized with MK-2, utilizing a $Co^{(2+/3+)}$ based electrolyte and Pt counter electrode); b) incident photon to current conversion efficiency (IPCE) response of Dyesol- and MASC-based DSCs; c) diffuse reflectance spectra of Dyesol and MASC films.

Table 5.1 Detailed photovoltaic parameters of cells based on Dyesol and MASC photoanodes, measured under air mass (AM) 1.5 global (1.5G) one sun illumination (100 mW cm^{-2}). The active areas were ~ 0.16 cm^2 for all of the cells (with the mask area 0.25 cm^2), [42] the thickness[a)] was 4.0 ± 0.2 μm, and the data presented were the average values obtained after testing four devices and the standard deviation thereof.

Samples	J_{sc} [mA cm^{-2}]	V_{oc} [V]	*FF* [%]	η [%]	Specific Surface Area [m^2 g^{-1}]	Porosity[b)] (%)	Amount of dye[c)] [10^{-7} mol cm^{-2}]
Dyesol	13.8 ± 0.3	0.850 ± 0.02	54.0 ± 3	6.3 ± 0.3	74.0	64.2	7.5
MASCs	14.5 ± 0.5	0.855 ± 0.02	67.0 ± 3	8.3 ± 0.4	50.1	58.0	6.1

[a)] Measurements of film thickness were carried out on a surface profile system (Veeco Dektak 150);

[b)] The porosities (*P*) of Dyesol and MASCs were calculated according to: $P=V_p/(\rho^{-1} + V_p)$, where V_p is the specific cumulative pore volume (cm^3 g^{-1}) and ρ^{-1} is the inverse of the density of anatase TiO_2 (ρ^{-1} = 0.257 cm^3 g^{-1}). [32]

[c)] 0.1 M NaOH solution in mixed toluene and ethanol (1:1) solvent was employed as the desorbent. The amount of desorbed dye was quantified by measuring its optical absorption against known concentrations.

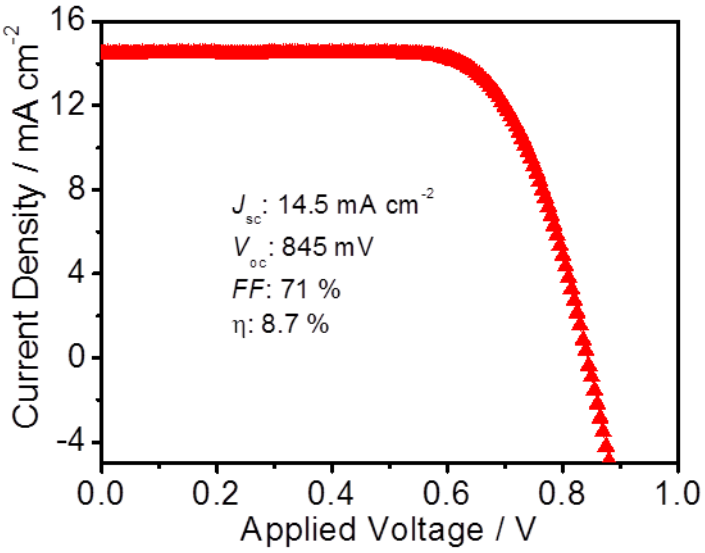

Figure 5.11 *J-V* characteristics of champion device among the MASC-based DSCs.

In addition, devices were constructed using Ruthenium dye N719 as a sensitizer and an I_3^-/I^- based electrolyte. For film thicknesses of 12 µm, an efficiency of 7.8 % was attained when MASCs were employed, higher than the 6.4 % attained from using the commercial Dyesol paste (Table 5.2).

Figure 5.10(b) shows the incident photon-to-current conversion efficiency (IPCE) spectra of both Dyesol- and MASC-based DSCs, which show high values, that is, 60-75 % in the 400 to 600 nm wavelength range. The enhancement in IPCE for the MASC-based device is the most marked for $\lambda > 550$ nm (Figure 5.12), as light scattering generally serves to improve light harvesting efficiency (LHE) at weakly absorbed wavelengths. The increased IPCE for wavelength greater than 550 nm is because of the increased light harvesting efficiency of the MASCs due to increased scattering. Because at the absorption peak of the MK-2–sensitized films around 500 nm, almost all photons are absorbed by both films and any increase in film thickness or scattering has a negligible effect the light harvesting efficiency (and hence IPCE).

Table 5.2 Detailed photovoltaic parameters of cells based on Dyesol and MASCs photoanodes measured under different illumination intensities. J_{sc}: short-circuit photocurrent density; V_{oc}: open-circuit photovoltage; *FF*: fill factor; η: total power conversion efficiency. The active areas were ~ 0.16 cm^2 for all of the cells (with the mask area 0.25 cm^2), the thickness[a] is 12 ± 0.5 μm, and the data presented are average values obtained after testing four cells and the standard deviation thereof.

Samples	J_{sc} ($mA\ cm^{-2}$)	V_{oc} (V)	*FF* (%)	η (%)
Dyesol	11.3	0.805	70.3	6.4
	± 0.5	± 0.02	± 2	± 0.2
MASCs	12.4	0.830	75.8	7.8
	± 0.5	± 0.02	± 2	± 0.2

[a] Measurements of film thickness were carried out on a surface profile system (Veeco Dektak 150).

This is not the case at wavelengths longer than 550 nm, where the molar extinction coefficient of MK-2 is lower; hence increased scattering contributes more significantly to increased light harvesting efficiency for the MASCs.

IPCE is measured at short circuit condition where recombination is generally less prevalent. At the maximum power point, improved transport properties of MASCs is proposed to lead to a better electrochemical performance indicated by the improved fill factor FF. Compared to Dyesol-based device, approximately 20 % lower dye loading but higher IPCE showed strong light harvesting capability of MASCs material. Figure 5.10(c) shows the diffuse reflectance spectra of the two films. The light scattering properties of MASCs were compared to those of a commercially available

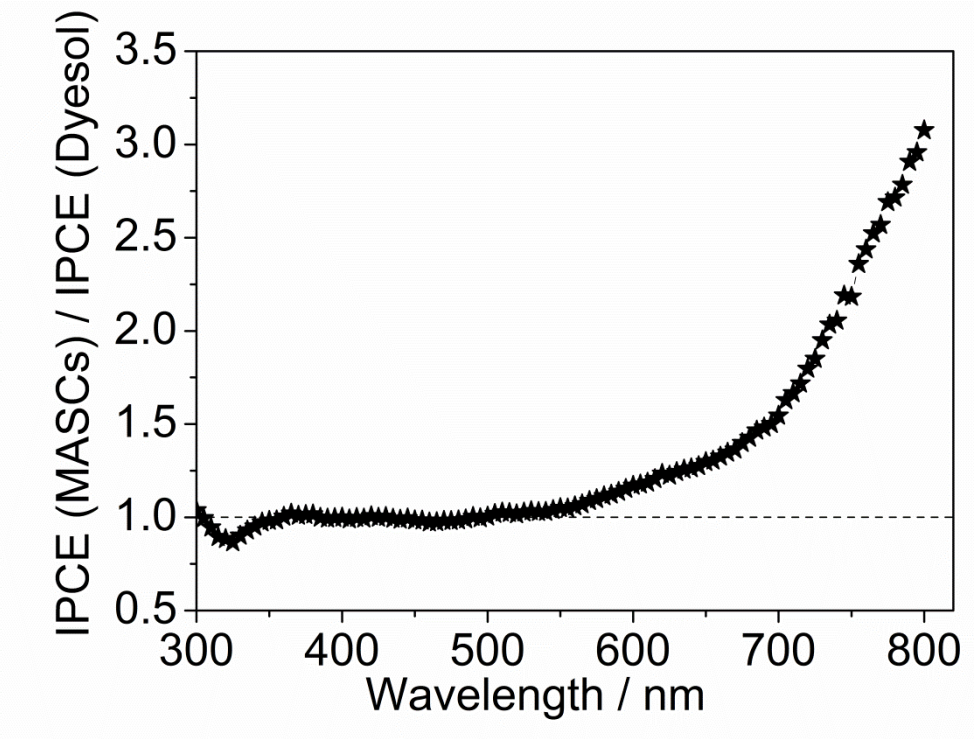

Figure 5.12 Ratio of IPCE value of MASCs to that of Dyesol, depending on the wavelength of the incident light.

reflective TiO_2 paste [WER2-O, denoted as Reflector, obtained from Dyesol (Australia)], and the IPCE curves, diffuse reflectance, and photovoltaic properties are shown in Figure 5.13 and Table 5.3. The MASCs showed even better scattering ability than the Reflector. As an additional experiment, the photovoltaic properties of Dyesol + Reflector are shown in Table 5.3. From this, it can be found that the overall energy conversion efficiency (η) of Dyesol + Reflector is similar to that of Dyesol but much lower than that of MASCs.

The light scattering properties of MASCs were compared to those of a commercially available reflective TiO_2 paste [WER2-O, denoted as Reflector, obtained from Dyesol (Australia)]. Reflector has been used by a number of groups around the world in order to produce high efficiency devices.

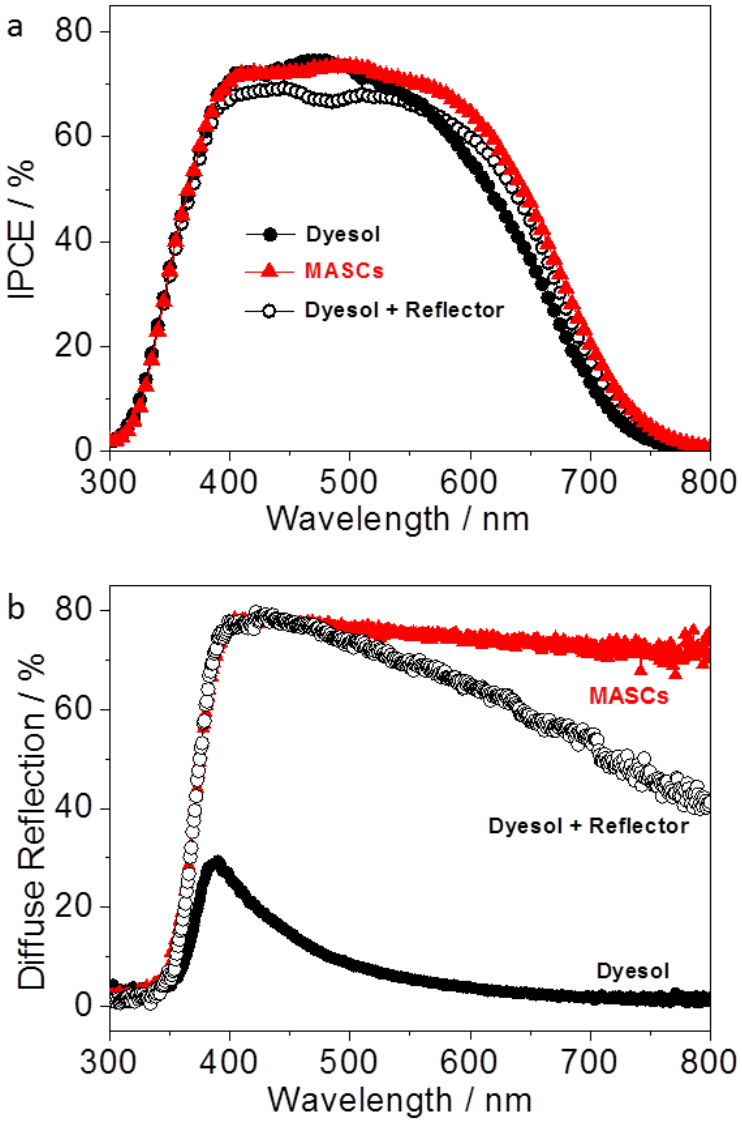

Figure 5.13 a) IPCE curves of Dyesol (~ 4 µm)-, MASC (~ 4 µm)-, and Dyesol (~ 2 µm) + Reflector (~ 2 µm)-based DSCs; b) diffuse reflectance spectra of Dyesol (~ 4 µm), MASC (~ 4 µm), and Dyesol (~ 2 µm) + Reflector (~ 2 µm) films.

Reflector (~ 2 µm) was applied on top of a ~ 2 µm thick layer of Dyesol (denoted as Dyesol + Reflector), and the diffuse reflectance spectra of Dyesol (~ 4 µm), MASC (~ 4 µm), and Dyesol (~ 2 µm) / Reflector (~ 2 µm) films are shown in Figure 5.13.

Table 5.3 Detailed photovoltaic parameters of cells based on Dyesol, MASC, and Dyesol + Reflector photoanodes, measured under air mass (AM) 1.5 global (1.5G) one sun illumination (100 mW cm^{-2}). The active areas were ~ 0.16 cm^2 for all of the cells (with the mask area 0.25 cm^2), the thickness was 4.0 ± 0.2 µm. The data was obtained after 15 h, after SLIM-PCV measurements.

Samples	J_{sc} (mA cm^{-2})	V_{oc} (mV)	*FF* (%)	η (%)
Dyesol	13.8	850	54.0	6.3
MASCs	14.5	855	67.0	8.3
Dyesol + Reflector	12.1	795	70.5	6.8

It can be seen from Figure 5.13(a) that both the MASC and the Dyesol + Reflector films result in a clearly broader IPCE response than for Dyesol alone, with the MASC film giving a higher response across the spectral range between 370 nm and 650 nm. Compared to the MASC film, the diffuse reflectivity is observed to be lower for the Dyesol + Reflector film for wavelengths from 450 nm to 800 nm. It is worth noting that the MASC film scattered the light (from 500 nm to 800 nm, in the region where diffuse reflectivity is most critical) more effectively, which gave it a higher probability of being absorbed. Films produced from the MASCs show superior diffuse reflection capabilities for longer wavelengths (500-800 nm) due to the larger particle size, which is comparable to the wavelength of the incident light in question.

Table 5.4 Detailed photovoltaic parameters of cells based on Dyesol and MASC photoanodes measured under air mass (AM) 1.5 global (1.5G) one sun illumination (100 mW cm^{-2}). The active areas were ~ 0.16 cm^2 for all of the cells (with the mask area 0.25 cm^2).

Samples	J_{sc} (mA cm^{-2})	V_{oc} (mV)	*FF* (%)	η (%)
Dyesol-1	13.8	850	54.0	6.3
Dyesol-2	13.8	850	51.0	6.0
MASCs-1	14.5	855	67.0	8.2
MASCs-2	14.4	856	64.0	7.9

In order to better understand the differences in the charge transport properties and how they affect device performance, devices utilizing both TiO_2 materials were characterized using stepped light-induced transient measurements of photocurrent and photovoltage (SLIM-PCV) (with the detailed photovoltaic parameters for these devices shown in Table 5.4). [37] Figure 5.14(a) shows a log-log plot of electron lifetime versus J_{sc}, showing that the MASC-based devices display slightly lower electron lifetimes compared to that of the Dyesol-based devices at the same J_{sc}. Figure 5.14(b) shows similar electron lifetimes when plotted versus log (electron density), which was obtained by a charge extraction measurement. Note that the electron density calculation used here takes into account the porosity of the films (0.64 for Dyesol and 0.58 for MASCs) in estimating the volume of the TiO_2 films.

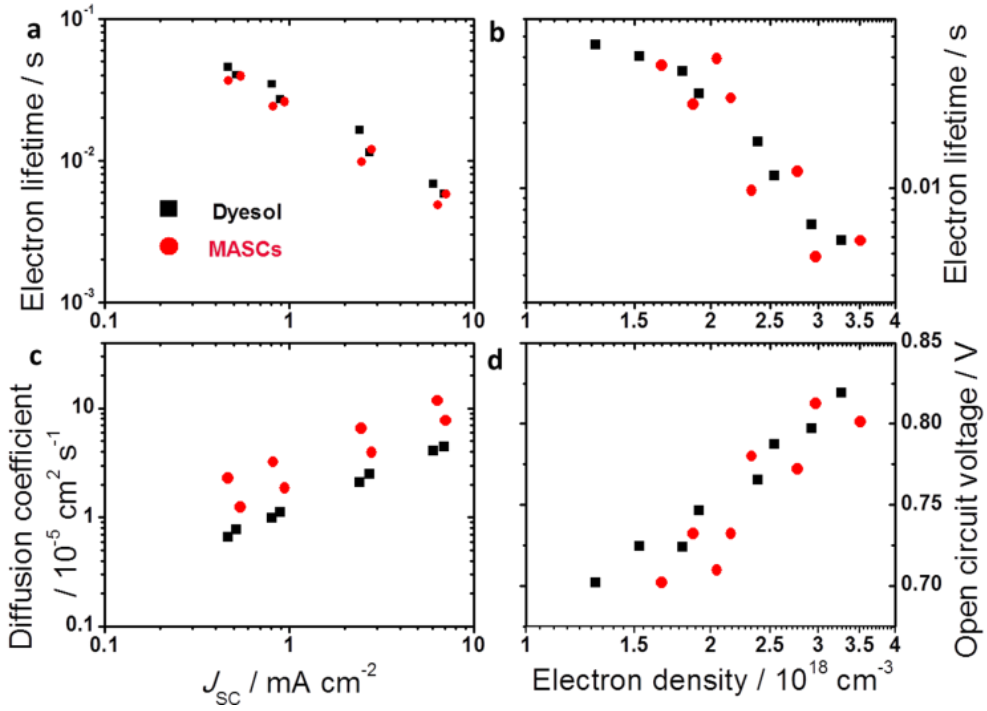

Figure 5.14 Electron lifetime versus a) short circuit current density (J_{sc}) and b) electron density (ED); c) diffusion coefficient versus J_{sc}; and d) open circuit voltage (V_{oc}) versus ED for the devices fabricated with MK-2 dye containing Dyesol or MASCs (two devices for each dye).

ED = ED (bulk)/ porosity.

Figure 5.14(d) shows plots of V_{oc} vs. log (electron density), with similar slopes and y-axis intercepts for both devices. The latter indicates that the conduction band edge potentials (E_{CB}) of these two materials, as well as the electron trap state distributions, are quite similar. [38] The similar electron lifetimes and E_{CB}s of MASC- and Dyesol-based devices lead to similar values of V_{oc} for the two materials (as seen in Figure 5.10 and Table 5.1), despite the slightly higher J_{sc} of the former.

The mainly noticeable difference is observed in Figure 5.14(c). The diffusion coefficient (D) is twice as high in MASC-based devices as in Dyesol-based devices at the same J_{sc}. [39-41] This may be attributed to the single crystalline nature of the MASCs with fewer defects. Charge transport, however, is likely to be limited by

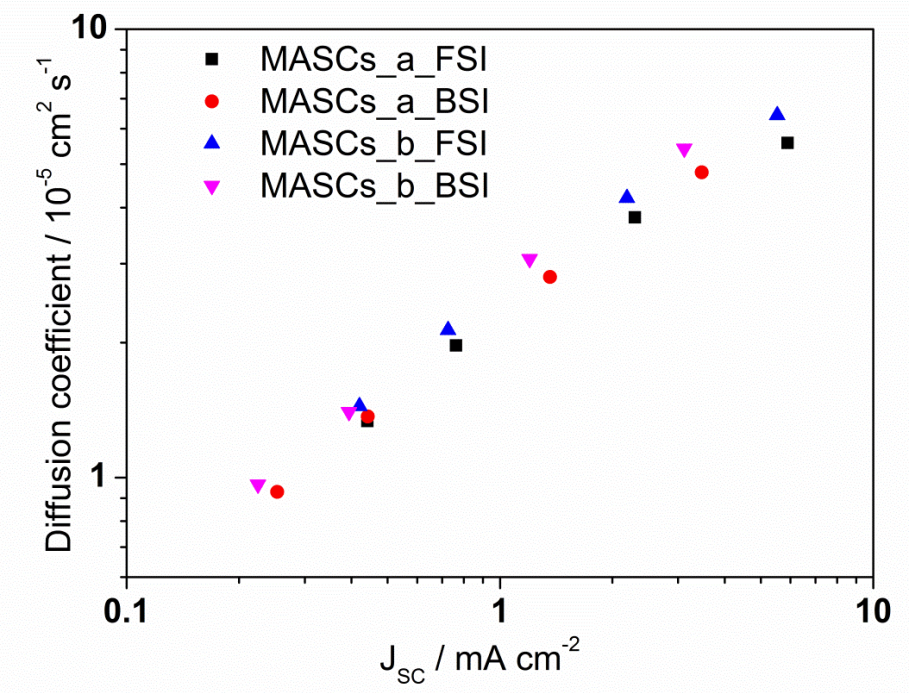

Figure 5.15 Diffusion coefficient versus short circuit current density (J_{sc}) of the devices fabricated with MK-2 dye using MASCs, with both front side illumination (FSI) and back side illumination (BSI). (a and b indicate two different devices.)

interparticle electron transfer between the particles in both films, with the former having fewer grain boundaries due to larger size. The faster electron transport and similar electron lifetime could cause longer electron diffusion lengths and higher *FF*.

Front and back side illumination (FSI/BSI) SLIM-PCV experiments (Figure 5.15) were performed showing similar diffusion coefficients for front and back illumination. This indicates that the difference in measured *D* is not due to the non-uniform charge generation that may arise from stronger light scattering effects in MASC-based DSCs. The J_{sc} decay during diffusion coefficient measurements would be faster than for the non-scattering Dyesol paste, leading to higher *D* values, as shorter time constants would be obtained by simulating with a single exponential equation. (Note that $L^2 = 2.77 \times D \times \tau$, where *L* is the thickness of the TiO_2 film and τ is the time constant from

Table 5.5 Detailed photovoltaic parameters of cells based on Dyesol photoanodes measured under different illumination intensities. J_{sc}: short-circuit photocurrent density; V_{oc}: open-circuit photovoltage; *FF*: fill factor; η: total power conversion efficiency. The active areas were ~ 0.16 cm^2 for all of the cells (with the mask area 0.25 cm^2); the thickness was 16 ± 0.5 μm.

Light intensity (%)	J_{sc} (mA cm^{-2})	V_{oc} (V)	*FF* (%)	η (%)
100	9.65	0.696	46.0	3.09
58.4	6.71	0.681	63.7	4.98
37.8	4.53	0.665	69.7	5.56
12.8	1.62	0.624	76.5	6.02
2.5	0.32	0.567	77.9	5.72

the exponential equation.) To confirm this possibility, we measured the diffusion coefficients of MASCs with both front side illumination (FSI) and back side illumination (BSI), as shown in Figure 5.15. Similar values of *D* were obtained at matched J_{sc}, indicating uniform light harvesting throughout the ~ 4 μm MASC films.

Thick TiO_2 films (~17 μm) were also fabricated. As shown in Tables 5.5 and 5.6, MASC-based devices showed much higher J_{sc} and *FF* at full 100 mW cm^{-2} light intensity (and a weaker dependence on light intensity) compared to the Dyesol-based DSCs, suggesting longer electron diffusion length in the MASC-based devices.

Table 5.6 Detailed photovoltaic parameters of cells based on MASC photoanodes measured under different illumination intensities. J_{sc}: short-circuit photocurrent density; V_{oc}: open-circuit photovoltage; *FF*: fill factor; η: total power conversion efficiency. The active areas were ~ 0.16 cm^2 for all of the cells (with the mask area 0.25 cm^2); the thickness was 17 ± 0.5 μm.

Light intensity (%)	J_{sc} (mA cm^{-2})	V_{oc} (V)	*FF* (%)	η (%)
100	14.0	0.743	55.5	5.76
58.4	9.15	0.727	64.3	7.33
37.8	6.08	0.712	71.1	8.12
12.8	2.1	0.670	76.9	8.44
2.5	0.4	0.603	78.8	7.48

5.4 Conclusions

In summary, mesoporous anatase single crystals (MASCs) with unique polyhedral pores were successfully prepared by a facile one-step hydrothermal route for the first time, without additives or templates. A detailed mechanism is proposed for the formation of the MASCs. Photoanodes containing MASCs were sensitised with the organic dye MK-2 and employed in DSCs with a cobalt redox shuttle, displaying photon-to-electron conversion efficiencies up to an impressive 8.7 %. The enhanced performance is attributed to high light harvesting efficiency, as well as good electronic connectivity throughout the single crystal structure.

This work provide a reliable platform for the design of mesoporous architectures and open up a new avenue for large-scale synthesis of functional mesoporous single crystals with various compositions that are likely to be highly useful in energy applications.

5.5 References

1. B. O'regan, and M. Grätzel, *Nature*, 1991, **353**, 737-740.
2. B. Weintraub, Y. Wei, and Z. L. Wang, *Angew. Chem., Int. Ed.*, 2009, **48**, 1-6.
3. Y. Wei, C. Xu, S. Xu, C. Li, W. Wu, and Z. L. Wang, *Nano Lett.*, 2010, **10**, 2092-2096.
4. A. Hagfeldt, G. Boschloo, L. Sun, L. Kloo, and H. Pettersson, *Chem. Rev.*, 2010, **110**, 6595-6663.
5. W. Guo, C. Xu, G. Zhu, C. Pan, C. Lin, and Z. L. Wang, *Nano Energy*, 2012, **1**, 176-182.
6. W. Guo, X. Xue, S. Wang, C. Lin, and Z. L. Wang, *Nano Lett.*, 2012, **12**, 2520-2523.
7. W. Guo, C. Xu, X. Wang, S. Wang, C. Pan, C. Lin, and Z. L. Wang, *J. Am. Chem. Soc.*, 2012, **134**, 4437-4441.
8. L. Li, T. Zhai, Y. Bando, and D. Golberg, *Nano Energy*, 2012, **1**, 91-106.
9. H. C. Weerasinghe, F. Huang, and Y. B. Cheng, *Nano Energy*, 2013, **2**, 174-189.
10. D. Y. Kim, S. Lee, Z. H. Lin, K. H. Choi, S. G. Doo, H. Chang, J. Y. Leem, Z. L. Wang, and S. O. Kim, *Nano Energy*, 2014, **9**, 101-111.
11. S. G. Hashmi, M. Ozkan, J. Halme, J. Paltakari, and P. D. Lund, *Nano Energy*, 2014, **9**, 212-220.
12. A. B. Martinson, T. W. Hamann, M. J. Pellin, and J. T. Hupp, *Chem. Euro. J.*, 2008, **14**, 4458-4467.
13. A. Yella, H.-W. Lee, H. N. Tsao, C. Yi, A. K. Chandiran, M. K. Nazeeruddin, E. W.-G. Diau, C.-Y. Yeh, S. M. Zakeeruddin, and M. Grätzel, *Science*, 2011, **334**, 629-634.
14. S. Mathew, A. Yella, P. Gao, R. Humphry-Baker, B. F. Curchod, N. Ashari-

Astani, I. Tavernelli, U. Rothlisberger, M. K. Nazeeruddin, and M. Grätzel, *Nat. Chem.*, 2014, **6**, 242-247.

15. L. E. Polander, A. Yella, B. F. Curchod, N. Ashari Astani, J. Teuscher, R. Scopelliti, P. Gao, S. Mathew, J. E. Moser, and I. Tavernelli, *Angew. Chem., Int. Ed.*, 2013, **52**, 8731-8735.
16. P. J. Cameron, L. M. Peter, S. M. Zakeeruddin, and M. Grätzel, *Coor. Chem. Rev.*, 2004, **248**, 1447-1453.
17. H. Nusbaumer, S. M. Zakeeruddin, J. E. Moser, and M. Grätzel, *Chem. Euro. J.*, 2003, **9**, 3756-3763.
18. D. Kuang, S. Ito, B. Wenger, C. Klein, J.-E. Moser, R. Humphry-Baker, S. M. Zakeeruddin, and M. Grätzel, *J. Am. Chem. Soc.*, 2006, **128**, 4146-4154.
19. Y. Bai, J. Zhang, D. Zhou, Y. Wang, M. Zhang, and P. Wang, *J. Am. Chem. Soc.*, 2011, **133**, 11442-11445.
20. H.-S. Kim, S.-B. Ko, I.-H. Jang, and N.-G. Park, *Chem. Commun.*, 2011, **47**, 12637-12639.
21. P. Yang, D. Zhao, D. I. Margolese, B. F. Chmelka, and G. D. Stucky, *Nature*, 1998, **396**, 152-155.
22. C. K. Tsung, J. Fan, N. Zheng, Q. Shi, A. J. Forman, J. Wang, and G. D. Stucky, *Angew. Chem., Int. Ed.*, 2008, **47**, 8682-8686.
23. Y. Deng, J. Wei, Z. Sun, and D. Zhao, *Chem. Soc. Rev.*, 2013, **42**, 4054-4070.
24. B. P. Bastakoti, S. Ishihara, S. Y. Leo, K. Ariga, K. C. W. Wu, and Y. Yamauchi, *Langmuir*, 2014, **30**, 651-659.
25. W. Yue, X. Xu, J. T. S. Irvine, P. S. Attidekou, C. Liu, H. He, D. Zhao, and W. Zhou, *Chem. Mater.*, 2009, **21**, 2540-2546.
26. K. E. Shopsowitz, A. Stahl, W. Y. Hamad, and M. J. MacLachlan, *Angew. Chem.*

Int. Ed., 2012, **51**, 6886-6890.

27. R. Zhang , A. A. Elzatahry, S. S. Al-Deyab, and D. Zhao, *Nano Today*, 2012, **7**, 344-366.
28. E. J. W. Crossland, N. Noel, V. Sivaram, T. Leijtens, J. A. Alexander-Webber, and H. J. Snaith, *Nature*, 2013, **495**, 215-219.
29. D. Chen, F. Huang, Y. B. Cheng, and R. A. Caruso, *Adv. Mater.*, 2009, 21, 2206-2210.
30. J. M. Szeifert, D. Fattakhova-Rohlfing, D. Georgiadou, V. Kalousek, J. Rathouský, D. Kuang, S. Wenger, S. M. Zakeeruddin, M. Grätzel, and T. Bein, *Chem. Mater.*, 2009, **21**, 1260-1265.
31. T. Brezesinski, J. Wang, J. Polleux, B. Dunn, and S. H. Tolbert, *J. Am. Chem. Soc.*, 2009, **131**, 1802-1809.
32. J. Lin, A. Nattestad, H. Yu, Y. Bai, L. Wang, S. X. Dou, and J. H. Kim, *J. Mater. Chem. A*, 2014, **2**, 8902-8909.
33. L. Li, and C. Liu, *CrystEngComm*, 2010, **12**, 2073-2078.
34. S. Doeuff, M. Henry, C. Sanchez, and J. Livage, *J. Non-Crystalline Solids*, 1987, **89**, 206-216.
35. A. Verma, and S. Agnihotry, *Electrochim. Acta*, 2007, **52**, 2701-2709.
36. J. Ye, W. Liu, J. Cai, S. Chen, X. Zhao, H. Zhou, and L. Qi, *J. Am. Chem. Soc.*, 2010, **133**, 933-940.
37. P. R. F. Barnes, K. Miettunen, X. Li, A. Y. Anderson, T. Bessho, M. Gratzel, and B. O'Regan, *Adv. Mater.*, 2013, **25**, 1881-1922.
38. A. J. Mozer, P. Wagner, D. L. Officer, G. G. Wallace, W. M. Campbell, M. Miyashita, K. Sunahara, and S. Mori, *Chem. Commun.*, 2008, **39**, 4741-4743.
39. P. Wang, S. M. Zakeeruddin, I. Exnar, and M. Grätzel, *Chem. Commun.*, 2002,

24, 2972-2973.

40. F. Cao, G. Oskam, G. J. Meyer, and P. C. Searson, *J. Phys. Chem.*, 1996, **100**, 17021-17027.

41. K. D. Benkstein, N. Kopidakis, J. van de. Lagemaat, and A. J. Frank, *J. Phys. Chem. B*, 2003,**107**, 7759-7767.

42. S. Ito, M. K. Nazeeruddin, P. Liska, P. Comte, R. Charvet, P. Pećhy, M. Jirousek, A. Kay, S. M. Zakeeruddin, and M. Grätzel, *Prog. Photovolt: Res. Appl.*, 2006, **14**, 589-601.

6 3D HIERARCHICAL RUTILE TiO_2 AND METAL-FREE ORGANIC SENSITIZER PRODUCING DYE-SENSITIZED SOLAR CELLS 8.6 % CONVERSION EFFICIENCY

This chapter combined 3D hierarchical rutile TiO_2 architecture and metal-free organic sensitizer (D149) for rutile TiO_2-based DSCs, and achieved 8.6 % conversion efficiency.

Rutile is often ignored in DSCs, possibly due to the expectation that it would result in devices having lower open-circuit voltage (V_{oc}) than anatase because rutile has a more positive conduction band edge potential. Slow electron transport is also often seen as a detracting feature of rutile TiO_2, this, however, may lead to higher electron densities within the conduction band, subsequently increasing the quasi Fermi-level, and mitigating the concern about conduction band edge potential. Indeed, studies show that rutile TiO_2 can achieve a similar or even higher V_{oc} through doping. Furthermore, compared to anatase, the rutile polymorph exhibits some superior physical properties, such as enhanced light-scattering properties on account of its higher refractive index, which is beneficial from the perspective of effective light harvesting. Rutile TiO_2 is also chemically more stable and potentially cheaper to produce than anatase.

The majority of DSCs use Ru-based complexes (e.g., N3, N719, and black dye), as sensitizers of TiO_2, offering a high solar-to-electric conversion efficiency and good stability. The cost of the Ru-based sensitizers, however, is high and their synthesis and purification are complicated. Indoline-based dyes, such as D149 are promising all-organic alternatives. Furthermore, D149 has peak extinction co-efficient of 68700 M^{-1} cm^{-1} at 540 nm, significantly higher than 13900 M^{-1} cm^{-1} at 535 nm for N719. In

addition, it has been reported that rutile TiO_2 has a tendency for low dye loading, even on relatively high surface area materials, compared to anatase. The use of high extinction dye should help to overcome this constraint, allowing for comparable light harvesting.

In this chapter, we report a new series of 3D hierarchical rutile TiO_2 architectures (HRT) with controlled morphologies and sized subunits by the aid of a facile acid-hydrothermal method, without any surfactant or template. We report a solar-to-electric conversion efficiency of 5.5 %, achieved using a HRT as the photoelectrode with D149 dye, which is significantly better than devices made using P25 (4.5 %) and comparable to state-of-the-art commercial transparent titania anatase paste (5.8 %). This power conversion efficiency is due to a considerable surface area for the high dye adsorption and a superior light scattering ability. In addition, the overall conversion efficiency 8.6 % was achieved when HRT was further used as the light scattering layer, a considerable improvement over commercial transparent/reflective titania anatase paste (7.6 %).

This chapter has been published in *Scientific Reports*, 2014, **4**, 5769.

6.1 Introduction

The design and growth of inorganic nanostructures with well-controlled sizes and morphologies have been the focus of intensive research in recent years due to their wide ranging applications. TiO_2 is a functional material used in many ways, such as in photocatalysis, photoelectrochemical solar energy conversion, and Li-ion batteries. [1, 2] The properties and applications of TiO_2 are generally correlated to crystalline phase, dimensions, morphology, and surface properties. As such, rationally designed and controlled nanostructured TiO_2 has attracted great interest. [3, 4] Various TiO_2 nanostructures in the forms of spheres, tubes, wires, rods, sheets, belts, flowers, and trees have been reported. [5-12] Three-dimensional (3D) hierarchical structures are of particular interest as many of these architectures have distinctive physicochemical properties in comparison with simple nanocrystallites. [13, 14] When employed as the photoanode in a Dye-sensitized Solar Cell (DSC), hierarchical architectures can offer larger surface areas for dye adsorption while simultaneously enhancing light scattering for efficient photon harvesting, and thereby, improving power conversion efficiency. [15-18] Chemical vapor deposition, applications of templates, catalysts and electrochemical methods are known to be used for the direct growth of inorganic material with controlled morphologies and architectures, [19-24] however, in most cases, the mechanisms involved in the formation of these hierarchical structures are complicated and not well-understood.

Crystalline TiO_2 mainly exists in three polymorphs: anatase (tetragonal), rutile (tetragonal) and brookite (orthorhombic).The majority of research has been carried out on anatase. Rutile is often ignored in DSCs, possibly due to the expectation that it would result in a lower open-circuit voltage (V_{oc}) than anatase because rutile has a more positive conduction band edge potential. [4, 25] Slow electron transport is also

often seen as a detracting feature of rutile TiO_2, this, however, may lead to higher electron densities within the conduction band, subsequently increasing the quasi Fermi-level, and mitigating the aftermentioned concern about conduction band edge potential. Indeed, studies show that rutile TiO_2 can achieve a similar or even higher V_{oc} through doping. [26, 27] Furthermore, compared to anatase, the rutile polymorph exhibits some superior physical properties, such as enhanced light-scattering properties on account of its higher refractive index, which is beneficial from the perspective of effective light harvesting. [28] Rutile TiO_2 is also chemically more stable and potentially cheaper to produce than anatase. [26] These findings suggest that additional research on rutile TiO_2 from the perspective of solar energy conversion would be fundamentally interesting.

The majority of DSCs use Ru-based complexes (e.g., N3, N719, and black dye), as sensitizers of TiO_2, offering a high solar-to-electric conversion efficiency and good stability. [29-32] The cost of the Ru-based sensitizers, however, is high and their synthesis and purification are complicated. Indoline-based dyes, such as D149 are promising all-organic alternatives. [33] Gratzel and co-workers have produced devices based on D149, which have displayed power conversion efficiency of up to 9 %. [34] Furthermore, D149 has a peak extinction co-efficient of 68700 M^{-1} cm^{-1} at 540 nm, significantly higher than 13900 M^{-1} cm^{-1} at 535 nm for N719. [35] In addition, it has been reported that rutile TiO_2 has a tendency for low dye loading, even on relatively high surface area materials, compared to anatase. [26, 28] The use of high extinction dye should help to overcome this constraint, allowing for comparable light harvesting.

In the present paper, we report a new series of 3D hierarchical rutile TiO_2 architectures (HRT) with controlled morphologies and sized subunits by the aid of a

facile acid-hydrothermal method, without any surfactant or template. We demonstrate that the hydrochloric acid (HCl) concentration plays an important role in controlling the hydrolysis rate of tetrabutyl titanate (TT) in the acid-hydrothermal process, which in turn enables us to fine-tune the final properties of rutile TiO_2. Different, well-defined 3D HRT were produced using 1-8 M HCl (denoted as HRT-1 - HRT-8, respectively). Importantly, to the best of our knowledge, this work represents the first observation of ledgewise growth for rutile TiO_2.

Furthermore, we report a solar-to-electric conversion efficiency of 5.5 %, achieved using a HRT as the photoelectrode with D149 dye, which is significantly better than devices made using P25 (4.5 %) and comparable to state-of-the-art commercial Transparent Titania Anatase paste (5.8 %). This power conversion efficiency is due to a considerable surface area for the high dye adsorption and a superior light scattering ability. In addition, the overall conversion efficiency 8.6 % was achieved when HRT was further used as the light scattering layer, a considerable improvement over commercial Transparent / Reflector Titania Anatase paste (7.6 %).

6.2 Experimental

6.2.1 Synthesis of 3D Hierarchical Rutile TiO_2 Architectures (HRT)

Tetrabutyl titanate ($Ti(OCH_2CH_2CH_2CH_3)_4$, 97 %, TT, analytical reagent grade) and hydrochloric acid (37 % HCl, analytical reagent grade) were purchased from Sigma-Aldrich, and used without purification or additives. The typical experimental procedures are described as follows: firstly, 0.5 mL of TT was added dropwise into an amount of concentrated HCl under magnetic stirring. Then, the above solution was diluted by distilled water to meet a total volume of 25.5 mL under different HCl concentrations (1 M-8 M). After vigorously stirring for another 1.5 h and aging for 1 h, the whole mixture was transferred into a 45 mL Teflon-lined stainless steel autoclave and sealed. The hydrothermal synthesis was conducted at 150 $^{\circ}$C for 5 h in an electric oven. After ambient cooling to room temperature, the resultant powder was collected and centrifuged, rinsed with absolute ethanol repeatedly, and finally dried at 110 $^{\circ}$C under vacuum. The powders were named as HRT-1 to HRT-8, respectively, with the number representing the concentration (in M) of HCl used during synthesis.

6.2.2 Materials Characterizations

The crystal phase of the 3D hierarchical TiO_2 architectures were measured with a powder X-ray diffractometer (XRD, MMA, GBC Scientific Equipment LLC, Hampshire, IL, USA) with Cu Kα radiation. The morphology of the samples was examined by Field Emission Scanning Electron Microscopy (FESEM, JSM-7500FA, JEOL, Tokyo, Japan) and High Resolution Transmission Electron Microscopy (HRTEM, JEM-2100F). Brunauer–Emmett–Teller (BET) surface areas (S_{BET}) were determined by using a nitrogen adsorption apparatus (Tristar 3030, Micromeritics Instrument Corporation). All samples were degassed at 120 $^{\circ}$C overnight before measurement. Dye desorption was performed by dipping the sensitized sample into

0.4 M NaOH in methanol solution. Film thickness was measured with a Veeco Dektak 150 Surface Profiler. The light scattering properties of the samples were investigated by ultraviolet (UV)-visible light absorption/diffuse reflectance spectrometry (Shimadzu UV-3600).

6.2.3 Preparation of TiO_2 Photoanodes

To prepare the DSC working electrodes, fluorine doped tin oxide (FTO) glass (2.3 mm thick, 8 Ω/sq, Hartford Glass), used as current collector, was first cleaned with soapy water for 20 min, rinsed with distilled water, immersed in an ultrasonic bath in acetone and then again in ethanol for 30 min each. Following this, a dense TiO_2 blocking layer was deposited on the clean FTO glass by spray pyrolysis of a solution of diluted titanium diisopropoxide bis(acetylacetonate), 75 % in isopropanol (Aldrich, 32525-2), in absolute ethanol in the volume ratio of 1:9. Next, a layer of TiO_2 paste was cast onto the FTO glass plates by the doctor-blade method. These pastes were produced as follows: 0.1 g of TiO_2 powder was ground with a mixture of ethanol (10 mL), distilled water (10 mL), nitric acid (0.167 mL), polyethylene glycol solution (4 mL, 10 wt % in distilled water, MW = 100,000), and triton X-100 (one small drop) to form a slurry, and then the slurry was sonicated for 1 h in an ultrasonic bath and stirred for 2 h. A viscous white TiO_2 paste was finally obtained. After a heating process (at 150 $^{\circ}$C for 10 min, at 325 $^{\circ}$C for 5 min, at 375 $^{\circ}$C for 5 min, at 450 $^{\circ}$C for 30 min, and then at 500 $^{\circ}$C for 15 min) to remove organic components and improve interparticle connectivity, the TiO_2 films were soaked in 0.02 M aqueous titanium tetrachloride solution ($TiCl_4$) at 70 $^{\circ}$C for 30 min, before being sintered again (500 $^{\circ}$C for 30 min). State-of-the-art commercial Transparent Titania Anatase paste (18NR-T, denoted as Dyesol-T), and commercial Reflector Titania Anatase paste

(WER2-O, denoted as Dyesol-S), [both obtained from Dyesol (Australia)] were used for the references.

6.2.4 Fabrication of Dye-Sensitized Solar Cells

The porous TiO_2 films were immersed in a 0.5 mM D149 (1-material, Canada) dye solution in a 1:1 (v/v) mixture of acetonitrile (HPLC, Lab-scan) and *tert*-butanol (LR, Ajax Chemicals) for overnight once their temperature decreased to approximately 110 $^{\circ}$C. The samples were then taken out of the dye bath, washed with acetonitrile, and dried. The working electrode and Pt counter electrode [produced using a pre-drilled piece of 2.3 mm FTO glass, coated with one drop of 10 mM platinic acid solution [H_2PtCl_6 (Sigma)] and heated to 400 $^{\circ}$C for 20 min] were assembled into a sandwich type cell and sealed with a spacer of 25 μm Surlyn (Solaronix). An I^-/I_3^- organic solvent based electrolyte solution [50 mM iodine (Sigma), 0.6 M 1,2-dimethyl-3-propylimidazelium iodide (Solaronix), 0.1 M lithium iodide (Sigma) in methoxypropionitrile (Sigma)] was introduced via vacuum back-filling. The hole was sealed with a piece of aluminium foil-backed Surlyn.

6.2.5 Solar Cell Characterizations

Photocurrent density – voltage (*J*–*V*) curves were measured using a Keithley 2400 sourcemeter, a simulated 100 mW cm^{-2} air mass (AM) 1.5 light source (Oriel), and customized LabView software. The device area was masked with a metallic mask slightly larger than the active area. Incident photon-to-current quantum conversion efficiency (IPCE) was measured using a 300 W Xe lamp, a monocromator with sorting filters, focused to a spot with additional optics. The short circuit current response of the devices was recorded in 5 nm steps using a Keithley 2400

sourcemeter. The measured currents were referenced to a calibrated Si photodiode (PECCELL).

6.3 Results and Discussion

All the prepared samples are of the rutile phase (a = b = 0.45927 nm, c = 0.29544 nm, space group $P4_2/mnm$), as shown by the XRD pattern in Figure 6.1, with all the peaks corresponding well with JCPDS No. 21-1276. No characteristic peaks of impurities such as anatase TiO_2, brookite TiO_2 or $Ti(OH)_4$ were detected and all the observed diffraction peaks suggest that the products are well crystallized. These peaks are essentially invariant with HCl concentration, as all of the morphologies appear to be of the rutile TiO_2 phase, with the Raman spectrum in Figure 6.2 further confirming the formation of rutile crystals. The two Raman active fundamental modes, E_g (~ 438

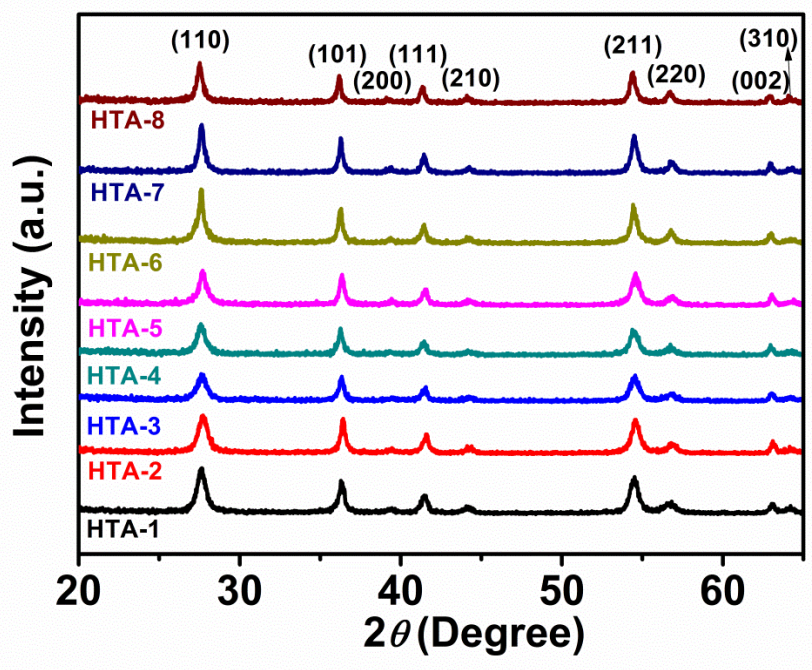

Figure 6.1 XRD patterns of the as-prepared 3D hierarchical rutile TiO_2 architectures (HRT) [denoted as from HRT-1 to HRT-8] from a reaction solution containing 0.5 mL aqueous tetrabutyl titanate (TT) solution with 25 mL X M HCl (X = 1-8).

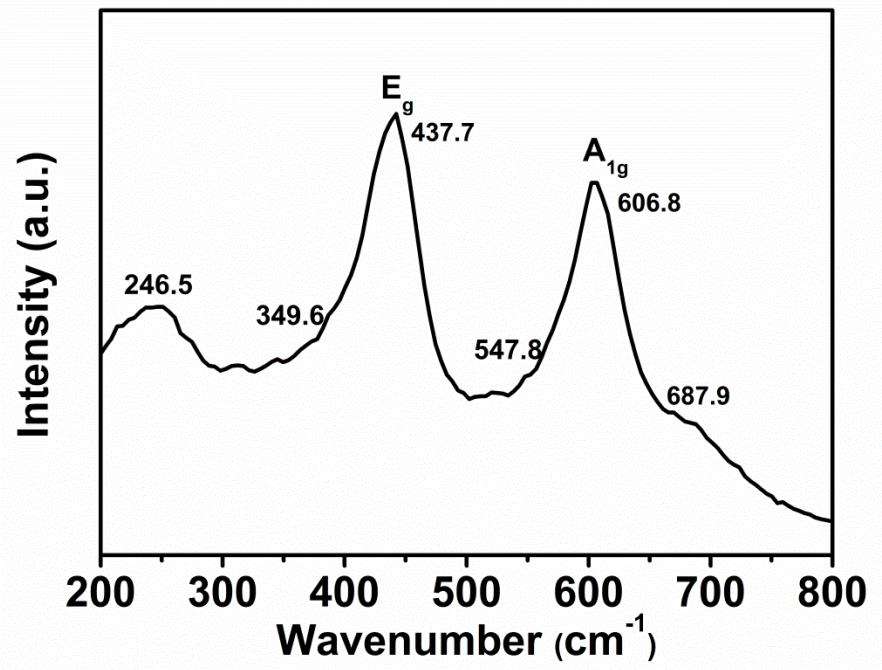

Figure 6.2 A typical Raman spectrum collected from the as-prepared HRT-1 with nanorod constituent units.

cm^{-1}) and A_{1g} (~ 607 cm^{-1}), as well as a second-order phonon as identified by Porto *et al*., (~ 247 cm^{-1}), and the combination of shoulders at 350, 548, and 688 cm^{-1}, which are assigned to rutile TiO_2, can be clearly distinguished. [36]

Figure 6.3 (a-h) shows typical field emission scanning electron microscopy (FESEM) images of HRT samples, synthesized in a tightly sealed 45 mL Teflon-lined autoclave, from a reaction solution containing 0.5 mL precursor aqueous tetrabutyl titanate (TT) solution with 25 mL of 1 M-8 M hydrochloric acid (HCl), at 150 °C for 5 h.

For the lowest HCl concentration, 1 M, HRT-1, uniform, textured microspheres with diameters of ~ 1-1.5 μm are observed in low magnification SEM [Figure 6.4(a)]. It can be seen from higher magnification SEM [Figure 6.3(a)] that the structure is composed of large quantities of elongated crystalline nanorods, which are closely packed and possess square profiles. FESEM of a fractured microsphere of the same

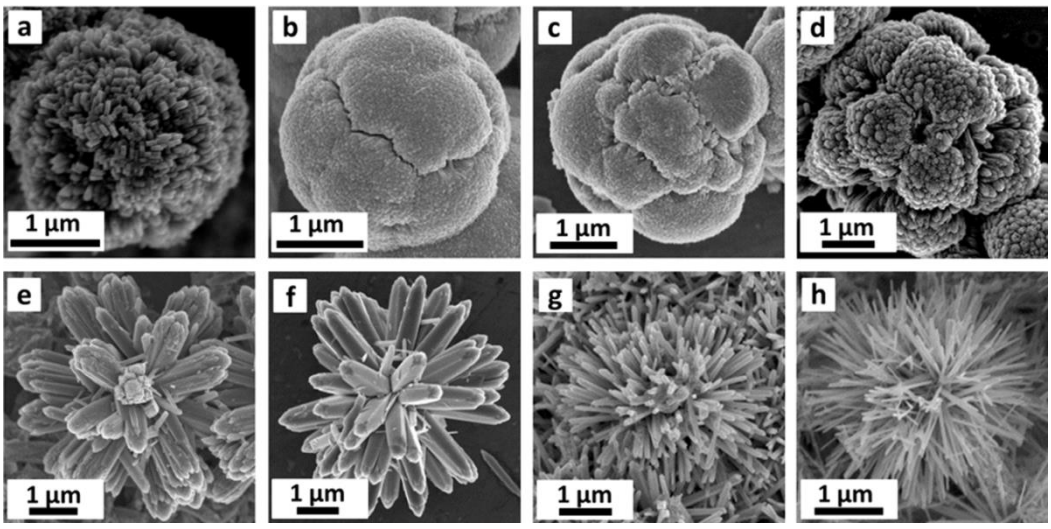

Figure 6.3 FESEM images of the as-prepared 3D hierarchical rutile TiO_2 architectures (HRT) [denoted as HRT-1 (a), HRT-2 (b), HRT-3 (c), HRT-4 (d), HRT-5 (e), HRT-6 (f), HRT-7 (g), HRT-8 (h)], synthesized from a reaction solution containing 0.5 mL aqueous tetrabutyl titanate (TT) solution with 25 mL X M hydrochloric acid (HCl) (X = 1-8).

material, in Figure 6.4(b), reveals that these densely packed crystalline nanorods (each with diameters of 15-30 nm) are radially arranged. It was found that the microsphere was formed by radial growth of nano-acicular crystals on the TiO_2 nanoparticulate core. Noticeably, smaller but also radially aligned nanorods form the core. It is from this surface that, nanorods with a mean width of ~ 20 nm and a length of ~ 500 nm, grew forming the TiO_2 microsphere.

The structure of HRT-2 and HRT-3 in the hydrothermal process, some-what resembling tennis balls, are 2-2.5 µm in diameter, as shown in Figure 6.3(b and c). The domain like arrangements of the TiO_2 nanorods form quasi spheres leading to an apparently smooth surface. The surfaces of these spheres are in fact densely packed nanorods. Samples prepared with 4 M HCl resulted in the formation of morphology

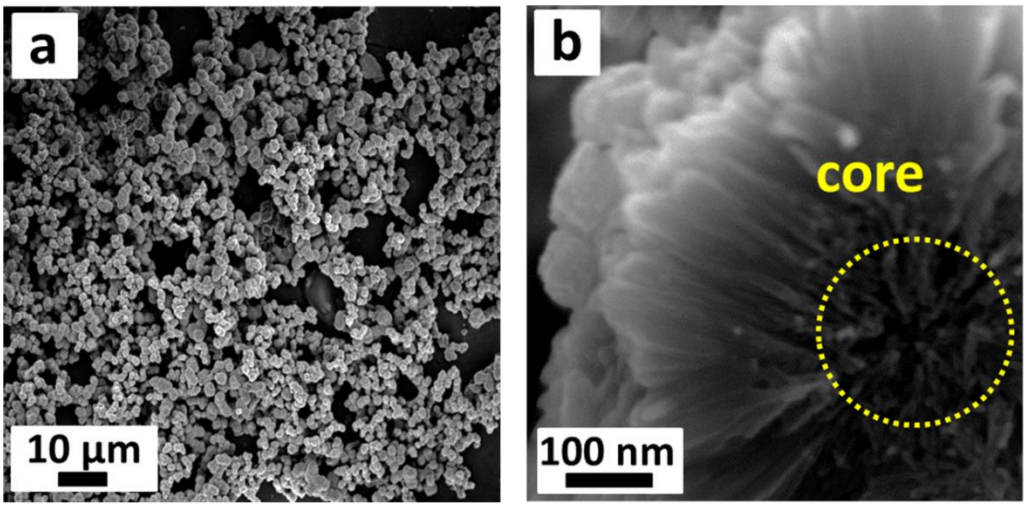

Figure 6.4 (a) Low magnification SEM image of the as-prepared HRT-1 synthesized from a reaction solution containing 0.5 mL aqueous TT solution with 1M HCl; (b) a cross-sectional view, showing the core.

likened to a cauliflower, comprised of the near-perfect assemble of numerous TiO_2 nanorods, as the nanorod bundles are smaller and more disparate [Figure 6.3(d)].

SEM of samples HRT-5 and HRT-6 [Figure 6.3(e and f)] revealed even more open morphologies with the nanorod bundles more separated from each other. Each of these bundles is assembled from several dozen nanorods of lengths of up to 3 µm. The distribution of quasi-cubic primary nanocrystallites with sizes 15-25 nm led to the observation of surfaces which may be likened to flowers. These differences are due to the initial differences in crystal growth of the titanium precursor in the stronger acidic medium (described in more detail below). The observation of nanostructures indicate that the formation of prisms and the flower-like structures, possibly stemmed from the crystal growth of the primary nanoparticles and the further epitaxial process of these prisms.

High HCl concentrations of HRT-7 and HRT-8 resulted in even more open structures again, as the surface etching rate is much faster and thus tends to result in

more nucleation sites at early stages of synthesis. The resulting nanorods bundles are thinner as they contain fewer rods [Figure 6.3(g, h)]. At these concentrations, structures composed of hundreds of nanoneedles were produced. It is known that high HCl concentration is favorable for the formation of smaller-scale building blocks. [37]

To elucidate the microstructural origin of the growth mechanisms, the architectures of the HRT obtained under different HCl concentrations were further investigated by high resolution SEM, high resolution transmission electron microscopy (HRTEM) and fast Fourier transforms (FFTs) of the HRTEM images. Figure 6.5(a) presents a high-magnification SEM image obtained from the synthesis completed using 0.5 mL of TT and 1M HCl. Figure 6.5(b) shows the TEM image of a single nanorod (prepared under the same conditions) with a width of ~ 20 nm. The FFTs pattern is shown in inset of Figure 6.5(b) and, along with the associate HRTEM image, confirm the single-crystal nature of the rutile TiO_2 rods.

It can be observed from Figure 6.5 that the rutile crystals (HRT-1 to HRT-5) can be described by a combination of an elongated cuboid structure and pyramid shaped cap [this is also seen in Figure 6.6(a) and schematically in Figure 6.7(a)]. Two sets of lattice fringes perpendicular to each other with distances of 0.29 and 0.32 nm can be readily ascribed to the lattice spacings of the (001) and (110) planes of the rutile TiO_2 respectively [Figure 6.7(b)].

The FFTs pattern [inset of Figure 6.5(b)] further confirms that (1) the cuboid crystal facets are parallel to {110}, (2) the pyramid-shaped crystal facets are parallel to {111}, and (3) a preferred growth along the [001] direction takes place.

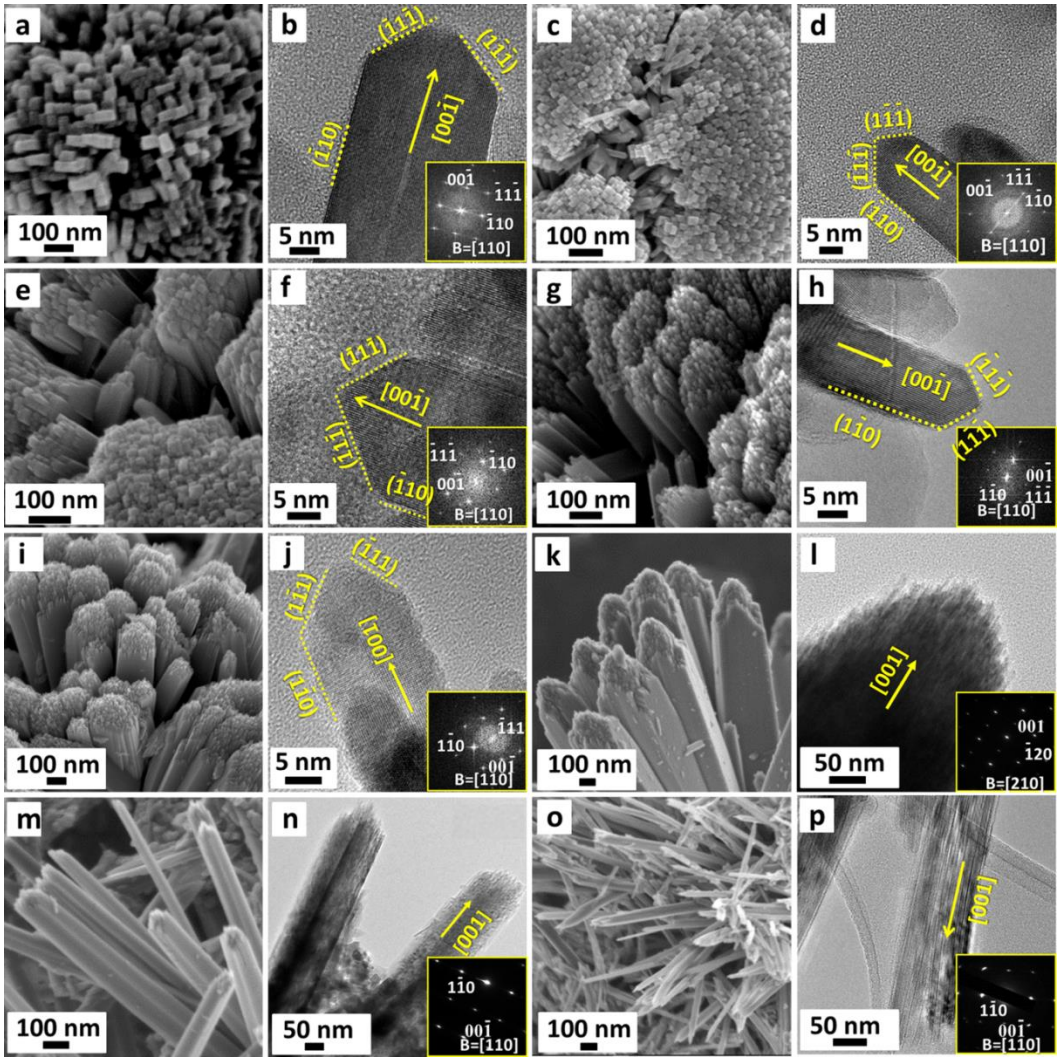

Figure 6.5 (a, c, e, g, i, k, m, o) High-magnification SEM images of HRT-1 to HRT-8, respectively; (b, d, f, h, j) TEM images of individual nanorods; (l, n, p) TEM images of nanorod bundles. The insets of (b, d, f, h, j, l, n, p) are the corresponding FFTs (b, d, f, h, j) and electron diffraction patterns (l, n, p).

Moreover, according to periodic bond chain (PBC) theory, PBCs result in the formation of the crystal and control the direction of crystal growth (the strongest chemical bonds are usually the ones at which the crystal has the fastest growth rate). [38, 39] Theoretical calculation shows that for a rutile lattice, the surface energy is E (110) $<E$ (100) $<$ E (101) $<$ E (001). [40] In crystal growth, a fast growing plane generally tends to disappear leaving behind slower growing planes with lower surface

energies. Thus, crystal growth along the [001] direction (i.e., *c* -axis) would have the fastest growth rate compared to other directions.

Interestingly, the top of all the rods are pyramidally capped, as shown in Figure 6.5. HRTEM imagery of the rod [Figure 6.5(b)] indicates that the plane of the pyramid has a contact angle of approximately 130° to the lateral {110} plane. The most appropriate plane is considered to be {111} under this condition because contact angles between {110} and {101}, {110} and {111}, and {110} and {221} planes are calculated to be 112.5°, 132.3°, and 151.2°, respectively, using the tetragonal rutile unit

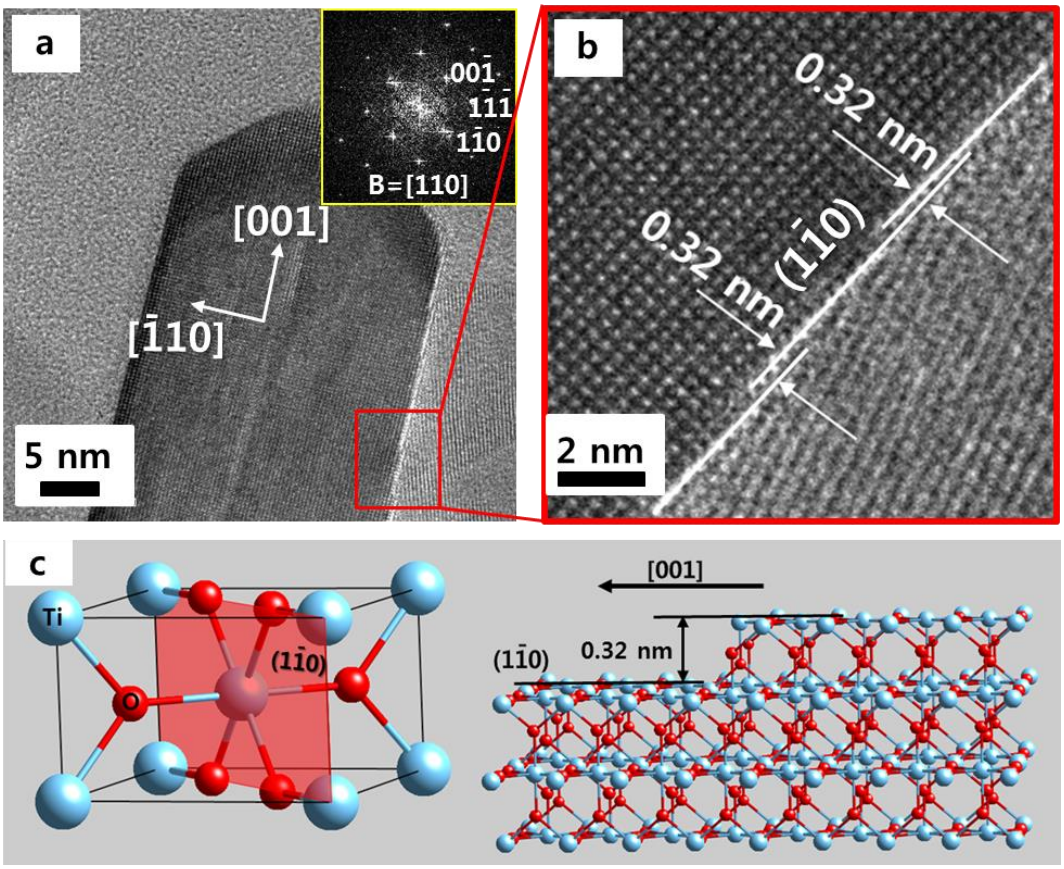

Figure 6.6 Ledgewise growth of rutile nanorod (HRT-1). (a) Macro growth direction of a rutile nanorode; preferential growth to [001] direction, (b) Thickening of a nanorode by ledgewise growth of $(1\bar{1}0)$ surface, (c) atomic structure of a rutile nanorod.

cell. [41]

No crystallographic differences were observed between HRT-1 and HRT-8. Our results then demonstrate that {111} and {110} faceted rods are obtained during the hydrothermal growth. It should be noted that the {111} planes observed at the top surface of the rods are a minor surface in the equilibrium shape of a macroscopic rutile TiO_2 crystal using the Wulff construction and the calculated surface energies. According to the atomistic simulation reported by Oliver *et al*., rutile TiO_2 shows four surfaces namely {011}, {110}, {100}, and {221}, with surface energies of 1.85, 1.78, 2.08, and 2.02 J m^{-2} respectively in the relaxed equilibrium morphology. [42] Nevertheless, the surface identified as the {221} plane had formerly been thought to be the lower index plane of {111}. Because the {111} plane, or alternatively {221}, governs a very small surface area in the equilibrium shape, experimental observation of this plane has been considerably difficult. [41]

In contrast to the simulation by Oliver *et al.*, [42] our results have shown the presence of the {111} facet with the large surface area, giving the pyramid-type

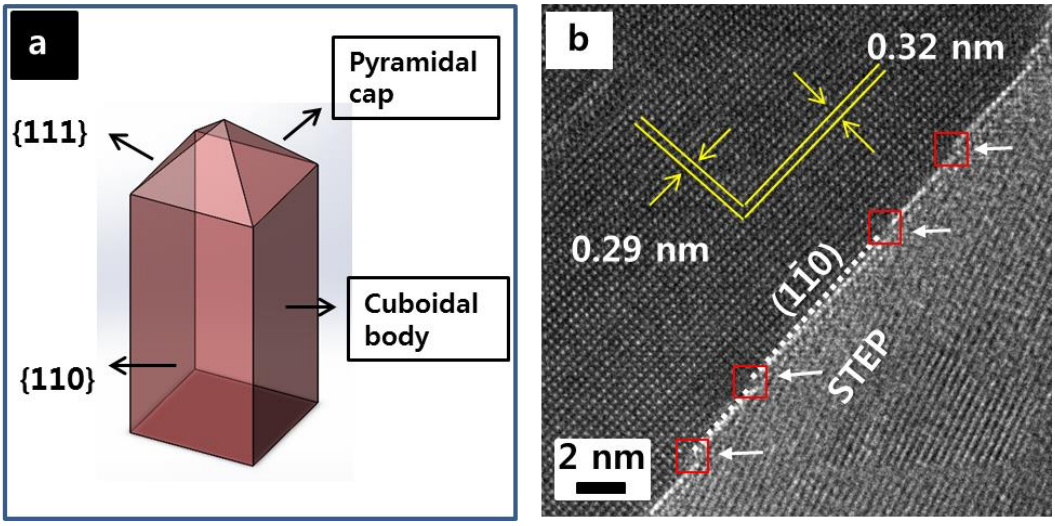

Figure 6.7 (a) Schematic description of growth morphology of a rutile nanorod, (b) Enlarged image of stepped surface of Figure 6.6(a).

morphology. The authors believe these results give important new insight into the surface chemistry of rutile TiO_2. It is reasonable to expect that the TiO_2 nanorods preferentially exposes the {110} side facets and the {111} top facets and grows along the [001] direction on the basis of the FESEM and HRTEM results together with the XRD pattern.

Figure 6.5 (c-p) shows the morphology and structure of the nanorods bundles and individual rods for HRT-2 to HRT-5. To further obtain structural information for the radial rods, TEM images and the corresponding FFT patterns are also recorded on a single nanorod of each (for HRT-6 to HRT-8, however, only bundles of nanorods were taken because the samples were brittle and no loose bundles could be identified, probably because of bundles more open but rods within each bundle more tightly held together). Based on Figure 6.5 it can be seen that, similar to HRT-1, the TiO_2 nanorod synthesized with 2 M-5 M HCl, also preferentially exposes the {110} side facets and the {111} top facets and grows along the [001] direction. In addition, the nanorod crystals of the HRT synthesized in the highest HCl concentration solutions (6 M-8 M) grew along the [001] direction. The exposed surfaces of the nanorods are {110} facets. The variation of HCl concentration in the reaction solutions did not affect the crystal growth direction of the nanorods.

In spite of the differences in micron-scale morphologies, all the architectures are composed of very similar crystalline nanorod units. It has been demonstrated previously that Cl^- plays an important role in the growth of TiO_2 grains into nanorods (as opposed to nanoparticles). This is because the {110} planes of rutile have a positive polar face and Cl^- is preferentially adsorbed on this surface, which serves to restrain the contact of TiO_2 grains on the {110} surfaces and thus greatly retards crystal growth along the (001) plane. [43, 44] As a result, TiO_2 grain growth was

suppressed in the <110> directions and accelerated in the [001] direction, thereby forming rod-like structures. Additionally, the presence of 4_2 screw axes along the crystallographic *c*-axis within rutile TiO_2 is also believed to be a guiding force for the formation of rutile nanorods. [45]

It is interesting that a ledgewise growth mechanism was observed for HRT-1, as shown in Figure 6.6. Preferential growth of a rutile nanorod to the [001] direction is also confirmed by overview of a nanorod [Figure 6.6(a)]. The growth rate in the [001] direction is much faster than that of the $[\bar{1}10]$ direction, resulting in an elongated morphology in the [001] direction. Lateral growth of a nanorod, ie. the diameter increasing, occurs with the generation of a fresh $(1\bar{1}0)$ surface. High resolution images of the side of a nanorod show several steps on a $(1\bar{1}0)$ plane [Figure 6.6(b), Figure 6.7(b)].

Table 6.1 Surface areas of the as-prepared HRT-1, HRT-2, HRT-3, and HRT-4, synthesized from a reaction solution containing 0.5 mL aqueous TT solution with 25 mL 1 M-4 M HCl, along with P25.

Samples	Specific Surface Area ($m^2 g^{-1}$)
HRT-1	67
HRT-2	29
HRT-3	20
HRT-4	17
P25	42

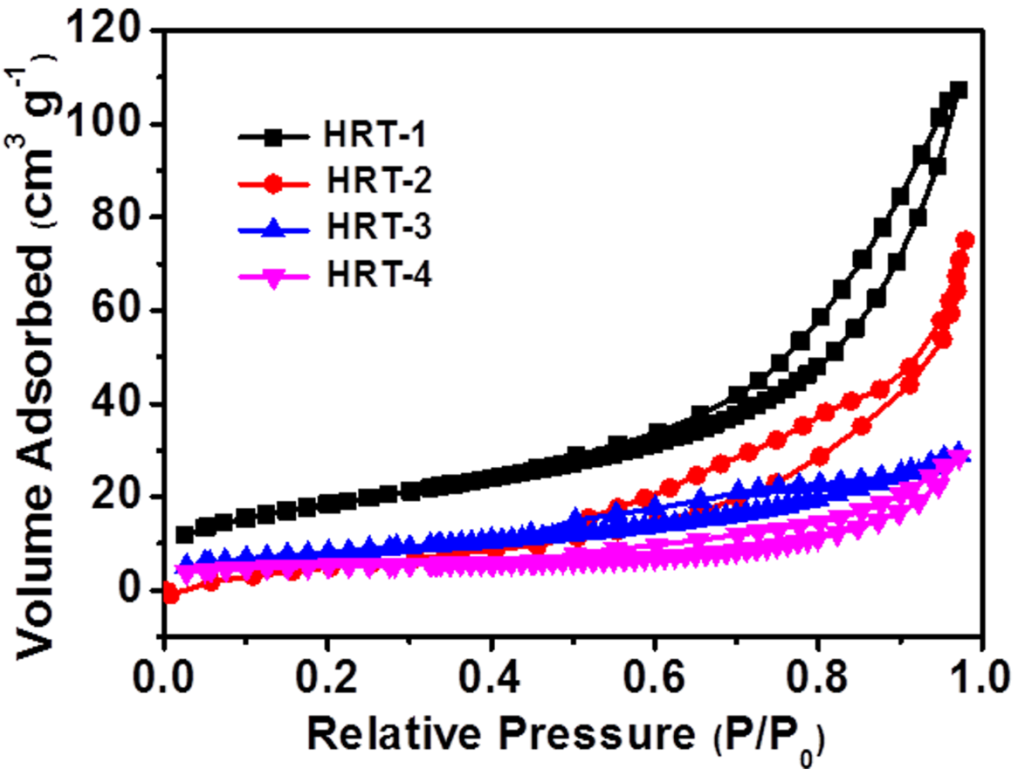

Figure 6.8 N_2 adsorption/desorption isotherms of the as-prepared HRT-1, HRT-2, HRT-3, and HRT-4, synthesized from a reaction solution containing 0.5 mL aqueous TT solution with 25 mL 1 M-4 M HCl concentrations.

Importantly, these steps have a step height of 0.32 nm, coincident with interplanar spacing of a $(1\bar{1}0)$ plane. This ledgewise growth mechanism minimizes the total surface energy during growth of nanorod [Figure 6.6(c)], as a monolayer step will minimize the amount of high surface energy area. The total $(1\bar{1}0)$surface area which has minimum surface energy is kept constant during growth. The growth of a rutile nanorod is displayed schematically in Figure 6.7(a). The cuboidal body has {110} type surface and the upper pyramidal cap is composed of {111} planes.

Brunauer-Emmett-Teller (BET) calculations of specific surface area based on N_2 adsorption-desorption were performed (Table 6.1), however, HRT-5 –HRT-8 were omitted from this due to the low yields which lead to large measurement errors. The

Table 6.2 Specific surface area, porosity, and roughness factor of P25, HRT-1 and Dyesol-T materials.

Samples	Specific surface area ($m^2\ g^{-1}$)	Porosity [a] (%)	Roughness factor [b] (μm^{-1})	Amount of dye [c] (10^{-7} mol cm^{-2})
P25	42	34.9	118	2.4
HRT-1	67	56.6	125	2.7
Dyesol-T	74	64.2	103	3.4

[a] The porosities (P) of P25, HRT-1 and Dyesol-T were calculated according to: $P = V_p / (q^{-1} + V_p)$, where V_p is the specific cumulative pore volume ($cm^3\ g^{-1}$) and q is the density of TiO_2 (q = 4.3 g·cm^{-3}). [50]

[b] An estimation of the roughness factor (R) per unit film thickness of the films is obtained by $R = q\ (1\text{-}P)\ S$, where q is the density (g cm^{-3}) of TiO_2, P is the porosity (%) of the film, and S is the specific surface area ($m^2\ g^{-1}$). [51]

[c] The dyed electrodes were soaked in a 0.4 M alkaline solution in methanol to desorb the dye from the electrodes. The amount of desorbed dye was quantified by measuring its optical absorption spectrum (Figure 6.9).

specific surface area is found to decrease with increasing concentration of HCl used in synthesis. N_2 adsorption-desorption isotherms (shown in Figure 6.8) of the samples (HRT-1 – HRT-4) exhibited typical type IV sorption behavior with hysteresis loops, ascribed to the existence of the mesoporous structure.

On account of it having the highest specific surface area (and highest yield among all the samples), HRT-1 was applied in photoanodes for DSCs. Two control materials were employed for comparative purposed. Firstly, P25 was used, as it is low cost and widely reported in this field. P25 also represents a mixed phase material

(mostly anatase, with a significant rutile impurity). A commercial Transparent Titania Anatase paste [18NR-T, denoted as Dyesol-T, obtained from Dyesol (Australia)] was also chosen for its role in some of the highest reported DSC efficiencies to date.

The porosity (*P*) and surface roughness factor (*R*) based on adsorption-desorption measurements were measured for the two controls and compared with HRT-1, summarized in Table 6.2 and Figure 6.10.

HRT-1 is > 50 % porous, which is promising as porosities of nanocrystalline TiO_2 films employed in high efficiency DSCs are typically in the range of 50-65 %. HRT-1 has a similar specific surface area as Dyesol-T (74 m^2 g^{-1}), but significantly higher than P25. Furthermore, the calculated roughness factor for HRT-1, approximately 125 μm^{-1}, which is higher than both P25 and Dyesol-T.

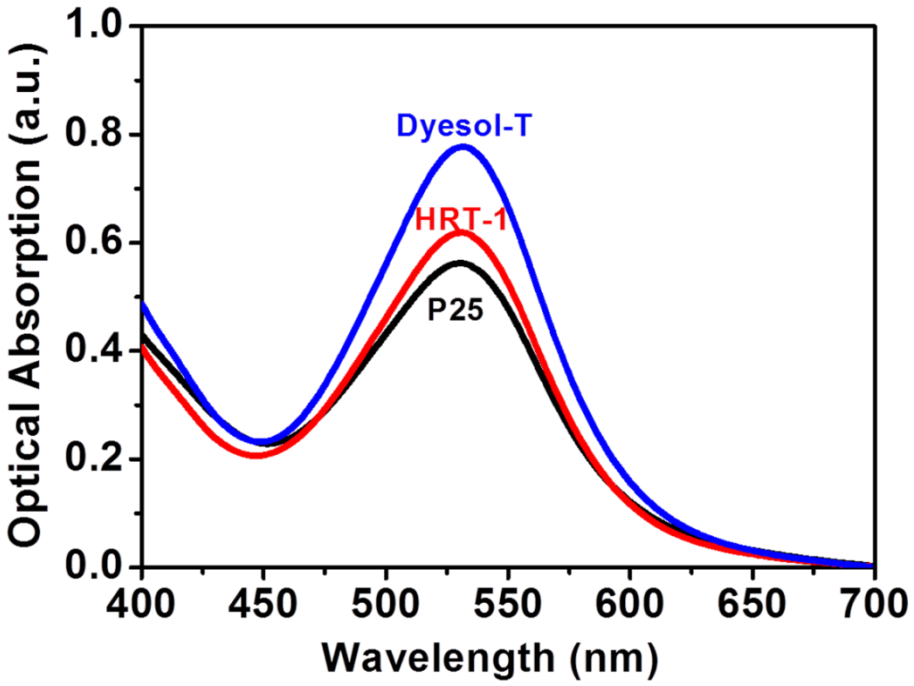

Figure 6.9 Optical absorption of dye desorbed from P25, HRT-1 and Dyesol-T films by dissolving sensitized samples into 0.4 M NaOH in methanol solution.

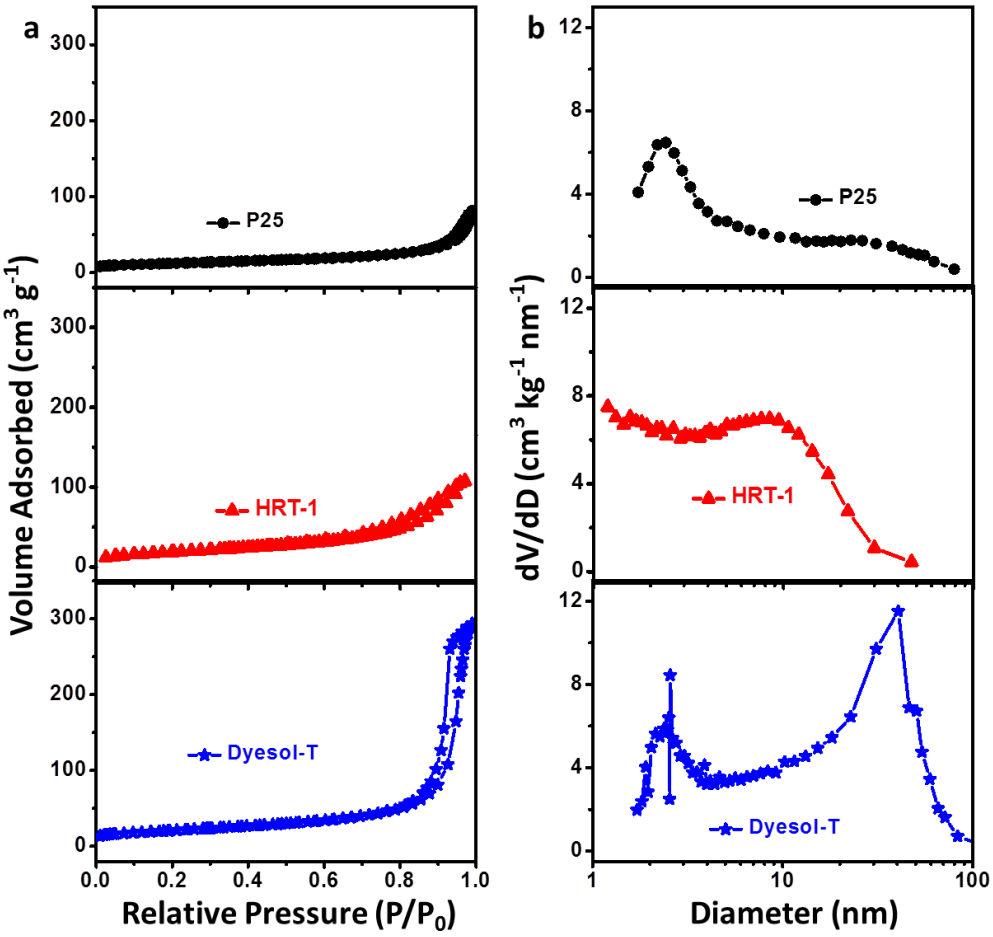

Figure 6.10 (a) N_2 adsorption-desorption isotherms of P25 (black closed circles), HRT-1 (red closed triangles) and Dyesol-T (blue closed stars); and (b) corresponding pore size distributions calculated by the BJH method from the adsorption branch.

The photocurrent density-voltage (*J*-*V*) characteristics curves and photovoltaic properties of P25, HRT-1 and Dyesol-T based DSCs (each with ~ 12 μm porous TiO_2 layer), are shown in Figure 6.11, (summarized in Table 6.3). From this, it can be found that the overall energy conversion efficiency (η) of HRT-1 was higher than P25 but lower than Dyesol-T. The short-circuit photocurrent density (J_{sc}) is highest in the devices with Dyesol-T, then HRT-1, and lowest when P25 is used. This order

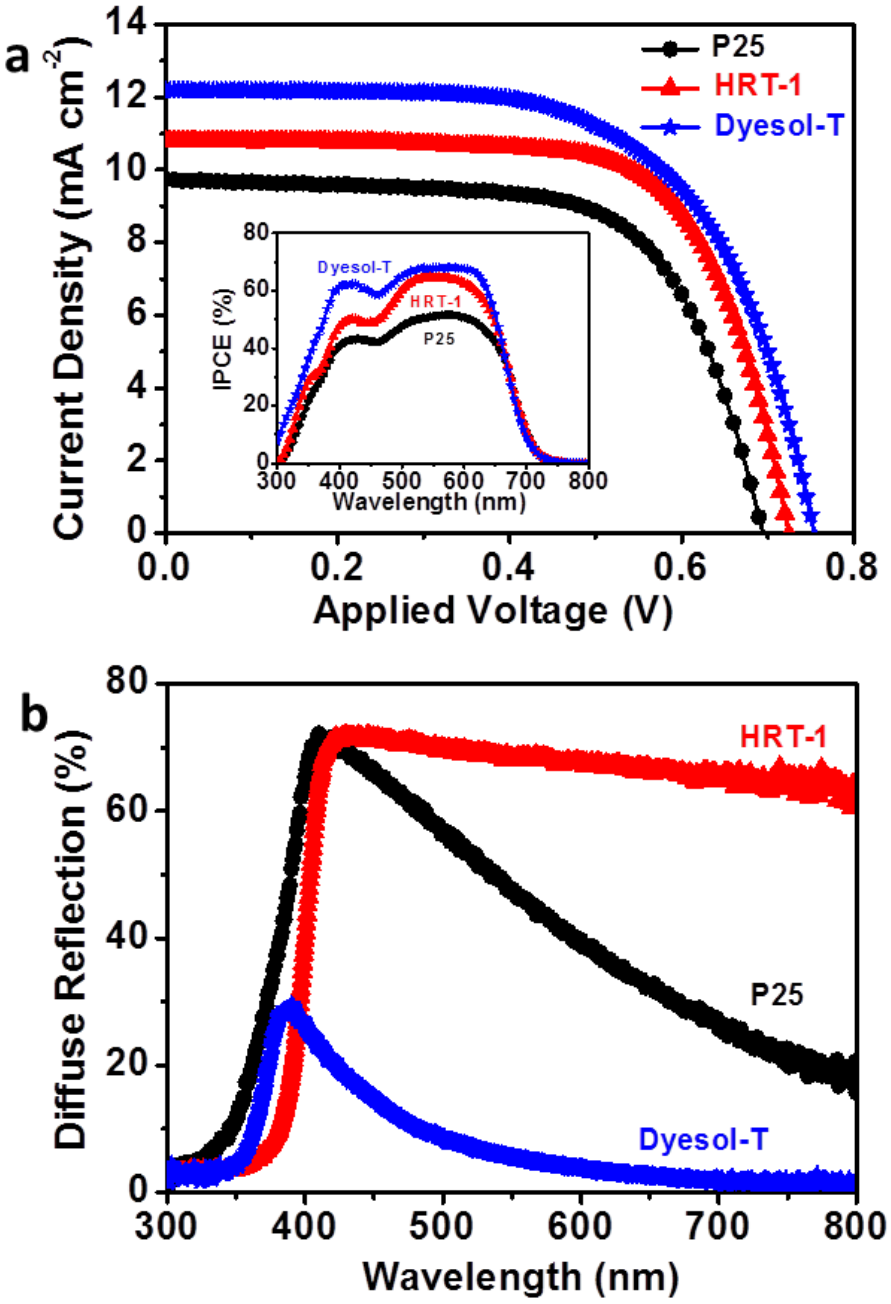

Figure 6.11 (a) *J-V* characteristics of P25-, HRT-1- and Dyesol-T-based DSCs. Cells were illuminated at an intensity of 100 mW cm^{-2} with a spectrum approximately AM 1.5 G and an active area of 0.16 cm^2; inset: incident photon to current conversion efficiency (IPCE) curves of P25-, HRT-1- and Dyesol-T-based DSCs. (b) diffuse reflectance spectra of P25, HRT-1 and Dyesol-T films.

is repeated in the dye loading data collected (Table 6.2, Figure 6.9), however is probably not the whole story with regard to light harvesting efficiency (LHE).

The higher J_{sc} for HRT-1 based devices than P25 could be mainly attributed to the improved dye loading capacity, attributable to measured *R* and BET surface area results, as well as light scattering properties of the TiO_2 films. In both cases the materials are scattering. It can be expected that this will actually cause some problems, with reflection near to the front surface causing light to be lost. [46]

Light scattering generally serves to improve LHE. As shown in Figure 6.11(b), HRT-1 is a much more effective light scattering material than either P25 or Dyesol-T (the reflectance spectrum from 400 to 800 nm). In order to better scrutinize the different photovoltaic performances of these three solar cells, the incident photon-to- current efficiency (IPCE) spectra as a function of wavelength was collected. The IPCE [inset of Figure 6.11(a)] is defined as the ratio of the number of electrons extracted the external circuit (under short circuit conditions) divided by the number of incident photons as a function of the wavelength of incident light. As such, it is a function of LHE as well as charge injection, φ_{inj}, and charge transport efficiencies, φ_{cc}.

It is observed that devices made with HRT-1 possess a marginally lower peak IPCE values than that of Dyesol-T devices and significantly higher than P25. This is an important point to obeseve as it suggests that φ_{inj} for HRT-1 should be similar to Dyesol-T [and close to unity, given the light transmission of the fluorine-doped tin oxide (FTO) substrate].

The lower IPCE values recorded away from the dye peak absorbance wavelength can be attributed to either lower φ_{cc} (addressed below) or light being reflected out of the cell before it can be absorbed by a dye molecule. At the maximum value of the IPCE spectrum at around 530 nm, the IPCE of the HRT-1 film is approximately 10 %

Table 6.3 Photovoltaic parameters of cells based on P25, HRT-1 and Dyesol-T photoanodes measured under air mass (AM) 1.5 global (1.5G) one sun illumination (100 mW cm^{-2}). J_{sc}: short-circuit photocurrent density; V_{oc}: open-circuit photovoltage; *FF*: fill factor; η: total power conversion efficiency. The active areas were ~ 0.16 cm^2 for all of the cells (with the mask area 0.25 cm^2), and the data presented are average values obtained after testing four cells and the standard deviation thereof.

Samples	J_{sc} ($mA\ cm^{-2}$)	V_{oc} (V)	*FF* (%)	η (%)	Film thickness[a)] (μm)
P25	9.8	0.695	66.5	4.5	12 ± 0.2
	± 0.5	± 0.01	± 1	± 0.2	
HRT-1	10.8	0.725	70.0	5.5	12 ± 0.2
	± 0.5	± 0.02	± 2	± 0.3	
Dyesol-T	12.2	0.755	63.0	5.8	12 ± 0.2
	± 0.2	± 0.02	± 1	± 0.2	

[a)] Measurement of film thickness was carried out on a surface profile system (Veeco Dektak 150).

higher than that of the P25 film. This increase is in good agreement with the increased J_{sc} and η observed in Figure 6.11(a) and Table 6.3.

The highly faceted nature of these structures results in less defect sites compared to flame pyrolysed P25, which should serve to decrease electron recombination for TiO_2 to I_3^- in the electrolyte. Electrochemical impedance spectroscopy (EIS) is a very useful tool for understanding the kinetics of electrochemical and photoelectrochemical processes occurring in DSCs. [47, 48] Figure 6.12(a) presents

the Nyquist plots of the impedance spectra obtained under illumination for DSCs assembled with P25, HRT-1 and Dyesol-T films under V_{oc}, and the equivalent circuit is shown as the inset.

Measured V_{oc} under one sun illumination follows the same trend as J_{sc} (Dyesol-T > HRT-1 > P25). Having said this, the difference between the pure anatase and pure rutile devices here is much less (~ 30 mV) than would be expected based solely on conduction band offsets (~ 200 mV). Perhaps the most surprising aspect of these results however is the enhanced fill factor (*FF*) for HRT-1 compared to the other two materials. This is analyzed in greater detail below.

The figure demonstrates that the Nyquist plots have two semicircles with a contact series resistance (R_s) on the FTO substrate [(all R_s values are similar (7.0 – 7.5 Ω)]. The left semicircle (high frequency) represents the resistance at the counter electrode (R_{ct1}) for the reduction reaction of I_3^- ions in the electrolyte using Pt as the counter electrode. The second semicircle in the intermediate frequency range results from charge transport through the semiconductor, while the corresponding chemical capacitance (C_μ) describes the density of states in the bandgap of TiO_2. These parameters were calculated from measured data by using an equivalent circuit [inset of Figure 6.12(a)] as shown in Figure 6.13 and Table 6.4.

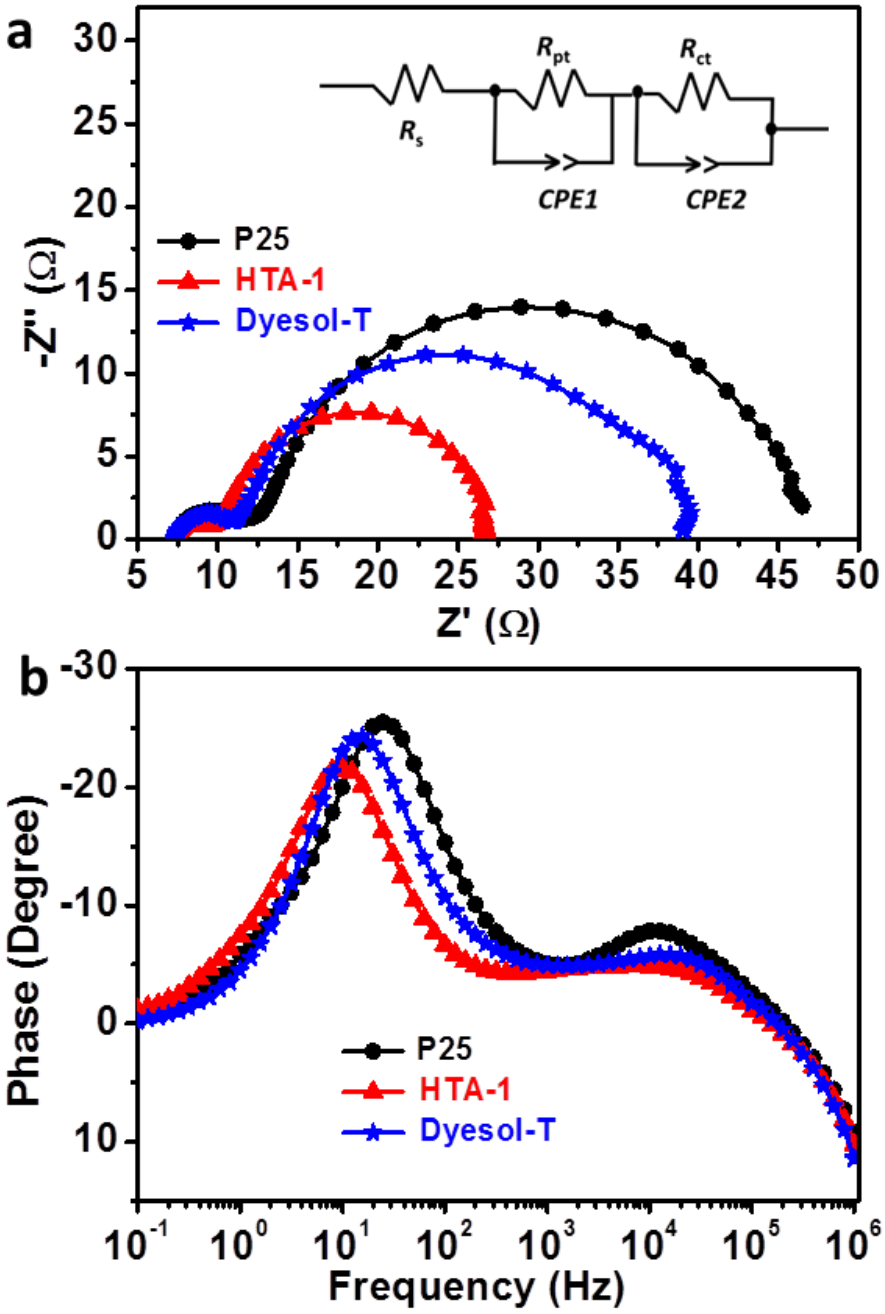

Figure 6.12 Impedance spectra of DSCs containing P25, HRT-1 and Dyesol-T photoanodes measured at V_{oc} under illumination of 100 mW cm^{-2}: (a) Nyquist plots, with the inset showing the equivalent circuit, and (b) Bode phase plots.

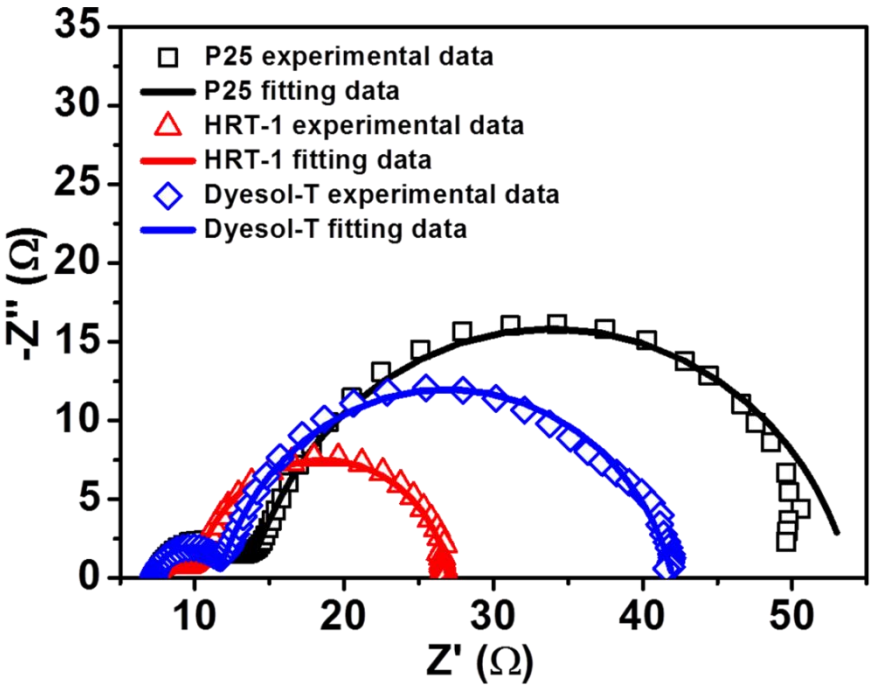

Figure 6.13 Impedance spectra of DSCs containing P25, HRT-1 and Dyesol-T photoanodes measured at V_{oc} under illumination at 100 mW cm^{-2}: Nyquist plots, with the experimental data and the fitting data.

According to Adachi *et al.*, several parameters related to the properties of electron transport in the semiconductor can be deduced from the Nyquist plot. [49] In particular, the charge transport resistance (R_{ct2}) related to electron-hole recombination can be determined from the central arc diameter. In our case, it was found that R_{ct2} at the TiO_2/dye/electrolyte interface for HRT-1 was much smaller than for P25 and Dyesol-T, implying a relatively faster electron transfer process and a slower electron recombination at the HRT-1 photoanode interface. Meanwhile, the higher C_μ value of the HRT-1-based DSC indicates that more states on the TiO_2 surface are able to accept electrons from the excited state of the dye, yielding an increased photocurrent.

Table 6.4 EIS parameters of P25, HRT-1 and Dyesol-T-based DSCs obtained by fitting the experimental data according to the equivalent circuit model [inset in Fig. 4(c)].

Samples	R_s (Ω)	R_{ct1} (Ω)	R_{ct2} (Ω)	C_μ (F cm^{-2})
P25	7.3	6.7	38.1	0.00068
HRT-1	7.0	3.7	16.6	0.00138
Dyesol-T	7.3	3.7	28.4	0.00094

Furthermore, the Bode phase plots shown in Figure 6.12(b) likewise support the differences in the electron lifetime for the TiO_2 films derivatized with P25, HRT-1 and Dyesol-T. The electron lifetime (τ_{eff}) could be calculated from the low frequency results as:

$$\tau_{eff} = \frac{1}{2\pi f_{max}} \qquad (1)$$

where the characteristic f_{max} is the maximum phase shift in the mid-frequency peak. The middle-frequency peaks of the DSCs containing P25 and Dyesol-T shift to higher frequency relative to HRT-1, indicating a longer electron lifetime for the latter material. The longer electron lifetime observed with HRT-1-sensitized solar cells indicates more effective suppression of the back-reaction of the injected electrons with the I_3^- ions in the electrolyte. With these considerations, it seems likely that the limitations of the rutile materials are not connected to φ_{cc}, implying that reflecting light out of the cell before it can be absorbed is the major limiting factor here.

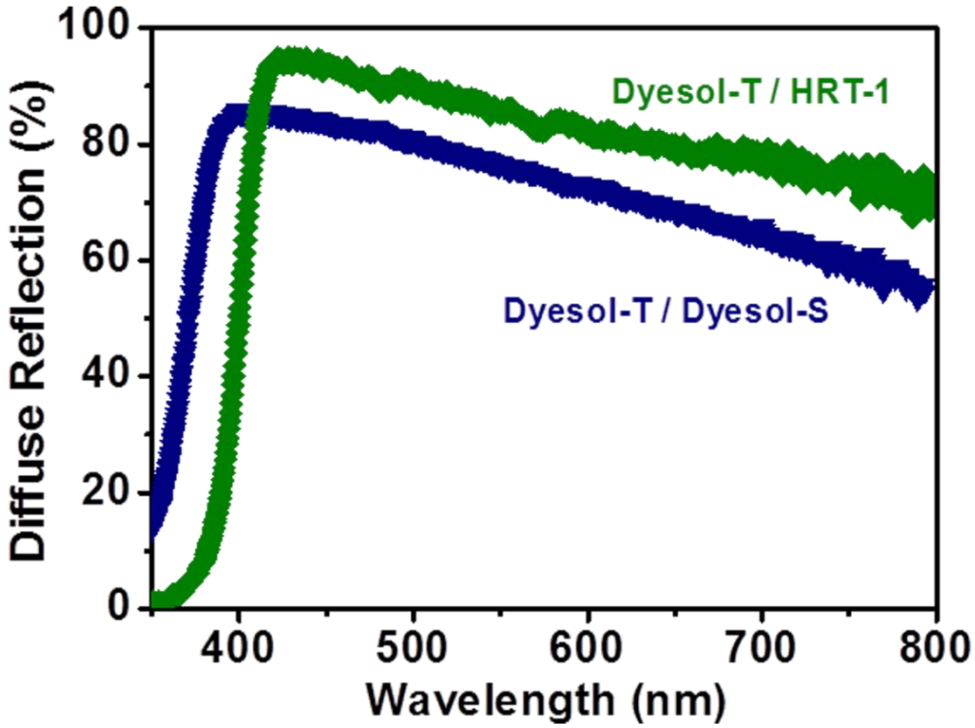

Figure 6.14 Diffuse reflectance spectra of Dyesol-T (~ 12 µm) / Dyesol-S (~ 4 µm) and Dyesol-T (~ 12 µm) / HRT-1 (~ 4 µm) films.

It is quite interesting to note that charge transport through HRT-1 is better than for the other materials, in spite of the bulk charge transport values being lower in rutile than anatase. The longer electron lifetime is likely due to morphology of rods in the larger constructs.

Previous studies showed that, lower dye loadings (N719) on rutile compared to anatase, for the same thickness, is the main reason for lower J_{sc} and η. [26] However, using organic sensitizer (D149) in our study allows us to realize similar dye loading for both rutile and anatase.

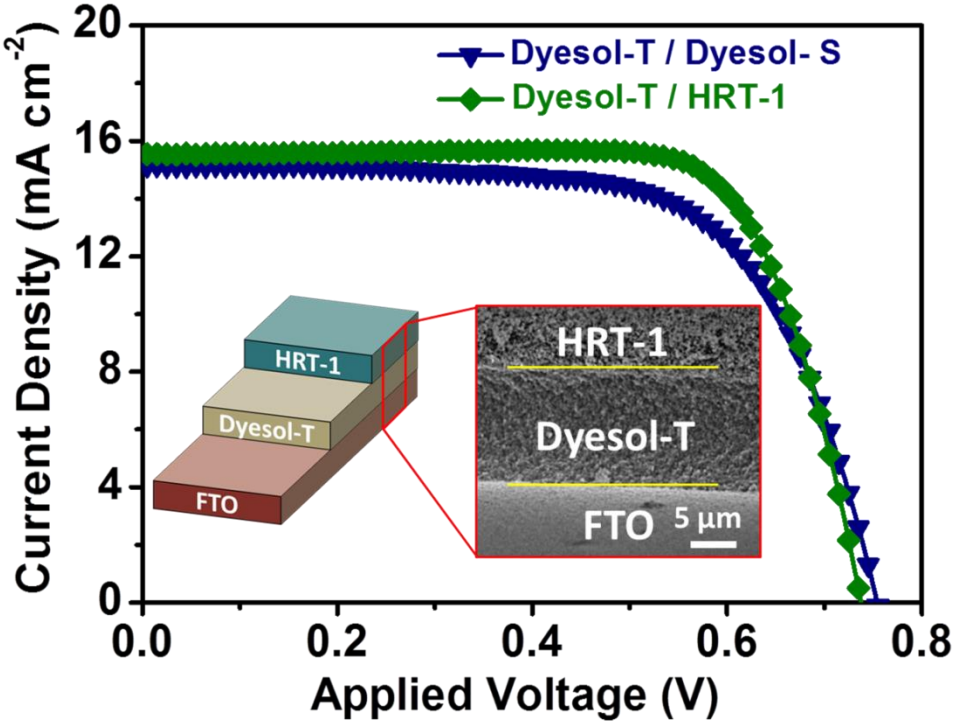

Figure 6.15 *J-V* curves of optimized DSCs based on a Dyesol-S film as the light scattering layer over a Dyesol-T under layer [Dyesol-T (12 µm) / Dyesol-S (4 µm)] and a HRT-1 film as the light scattering layer over a Dyesol-T under layer [Dyesol-T (12 µm) / HRT-1 (4 µm)] under AM 1.5 G one sun intensity. Inset is a titled SEM cross-sectional image of Dyesol-T (12 µm) / HRT-1 (4 µm) on the fluorine-doped tin oxide (FTO) and its schematic illustration.

Table 6.5 Photovoltaic parameters of cells based on Dyesol-T (~ 12 μm) / Dyesol-S (~ 4 μm) and Dyesol-T (~ 12 μm) / HRT-1 (~ 4 μm) photoanodes measured under air mass (AM) 1.5 global (1.5G) one sun illumination (100 mW cm^{-2}). J_{sc}: short-circuit photocurrent density; V_{oc}: open-circuit photovoltage; *FF*: fill factor; η: total power conversion efficiency. The active areas were ~ 0.16 cm^2 for all of the cells (with the mask area 0.25 cm^2), and the data presented are average values obtained after testing four cells and the standard deviation thereof.

Samples	J_{sc} ($mA\ cm^{-2}$)	V_{oc} (V)	*FF* (%)	η (%)	Film thickness[a)] (μm)
Dyesol-T / Dyesol-S	15.1 ± 0.2	0.755 ± 0.02	66.7 ± 2	7.6 ± 0.2	16 ± 0.2
Dyesol-T / HRT-1	15.5 ± 0.2	0.740 ± 0.02	75.0 ± 1	8.6 ± 0.2	16 ± 0.2

[a)] Measurement of film thickness was carried out on a surface profile system (Veeco Dektak 150).

As an additional experiment, the light scattering properties of HRT-1 were compared to a commercially available Reflector Titania Anatase paste [WER2-O, denoted as Dyesol-S, obtained from Dyesol (Australia)]. Once again, this has been used by a number of groups around the world in order to produce high efficiency devices.

Both scattering layers were applied on top of a ~ 12 µm thick layer of Dyesol-T, with diffuse reflectance spectra of Dyesol-T (~ 12 µm) / Dyesol-S (~ 4 µm) and Dyesol-T (~ 12 µm) / HRT-1 (~ 4 µm) films shown in Figure 6.14.

Both these materials provided enhanced performance efficiencies, with the most marked improvement being seen when HRT-1 is employed. Figure 6.15 (summarized in Table 6.5) shows the *J-V* curves of DSCs using the two scattering layers. A J_{sc} of 15.5 mA cm^{-2}, V_{oc} of 740 mV, *FF* of 75.0 %, and an overall η of 8.6 % was obtained for Dyesol-T/HRT-1 films, under AM 1.5 G one sun intensity, which is superior than the optimized Dyesol-T/Dyesol-S (7.6 %). Much of this improvement can be attributed to high *FF* when HRT-1 is used, compared to Dyesol-S.

6.4 Conclusions

In summary, different well-defined 3D hierarchical rutile TiO_2 architectures (HRT) were synthesized via a facile hydrothermal method without any surfactant or template. A ledgewise growth was observed for the first time on rutile TiO_2. A 3D architecture has been demonstrated as an effective photoelectrode when employed in a DSC along with a metal-free organic dye (D149). Although the performance of HRT based devices was inferior to those of state-of-the-art commercial antase Dyesol-T paste, this study provided some important insights into rutile TiO_2, and in particular its possible applications in DSCs. The difference in J_{sc} here is significantly lower than in previous studies. [26] Charge rates are seen to be less of a problem than it was initially anticipated to be.

An energy conversion efficiency of 5.5 % was achieved, which is superior to that of an analogous device using P25 (4.5 %), and comparable to Dyesol-T (5.8 %). The overall conversion efficiency 8.6 % was achieved when HRT was used as the light scattering layer, a considerable improvement over commercial anatse Dyesol-T (~ 12

μm) / Dyesol-S (~ 4 μm) system (7.6 %). The 3D rutile TiO_2 and metal-free indoline sensitizer may present an alternative candidate with regard to producing high-performance DSCs.

6.5 References

1. B. O'Regan, and M. Grätzel, *Nature*, 1991, **353**, 737-740.
2. A. Wold, *Chem. Mat.*, 1993, **5**, 280-283.
3. X. Chen, and S. S. Mao, *Chem. Rev.*, 2007, **107**, 2891-2959.
4. D. V. Bavykin, J. M. Friedrich, and F. C. Walsh, *Adv. Mater.*, 2006, **18**, 2807-2824.
5. J. Wang, and Z. Lin, *Chem. Mat.*, 2008, **20**, 1257-1261.
6. X. Feng, K. Shankar, O. K. Varghese, M. Paulose, T. J. Latempa, and C. A. Grimes, *Nano Lett.*, 2008, **8**, 3781-3786.
7. Y. J. Kim, M. H. Lee, H. J. Kim, G. Lim, Y. S. Choi, N.-G. Park, K. Kim, and W. I. Lee, *Adv. Mater.*, 2009, **21**, 3668-3673.
8. B. Liu, and E. S. Aydil, *J. Am. Chem. Soc.*, 2009, **131**, 3985-3990.
9. M. Ye, X. Xin, C. Lin, and Z. Lin, *Nano Lett.*, 2011, **11**, 3214-3220.
10. X. Li, Y. Xiong, Z. Li, and Y. Xie, *Inorg. Chem.*, 2006, **45**, 3493-3495.
11. T.-D. N. Phan, H.-D. Pham, T. V. Cuong, E. J. Kim, S. Kim, and E. W. Shin, *J. Cryst. Growth.*, 2009, **312**, 79-85.
12. B. Zhao, L. Lin, and D. He, *J. Mater. Chem. A*, 2013**, 1**, 1659-1668.
13. F. Zhu, D. Wu, Q. Li, H. Dong, J. Li, K. Jiang, and D. Xu, *RSC Adv.*, 2012, **2**, 11629-11637.
14. Z. Sun, J. H. Kim, Y. Zhao, F. Bijarbooneh, V. Malgras, Y. Lee, Y.-M. Kang, and S. X. Dou, *J. Am. Chem. Soc.*, 2011, **133**, 19314-19317.
15. Q. Zhang, and G. Cao, *J. Mater. Chem.*, 2011, **21**, 6769-6774.

16. N. Tétreault, and M. Grätzel, *Energy Environ. Sci.*, 2012, **5**, 8506-8516.

17. T. Beuvier, M. Richard-Plouet, M. M.-L. Granvalet, T. Brousse, O. Crosnier, and L. Brohan, *Inorg. Chem.*, 2010, **49**, 8457-8464.

18. Y. P. Lin, S. Y. Lin, Y. C. Lee, and Y. W. Chen-Yang, *J. Mater. Chem. A*, 2013, **1**, 9875-9884.

19. B. Geng, J. You, F. Zhan, M. Kong, and C. Fang, *J. Phys. Chem. C*, 2008, **112**, 11301-11306.

20. M. Rauber, I. Alber, S. Muller, R. Neumann, O. Picht, C. Roth, A. Schokel, M. E. Toimil-Molares, and W. Ensinger, *Nano Lett.*, 2011, **11**, 2304-2310.

21. H. Chen, T. Hu, X. Zhang, K. Huo, P. K. Chu, and J. He, *Langmuir*, 2010, **26**, 13556-13563.

22. B. Nikoobakht, and M. A. El-Sayed, *Chem. Mat.* 2003, **15**, 1957-1962.

23. G. K. Mor, O. K. Varghese, M. Paulose, and C. A. Grimes, *Adv. Funct. Mater.*, 2005, **15**, 1291-1296.

24. J. Li, Y. Shi, Q. Cai, Q. Sun, H. Li, X. Chen, X. Wang, Y. Yan, E. G. Vrieling, *Cryst. Growth Des.*, 2008, **8**, 2652-2659.

25. M. R. Hoffmann, S. T. Martin, W. Choi, and D. W. Bahnemann, *Chem. Rev.*, 1995, **95**, 69-96.

26. N.-G. Park, J. Van de Lagemaat, and A. Frank, *J. Phys.Chem. B*, 2000, **104**, 8989-8994.

27. X. Feng, K. Shankar, M. Paulose, and C. A. Grimes, *Angew. Chem.*, 2009, **121**, 8239-8242.

28 N.-G. Park, G. Schlichthorl, J. van de Lagemaat, H. M. Cheong, A. Mascarenhas, and A. J. Frank, *J. Phys.Chem. B*,1999, **103**, 3308-3314.

29. M. Grätzel, *J. Photochem. Photobiol. A*, 2004, **164**, 3-14.

30. M. K. Nazeeruddin, R. Splivallo, P. Liska, P. Comte, and M. Grätzel, *Chem. Commun.*, 2003, **12**, 1456-1457.

31. M. K. Nazeeruddin, F. D. Angelis, S. Fantacci, A. Selloni, G. Viscardi, P. Liska, S. Ito, B. Takeru, and M. Grätzel, *J. Am. Chem. Soc.*, 2005, **127**, 16835-16847.

32. M. K. Nazeeruddin, P. Pechy, T. Renouard, S. M. Zakeeruddin, R. Humphry-Baker, P. Comte, P. Liska, L. Cevey, E. Costa, V. Shklover, L. Spiccia, G. B. Deacon, C. A. Bignozzi, and M. Grätzel, *J. Am. Chem. Soc.*, 2001, **123**, 1613-1624.

33. W. H. Howie, F. Claeyssens, H. Miura, and L. M. Peter, *J. Am. Chem. Soc.*, 2008, **130**, 1367-1375.

34. S. Ito, S. M. Zakeeruddin, R. Humphry-Baker, P. Liska, R. Charvet, P. Comte, M. K. Nazeeruddin, P. Pechy, M. Takata, H. Miura, S. Uchida and M. Grätzel, *Adv. Mater.*, 2006, **18**, 1202-1205.

35. M. K. Nazeeruddin, S. M. Zakeeruddin, R. Humphry-Baker, M. Jiousek, P. Liska, N. Vlachopoulos, V. Shklover, C.-H. Fischer, and M. Grätzel, *Inorg. Chem.*, 1999, **38**, 6298-6305.

36. S. Porto, P. Fleury, and T. Damen, *Phys. Rev.*, 1967, **154**, 522.

37. W. Guo, C. Xu, X. Wang, S. Wang, C. Pan, C. Lin, and Z. L. Wang, *J. Am. Chem. Soc.*, 2012, **134**, 4437-4441.

38. P. Hartman, and W. Perdok, *Acta Crystallogr.*, 1955, **8**, 521-524.

39. P. Hartman, and W. Perdok, *Acta Crystallogr.*, 1955, **8**, 525-529.

40. B. J. Morgan, D. O. Scanlon, and G. W. Watson, *J. Mater. Chem.*, 2009, **19**, 5175-5178.

41. K. Kakiuchi, E. Hosono, H. Imai, T. Kimura, and S. Fujihara, *J. Cryst. Growth*, 2006, **293**, 541-545.

42. G. Watson, P. Oliver, S. Parker, *Phys. Chem. Miner.*, 1997, **25**, 70-78.

43. S. J. Kim, S. D. Park, Y. H. Jeong, and S. Park, *J. Am. Ceram. Soc.*, 1999, **82**, 927-932.

44. E. Hosono, S. Fujihara, K. Kakiuchi, and H. Imai, *J. Am. Chem. Soc.*, 2004, **126**, 7790-7791.

45. D. Sarkar, C. K. Ghosh, and K. K. Chattopadhyay, *CrystEngComm.*, 2012, **14**, 2683-2690.

46. Z. Zhang, S. Ito, B. O'Regan, D. Kuang, S. M. Zakeeruddin, P. Liska, R. Charvet, P. Comte, M. K. Nazeeruddin, P. Pechy, *Z. Phys. Chem.*, 2007, **221**, 319-328.

47. Q. Wang, J. E. Moser, and M. Grätzel, *J. Phys. Chem. B*, 2005, **109**, 14945-14953.

48. Q. Wang, S. Ito, and M. Grätzel, *J. Phys. Chem. B*, 2006, **110**, 25210-25221.

49. M. Adachi, M. Sakamoto, J. Jiu, Y. Ogata, and S. Isoda, *J. Phys. Chem. B*, 2006, **110**, 13872-13880.

50. J. Van de Lagemaat, K. D. Benkstein, and A. J. Frank, *J. Phys. Chem. B*, 2001, **105**, 12433-12436.

51. K. D. Benkstein, N. Kopidakis, J. Van de Lagemaat, and A. J. Frank, *J. Phys. Chem. B*, 2003, **107**, 7759-7767.

7 N719- AND D-149-SENSITIZED 3D HIERARCHICAL RUTILE TIO_2 SOLAR CELLS – A COMPARATIVE STUDY

This chapter compared two dyes (N719 and D149) used as sensitizers for the rutile TiO_2-based DSCs.

Poor dye loading on rutile TiO_2 is one of the chief reasons for lower solar-to-electric conversion efficiency (η) in DSCs, compared to their anatase based counterparts. In chapter 6, similar light harvesting for both rutile and anatase was realized by using a metal-free organic indoline dye, D149. This was in contrast to the bulk of previous studies, which employed ruthenium based N719, leading to significant differences in light harvesting.

In this chapter, three-dimensional hierarchical rutile TiO_2 architecture (HRTA) with diameters of ~ 200 nm, which are much smaller than previous ones (~ 1-1.5 μm) and higher specific surface area (84 m^2g^{-1} compared to 67 m^2g^{-1}), was successfully prepared via a facile hydrothermal method, and subsequently optimized as effective photoelectrodes for DSCs. Two dyes, N719 and D149, were used as sensitizers of the HRTA-based DSCs, with maximum η of 5.6 % and 5.8 % achieved, respectively. The higher η of D149-sensitized DSC is ascribed to its higher extinction co-efficient, allowing a greater amount of light to be harvested with a thinner TiO_2 layer. This study suggests that some of the limitations typically observed for rutile TiO_2 based DSCs can be overcome through the use of strongly absorbing metal-free organic sensitizers. Furthermore, it reemphasises the importance of viewing DSCs as whole systems, rather than individual components.

This chapter has been published in *Physical Chemistry Chemical Physics*, 2015, **17**, 7208.

7.1 Introduction

Renewable energy resources continue to gain attention due to increasing global energy demands, limited access to fossil fuels, and an increasing awareness of the negative impacts of these carbon based resources. In the field of renewable energy, dye-sensitized solar cells (DSCs) have attracted significant attention, with much research conducted to enhance the efficiency of DSCs by developing or modifying individual DSC components, such as photoanodes, sensitizers, electrolytes, and counter electrodes. [1-12] As one of the key elements of the DSC, substantial research efforts have been focused on building TiO_2 micro/nanostructures with high surface area to provide improved charge transport while facilitating good light harvesting. Different TiO_2 architectures in the forms of 1D (tubes, wires, fibres, rods), 2D (sheets, belts), and 3D (spheres, trees, flowers) nanostructures have been developed, and to date, large size TiO_2 structures have been extensively used as scatterers to improve the light harvesting efficiency of DSCs. [13-28]

Less attention has been paid to rutile, especially three-dimensional (3D) hierarchical rutile architectures for use in DSCs. It is the authors' opinion that rutile has been ignored due to perceived issues such as its more positive conduction band edge potential, which are expected to result in lower open-circuit voltages (V_{oc}) than for anatase. [29] Previous studies have, however, shown that rutile-based DSCs can attain a similar V_{oc} to those made with anatase. [30] In this case, device performance seems to be mainly hindered by lower dye loading. In our previous study, we demonstrated that similar light harvesting for both rutile and anatase could be realized by using a metal-free indoline dye, D149, with a high peak extinction co-efficient (68700 M^{-1} cm^{-1} at 540 nm), hence comparable

efficiencies were obtained. [31] As yet there are no reports (to the best of our knowledge) comparing N719 and D149 rutile based DSCs. It is hoped that this work will demonstrate that the observed shortfalls of rutile are not inherent. Furthermore, it is hoped that this research will help to illustrate the importance of viewing a DSC as a system, rather than a collection of individual parts.

In this work, we report a modified 3D hierarchical rutile TiO_2 architecture (HRTA), which consists of 1D nanorods that were self-assembled to form microspheres, which were successfully prepared via a facile hydrothermal method without any surfactant or template, and optimized as an effective photoelectrode for DSCs. Two commercially available dyes, a ruthenium complex, N719 and a metal-free organic indoline D149, were used as sensitizers, with maximum solar-to-electric conversion efficiency (η) of 5.6 % and 5.8 % achieved, respectively. The higher η of D149-sensitized DSC is ascribed to its higher molar extinction co-efficient. Hence, metal-free organic D149 sensitizer can be considered as a better candidate for low-cost rutile-based DSC application.

7.2 Experimental

7.2.1 Synthesis of 3D Hierarchical Rutile TiO_2 Architectures (HRTA)

HRTA was prepared via a modified acid thermal process. [31] Briefly, 1.0 mL of Tetrabutyl titanate ($Ti(OCH_2CH_2CH_2CH_3)_4$, 97 %, analytical reagent grade) was added dropwise into 25 mL 1M hydrochloric acid (37 % HCl) whilst under stirring (for 1.5 h). This solution was transferred to a 45 mL Teflon lined reactor and sealed, then heated to 150 $^{\circ}$C for 5 h. Afterwards, the sample was cooled before being centrifuged and washed with ethanol three times, and finally dried at 90 $^{\circ}$C overnight under vacuum.

7.2.2 Preparation of Photoanode

Photoanodes were prepared in a manner similar to that reported previously. [31] Briefly, a dense TiO_2 layer [using spray pyrolysis of a titanium (IV) diisoproxide-*bis*-acetylacetonate (75 wt % in isopropanol, Aldrich) solution (dilution 1:9 in ethanol) at 450 $^{\circ}$C] was firstly applied on top of F: SnO_2 (FTO) glass. Then a layer of TiO_2 paste was cast onto the FTO glass plates by the doctor-blade method. Then the electrodes were subjected to a sintering process (150 $^{\circ}$C for 10 min, 325 $^{\circ}$C for 5 min, 375 $^{\circ}$C for 5 min, 450 $^{\circ}$C for 30 min, 500 $^{\circ}$C for 15 min).

7.2.3 Preparation of DSCs

The films were immersed in a 0.5 mM D149 (1-material, Canada) dye solution [1:1 (v/v) mixture of acetonitrile (HPLC, Lab-scan) and *tert*-butanol (LR, Ajax Chemicals)] or in a 0.5 mM N719 (Solaronix) dye solution [1:1 (v/v) mixture of *tert*-butanol (LR, Ajax Chemicals) and acetonitrile (HPLC, Lab-scan)] for overnight once their temperature decreased to ~ 110 $^{\circ}$C. The photoelectrode was sandwiched together

with the counter electrode [coated with one drop of 10 mM platinic acid solution (H_2PtCl_6 , Sigma)], using a 25 μm Surlyn (Solaronix) spacer. The I^-/I_3^- electrolyte solution [50 mM iodine (Sigma), 0.6 M 1,2-dimethyl-3-propylimidazelium iodide (Solaronix), 0.1 M lithium iodide (Sigma) in methoxypropionitrile (Sigma) for D149] [acetonitrile/valeronitrile (85:15 vol %), iodine (I_2) (0.03 M), 4 tertbutylpyridine (4-tBP) (0.5 M), 1-butyl-3-methylimidazolium iodide (BMII) (0.6 M), and guanidinium thiocyanate (GuSCN) (0.1 M) for N719] was introduced into the filling port by a vacuum back-filling technique.

7.2.4 Characterizations

XRD was employed to examine the crystal structures using an X-ray diffractometer (Bruker Advance, 40 kV, 30 mA) (Cu Kα, λ = 0.15406 nm) from 5º to 80º (2θ) (1 º/min). The morphology was examined by FE-SEM (Megallan 200) and TEM (JEM-2100F). The surface area and porosity were examined on a Tristar 3030 system (Micrometrics Instrument Corporation). A Veeco Dektak 150 Surface Profiler was used for the film thickness measurements. A Keithley 2400 source meter was used for *J-V* curve measurements, under air mass (AM) 1.5 global (1.5G) one sun illumination (100 mW cm^{-2}). A 300 W Xe lamp was used for IPCE measurements, a monocromator with sorting filters focused on a spot with additional optics. Electrochemical impedance spectroscopy (EIS) was performed at open circuit under illumination (0.1-1.0 MHz).

7.3 Results and Discussion

Figure 7.1(a, b) shows scanning electron microscope (SEM) and dark-field transmission electron microscope (DF-TEM) images of HRTA, synthesized by a facile hydrothermal treatment. Compared to our previous work, the increased quantity of titanium butoxide (from 0.5 mL to 1.0 mL) can be seen to result in more textured hierarchical spheres with diameters of ~ 200 nm, which are much smaller than previous ones (~ 1-1.5 μm). [31] Furthermore, the average specific surface area is higher (84 m^2g^{-1} compared to 67 m^2g^{-1}), which is further discussed below. High magnification SEM images of a full particle [Figure 7.1(c)] and a fractured one [Figure 7.1(d)] show that the structure is constructed from many radially structured, dendritic, and densely packed crystalline nanorods.

Figure 7.1(e, f) shows TEM images of a small fraction of one microsphere and a typical nanorod, respectively. The nanorod appears to be a 1D tetragonal prism with a width of 10 nm, similar to the SEM observations. The nanorods have a high aspect ratio (~ 20), calculated from an average width of ~ 10 nm and a diameter of ~ 200 nm.

The structure of the corresponding selected area electron diffraction (SAED) pattern [the inset of Figure 7.1(f)], confirms the nanorods to be single-crystal rutile TiO_2 structures, in agreement with the X-ray diffraction (XRD) pattern [Figure 7.2(a)], which can be indexed to a pure rutile TiO_2 crystal structure (JCPDS No. 21-1276; space group $P4_2/mnm$; a = 0.45927 nm, c = 0.29544 nm), the Raman spectrum [Figure 7.2(b)], indicating that the as-prepared sample possesses rutile phase according to the characteristic Raman modes at 118 cm^{-1} (B_{1g}), 438 cm^{-1} (E_g), and 607 cm^{-1} (A_{1g}) with a broad band near 240 cm^{-1} assigned to a second-order photon,

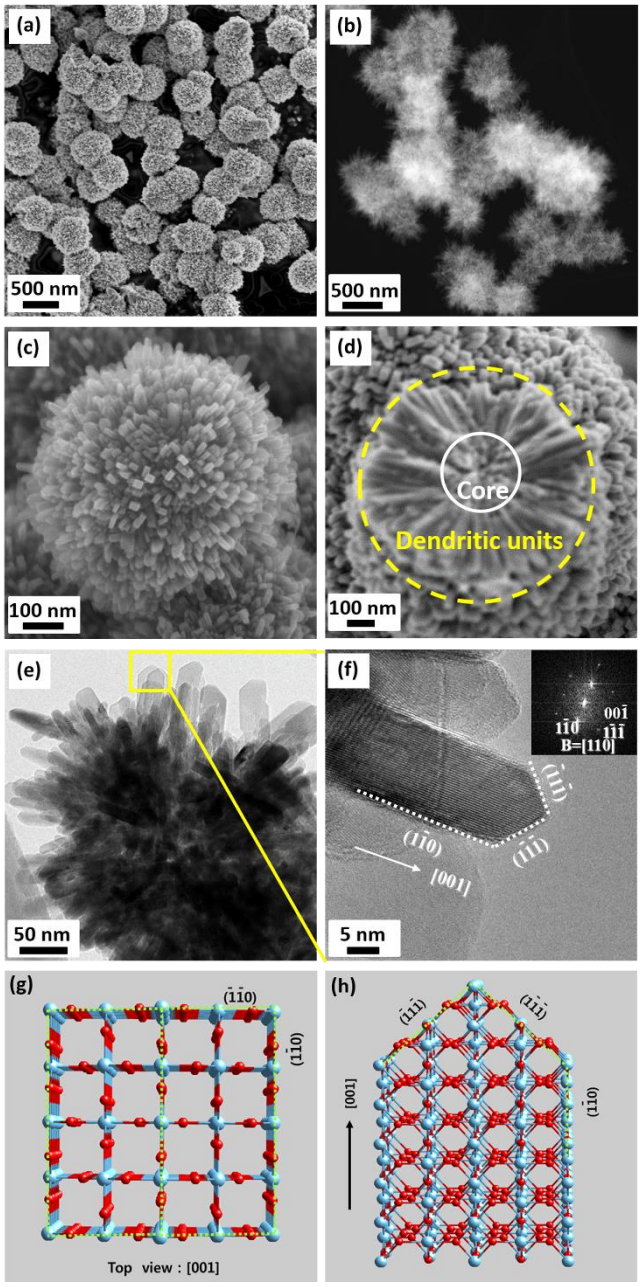

Figure 7.1 (a) Low magnification SEM image and (b) DF STEM image of 3D hierarchical rutile TiO_2 architecture (HRTA). (c) SEM image of an individual HRTA microsphere. (d) SEM image of a fractured microsphere. (e) TEM image of a quarter microsphere. (f) TEM image of individual nanorod; inset: corresponding SAED pattern. (g, h) atomic structure of a rutile nanorod.

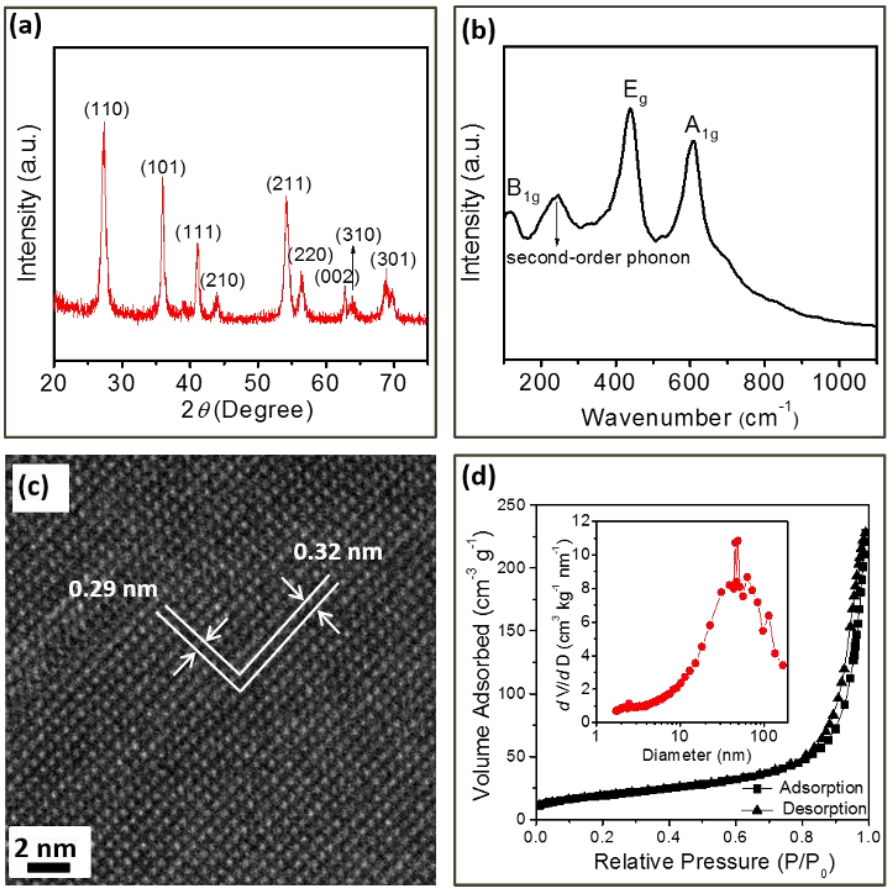

Figure 7.2 (a) XRD pattern, (b) Raman spectrum, (c) HRTEM image, (d) N_2 adsorption-desorption isotherms of the as-prepared HRTA; inset: corresponding pore size distribution calculated by the Barrett-Joyner-Halenda (BJH) method from the adsorption branch.

and high-resolution TEM (HRTEM) image [Figure 7.2(c)], showing the fringe spacings of rutile TiO_2 nanocrystal, with two kinds of fringes perpendicular to each other with *d*-spacings of 0.29 nm and 0.32 nm, which can be readily ascribed to the lattice spacings of the (001) and (110) planes, and is consistent with the *d* values of the (001) and (110) planes of the tetragonal rutile TiO_2, respectively.

SAED also reveals that the cuboid crystal facets are parallel to [110], and the pyramid-shaped crystal facets are parallel to [111], indicating that preferred growth takes place along the [001] direction, with the atomic structure as shown in Figure 1(g,

h). In general, the (110) crystal plane is perpendicular to the (001) crystal plane, and thus the nanorods grow along the (110) crystal plane with a preferred [001] orientation. It is reasonable to assume that the TiO_2 nanorod preferentially exposes the {110} side facets and the {111} top facets and grows along the [001] direction on the basis of above results together with the XRD pattern.

Brunauer-Emmett-Teller (BET) analysis of nitrogen adsorption-desorption measurements was performed to determine the specific surface area, porosity, and surface roughness factor for the HRTA materials, with the isotherm shown in Figure 7.2(d) and the data summarized in Table 7.1. The average specific surface area,

Table 7.1 Specific surface area, porosity, and roughness factor of 3D hierarchical rutile TiO_2 architecture (HRTA) material compared to a previous report (HRT-1).[31]

Samples	Specific surface area (m^2 g^{-1})	Porosity [a)] (%)	Roughness factor [b)] (μm^{-1})
HRTA	84	62.0	137.3
HRT-1	67	56.6	125

[a)] The porosity (P) of HRTA was calculated according to: $P = V_p / (q^{-1} + V_p)$, where V_p is the specific cumulative pore volume (cm^3 g^{-1}) and q is the density of TiO_2 (q = 4.3 g·cm^{-3}).

[b)] An estimation of the roughness factor (R) per unit film thickness of the films is obtained by $R = q\ (1\text{-}P)\ S$, where q is the density (g cm^{-3}) of TiO_2, P is the porosity (%) of the film, and S is the specific surface area (m^2 g^{-1}).

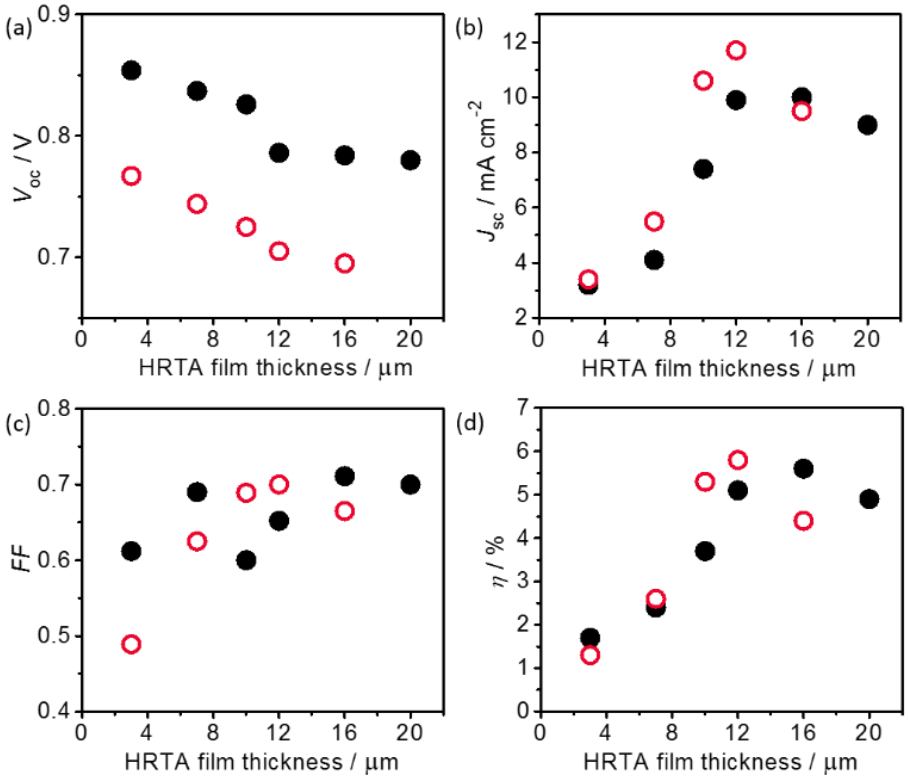

Figure 7.3 Photovoltaic characteristic of DSCs containing N719-based (black solid dots) and D149-based (red open dots) sensitizers as a function of nanocrytalline HRTA film thickness: (a) open-circuit voltage, V_{oc}, (b) short circuit photocurrent density, J_{sc}, (c) fill factor, *FF*, and (d) solar-to-electric energy conversion efficiency, η.

porosity, and roughness factor of HRTA were calculated to be 84 m^2g^{-1}, 62.0 % and 137.3 μm^{-1}, respectively. This is important given the previously mentioned concerns regarding dye loading.

Films of nanocrystalline HRTA particles with different thicknesses were manually doctor-bladed onto F-doped SnO_2 (FTO) glass substrates. These were used as the mesoporous working electrodes. Films were sintered and sensitised with either D149 or N719 before being assembled into devices with a Pt-loaded counter electrode and iodide-triiodide (I^-/I_3^-) based electrolyte.

Table 7.2 Photovoltaic parameters of N719- and D149-based DSCs measured under air mass (AM) 1.5 global (1.5G) one sun illumination (100 mW cm^{-2}). J_{sc}: short-circuit photocurrent density; V_{oc}: open-circuit photovoltage; *FF*: fill factor; η: total power conversion efficiency. The active areas were ~ 0.16 cm^2 for all of the cells (with the mask area 0.25 cm^2).

Samples	Film thickness[a)] (μm)	J_{sc} (mA cm^{-2})	V_{oc} (V)	*FF* (%)	η (%)
N719-DSCs	3	3.2	0.854	61.2	1.7
	7	4.1	0.837	69.0	2.4
	10	7.4	0.826	60.0	3.7
	12	9.9	0.786	65.2	5.1
	16	10.0	0.784	71.1	5.6
	20	9.0	0.780	70.0	4.9
D149-DSCs	3	3.4	0.767	48.9	1.3
	7	5.5	0.744	62.5	2.6
	10	10.6	0.725	68.9	5.3
	12	11.7	0.705	70.0	5.8
	16	9.5	0.695	66.5	4.4

[a)] Measurement of film thickness was carried out on a surface profile system (Veeco Dektak 150).

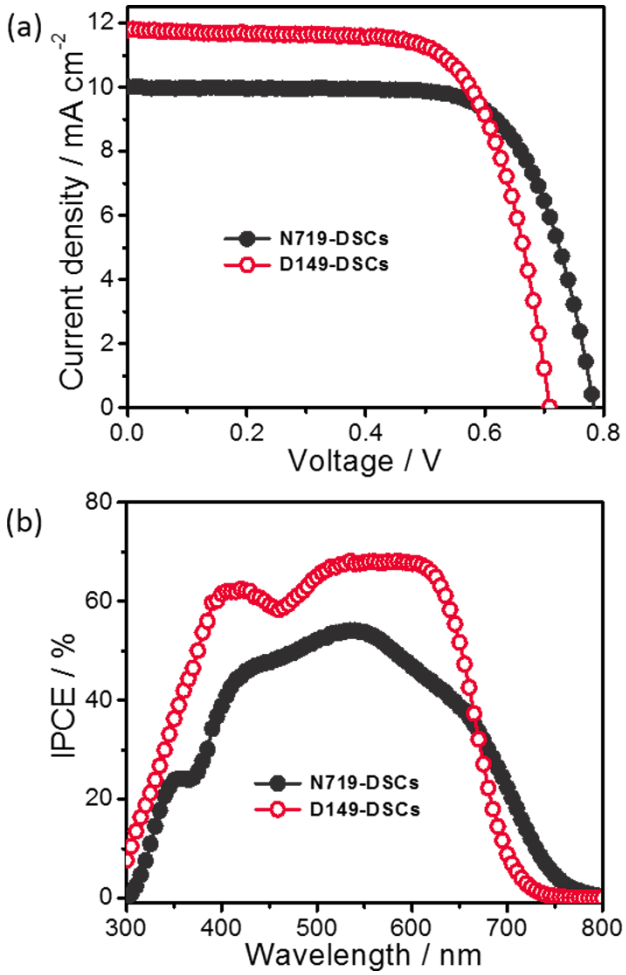

Figure 7.4 (a) *I-V* curves, (b) IPCE spectra of champion DSCs with N719-based (black solid dots) and D149-based (red open dots) sensitizers (light intensity: 100mA cm^{-2}, AM 1.5).

Current density-voltage results obtained under one sun illumination are shown in Figure 7.3, with key photovoltaic parameters summarized in Table 7.2. The open-circuit voltage [V_{oc}, Figure 7.3(a)] decreases for both the N719- and the D149-based DSCs with increasing HRTA film thickness, as per expectation, since (1) charge density, and hence the quasi Fermi level, decreases because the injected electrons are distributed throughout a larger volume and there are diminishing returns with regards

to light harvesting; and (2) the increased material surface area leads to more opportunities for charge-recombination to occur.

In contrast, the short circuit photocurrent densities (J_{sc}) [Figure 7.3(b)] increase up to a maximum value, before decreasing again for thicker HRTA films. For N719-based DSCs, J_{sc} increases continuously with film thickness from 3 μm to 16 μm, reaching a maximum value of 10.0 mA cm^{-2}, leading to a maximum η of 5.6 % [with *J-V* curve shown in Figure 7.4(a)], up from 5.3 % [Figure 7.3(d)], while D149-based DSCs attain their highest J_{sc} at 12 μm (just under 12 mA cm^{-2}, giving an overall conversion efficiency of 5.8 %). Aside from the thinnest D149-sensitized device, all revealed fill factor (*FF*) values [Figure 7.3(c)] are in the range of 0.65 ± 0.05, with no strong dependence observed.

Incident photon-to-current conversion efficiency (IPCE) spectra of champion DSCs with N719 and D149 dyes are presented in Figure 7.4(b). Higher IPCE values were obtained for D149-based DSCs than for N719-based DSCs; the peak IPCE values were observed at 535 nm for N719 and 540 nm for D149, reaching 54 % and 68 %, respectively. The D149-based DSCs have an impressive response over a wide spectral range; the IPCE values exceeded 60 % from 450 to 650 nm, resulting in the high J_{sc} value observed (~ 12 mA cm^{-2}). The average IPCE of the N719-based DSCs was 14 % lower than that of the D149-based DSCs from 350 to 650 nm, in contrast to the much wider photo-response range and much higher IPCE values for D149-based DSCs.

To better understand the electron transport properties in N719 and D149 sensitized DSCs, electrochemical impedance spectroscopy (EIS) measurements were performed at V_{oc} under 1 sun illumination (with both devices having a HRTA thickness of 10 μm), as shown in Figure 7.5(a). The equivalent circuit [in the inset of

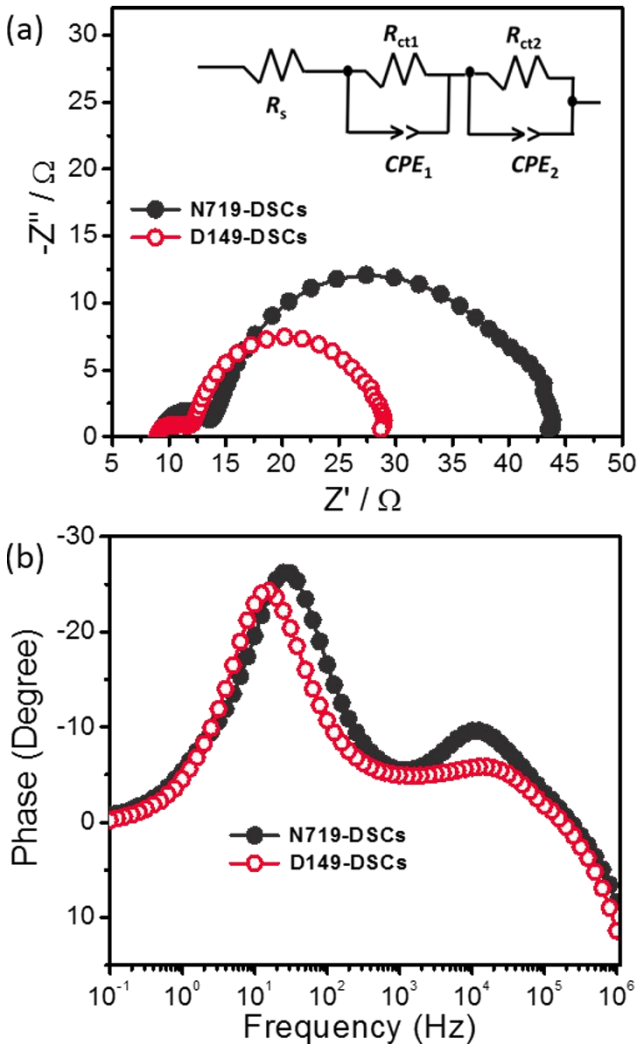

Figure 7.5 (a) Nyquist plots, inset: the equivalent circuit, (b) Bode phase plots of DSCs with N719-based (black solid dots) and D149-based (red open dots) sensitizers at V_{oc} under 1 sun illumination.

Figure 7.5(a)] was given to fit the series resistance (R_s), charge-transfer resistance (R_{ct}) and the corresponding constant phase angle element (*CPE*) in DSCs. [32-34] The large semicircle in the Nyquist plots at low frequency corresponds to the charge transfer resistance at the photoanode TiO_2/dye/electrolyte interface. It can be seen that the resistance at the HRTA/D149/electrolyte interface (R_{ct2}) is much smaller than that of the HRTA/N719/electrolyte interface, indicating a faster electron transfer process

relative to the electron recombination at the interface between HRTA and I_3^-/I^- for D149-based DSCs.

No currents pass through the external circuit at V_{oc} under 1 sun illumination, where electrons injected into the TiO_2 conduction band would trap and detrap and the trap states would be recombined by I_3^-. [35] Therefore, the electron lifetime (τ_{eff}) in the HRTA film can be estimated from the maximum angular frequency (ω_{max}) of the impedance semicircle arc at middle frequency in the Bode phase plots as:

$$\tau_{\text{eff}} = \frac{1}{\omega_{\max}} = \frac{1}{2\pi f_{\max}} \qquad (1)$$

Where f_{max} is the maximum frequency in the mid-frequency peak. Figure 7.5(b) shows that the middle frequency peak of D149-based DSCs shifts to higher frequency comparing to that of N719, indicating a longer electron lifetime and lower recombination rate. Thus, the efficient charge transfer at the TiO_2/D149/electrolyte interface, combined with the higher extinction coefficient of D149 (68700 M^{-1} cm^{-1} at 540 nm, compared to 13900 M^{-1} cm^{-1} at 535 nm for N719) may synchronously contribute to higher J_{sc} and η for the D149-based DSCs. [36]

7.4 Conclusions

3D hierarchical rutile TiO_2 architecture (HRTA) particles were successfully synthesized by a modified facile hydrothermal method, optimized for use in DSC photoanodes. N719 and D149 (a metal-free indoline dye) were compared as sensitizers, with efficiencies of 5.6 % and 5.8 % achieved for 16 µm-thick and 12 µm-thick films, for N719- and D149-based DSCs, respectively. The improved performance could be explained by enhanced light harvesting and reduced electron transfer resistance, with a faster electron transfer process relative to the electron recombination at the interface between HRTA and I_3^-/I^- for D149-based DSCs.

Not only does this work show that rutile TiO_2 may be a viable material for use in DSCs, but it also shows the importance of viewing the DSC as a system rather than simply focusing on the individual components therein.

7.5 References

1. A. B. F. Martinson, T. W. Hamann, M. J. Pellin, and J. T. Hupp, *Chem. Eur.* J., 2008, **14**, 4458-4467.

2. Q. Miao, L. Wu, J. Cui, M. Huang, and T. Ma, *Adv. Mater.,* 2011, **23**, 2764-2768.

3. J. Lin, L. Zhao, Y.-U. Heo, L. Wang, F. H. Bijarbooneh, A. J. Mozer, A. Nattestad, Y. Yamauchi, S. X. Dou, J. H. Kim, *Nano Energy*, 2015, **11**, 557-567.

4. S. Mathew, A. Yella, P. Gao, R. Humphry-Baker, B. F. E. Curchod, N. Ashari-Astani, I. Tavernelli, U. Rothlisberger, M. Nazeeruddin, and M. Grätzel, *Nat. Chem.,* 2014, **6**, 242-247.

5. J. Lu, X. Xu, K. Cao, J. Cui, Y. Zhang, Y. Shen, X. Shi, L. Liao, Y. Cheng, and M. Wang, *J. Mater. Chem. A*, 2013, **1**, 10008-10015.

6. T. Kinoshita, J. T. Dy, S. Uchida, T. Kubo, and H. Segawa, *Nat. Photonics.*, 2013, **7**, 535-539.

7. A. Yella, H. W. Lee, H. N. Tsao, C. Yi, A, K. Chandiran, M. K. Nazeeruddin, E. W. G. Diau, C. Y. Y, S. M. Zakeeruddin, and M. Grätzel, *Science,* 2011, **334**, 629-634.

8. J. Lin, Y.-U. Heo, A. Nattestad, Y. Yamauchi, S. X. Dou, J. H. Kim, Electrochim. Acta., 2015, **153**, 393-398.

9. W. Xiang, F. Huang, Y.-B. Cheng, U. Bach, and L. Spiccia, *Energy Environ. Sci.,* 2013, **6**, 121-127.

10. G. Li, X. Chen, and G. Gao, *Nanoscale*, 2014, **6**, 3283-3288.

11. M. Myahkostupov, M. Zamkov, and F. N. Castellano, *Energy Environ. Sci.*, 2011, **4**, 998-1010.

12. S. Rani, S. C. Roy, M. Paulose, O. K. Varghese, G. K. Mor, S. Kim, S.

Yoriya, T. J. Latempa and C. A. Grimes, *Phys. Chem. Chem. Phys.*, 2012, **12**, 2780-2785.

13. S. Wang, X. Zhou, X. Xiao, Y. Fang, and Y. Lin, *Electrochim. Acta,* 2014, **116**, 26-30.

14. O. K. Varghese, M. Paulose, and C. A. Grimes, *Nat. Nanotechnol.,* 2009, **4**, 592-597.

15. J. Liang, J. Yang, G. Zhang, and W. Sun, *Electrochem. Comm.,* 2013, **37**, 80-83.

16. Q. Zhang, D. Myers, J. Lan, S. A. Jenekhe, and G. Cao, *Phys. Chem. Chem. Phys.*, 2012, **14**, 14982-14998.

17. M. Law, L. E. Greene, J. C. Johnson, R. Saykally, and P. Yang, *Nat. Mater.,* 2005, **4**, 455-459.

18. S. Lee, G. S. Han, J.-H. Lee, J.-K. Lee, and H. S. Jung, *Electrochim. Acta,* 2012, **74**, 83-86.

19. F. H. Bijarbooneh, Y. Zhao, Z. Q. Sun, Y. U. Heo, V. Malgras, J. H. Kim, and S. X. Dou, *APL Mater.,* 2013, **1**, 032106/1-7.

20. N. T. Hieu, S. J. Baik, Y. Jun, M. Lee, O. H. Chung, and J. S. Park, *Electrochim. Acta,* 2014, **142**, 144-151.

21. Z. Wang, H. Wang, B. Liu, W. Qiu, J. Zhang, S. Ran, H. Huang, J. Xu, H. Han, D. Chen, and G. Shen, *ACS Nano,* 2011, **5**, 8412-8419.

22. B. Liu, and E. S. Aydil, *J. Am. Chem. Soc.,* 2009, **131**, 3985-3990.

23. W. Yang, J. Li, Y. Wang, F. Zhu, W, Shi, F. Wan, and D. Xu, *Chem. Commun.,* 2011, **47**, 1809-1811.

24. J. Yu, J. Fan, and K. Lv, *Nanoscale,* 2010, **2**, 2144-2149.

25. Q. Chen, H. Liu, Y. Xin, and X. Cheng, *Electrochim. Acta,* 2013, **111**, 284-291.

26. F. Sauvage, F. D. Fonzo, A. L. Bassi, C. S. Casari, V. Russo, G. Divitini, C. Ducati, C. E. Bottani, P. Comte, M. Grätzel, *Nano Lett.,* 2010, **10**, 2562-2567.

27. J. Lin, A. Nattestad, Y. Hua, Y. Bai, L. Wang, S. X. Dou, and J. H. Kim, *J. Mater. Chem. A*, 2014, **2**, 8902-8909.

28. W.-Q. Wu, Y.-F. Xu, H.-S. Rao, C.-Y. Su, and D.-B. Kuang, *Nanoscale*, 2013, **5**, 4362-4369.

29. M. R. Hoffmann, S. T. Martin, W. Choi, and D. W. Bahnemann, *Chem. Rev.,* 1995, **95**, 69-96.

30. N.-G. Park, J. Van de Lagemaat, and A. Frank, *J. Phys. Chem. B,* 2000, **104**, 8989-8994.

31. J. Lin, Y.-U. Heo, A. Nattestad, Z. Sun, L. Wang, J. H. Kim, and S. X. Dou, *Sci. Rep.,* 2014, **4**, 5769.

32. Q. Wang, J. E. Moser, and M. Grätzel, *J. Phys. Chem. B* 2005, **109**, 14945-14953.

33. P. Kern, P. Sastrawan, J. Ferber, R. Stangl, and J. Luther, *Electrochim. Acta,* 2002, **47**, 4213-4225.

34. M. Adachi, M. Sakamoto, J. Jiu, Y. Ogata, and S. Isoda, *J. Phys. Chem. B,* 2006, **110**, 13872-23880.

35. K.-M. Lee, V. Suryanarayanan, and K.-C. Ho, *Sol. Energy Mater. Sol.*, Cells, 2007, **91**, 1416-1420.

36. M. K. Nazeeruddin, S. M. Zakeeruddin, R. Humphry-Baker, M. Jiousek, P. Liska, N. Vlachopoulos, V. Shklover, C.-H. Fischer, and M. Grätzel, *Inorg. Chem.,* 1999, **38**, 6298-6305.

8 CONCLUSION

This thesis investigates different TiO_2 architectures for high efficient dye-sensitized solar cells. In general, to obtain higher solar-to-electric conversion efficiency in DSC, a photoanode material which is usually composed of TiO_2 architectures should meet the following requirements: 1) the surface area should be high enough to efficiently absorb the dye solution; 2) the porosity should be high enough for efficient electrolyte diffusion and effective mass transportation; 3) particle size should be big enough for efficient light scattering; 4) grain boundaries should be minimized for faster electron transportation. However, the requirements cannot be met in one system. Therefore, the thesis emphasies on the materials design and synthesis (having high surface area, broad pore size distribution, 1D/2D building blocks, micro-sized particles, *etc*), as well as different design for different types of DSCs, such as flexible DSCs, cobalt electrolyte-based DSCs, and rutile TiO_2-based DSCs. In particular, three-dimensional TiO_2 architectures composed of 1D/2D nanoribbon/nanorod/nanosheet have clearly demonstrated their electrochemical performance in the application of DSC filed, which contributes to the high specific surface area, enhanced light scattering capability, and faster electron transport.

In chapter 3, a new type of highly connected hierarchical textured TiO_2 spheres was rationally designed. These spheres are sea urchin-like assemblies, composed of high aspect-ratio nanosheets, with a bimodal distribution of sizes, leading to both effective dye adsorption and effective light-scattering behaviour, as well as enhanced electronic interconnectivity within the photoanode. An overall energy conversion efficiency of up to 9.0 % can be achieved by using these spheres as the photoelectrode with N719 dye, a considerable improvement over commercial Dyesol paste (8.2 %) under the same conditions.

In chapter 4, another type of photoanode, where microstructured TiO_2 sea urchin-like assembly, composed of high aspect-ratio nanoribbons was deposited onto nanoparticle layer (P25), with 5.8 % conversion efficiency realized, a considerable improvement compared to P25 (4.5 %) under the same conditions. It was demonstrated that this hierarchical TiO_2 nanostructure is beneficial due to its enhanced dye loading as well as enhanced light scattering. Importantly, it also showed the benefits of a bi-layer structure where the nanoribbons penetrate into the nanoparticle layer (P25) after CIP, resulting in improved adhesion between the TiO_2 anode film and the P25 under layer on the indium tin oxide-coated polyethylene naphthalate (ITO|PEN) substrate, leading to improved mechanical stability and durability, efficient electron transfer pathways, and ultimately, higher solar-to-electric conversion efficiencies.

In chapter 5, the preparation of mesoporous anatase single crystals (MASCs) by a facile one-step hydrothermal route, without additives or templates, is reported for the first time. The resultant material comprises ellipsoidal mesoporous particles with long range crystallinity. Films composed of these particles were sensitised with an organic dye, MK-2, and employed as a photoanode in DSCs with a cobalt redox shuttle. These devices displayed photon-to-electron conversion efficiencies up to an impressive 8.7 % under air mass (AM) 1.5 irradiation, significantly higher than for analogous devices based on commercial Dyesol TiO_2 (6.3 %). The enhanced performance for devices containing MASCs is mainly attributable to the good electronic connectivity throughout the single crystal structure, resulting in faster electron transportation in the TiO_2, and thus a higher fill factor (*FF*). The well-defined mesoporous structure allows fast diffusion of electrolyte components, as well as leading to high surface area without compromising the large crystal size, which

affords a high light harvesting efficiency (LHE). Additionally, the crystals are large enough that the material effectively scatters incident light, further increasing the LHE.

In chapter 6, a new series of 3D hierarchical rutile TiO_2 architectures (HRT) with controlled morphologies and sized subunits by the aid of a facile acid-hydrothermal method, without any surfactant or template. A solar-to-electric conversion efficiency of 5.5 % was achieved using a HRT as the photoelectrode with D149 dye, which is significantly better than devices made using P25 (4.5 %) and comparable to state-of-the-art commercial transparent titania anatase paste (5.8 %). This power conversion efficiency is due to a considerable surface area for the high dye adsorption and a superior light scattering ability. In addition, the overall conversion efficiency 8.6 % was achieved when HRT was further used as the light scattering layer, a considerable improvement over commercial transparent/reflective titania anatase paste (7.6 %).

In chapter 7, two commercially available dyes, a ruthenium complex, N719 and a metal-free organic indoline D149, were used as sensitizers, with maximum solar-to-electric conversion efficiency (η) of 5.6 % and 5.8 % achieved, respectively. The higher η of D149-sensitized DSC is ascribed to its higher molar extinction co-efficient. Hence, metal-free organic D149 sensitizer can be considered as a better candidate for low-cost rutile-based DSC application. Not only does this show that rutile TiO_2 may be a viable material for use in DSCs, but it also shows the importance of viewing the DSC as a system rather than simply focusing on the individual components therein.